

# ATOMISTIC MODELLING OF HYDROCARBONS IN PLASMA-WALL INTERACTION

Inauguraldissertation  
zur  
Erlangung des akademischen Grades  
doctor rerum naturalium (Dr. rer. nat.)  
an der Mathematisch-Naturwissenschaftlichen Fakultät  
der  
Ernst-Moritz-Arndt-Universität Greifswald



vorgelegt von

Amit Raj Sharma

geboren am 02.06.1973  
in Kanker, Indien

Greifswald, 2007

**Dekan:** \_\_\_\_\_

**1. Gutachter:** \_\_\_\_\_

**2. Gutachter:** \_\_\_\_\_

**Tag der Promotion:** \_\_\_\_\_

© Copyright by  
Amit Raj Sharma  
2008

# Table of Contents

<b>Table of Contents</b> . . . . .	iv
<b>Abstract</b> . . . . .	vii
<b>List of Tables</b> . . . . .	ix
<b>List of Figures</b> . . . . .	x
<b>Acknowledgments</b> . . . . .	xi
<b>Dedication</b> . . . . .	xii
<b>Preface</b> . . . . .	xiii
<b>1 Introduction</b> . . . . .	1
1.1 Hydrocarbons . . . . .	1
1.2 Fusion . . . . .	2
1.3 Astrophysics . . . . .	4
1.4 Combustion . . . . .	7
1.5 Motivation . . . . .	8
1.6 Dissertation outline . . . . .	11
<b>2 Basic theory and Methods</b> . . . . .	13
2.1 Introduction . . . . .	13
2.2 Molecular dynamics . . . . .	13
2.2.1 Historical Background . . . . .	14
2.2.2 Basic Approach . . . . .	14
2.2.3 Statistical Ensemble . . . . .	16
2.2.4 Macroscopic Parameters . . . . .	16
2.2.5 Temperature Scaling . . . . .	17
2.2.6 Pressure Scaling . . . . .	18
2.3 Ab initio molecular dynamics . . . . .	18
2.4 Molecular Potential Energy Surface . . . . .	20
2.4.1 Topography . . . . .	21
2.4.2 Electronic structure calculations . . . . .	21
2.5 Methods . . . . .	22
2.6 Many-body Quantum Mechanics . . . . .	22
2.7 The Born-Oppenheimer Approximation . . . . .	24
2.7.1 Hartree-Fock theory . . . . .	24
2.7.2 Post Hartree-Fock techniques . . . . .	29
2.8 Spectroscopic analysis . . . . .	31
2.8.1 Brief description of theory: VSCF . . . . .	32
2.8.2 VSCF-CI theory . . . . .	35

---

2.8.3	VCI theory	35
2.9	Quasi-classical trajectory calculations: Description of theory	36
2.9.1	Initial conditions	36
2.9.2	Product properties	38
2.10	Density Functional Theory	40
2.10.1	The Hohenberg and Kohn theorems	41
2.10.2	Kohn and Sham Method	42
2.10.3	The local density approximation	44
2.10.4	Implementations of Kohn and Sham method	45
2.10.5	Periodic systems	46
2.10.6	Brillouin zone sampling	48
2.10.7	The pseudopotential approximation	49
2.10.8	Performance of DFT	50
2.11	Subsumption	51
<b>3</b>	<b>Potential Energy Surface</b>	<b>52</b>
3.1	Introduction	52
3.2	Coordinate	52
3.3	Many-body expansion	53
3.4	Invariant Polynomials	53
3.5	Dipole moment surface	55
3.6	Potential Energy Surface of $C_2H_3^+$	56
3.6.1	Potential Energy Surface	56
3.6.2	Properties of the PES	58
3.7	Potential Energy Surface of $C_2H_5^+$	59
3.7.1	Potential Energy Surface	61
3.7.2	Properties of the PES	61
3.8	Subsumption	62
<b>4</b>	<b>Spectroscopic calculation</b>	<b>63</b>
4.1	Introduction	63
4.2	Vibrational Analysis of $C_2H_3^+$	63
4.2.1	Single Reference Calculations	65
4.2.2	Reaction Path Hamiltonian Analysis	66
4.3	Results and Discussion	68
4.3.1	Single Reference Calculation	68
4.3.2	Reaction Path Hamiltonian	70
4.4	Spectroscopic calculations for $C_2H_5^+$	72
4.4.1	Single Reference Calculations	77
4.5	Subsumption	79
<b>5</b>	<b>Global potential energy surface and dynamics</b>	<b>80</b>
5.1	Introduction	80
5.2	Global potential energy surface	80
5.3	Results and Discussion	82
5.4	Subsumption	85

<b>6</b>	<b>DFT studies</b>	87
6.1	Introduction	87
6.2	Motivation	89
6.3	Ab initio MD	89
6.4	Hydrogen diffusion in bulk Graphite	90
6.4.1	Ab initio molecular dynamics	94
6.5	Hydrocarbon interaction with amorphous a-C:H surface	96
6.6	Subsumption	98
<b>7</b>	<b>MD simulation of hydrocarbon interaction with a-C:H</b>	99
7.1	Introduction	99
7.2	Modelling	99
7.3	Results and discussion	101
7.3.1	Reflection coefficients	101
7.3.2	Reflection coefficients for CH <sub>x</sub> (x=1-4)	102
7.3.3	Reflection coefficients for C <sub>2</sub> H <sub>x</sub> (x=1-6)	103
7.3.4	Break-up pattern	104
7.4	Subsumption	105
<b>8</b>	<b>Conclusions and Summary</b>	107
<b>Bibliography</b>		110

# Abstract

Hydrocarbons are of great interest in the low-temperature plasmas, interstellar medium and most importantly in the plasma-wall interaction region. Chemical reactions and physical sputtering of the wall material due to the incident hydrogenic species lead to the formation of volatile hydrocarbon molecules resulting in hydrocarbon co-deposits, which are of great importance due to their high absorbing capacity of tritium. The energetic hydrogenic species also penetrate into solid carbon and are trapped within the solid, creating broken carbon bonds where hydrogen can be strongly bound through the formation of C-H chemical bonds. The importance of hydrocarbon ions in the plasma-wall interaction as well as neutral media motivates the present work.

Modelling of hydrocarbons under such varying conditions and with varying system sizes requires an atomistic multi-scale approach, which uses the most accurate methods to compute the inter-atomic potential at different length scales (ranging from systems with small molecules to system with thousands of atoms). This approach is followed in the present work. A key tool in the computational modelling of small hydrocarbon molecules, molecule-, molecule-radical interaction such as those in the low-temperature plasmas and interstellar medium is the construction of accurate fitted potential energy and dipole moment surfaces (PES and DMS) that are full-dimensional, obey the required symmetry under permutation of like nuclei, and describe all relevant spectroscopic information and reaction channels. Accurate quantum-mechanical calculations are affordable for such small molecules and result in the most accurate inter-atomic potential description. For systems with few hundreds of atoms such as atomic clusters, biomolecules and crystalline systems, Density Functional Theory (DFT) provides the most reasonable potential description and for systems with thousands of atoms such as those in amorphous co-deposits semi-empirical potentials can be used.

To develop a potential energy surface (PES) which has the form of a many-body (cluster) expansion a unique method developed by Braams and co-workers is used. The PES uses basis functions that satisfy the criterion of invariance under interchange of like nuclei, with coefficients fitted to *ab initio* calculations. High accuracy electronic structure calculations are performed for thousands of configurations spanning the nuclear configuration hypersurface. The sampling of the configuration space is done by the use of molecular dynamics (MD) and diffusion Monte Carlo (DMC) runs. Based on these *ab initio* calculation a PES is generated for carbocations  $C_2H_3^+$  and  $C_2H_5^+$ . Important stationary points, such as the global minimum, local minima and higher order saddle points are accurately identified on the surface, although these points are not added explicitly. Normal mode analysis on the PES shows excellent agreement with the direct *ab initio* calculations and also with the values published in the literature.

Vibrational self-consistent field (VSCF) method in conjunction with the PES developed in the present work is used to obtain anharmonic frequencies. The VSCF method is based on a representation of the vibrational wavefunction as a product of single-mode wavefunctions. Following VSCF, virtual configuration interaction (VCI) calculations are performed, which is the vibrational analog of the electronic structure configuration interaction (CI) theory. The VCI method can accurately solve the problem of coupled vibrations, which physically arise because

the vibrationally excited states of polyatomic molecules exhibit displacements so large that anharmonicities become important, causing the harmonic modes to mix. Full-dimensional calculations of vibrational energies for  $C_2H_3^+$  and  $C_2H_5^+$  are performed using the “single-reference” vibrational methods. Tunneling splittings for the fundamental excitations and zero point energy are derived from “reaction path” Hamiltonian calculations.

A global potential energy surface is developed for  $C_2H_3^+$  by adding fragment data to the complex region data. Multi-reference calculations show that the potential energy curves for charge-exchange reaction cross each other and excited electronic states are needed. However, the hydrogen abstraction reaction can be calculated on the ground state surface. In order to simulate the ground state dynamics, the quasi-classical trajectory program VENUS96 is modified to perform H abstraction reaction ( $C_2H^+ + H_2 \rightarrow C_2H_2^+ + H$ ) dynamics on the global PES. Fixed mode energies are used to sample the initial vibrational state of the reactants by the use of normal mode analysis on the fitted PES. It is observed that the global PES is able to accurately represent the normal mode energies of the reactants, thus validating the fit. The trajectories at relative translational energy of 1 eV, integrated up to 5.0 ps ended up as long lived trajectories and the products did not separate by an appreciable distance for the calculations to be stopped.

The density functional methods based on plane waves and normconserving pseudopotentials are an important tool to perform larger length scale simulations. This method is applied in the present work to perform *ab initio* molecular dynamics to study the diffusion of atomic hydrogen trapped within crystalline graphite. Important differences are observed between *ab initio* dynamical calculations and the classical molecular dynamics simulations using the famous empirical Brenner potential. The *ab initio* molecular dynamics calculations at 10 and 300 K shows that the H atom quickly finds a lower energy configuration towards the graphene plane and forms a chemical bond with one of the C atoms in graphite. At these temperatures the H atom is not able to overcome the barrier and thus is not able to diffuse. These results are drastically different from those obtained by the use of empirical Brenner potential, which shows that the H atom is able to freely diffuse. The potential energy curves calculated using Brenner potential show a flat potential in the central region between graphite planes whereas for DFT calculations a higher potential energy region between the two planes is observed due to the contribution from the non-local pseudopotential energy term.

Finally, to simulate hydrocarbon co-deposits and interaction of hydrocarbon radicals and molecules with the amorphous surface, further larger length scale classical molecular dynamics simulations are performed to calculate the sticking probability and break-up patterns. Sticking/reflection probability as a function of incident energy is calculated for atomic carbon,  $C_2$ , CH,  $CH_2$ ,  $CH_3$ ,  $CH_4$ ,  $C_2H$ ,  $C_2H_2$ ,  $C_2H_3$  and  $C_2H_4$ . The reflection coefficients shows a decreasing trend with increasing incident energy. It is observed that the numerical values of the reflection coefficient and reflection break-up pattern is sensitive to the hydrogen and carbon stacking in the sample surface. Further on, it is observed that the reflection coefficient increases as the hybridization changes from *sp* to *sp*<sup>3</sup>.

Hydrocarbons are still a complex problem and this thesis tries to contribute to a better fundamental understanding utilizing a multi-scale approach: small systems are studied with *ab initio* quantum-mechanical methods (Hartree-Fock and post Hartree-Fock, DFT), larger systems with classical MD.

# List of Tables

4.1	Harmonic freq. and ZPE for Bridged structure . . . . .	64
4.2	Harmonic freq. and ZPE for Y Structure . . . . .	65
4.3	Vibrational energies at 5, 4 and 3 mode coupling . . . . .	69
4.4	Multimode SR and RPH results . . . . .	71
4.5	Harmonic frequencies ( $\text{cm}^{-1}$ ) for the nonclassical bridged structure of $\text{C}_2\text{H}_5^+$ . . . . .	73
4.6	Harmonic frequencies ( $\text{cm}^{-1}$ ) for the classical Y-Shaped structure of $\text{C}_2\text{H}_5^+$ . . . . .	75
4.7	Harmonic frequencies ( $\text{cm}^{-1}$ ) of first order saddle point . . . . .	76
4.8	Harmonic frequencies ( $\text{cm}^{-1}$ ) of second order saddle point . . . . .	76
4.9	Harmonic frequencies ( $\text{cm}^{-1}$ ) of low lying stationary points . . . . .	77
4.10	Vibrational energies of $\text{C}_2\text{H}_5^+$ using 4 and 3 mode coupling . . . . .	78

# List of Figures

1.1	Schematics showing atomistic multiscale approach. . . . .	10
2.1	Volume element for a particle . . . . .	23
3.1	Minimum and stationary point configuration for $C_2H_3^+$ . . . . .	58
3.2	Global min and low lying stationary points on $C_2H_5^+$ PES . . . . .	60
4.1	Normal modes vector plot for Bridged structure . . . . .	65
4.2	Reaction path definition . . . . .	67
4.3	PES vs <i>ab-initio</i> energy along the reaction path . . . . .	68
4.4	Normal Modes of the $C_2H_5^+$ non-classical bridged structure . . . . .	74
5.1	Schematics showing fragment energies w.r.t global minimum . . . . .	81
5.2	Potential energy vs distance of bridging hydrogen . . . . .	83
5.3	Potential energy curves (MRCI) of singlet $C_2H_3^+$ . . . . .	84
5.4	Potential energy profile for a sample QCT trajectory . . . . .	85
6.1	H atom sites between graphene planes . . . . .	90
6.2	Radial distribution function of <i>ab initio</i> MD sample. . . . .	91
6.3	1-D potential energy cuts . . . . .	92
6.4	RDF of equilibrated graphite structure used in classical MD simulation . . . . .	93
6.5	1-D potential energy cuts using empirical Brenner potential . . . . .	94
6.6	Effect of nonlocal pseudopotential energy . . . . .	95
6.7	Energy profile of H-diffusion at 10 Kelvin . . . . .	96
6.8	Sticking of H atom in MD simulation at 10 Kelvin . . . . .	97
7.1	Depth profile showing H to C ratio . . . . .	101
7.2	Radial distribution function . . . . .	101
7.3	Statistically uncertainty due to orientation . . . . .	102
7.4	Atomic C and $C_2$ reflection coefficient . . . . .	103
7.5	Reflection coefficient for $CH_x$ (x=1-4) . . . . .	104
7.6	Reflection coefficient for $C_2H_x$ (x=1-6) . . . . .	105
7.7	Break-Up pattern for $C_2H_6$ . . . . .	106

# Acknowledgments

Firstly, I express my deep and sincere gratitude to my supervisor, Dr. Ralf Schneider. I wish to sincerely thank him for making this period of work, my best years. I could not have imagined having a better advisor and mentor for my PhD. His scientific guidance, inspiration, perspiciveness and joyous nature always made work more enjoyable. I also thank him for his constant encouragement and unconditional support.

I am deeply indebted to Dr. Bas Braams and Prof. Joel Bowman for their hospitality during my visits to Emory and introducing me to the world of quantum chemistry. I wish to express my sincere thanks for their guidance, insight, and support during this research.

I would like to extend a special word of appreciation and gratitude towards Henry Leyh and Dr. Matthias Borchardt for patiently addressing my computer problems and promptly responding to it.

A special thank to Jutta Gauger, the real work-force of Stellarator Theory group, who made my life so much simpler by helping me in many different ways.

Many thanks to everyone in the Stellarator Theory group and at Institute für Physik, Greifswald University for being nice and friendly. It was a pleasure for me to have spend time with such wonderful people.

I would like to thank Dr. Olaf Grulke for maintaining a good spirit within the International Max-Planck Research School (IMPRS) in Greifswald and his constant efforts towards betterment of the IMPRS.

I am indebted to Dr. Shashank Chaturvedi from whom I learnt a lot during my early years as a researcher and I thank him for letting me have this opportunity. I would also like to thank my colleagues and friends at the Institute for Plasma Research for their unconditional support.

Many thanks to the gang, all my friends and my colleagues in Greifswald. You made my stay enjoyable and something to remember for life.

Finally, I have to say “thank-you” to: all my friends and family, wherever they are, particularly my parents; and, most importantly of all, to Swati, for everything and for giving me the most wonderful gift of “life”.

# Dedication

*This thesis is dedicated to my parents who taught me the value of education  
and to my loving wife who supported me throughout this venture.*

# Preface

This thesis is the final work of my Ph.D. study at the Max-Planck-Institut für Plasmaphysik, Greifswald, Germany. It serves as a documentation of my work during the study, which has been made from June 2005 until December 2007, in the Computational Material Science group (COMAS), under the supervision of Dr. Ralf Schneider.

# Chapter 1

## Introduction

During the initial big bang, the universe could only manufacture the very lightest elements: hydrogen, helium, lithium, and beryllium. While the necessary helium was being made, the burst was still expanding and cooling. After about 1000 seconds the temperature of the universe had dropped from a temperature of few billion Kelvins to a few hundred million Kelvins, a tenfold decrease.

At these relatively “cool” temperatures the helium nuclei could not overcome the repulsive forces of the two protons in each helium nucleus. So nuclear reactions fusing helium into heavier elements could not ignite. Soon it became too cool to even maintain the hydrogen fusion reactions. The other 88 elements were not made during the big bang because the universe was too cool. Nuclear fusion reactions need very high temperatures, densities, and pressures to survive. However, as the universe expands, it behaves like a gas and the temperature, density, and pressure decrease.

A second opportunity for nuclear activity arose only when the original fluctuations of the early universe had grown sufficiently large for haloes of dark matter to begin to form. This triggered gravitational instabilities and the collapse of conventional baryonic matter into clouds of gas, from which stars then formed; in the cores of these stars, both the temperature and density reached values that again made nuclear reactions possible. Practically all the heavier elements, from carbon to uranium – the elements from which later solid planets and organic life formed – were synthesized in these first stars.

Since its inception, carbon has become the key elemental building block for all terrestrial life. It's commonly assumed in astrobiology that it will also provide the basis for most life elsewhere in the universe. The reason for this is carbon's ability to form a staggering range of complex, stable molecules with itself and other elements, especially hydrogen, oxygen, and nitrogen.

### 1.1 Hydrocarbons

Hydrocarbons are a chemical compound consisting of only hydrogen and carbon atoms bonded together. Chemically, hydrocarbons can be in the form of straight-chains, branched chains, or cyclic molecules. Hydrocarbons are among the most widely observed chemical compounds naturally occurring in petroleum, natural gas, coal and wood, which are often used as fuels.

Hydrocarbons have been classified as, Saturated hydrocarbons (alkanes) which are the most simple of the hydrocarbon species and are composed entirely of single bonds and are saturated with hydrogen. The second class of hydrocarbons are, Unsaturated hydrocarbons having one or more double or triple bonds between carbon atoms. The ones with double bond are called alkenes, with the formula  $C_nH_{2n}$  (assuming non-cyclic structures). Those containing triple bonds are called alkynes. The third class of hydrocarbons are termed; Cycloalkanes, which are hydrocarbons containing one or more carbon rings to which hydrogen atoms are attached.

The general formula for a saturated hydrocarbon containing one ring is  $C_nH_{2n}$ . The fourth class are, Aromatic hydrocarbons, also known as arenes which have at least one aromatic ring. Hydrocarbons can be gases (e.g. methane and propane), liquids (e.g. hexane and benzene), waxes or low melting solids (e.g. paraffin wax and naphthalene) or polymers (e.g. polyethylene, polypropylene and polystyrene).

The inherent ability of hydrocarbons to bond to themselves is referred to as catenation, and allows hydrocarbon to form more complex molecules, such as cyclohexane, and in rarer cases, arenes such as benzene. Catenation arises due to the non-polar bond character between carbon atoms, in that the distribution of electrons between the two elements is somewhat even due to the same electronegativity values of the elements ( $\sim 0.30$ ), and does not result in the formation of an electrophile. Catenation give rise to loss of the total amount of bonded hydrocarbons and an increase in the amount of energy required for bond cleavage due to strain exerted upon the molecule; in molecules such as cyclohexane, this is referred to as ring strain, and occurs due to the “established” spatial electron configuration of the atom.

## 1.2 Fusion

Fusion power refers to power generated by nuclear fusion reactions. In this kind of reaction, two light hydrogenic atomic nuclei fuse together to form a heavier helium nucleus and release energy. Fusion between the atoms is opposed by their shared electrical charge, specifically the net positive charge of the nuclei. In order to overcome this electrostatic force, or “Coulomb barrier”, some external source of energy must be supplied, or the reactants should be confined in a small region in space by brute force, provided by gravity in all the stars. The alternative approach followed in laboratories is to heat the atoms, which has the side effect of stripping the electrons from the atoms and leaving them as ions or bare nuclei. In most experiments the ions and electrons are left in a fluid known as a plasma. Such a hot plasma can be confined by the use of the closed mesh of magnetic field lines. Thus, fusion energy research is concerned with the study of hot plasma in a magnetic field and with the design and optimization for magnetic plasma confinement systems for fusion experiments.

A magnetically confined plasma is an extraordinarily complicated medium by any standards of scientific research. However, a lot of knowledge has been gained in the past, both experimentally and theoretically. Magnetically confined plasma is extremely anisotropic, with typical particle mean free paths of the order of  $10^4$  m along the magnetic field lines and a ion gyro-radius of the order of millimeters around the field lines. The collision time is long compared to the timescale of many dynamical phenomena, timescales of interest range from the sub-microsecond timescale for plasma turbulence, via, anywhere from  $10^{-6}$  s to  $10^{-3}$  s for fast MHD (Magneto-hydrodynamics) phenomena, to many seconds for slow plasma evolution. The magnetic field is itself a dynamical quantity of interest, and the electric field and magnetic field perturbations created by the plasma provide global coupling in the plasma evolution. The confined plasma supports a large variety of electromagnetic waves, of interest for plasma heating and for plasma diagnostics, which may have widely disparate wavelengths and yet are tightly coupled through mode conversion processes.

Such complexities have challenged research and engineers for many decades. Various plasma confinement devices have been built and operated around the world. Learning from these experiments tell us that the magnetic trap in a plasma confinement device for the confinement of particles and energy is not perfect. Energy and matter diffuse radially outwards from the high

temperature and high density region in the center, where the magnetic field lines are in a closed circuit. This has the result of taking large quantities of energy (heat) and particles towards the plasma edge (with heat flows higher than the surface of sun!), where the field lines are open, thus providing a escape path for the high energy charged particles. In order to control the flow of particles and energy towards the outer edge, the open field lines have to be interrupted by a solid obstacle, broadly classified as the plasma facing components. The charged particles, whether they are in the central or edge region, always follow the field lines and will therefore enter into collision with the solid body: this is what is normally defined as plasma-wall interactions. Also, due to charge-exchange reactions, neutrals are produced in the bulk of hot plasma. Since the neutrals cannot be trapped by the magnetic field lines these high energy neutrals stream radially outwards, thus depositing energy on the plasma facing components. The heat and energy carried to the plasma facing material should be removed in real time for steady state operation of the machine. The ability to exhaust the plasma power loss from a large fusion device onto material walls surrounding the plasma has been perceived to be a large obstacle to the successful production of a fusion power reactor. There have been tremendous strides in understanding the physics relevant to this power exhaust and to understand and optimize the plasma-material interaction processes.

The key decision for a next step device is the choice of plasma facing materials. Historically, carbon has been favoured as a plasma facing material as it has excellent thermal properties plasma radiative property. Carbon is currently chosen to clad the ITER divertor target, near the strike points, because of its greater resilience to excessive heat loads. Carbon has been extensively used in most of the plasma confinement devices due to its good power handling, good thermal shock and thermal fatigue resistance property. Also, carbon or carbon-fibre composites (CFCs) does not melt and preserves its shape even under extreme temperature excursions. It has low radiative power losses with influx to plasma due to low  $Z$ . The joining technology for CFCs is well established and there exist broad operational experience. Carbon erosion would play a beneficial role because of the reduction of the target power by radiation cooling of the divertor plasma. Carbon radiates efficiently for temperatures down to  $\sim 5$  eV. However, on the down side, it requires conditioning, has higher erosion rate and physical and mechanical properties deteriorate substantially under neutron irradiation. Also, chemical erosion leads to reduction in lifetime and formation of co-deposits, which are complex hydrocarbons deposited around the divertor region and also observed in remote areas of fusion devices. Detailed discussion of the materials aspects for fusion, especially sputtering can be found in standard literature.[1, 2, 3, 4]

The reaction of thermalised ions (mostly hydrogen) implanted within the surface proceeds via the hydrogenation of carbon atoms to form  $\text{CH}_n - \text{C}$  complexes. At temperatures above 400 K  $\text{CH}_3$  radicals can be released while at temperatures above 600 K recombinative hydrogen release ( $\text{H}_2$ ) starts to reduce the chemical erosion yield. This thermal chemical erosion was elucidated in detail by Küppers *et al.*[5, 6, 7] and described analytically by Roth and Garcí a-Rosales[8]. The thermal reaction is further enhanced by radiation damage introduced in the material which provides open bonds for hydrogen attachment. Damage is created by kinetic energy transfer from incident ions to lattice atoms and is therefore responsible for the dependence of the chemical erosion yield on hydrogen isotope. At low surface temperatures all available carbon atoms are essentially hydrated but no thermal release of hydrocarbons occurs. However, hydrocarbon radicals are bound to the surface with much smaller binding energy ( $\sim 1$  eV) than carbon surface atoms in their regular lattice environment ( $\sim 7.4$  eV). This leads to an ion induced desorption of hydrocarbon radicals which can be described in a manner analogous to physical sputtering using a threshold energy,  $E_{des}$ , in the low eV range. The fact that emitted hydrocarbon radicals partly stick to the vessel surfaces rather than being hydrated to volatile sat-

urated hydrocarbons leads to deposition and accumulation of hydrocarbons in the plasma vessel.

Although, carbon and carbon fibre composites (CFC) have excellent thermal properties, the problem of erosion and formation of hydrocarbon co-deposits have been a major concern and the limiting factor for many years. Thus, in conclusion, hydrocarbon research is an important and crucial research area in fusion due to active formation, desorption and adsorption of complex hydrocarbons in fusion. Various atomic and molecular process, such as elastic ion-neutral, neutral-neutral collisions, charge exchange collisions, molecular dissociation and recombination of hydrocarbons play an important role in the fusion research. The formation of co-deposits and its interaction with material surface or other amorphous deposits is important due to the fact that these co-deposits act as “sponge” for hydrogen and its isotopes. The trapping of tritium in these co-deposits would lead to loss of tritium, which is expensive, and also make the machine radioactive. The retention of tritium is a serious concern for ITER given that 100g is to be injected each discharge and the in-vessel limit may be as low as 350g[9].

### 1.3 Astrophysics

The space between the stars in the Milky Way and further on between galaxies is not empty. There is an interstellar medium (ISM) consisting of gas and dust that is immersed in radiation, magnetic fields, and cosmic ray particles. The ISM is very tenuous; the average density is only about one atom per cubic centimeter, although locally the density can be orders of magnitude higher. Interstellar clouds are also of much interest because stars are formed there. In order to interpret spectroscopic measurements as indicators of the conditions and history of the interstellar medium it is necessary to know cross-sections and rate coefficients of the relevant chemical reactions. On the other hand, there also exists giant molecular clouds (or GMCs for short) in which most of the molecular material can be found. These enormous clouds represent the coolest (10-20 Kelvin) and densest phase of the interstellar medium, and are the largest gravitationally bound objects in a galaxy and, in fact, the largest known objects in the universe made up of molecular material. The atomic nuclei, are present in approximately the same proportions as in most of the universe: about 75% hydrogen (by mass), 25% helium, and trace amounts of oxygen, carbon, nitrogen, silicon, sulfur and so on in successively smaller amounts.

Molecular clouds play a key role in the evolution of the Galaxy since, according to current knowledge, every star and planetary system was once formed inside such molecular clouds. The other types of interstellar clouds, in which the hydrogen is atomic, are too warm and diffuse to allow stars to form. Since star formation occurs when deeply embedded clumps of interstellar gas and dust collapse, stars that are newborn or in the very process of forming are always obscured from direct optical view, and the only source of information from the inside of these clumps is provided by longer-wavelength radio waves emitted by molecules. Because of this, star formation is one of the most important fields of study for molecular astrophysicists.

Another reason why star formation and astrochemistry is so intimately connected is that the dense gas located around or at least in close proximity to certain recently formed stars of high luminosity have been shown to be the most chemically diverse objects in the interstellar medium. Astrophysicists call these objects hot cores, and dozens of such objects have been found in our galaxy. They are, simply put, very compact (fractions of a light year), warm (a few hundred Kelvin, compared to 10 or 20 K for the general interstellar gas), and dense (more than  $10^6$  hydrogen molecules per  $\text{cm}^3$ ) gas condensations with remarkably rich millimeter-wave emission-line spectra. Hot cores also show up as powerful infrared objects. The beautiful ionized

nebula in Orion, known as Messier 42 to optical astronomers, contains two such hot cores, which also happen to be the most well-studied objects of this type since they are the most nearby. Many of the species in the list of all detected interstellar molecules have been seen only in hot cores, nowhere else.

About 120 different chemical compounds have been identified in interstellar clouds, circumstellar matter, and comets, each one of great chemical and physical interest. The chemical compounds range in complexity from the simplest diatomic ( $\text{H}_2$ ), through familiar ones like hydrogen cyanide (HCN), nitrous oxide or “laughing gas” ( $\text{N}_2\text{O}$ ), ethanol ( $\text{CH}_3\text{CH}_2\text{OH}$ ), to esteric carbon-chains (“cyano-polyynes”) like  $\text{HC}_{11}\text{N}$ . In addition, there is strong evidence for even larger aromatic molecules (polycyclic aromatic hydrocarbons, PAHs), although specific assignments are still being explored. As a rule of thumb, the more complex a molecule, the smaller its relative concentration in the interstellar clouds. Some molecules were not known on Earth at the time of their detection in space and required real detective work. An example of this was the identification of the molecular ion  $\text{HCO}^+$ . Therefore, space provides with a perfect ground for studying fundamental science. Stellar and interstellar astrophysics provides an opportunity to study atoms and molecules in extremely cold conditions, which is otherwise quite difficult to produce on earth. Molecules are found in cool astronomical environments such as the dark interior of dense interstellar clouds, in expanding envelopes around dying red giant stars, in comets, and in planetary atmospheres. Molecules live in symbiosis with dust grains, which shield them from the ultraviolet stellar radiation that would otherwise disrupt the chemical bonds.

The molecules in astrophysical conditions are formed through a complicated network of chemical reactions in situ, inside the interstellar or circumstellar clouds where they are found. According to the theory presented by astrochemists Eric Herbst and William Klemperer in 1973[10], the most important type of reaction is that between a positive ion and a neutral molecule in the gas-phase, for example  $\text{O}^+ + \text{H}_2 \rightarrow \text{OH}^+ + \text{H}$ . The reason why these reactions play such an important role is that the net charge carried by the ion gives it the ability to polarize and electrostatically attract the electrons in the neutral reactant. The electrostatic attraction is an efficient way for the reactants to meet. Positive ions exist everywhere in space, because they are constantly being created when fast cosmic-ray particles collide with atoms and molecules and tear off electrons in the process. In lack of this long-range electrostatic interaction, reactions between two neutrals are generally much slower, but may nevertheless work in some cases.

The presence of reactive radicals and the relative concentrations of certain molecules clearly tells us that the chemistry of the interstellar medium is far from equilibrium, on account of the extremely low pressure in even the densest molecular clouds. A good example of a non-equilibrium concentration ratio is the two conformations of HCN molecule ( $\text{HNC}/\text{HCN}$ ), which has been measured to be as high as of order unity, hence perhaps 105 times its equilibrium value at the relevant temperature. It is also clear that the surfaces of the interstellar dust grains have the ability to act as catalysts for certain reactions. Molecular hydrogen, for example, is formed only on dust grains. In the last decade or so it has been shown that also more complex molecules can be synthesized this way.

European Space Agency’s Huygens probe made an historic first ever descent to the surface of Titan, 1.2 billion kilometers from Earth and the largest of Saturn’s moons. Starting at about 150 kilometers altitude, six multi-function instruments on board Huygens recorded data during the descent and on the surface. Huygens’ data provide strong evidence for liquids flowing on Titan. However, the fluid involved is methane, a simple organic compound that can exist as a

liquid or gas at Titan's sub -170 C temperatures, rather than water as on Earth. Various other instrument on-board have recently started sending new and important results.

Recent observations have shown existence of molecules in the atmosphere of one of Saturn's moons that are responsible for its smog-like haze.[11] Titan's lower atmosphere has long been known to harbor organic aerosols (tholins) presumed to have been formed from simple molecules, such as methane and nitrogen ( $\text{CH}_4$  and  $\text{N}_2$ ). Up to now, it had been assumed that tholins were formed at altitudes of several hundred kilometers by processes as yet unobserved. Recent measurements from a combination of mass/charge and energy/ charge spectrometers on the Cassini spacecraft have provided evidence for tholin formation at high altitudes ( $\sim 1000$  kilometers) in Titan's atmosphere.

During the Cassini spacecrafts first encounters with Titan, the Ion Neutral Mass Spectrometer (INMS) revealed an atmosphere dominated by  $\text{N}_2$  and  $\text{CH}_4$ , accompanied by a rich mixture of hydrocarbon-nitrile compounds with masses up to 100 daltons (i.e. mass of carbon),[12] which was the upper detectable limit of the mass range of the INMS. The INMS measured the neutral mole fractions at closest approach of  $\text{N}_2$ ,  $\text{CH}_4$ ,  $\text{C}_2\text{H}_2$ ,  $\text{C}_2\text{H}_4$ ,  $\text{C}_2\text{H}_6$ ,  $\text{C}_3\text{H}_4$ ,  $\text{C}_4\text{H}_2$ ,  $\text{C}_2\text{N}_2$ ,  $\text{C}_6\text{H}_6$  and  $\text{C}_3\text{H}_6$  molecule. Also the following ions were observed during this mission,  $\text{CH}_5^+$ ,  $\text{C}_2\text{H}_5^+$ ,  $\text{HCNH}^+$ ,  $\text{C}_3\text{H}_3^+$ ,  $\text{C}_4\text{H}_3^+$ ,  $\text{C}_4\text{H}_5^+$ ,  $\text{C}_6\text{H}_5^+$ ,  $\text{C}_6\text{H}_7^+$ ,  $\text{C}_7\text{H}_7^+$ .

Of particular importance for the development of complex chemistry in the upper atmosphere was the tentative identification of benzene ( $\text{C}_6\text{H}_6$ ), which is a critical component in the formation of polycyclic aromatic hydrocarbon (PAH) compounds. Quantitative observations of hydrocarbon-nitrile compounds in Titan's upper atmosphere (950 to 1150 km) by the INMS, together with evidence from the Cassini Plasma Spectrometer (CAPS)[13] of heavy positively charged (100 to 350 daltons) and negatively charged (20 to 8000 daltons) ions (12) has been reported recently[14], The presence of negative ions in particular was a complete surprise, and it is argued that they could play an important role in tholin formation. These data were obtained during six recent Titan encounters indicating that the chemical processes are a persistent phenomenon.

Researchers have been developing theoretical models to simulate and model the Titan's atmosphere. It is known that the atmosphere consists mainly of molecular nitrogen and methane, which had been further verified by recent observations. Extreme ultraviolet and X-ray radiation from the sun and energetic electrons from Saturn's magnetosphere interact with the upper atmosphere producing an ionosphere, which serve as the dynamical ground for such hydrocarbons.

These ionospheric models have as input the neutral atmosphere density profiles, ion production rate profiles (both from solar EUV and from Saturnian magnetospheric electrons), an electron temperature profile (to determine temperature dependent electron recombination reaction rates), and the relevant ion-neutral reaction rates. Several of the ion species measured by the INMS were predicted by models (e.g.,  $\text{HCNH}^+$  and  $\text{C}_2\text{H}_5^+$ ). But the INMS also saw high densities at mass numbers not predicted by models. Improvement of the theoretical model is an active area of research in the present time. It has been realized that detailed hydrocarbon ion chemistry(as an input for the models), such as ion production rates and ion-neutral reaction rates are of significant importance.

Most astrophysical objects are observed via the electromagnetic radiation they emit. Therefore, the theory of radiative transfer is a key element for the understanding of the radiation and physical structure of these objects. To determine the structure of stellar objects, radiation

transport equation is solved and the “synthetic spectra” is compared with observations. The numerical solution of the radiation transport problems is an important prerequisite for the calculation of model stellar atmospheres. The simulated spectrum is then compared to observed spectra of objects such as stars, where the radiation is mostly emitted from the outer layers. In the case of very low mass stars and brown dwarfs, the atmosphere is also crucial in determining the interior structure of these objects since it serves as a boundary condition for the equations of stellar structure in a nearly fully convective “star”. In the objects such as supernovae, the explosion causes the “atmosphere” to expand rapidly, a time series of the spectra can reveal the entire structure of the object as the ejected material expands and rarefies and the atmosphere moves inward in the material. In the case of expanding objects such as hot stars (many with strong stellar winds), novae, and supernovae; the radiation transport equation is solved simultaneously with the hydrodynamical equations which presents itself to be a more difficult computational problem than static stars.

PHOENIX[15, 16, 17] is one such, very general non-Local Thermodynamic Equilibrium(NLTE) stellar atmosphere computer code which can handle very large model atoms as well as line blanketing by hundreds of millions of atomic and molecular lines. The code is used to compute model atmospheres and synthetic spectra for, e.g., novae, supernovae, M and brown dwarfs, O to M giants, white dwarfs and accretion disks in Active Galactic Nuclei (AGN). The radiative transfer in PHOENIX is solved in spherical geometry and includes the effects of special relativity (including advection and aberration) in the modelling. The PHOENIX code uses a large number of NLTE and Local Thermodynamic Equilibrium (LTE) background spectral lines and solves the radiative transfer equation for each of them without using simple approximations like the Sobolev approximation. The profiles of spectral lines is resolved in the co-moving (Lagrangian) frame. This requires many wavelength points (typically 150,000 to 300,000 points). The spectral lines required by such codes can be computed at high level of quantum mechanical theory, consistently covering a large number of hydrocarbons and spectral lines.

Thus from the astrophysical point of view, hydrocarbons are known to exist in planetary atmosphere, stellar atmosphere, interstellar medium, star forming clouds and on the surface of planetary satellites. For almost a century researchers have been recording observations from outer-space in the quest to understand the formation and dynamical evolution of galactic species. Knowing the spectral information at highest accuracy helps the experimentalist to look in the narrow frequency range and in interpreting the observed spectra from space. Also, ro-vibrationally resolved reaction cross-sections of formation and dissociation reaction of hydrocarbons under cold conditions would help in understanding the buildup hydrocarbons in space. The spectral information of various hydrocarbon species is also of great importance in understandings the dynamics and radiation transport of stellar atmosphere.

## 1.4 Combustion

Crude oils are mixtures of many different substances, from which various petroleum products are derived, such as: gasoline, kerosene propane, fuel oil, lubricating oil, wax, and asphalt. These substances are mainly compounds of only two elements: carbon (C) and hydrogen (H); hence known as hydrocarbons. Methane ( $\text{CH}_4$ ) is the primary constituent of liquefied or compressed natural gas, and Propane ( $\text{C}_3\text{H}_8$ ) is the primary constituent of liquefied petroleum gas. Petroleum fuels are blends of lots of different chemical species; in general, the molecules of a liquid petroleum fuel are pretty big and complex. Isooctane ( $\text{C}_8\text{H}_{18}$ ) is an example of a typical molecule found in gasoline and cetane, or n-hexadecane ( $\text{C}_{16}\text{H}_{34}$ ) is typical of the diesel fuel.

Hydrocarbons may be gaseous, liquid, or solid at normal temperature and pressure, depending on the number and arrangement of the carbon atoms in their molecules. Those with up to 4 carbon atoms are gaseous; those with 20 or more are solid; those in between are liquid.

When a hydrocarbon fuel burns completely, the oxygen in the air combines with the hydrogen to form water ( $\text{H}_2\text{O}$ ) and with the carbon to form carbon dioxide ( $\text{CO}_2$ ). If the burning is not complete, then some of the carbon atoms only combine with one oxygen atom rather than two, to form carbon monoxide ( $\text{CO}$ ), a highly poisonous gas. The standard enthalpy for the combustion of methane is 890.4 kJ/mole,



A simple estimate of standard enthalpy change when 1.0 cubic meter of natural gas is burned is 39 Mega-Joules. The chemical energy produced in the combustion process has long been used for producing work.

In the combustion process some of the carbon atoms may remain stuck together with each other and with some of the hydrogen atoms as well, so that unburned hydrocarbon molecules (mostly smaller than the ones in the original fuel) can also be produced. Carbon atoms can also remain stuck to one another with few or no hydrogen atoms attached, especially during incomplete combustion of diesel fuel, producing soot.

Researchers have brought together advances in theoretical chemical kinetics[18] and high-performance computing to speed research in the chemistry of fuel combustion that may lead to cleaner more efficient combustion devices. There has been development towards a new approach to predict the rates of chemical reactions that greatly increases efficiency while maintaining accuracy, cutting costs and allowing research on larger molecules.

Basic research on radical-radical reactions relevant to the combustion of hydrocarbons has gained impetus. There is also a lot of interest to develop accurate models of combustion chemistry which might be used to design more efficient or cleaner-burning combustion devices[19, 20, 21, 22]. Quantum dynamics study of a polyatomic combustion reaction, calculation of thermal rate constants, determination of structures of reactants, reaction products and transition states are of great importance in understanding the chemical combustion process. The study of hydrocarbons up to seven atoms, presented in this work would also be of interest to the hydrocarbon combustion community.

## 1.5 Motivation

Hydrocarbons are of interest in fusion due to the various atomic-molecular process and atomic-molecular-surface interactions occurring in the low temperature plasma and plasma-wall interaction near the divertor region. The low temperature plasma near the wall is dominated by the atomic-molecular processes. Elastic ion-neutral, neutral-neutral collisions, charge exchange collisions, molecular dissociation and volumetric recombination strongly influence divertor plasma behavior. Chemical sputtering of the carbon based plasma facing material by energetic hydrogenic species leads to formation and dissociation of hydrocarbon species near the divertor region. These hydrocarbon species are deposited and further sputtered/dissociated on the plasma facing material. Hydrocarbons are also of interest in the study of low-temperature, partially ionized hydrocarbon plasmas which are used in various plasma surface technologies, for example depo-

sition of diamond-like carbon films.

Hydrocarbons have long been known to exist in the stellar atmosphere and their ions are common as well in solar system atmospheres and in the interstellar medium. Researchers have been recording spectroscopic information from distant stars and galaxies, in order to assign spectroscopic lines to molecules, astrophysicists have to rely on high accuracy laboratory spectroscopic reference measurements or on high-accuracy quantum mechanical calculations. Hydrocarbon on hydrocarbon reactions (neutral and charged, including radical reactions) and hydrocarbon photochemistry play an important role in these media, while the neutral reactions have a key role also in combustion.

The most important chemical process governing the low temperature plasma are the ion-ion, ion-neutral, excitation and de-excitation, formation and dissociation hydrocarbon reactions. Whereas, to understand the dynamics of co-deposits, molecule-molecule and molecule-surface (crystalline and amorphous) interaction should be studied. These processes are relatively energetic compared to astrophysical conditions. Due to the low temperature of the inter-stellar medium, most of the hydrocarbons would be found in the vicinity of the global minimum of the potential energy hypersurface. The molecules leave spectroscopic signatures in the infrared through submillimeter range, and in order to make sense of those observations it is necessary to solve coupled chemical reaction equations for hundreds of species and thousands of channels.

To simulate hydrocarbons under such varying conditions and with varying system sizes, ranging from small molecules in the low-temperature plasmas and interstellar medium to hydrocarbons with thousands of atoms in the amorphous co-deposits, one needs to use a suite of methods, since one single approach is incapable of handling such variation in system sizes with consistent accuracy. Under the Born-Oppenheimer approximation, which states that the electronic structure energy of a  $N$ -body system can be calculated from the electronic hamiltonian for fixed nuclear coordinates, the nuclear degrees of freedom span the  $3N$  dimensional surface. In order to compute reaction dynamical evolution with time or spectroscopic lines one must know the inter-atomic potential with the best possible accuracy. As the system size increases, one has to adopt approximate methods or use parameterized potential information. The idea of atomistic multi-scale approach is shown in Fig.1.1.

For small molecules the Hartree-Fock formulation of Schrödinger equation can be solved exactly, which is the most accurate quantum mechanical method. However, Hartree-Fock method assumes that the electrons are un-correlated and one electron moves in the mean field of other electrons. Because of this assumption, the HF calculations are not able to recover correlation energy, which is difference between the HF energy and exact ground state energy. In order to recover correlation energy, which has been found to be extremely important, one needs a group of methods known as the post-HF method for achieving higher accuracy. However, the post-HF methods are extremely computer intensive thus limiting these methods to relatively small molecules. Since, the structural evolution and energetics of various dynamical processes take place on the Born-Oppenheimer surface, accurately evaluating the potential energy surface for these hydrocarbons is the first important step towards studying the relevant hydrocarbons.

Dimensionality of the Hartree-Fock approach is extremely high, due to the fact that the wave function depends on all coordinates of all particles, i.e., for  $N$  electrons, it depends on  $3N$  variables (or  $4N$  if spin is also included). Alternatively, electron density has always been more attractive, since it depends only on  $x, y, z$ , and eventually, there may be two densities for spin polarized systems, one for spin up electrons  $\rho_{\uparrow}(\mathbf{r})$  and one for spin down electrons  $\rho_{\downarrow}(\mathbf{r})$ , as op-

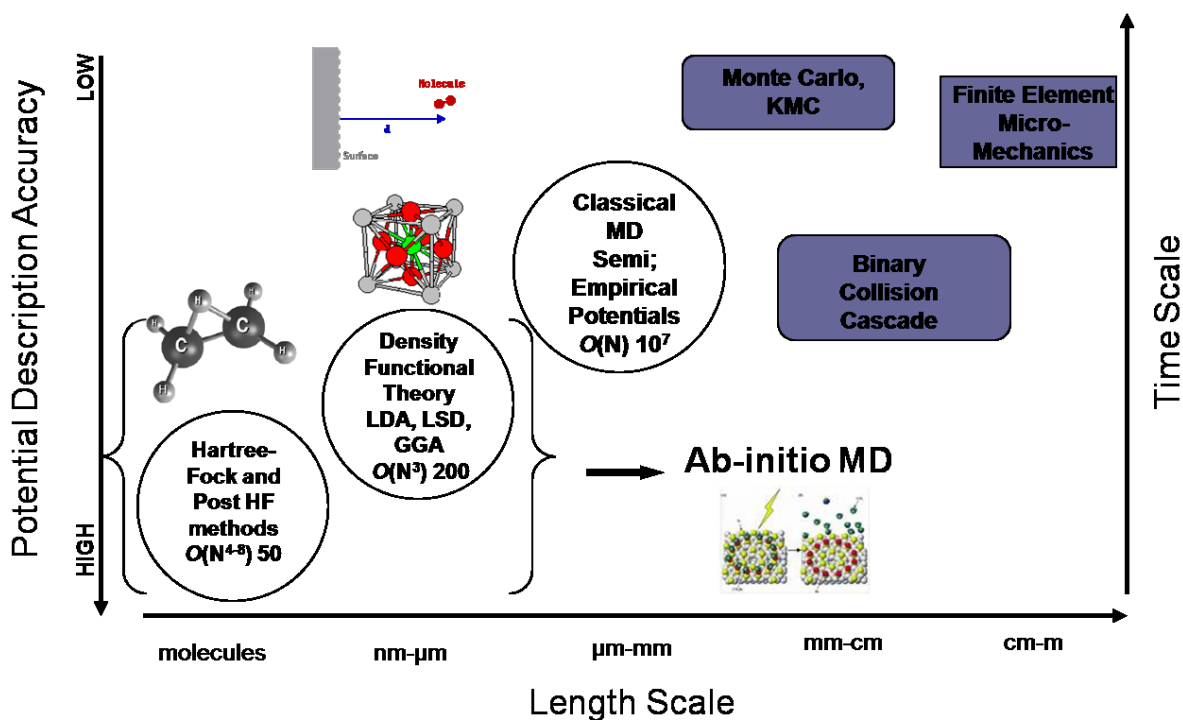


Figure 1.1: Schematics showing atomistic multiscale approach.

posed to many particle wavefunction. The fact that the ground state properties are functionals of the electron density  $\rho(\mathbf{r})$  was proved by Hohenberg and Kohn (1964) and it provides the basic framework for modern Density Functional Theory (DFT). DFT avoids the expense of the more traditional methods, deriving the energy directly from the electron probability density, rather than the molecular wavefunction, thus drastically reducing the dimensionality of the problem. However, DFT is not totally free from wavefunctions, as the electron density is expanded in a set of orbitals. If the Kohn-Sham orbitals are expanded in a plane-wave basis set, explicit treatment of core electrons becomes intractable due to the rapid oscillations of the wave function in the core region. Hence, atomic pseudopotentials are almost always employed. Fixed basis functions are used e.g., in plane-wave expansions, tight-binding or LCAO (linear combination of atomic orbitals) approximations, or the OPW (orthogonalized plane wave) method. Examples for methods using energy-dependent functions are the APW (augmented plane wave) or KKR (Korringa-Kohn-Rostoker) approaches. The most widely used methods for solving the Kohn-Sham equation in solid-state physics are LMTO (linear muffin tin orbitals) and LAPW (linear augmented plane waves). The plane-wave pseudopotential approach has had an immense impact on the way in which material properties are studied. In spite of this success, the system-size accessible to such techniques is limited because the algorithms scale with the cube of the number of atoms. Thus, DFT methods are most suitable for studying problems of hydrogen interaction with graphite, carbon nanotubes, and hydrocarbon co-deposits interaction with surfaces (up to 100's of atoms). Although these methods are known to be not as accurate as HF and post-HF methods, DFT is the only approach to treat crystalline, amorphous, proteins and bigger bio-molecules at quantum mechanical level, which presents substantial improvement over the empirical and semi-empirical potential used in classical molecular dynamics approach.

Quantum mechanical methods suffer from the drawback that they are extremely *cpu* intensive and would require large resources of achieving statistical accuracy. Also, for larger length scales,

HF and DFT methods become intractable due to bad scaling with system size. For systems with few 1000's of atoms, the only approach that can work is the classical molecular dynamics with pre-fitted inter-atomic potentials or analytic potentials. An example for hydrocarbons is the Brenner empirical many-body potential-energy expression developed for hydrocarbons that can model intramolecular chemical bonding in a variety of small hydrocarbon molecules as well as graphite and diamond lattices. Atomization energies for a wide range of hydrocarbon molecules predicted by the potential were compared with the experimental values. The potential function is short ranged and quickly evaluated so it should be very useful for large-scale molecular-dynamics simulations of reacting hydrocarbon molecules.

## 1.6 Dissertation outline

In the present work the atomistic multiscale approach outlined in Sec.1.5 is followed to study the hydrocarbons at varying length scales. High-accuracy *ab initio* calculations for small hydrocarbons are performed and thousands of such calculations spanning the nuclear configuration hypersurface are used to generate semi-global and global potential energy surface (PES). The generation of such PES allows us to study important stationary point configuration in nuclear configuration space. High accuracy fitting around the important minimum energy configuration allows to perform high-accuracy spectroscopic calculations. The studies presented in this dissertation are also of great relevance to the theoretical investigations in atomic and molecular astrophysics. The hydrocarbon studied in this dissertation is a small in number, but important sample: they are critical towards the build-up of larger polycyclic aromatic hydrocarbons and also critical for the anomalous deuterium fractionation found in the interstellar medium, also, these hydrocarbons have been found in the more dense, star-forming regions in the interstellar medium and also on Titan, largest moon of Jupiter. Generation of a global potential energy surface allows to study formation and dissociation of hydrocarbons on the Born-Oppenheimer surface. Accurate reaction rate coefficients are required in order to simulate hydrocarbon dynamics in the divertor region and model systems and processes relevant to fusion and astrophysics. The build-up of larger hydrocarbon chains starting from the methane and ethane families is one major issue. The relevant reactions for the build-up may include, besides ordinary bimolecular ones, radiative and three-body association reactions, depending on the environment. The scientific challenge is the study, both computational and experimental, of hydrocarbon chemistry in partially ionized plasma and neutral gases. The area of research focusing on the computation of model atmospheres and the numerical solution of the radiation transport equation in expanding media with known velocity fields[15, 16, 17, 23, 24, 25, 26, 27] is of more direct relevance to the work presented in this dissertation.

The present dissertation is structured in the following way; in chapter 2 the basic theory and methods which are of direct relevance to this work are introduced. Since the theory and methods used in the multiscale approach (introduced in Sec.1.5) are vastly different and involving, only the basic idea underlying each of these methods is presented in a way which would help the reader to connect between the methods and results. At the first level of atomistic multiscale approach, a semi-global and global potential energy surface for small hydrocarbons is developed. The potential energy surface are developed in a unique way proposed by Braams and co-workers, the methodology of potential energy surface generation and results are presented in chapter 3. The quantum mechanical methods applied for performing the electronic structure calculations are introduced in chapter 2; section 2.4. Important stationary points are identified on the surface and high accuracy fitting around the global minimum and stationary points allows us to calculate the normal mode frequencies on the PES. Most of the traditional methods for calculating normal mode frequencies assume harmonic potential along the normal coordinates. However,

it is well known that the potential along any of the normal mode is not harmonic. In order to accurately compute the vibrational levels for any molecule, the ro-vibrational hamiltonian for a nuclear configuration should be solved. An important prerequisite for such calculations is the accurate description of the potential energy surface around the reference configuration. The potential energy surface developed in the present work is highly accurate, as the points on the surface are computed using *ab initio* quantum mechanical calculations and the fit has a low rms error over all configurations. This allows us to perform ro-vibrational calculations for the molecules under study. The methodology for vibrational self-consistent field (VSCF) is introduced in chapter 2; section 2.8.1 and the results are presented in chapter 4. The semi-global potential energy surface only span the nuclear configuration space where the molecule is bounded or partially fragmented. However, in order to perform reaction dynamics, the potential energy surface should be able to represent the dissociation process accurately. Also, the hydrocarbon molecule can dissociate in various ways, thus one needs to identify all possible fragmentation paths (products) and include them in a global fit. Extending the semi-global potential energy surface, *ab initio* calculations for the possible fragments is performed and these are included in the global fit. Thus, a global potential surface is generated which is capable of representing the fragmentation process. Quasi-classical trajectory (QCT) method is adopted to perform dynamics on the global-PES. The theory underlying QCT method is introduced in chapter 2; section 2.9. Preliminary results of these calculations are reported in chapter 5.

Moving-on from small molecules to higher length scales, the problem of interaction and diffusion of H atom within crystalline graphite and hydrocarbon co-deposits in fusion is studied. These problems are of interest due to the fact that during ion irradiation, not only surface atoms are displaced from their lattice sites but atom displacements also occur throughout the ion ranges. In graphite, H atoms are assumed to be very mobile between graphene planes and atoms that escape recombination with vacancies can reach the surface and evaporate freely. Also, co-deposits are important because they are known to act as sponge for tritium and are formed and deposited in the divertor and remote areas of fusion devices. To treat these problems at the quantum mechanical level of theory DFT based *ab initio* simulations are performed. The underlying theory of DFT is introduced in chapter 2; section 2.10 and results of the calculations are reported in chapter 6. To perform Born-Oppenheimer (BO) dynamics wherein the wavefunction should be optimized at every MD step or Car-Parrinello (CP) molecular dynamics wherein the wavefunction is optimized only at the beginning and then adiabaticity is conserved, is extremely difficult for co-deposits and one needs to adopt classical MD methods to achieve statistical accuracy.

To perform larger length scale simulations, for example 1000's of atoms of co-deposits, classical molecular dynamics with the empirical Brenner hydrocarbon potential is performed. The basic theory and methods are introduced in chapter 2; section 2.2.2 and results of this study are presented in chapter 7.

Finally, conclusion with summary is presented in chapter 8.

# Chapter 2

## Basic theory and Methods

### 2.1 Introduction

Hydrocarbons are of great interest in plasma physics, astrophysics and in the field of hydrocarbon combustion (introduced in chapter 1). Hydrocarbon structures, such as the saddle points, local and global minima on the potential energy surface are of interest due to the fact that these structures play an important role in governing the dynamics. These nuclear configurations have been of interest over a long period of time and have been studied at the most accurate level of theory and also experimentally. Spectroscopic information and reaction cross-sections for hydrocarbons play an important role in understanding laboratory and astrophysical hydrocarbons observations and dynamical evolution and are used extensively in hydrocarbon research. As introduced in section 1.5, various theory and methods needs to be applied over different length scales, ranging from the most accurate quantum mechanical to ones with approximate empirical potential description. In order to understand underlying theory applied in the present work, a brief description of the theory and methods is presented in this chapter. The oldest existing and most well known area of classical molecular dynamics is outlined at the start. Following that, methods used for performing electronic structure calculations, which is the first and most important step in calculating the potential energy of the configurations on the hypersurface is presented. Then, the methods underlying the quantum mechanical ro-vibrational calculations and quasi-classical trajectory calculations are introduced. Towards the end the Density Functional theory, as applied for intermediate length scale simulations is outlined.

### 2.2 Molecular dynamics

Molecular dynamics (MD) has had a long history[28, 29, 30, 31] and has evolved into an important and widely used theoretical tool that allows researchers in chemistry, physics, and biology to model the detailed microscopic dynamical behavior of many different types of systems, including gases, liquids, solids, surfaces, and clusters.

In a MD simulation, the classical equations of motion governing the microscopic time evolution of a many-body system are solved numerically subject to boundary conditions appropriate for the geometry or symmetry of the system. Thus, MD methodology is founded upon the basic principles of classical mechanics and can provide a window into the microscopic dynamical behavior of the individual atoms that make up a given system. From this information, the microscopic mechanisms of energy and mass transfer in chemical processes can be "observed" and dynamical properties such as absorption spectra, rate constants, and transport properties can be calculated. In addition to providing a microscopic dynamical picture, MD can also be employed as a means of sampling from a statistical mechanical ensemble and determining equilibrium properties. These properties include average thermodynamic quantities (pressure, temperature, volume, etc.), structure, and free energies along reaction paths.

In order to provide a picture of the microscopic behavior of a system from the laws of classical mechanics, MD requires, as an input, a description of the interparticle interactions. The quality

of the results of an MD simulation depends on the accuracy of this description. One common approach involves the introduction of a model or force field. The relatively low computational overhead associated with a standard force-field has allowed large-scale calculations to be performed on proteins, membranes, and large biological assemblies. Recent applications employing common force fields include, among many other impressive examples that can be found in the literature, an exploration of protein folding pathways in solution[32], structural and dynamical properties of ion channels[33, 34].

The disadvantage of a model force-field is that a system is restricted to a single molecular connectivity. This prohibits force field models from describing chemical processes involving bond breaking and forming. An alternative approach is the combination of classical dynamics with electronic structure, which allows internuclear forces to be computed "on the fly" from an electronic structure calculation as a MD simulation proceeds[35, 36]. This method, known as *ab initio* molecular dynamics, requires no input potential model and is capable of describing chemical events, although it has high computational overhead. More details on this is presented in Sec. 2.3.

### 2.2.1 Historical Background

The molecular dynamics method was first introduced by Alder and Wainwright in the late 1950's [28, 29] to study the interactions of hard spheres. Many important insights concerning the behavior of simple liquids emerged from their studies. The next major advance was in 1964, when Rahman carried out the first simulation using a realistic potential for liquid argon[30]. The first molecular dynamics simulation of a realistic system was done by Rahman and Stillinger in their simulation of liquid water in 1974 [37]. The first protein simulations appeared in 1977 with the simulation of the bovine pancreatic trypsin inhibitor (BPTI)[38]. Today in the literature, one routinely finds molecular dynamics simulations of hydrocarbons, crystal bulk, nano-tubes, solvated proteins, protein-DNA complexes as well as lipid systems addressing a variety of issues including the thermodynamics of ligand binding and the folding of small proteins. The number of simulation techniques has greatly expanded; there exist now many specialized techniques for particular problems, including mixed quantum mechanical - classical simulations, that are being employed to study enzymatic reactions in the context of the full protein. Molecular dynamics simulation techniques are widely used in experimental procedures such as X-ray crystallography and NMR structure determination.

### 2.2.2 Basic Approach

Consider a system consisting of  $N$  particles moving under the influence of the internal forces acting between them. The spatial positions of the particles as functions of time will be denoted by  $\mathbf{r}_1(t), \dots, \mathbf{r}_N(t)$ , and their velocities,  $\mathbf{v}_1(t), \dots, \mathbf{v}_N(t)$ . If the forces,  $\mathbf{F}_1, \dots, \mathbf{F}_N$ , on the  $N$  particles are specified, then the classical motion of the system is determined by Newton's second law

$$m_i \ddot{\mathbf{r}}_i = \mathbf{F}_i \quad (2.1)$$

where  $m_1, \dots, m_N$  are the masses of the  $N$  particles. Since the force on each particle is, in principle, a function of all of the  $N$  position variables,  $\mathbf{F}_i = \mathbf{F}_i(\mathbf{r}_1, \dots, \mathbf{r}_N)$ , eqn. 2.1 constitute a set of  $3N$ , or more generally,  $dN$ , where  $d$  is the number of spatial dimensions, coupled second-order differential equations. A unique solution to eqn. 2.1 is obtained by choosing a set of initial conditions,  $\mathbf{r}_1(0), \dots, \mathbf{r}_N(0), \mathbf{v}_1(0), \dots, \mathbf{v}_N(0)$ . Newton's equations completely determine the full set of positions and velocities as functions of time and thus specify the classical state of the system at time  $t$ . Except in special cases, an analytical solution to the equations of motion, eqn.

2.1, is not possible. An MD calculation, therefore, employs an iterative numerical procedure, called a numerical integrator or a map, to obtain an approximate solution[31, 39]. The accuracy of the numerical solution is determined by the time discretization,  $\delta t$ , referred to as the time step. In most cases, the forces,  $\mathbf{F}_i(\mathbf{r}_1, \dots, \mathbf{r}_N)$ , are sufficiently nonlinear functions of position that, if the true solution could be obtained for a given choice of initial conditions, the numerical solution would bear little resemblance to it after enough iterations of the map. This is largely due to the fact that the initial conditions can only be specified to within a finite precision for numerical calculation. In a large system with highly nonlinear forces, small differences between two sets of initial conditions lead to a divergence between the trajectories that become exponentially large as time increases. However, the numerical solution is statistically equivalent to the true solution within a bounded error, and this is sufficient to ensure that the same physical observables are obtained on average. It is important to note that small systems with closed orbits possess other such statistical equivalences.

In order to demonstrate the conditions required for the statistical equivalence of the numerical and true solutions to the equations of motion, it is first useful to recast eqn. 2.1 in Hamiltonian form. The Hamiltonian for an  $N$ -particle system subject only to interparticle interactions is

$$H(\mathbf{p}, \mathbf{r}) = H(\mathbf{p}_1, \dots, \mathbf{p}_N, \mathbf{r}_1, \dots, \mathbf{r}_N) = \sum_{i=1}^N \frac{\mathbf{p}_i^2}{2m_i} + U(\mathbf{r}_1, \dots, \mathbf{r}_N) \quad (2.2)$$

where  $(\mathbf{p}_1, \dots, \mathbf{p}_N)$  are the momenta of the particles defined by  $\mathbf{p}_i = m_i \mathbf{v}_i$  and  $U(\mathbf{r}_1, \dots, \mathbf{r}_N)$  is the interparticle potential, in terms of which the forces are given by

$$\mathbf{F}_i = -\frac{\partial U}{\partial \mathbf{r}_i} \quad (2.3)$$

The equations of motion (2.1) can be derived from eqn. 2.2 according to Hamilton's equations,

$$\begin{aligned} \dot{\mathbf{r}}_i &= \frac{\partial H}{\partial \mathbf{p}_i} = \frac{\mathbf{p}_i}{m_i} \\ \dot{\mathbf{p}}_i &= -\frac{\partial H}{\partial \mathbf{r}_i} = -\frac{\partial U}{\partial \mathbf{r}_i} = \mathbf{F}_i(\mathbf{r}_1, \dots, \mathbf{r}_N) \end{aligned} \quad (2.4)$$

Taking the time derivative of both sides of the first of Hamilton's equations and substituting into the second, one easily arrives at eqn. 2.1. Therefore, the classical state of a system at any instant in time can also be determined by specifying the complete set of particle positions and corresponding momenta.

Two important properties of the equations of motion should be noted. One is that they are time reversible, i.e., they take the same form when the transformation  $t \rightarrow -t$  is made. The consequence of time reversal symmetry is that the microscopic physics is independent of the direction of the flow of time. The second important property of the equations of motion is that they conserve the Hamiltonian eqn. 2.2. This can be easily seen by computing the time derivative of  $H$  and substituting eqn. 2.4 for the time derivatives of position and momentum:

$$\frac{dH}{dt} = \sum_{i=1}^N \left[ \frac{\partial H}{\partial \mathbf{r}_i} \dot{\mathbf{r}}_i + \frac{\partial H}{\partial \mathbf{p}_i} \dot{\mathbf{p}}_i \right] = \sum_{i=1}^N \left[ \frac{\partial H}{\partial \mathbf{r}_i} \frac{\partial H}{\partial \mathbf{p}_i} - \frac{\partial H}{\partial \mathbf{p}_i} \frac{\partial H}{\partial \mathbf{r}_i} \right] = 0 \quad (2.5)$$

The conservation of the Hamiltonian is equivalent to the conservation of the total energy of the system and provides an important link between molecular dynamics and statistical mechanics.

### 2.2.3 Statistical Ensemble

Statistical mechanics connects the microscopic details of a system to physical observables such as equilibrium thermodynamic properties, transport coefficients, and spectra. Statistical mechanics is based on the Gibbs' ensemble concept. That is, many individual microscopic configurations of a very large system lead to the same macroscopic properties, implying that it is not necessary to know the precise detailed motion of every particle in a system in order to predict its properties. It is sufficient to simply average over a large number of identical systems, each in a different such microscopic configuration; i.e., the macroscopic observables of a system are formulated in terms of ensemble averages. Statistical ensembles are usually characterized by fixed values of thermodynamic variables such as energy,  $E$ ; temperature,  $T$ ; pressure,  $P$ ; volume,  $V$ ; particle number,  $N$ ; or chemical potential  $\mu$ . One fundamental ensemble is called the *microcanonical* ensemble and is characterized by constant particle number,  $N$ ; constant volume,  $V$ ; and constant total energy,  $E$ , and is denoted as the  $NVE$  ensemble. Other examples include the *canonical* or  $NVT$  ensemble, the *isothermal-isobaric* or  $NPT$  ensemble, and the *grand canonical* or  $\mu VT$  ensemble. The thermodynamic variables that characterize an ensemble can be regarded as experimental control parameters that specify the conditions under which an experiment is performed.

Now consider a system of  $N$  particles occupying a container of volume  $V$  and evolving under Hamilton's equations of motion. According to eqn. 2.5, the Hamiltonian will be a constant,  $E$ , equal to the total energy of the system. In addition, the number of particles and the volume are assumed to be fixed. Therefore, a dynamical trajectory of this system will generate a series of classical states having constant  $N$ ,  $V$ , and  $E$ , corresponding to a microcanonical ensemble. If the dynamics generates all possible states having a fixed  $N$ ,  $V$ , and  $E$ , then an average over this trajectory will yield the same result as an average in a microcanonical ensemble. The energy conservation condition,  $H(\mathbf{p}, \mathbf{r}) = E$ , which imposes a restriction on the classical microscopic states accessible to the system, defines a hypersurface in the phase space called the constant energy surface. A system evolving according to Hamilton's equations of motion will remain on this surface. The assumption that a system, given an infinite amount of time, will cover the entire constant energy hypersurface is known as the ergodic hypothesis. Thus, under the ergodic hypothesis, averages over a trajectory of a system obeying Hamilton's equations are equivalent to averages over the microcanonical ensemble.

Despite the utility of Hamiltonian molecular dynamics, its principle restriction is clear: although, given correct forces, the dynamics is exact in the classical limit; it can only generate equilibrium properties of the  $NVE$  ensemble. However, microcanonical conditions ( $NVE$ ) are not consistent with the many experimental measurements under conditions of constant temperature and pressure or constant temperature and volume. In order to describe the thermodynamic properties of a system under these conditions, it is necessary to generate the corresponding ensemble. One of the more fruitful and interesting approaches to generating alternative ensemble averages is based on properties of non-Hamiltonian dynamical systems. A complete statistical theory of non-Hamiltonian systems has been presented in Ref [40].

### 2.2.4 Macroscopic Parameters

Statistical mechanics provides a link between the macroscopic properties of matter (like temperature, pressure, etc.) and the microscopic properties (like positions, velocities, individual kinetic and potential energies) of atoms and molecules that constitute it. These macroscopic properties reflect the time average behavior of the atoms at equilibrium (i.e. in one of the many possible degenerate minimum energy states accessible to the system). Often even in an  $NVE$  simulation one does some simple tricks to control temperature and/or pressure. This give something of a

NVT or NVP and NVE hybrid. However temperature and pressure fluctuate, and the system does not behave as a true *NVT* or *NVP* ensemble in the thermodynamic sense. But on average temperature and pressure have the desired value. In true NVT or NPT (non-Hamiltonian) algorithms it is possible to have T and P have exactly the desired value, and the simulation directly corresponds to the thermodynamic ensembles.

At the start of the MD simulation the atomic positions and velocities have to be initialized. In the case of crystalline solids the starting positions will be defined by the crystal symmetry and positions of atoms within the unit cell of the crystal. The unit cell is then repeated to fill up the desired dimensions of the system. Realistic atomic displacements from crystal lattice sites can also be derived using the Debye model. For amorphous solids the particles can be randomly distributed within the desired dimensions making sure that there exists a minimum distance between the atoms so that strong local forces do not exist in the system.

The initial velocities are set by assuming a Maxwell-Boltzmann distribution for velocities along the three dimensions. This is done by using Gaussian distributed random numbers multiplied by a mean square velocity given by  $\sqrt{2k_B T/m}$  in each of the three directions and making sure that the system has total momentum equal to zero. Generally speaking, if sensible (tailored to avoid large impulsive forces) position and velocity distributions are chosen, particle positions at equilibrium relax to oscillating around the minimum energy locations of the potential  $\Phi$ . A Maxwellian distribution of velocities is naturally obtained in the simulation.

Therefore the initial temperature and total energy of the system has been fixed. The temperature is fixed by the velocity distribution. The total energy of the system is given by

$$E_{tot} = KE_{tot} + PE_{tot} \quad (2.6)$$

where  $KE_{tot}$  is the total kinetic energy in the system given by

$$KE_{tot} = \sum_i = 1N \frac{1}{2} m (v_{x,i}^2 + v_{y,i}^2 + v_{z,i}^2) \quad (2.7)$$

and  $PE_{tot}$  is the total potential energy of the system given by

$$PE_{tot} = \sum_i = 1N \Phi_i(r_i) \quad (2.8)$$

with  $v_{x,y,z}$  being the velocities,  $r$  being the positions of atoms, and  $i$  being the index that sums over all the atoms  $N$  in the system.  $\Phi_i(r_i)$  is the potential energy of the  $i^{th}$  atom due all other atoms in the system.

### 2.2.5 Temperature Scaling

In equilibrium simulations, especially if long range interactions are involved and a potential truncated at a cutoff radius is used, unavoidable slow drift occur that need correction. One of the possible trivial temperature scaling would be to force the system temperature to be exactly  $T$  during every time step. This may be a rather severe perturbation of the atom motion especially if there are only a few atoms. methods to control temperature and pressure[41, 42, 43].

The Berendsen method[41] is essentially a direct scaling but softened with a time constant. Let  $T_0$  be the desired temperature,  $\Delta t$  is the time step of the simulation and  $\tau_T$  be the time constant for temperature control. In the Berendsen temperature control scheme, all velocities are

scaled at each time step by a factor  $\lambda$  given by

$$\lambda = \sqrt{1 + \frac{\Delta t}{\tau_T} \left( \frac{T_o}{T} - 1 \right)} \quad (2.9)$$

$\tau_T$  has to be greater than  $\Delta t$ . According to Berendsen [41] if  $\tau_T > 100\Delta t$  then the system has natural fluctuations about the average.

### 2.2.6 Pressure Scaling

The Berendsen pressure control is implemented by changing all atom positions, and the system cell size during the simulation. If the desired pressure is  $P_0$  and  $\tau_P$  is the time constant for pressure control, which should be typically greater than  $100\Delta t$ , the scaling factor  $\mu$  is given by:

$$\mu = \left[ 1 - \frac{\beta \Delta t}{\tau_P} (P_o - P) \right]^{\frac{1}{3}} \quad (2.10)$$

where  $\beta$  is the isothermal compressibility of the system ( $= \frac{1}{\text{bulk modulus}}$ ) and  $P$  is the current pressure.

The change in all atom positions and the system size is given by

$$\begin{aligned} \mathbf{r}(t + \delta t) &= \mu \mathbf{r}(t) \\ \mathbf{S}(t + \delta t) &= \mu \mathbf{S}(t) \end{aligned} \quad (2.11)$$

whence the volume of the system also changes by

$$\mathbf{V}(t + \delta t) = \mu^3 \mathbf{V}(t) \quad (2.12)$$

This type of temperature and pressure scaling should be done after the solution of the equations of motions and gives realistic fluctuations in temperature and pressure for system in equilibrium and when large values of  $\tau_T$  and  $\tau_P$  are chosen.

## 2.3 Ab initio molecular dynamics

Classical molecular dynamics, introduced in Sec. 2.2.2, using “pre-defined potentials”, based on empirical data (eg. the famous Brenner potential for hydrocarbons) or on independent electronic structure calculations, is well established as a powerful tool to investigate many-body condensed matter systems. The reign of traditional molecular dynamics and electronic structure methods has been greatly extended by the family of techniques that are called “*ab initio* molecular dynamics”. Other names that are currently in use are for instance Car- Parrinello, Hellmann-Feynman, first principles, quantum chemical, on-the-fly, direct, potential-free, quantum, etc. molecular dynamics. The basic idea underlying every *ab initio* molecular dynamics method is to compute the forces acting on the nuclei from electronic structure calculations.

At the very core of any molecular dynamics scheme is the question of how to describe - that is in practice how to approximate the interatomic interactions. The traditional route followed in molecular dynamics is to determine these potentials in advance (Sec. 2.2.2). Typically, the full interaction is broken up into two-body, three-body and many-body contributions, long-range and short-range terms etc., which have to be represented by suitable functional forms. After decades of intense research, very elaborate interaction models including the non-trivial aspect to represent them analytically were devised.

The electronic structure based molecular dynamics calculations can be further sub-classified into *on-the-fly* method, where the electronic structure calculations are performed as the molecular dynamics trajectory is generated or into a technique where the potential energy surface is pre-constructed using high dimensional fitting of the most accurate *ab initio* electronic structure calculations. Latter method is adopted for the present work and more details are presented in Sec. 2.4. The broadness, diversity, and level of sophistication of the techniques is documented in several monographs as well as proceedings of conferences and scientific schools [44, 45, 46, 47, 48, 49, 50].

In the *on-the-fly* approach, the electronic variables are not integrated out beforehand, but are considered as active degrees of freedom. This implies that, given a suitable approximate solution of the many-electron problem, also “chemically complex” systems can be handled by molecular dynamics. But this also implies that the approximation is shifted from the level of selecting the model potential to the level of selecting a particular approximation for solving the Schrödinger equation. Studying the molecular dissociation of  $C_2H_3^+$ , it has been observed that during the dissociation process the post hartree-fock method such as restricted coupled cluster (RCCSD(T)) fails to converge for partially fragmented nuclear configurations. However, the high-dimensional fitting procedure using invariant polynomial allows us to consistently generate a potential energy surface which can handle molecular dissociation correctly. Also the fitting procedure allows us to cover the regions of configuration-space which otherwise could not be sampled. Following these arguments chemical dynamics calculations are performed on the pre-fitted potential energy surface, based on high accuracy *ab initio* methods.

Ab initio molecular dynamics can also be viewed from another corner, namely from the field of classical trajectory calculations [51, 52]. In this approach, which has its origin in gas phase molecular dynamics, a global potential energy surface is constructed in a first step either empirically or based on electronic structure calculations, such as the work presented in this dissertation. In the second step, the dynamical evolution of the nuclei is generated by using classical mechanics, quantum mechanics or semi / quasiclassical approximations of various sorts. More details of this methodology is presented in Sec. 2.9.

Despite obvious advantages of *ab initio* molecular dynamics, that the potential description for the dynamical calculation are highly accurate, it is evident that a price has to be paid for putting molecular dynamics on *ab initio grounds*: the correlation lengths and relaxation times that are accessible are much smaller than what is affordable via standard molecular dynamics. If in a dynamical calculation, the trajectory consists of about  $10^M$  molecular dynamics steps, then  $10^M$  electronic structure calculations are needed to generate one trajectory. Furthermore, it is assumed that  $10^n$  independent trajectories are necessary in order to average over different initial conditions so that  $10^{M+n}$  *ab initio* molecular dynamics steps are required in total. Finally, it is assumed that each single-point electronic structure calculation needed to devise the global potential energy surface and one *ab initio* molecular dynamics time step requires roughly the same amount of cpu time. Based on this simplistic order of magnitude estimate, the advantage of *ab initio* molecular dynamics vs. calculations relying on the computation of a global potential energy surface amounts to about  $10^{3N-6-M-n}$ . The crucial point is that for a given statistical accuracy (that is for  $M$  and  $n$  fixed and independent on  $N$ ) and for a given electronic structure method, the computational scaling of “on-the-fly” approaches grows like  $10^N$  with system size. With the hartree-fock scaling of  $N^{3-4}$  ( $N$  being the number of basis function) and post hartree-fock method scaling as  $N^7$  (RCCSD(T)) “on-the-fly” would only be suitable choice for small molecules. Finally, it is evident that the computational advantage of the “on-the-fly” approach diminish as more and more trajectories are needed for a given (small)

system. For instance extensive averaging over many different initial conditions is required in order to calculate quantitatively scattering or reactive cross sections.

## 2.4 Molecular Potential Energy Surface

The molecular potential energy surface is generally used within the adiabatic or Born-Oppenheimer approximation in quantum mechanics and statistical mechanics to model chemical reactions and interactions in simple chemical and physical systems. In the Born-Oppenheimer approximation the electrons adjust their position instantaneously to follow any movement of the nuclei, so that the potential energy surface can equally be thought of as the potential for the movement of atoms within a molecule or atoms in collision with one another. This type of motion is called adiabatic: the dynamics of the system are associated with a single potential energy surface. There are some molecular processes in which the system makes transitions between different potential energy surfaces. These are called non-adiabatic processes and they arise from factors which are ignored in the Born-Oppenheimer approximation.

The importance of adiabatic processes for chemical reactions was first emphasized by London,<sup>[53]</sup> who suggested that most chemical reactions are adiabatic and the probability of the reaction can, in principle, be calculated by considering the dynamics of the atoms under the influence of a single potential energy surface which is function of the relative positions of all the atoms in the system. Simple potential energy surface, which can be obtained analytically, only provide an adequate description of the very simplest chemical systems. To model an actual chemical reaction, a potential energy surface must be created to take into account every possible orientation of the reactant and product molecules and the electronic energy of each of these orientations.

The other important field of chemical physics that can be understood largely by adiabatic processes is spectroscopy. The bound states of molecules can be classified by assigning definite electronic, vibrational, rotational and nuclear spin states, and total energy can be represented as a sum of electronic, vibrational, rotational and nuclear spin energies. There are important features of spectroscopy for which this is not so, but the above description is almost always a useful first approximation. In particular, the potential energy surface associated with an individual electronic state of a molecule determines the vibrational energy levels associated with that states.

The potential energy surface associated with a specific electronic state is the electronic energy (including the nuclear-nuclear repulsion energy) for all configurations of the nuclei on that particular state. Hence to calculate the potential energy surface from the Schrödinger equation one must solve the equation for each of tens of thousands of possible configurations (referred to as *ab initio* calculations), so as, to build up an adequate representation of the surface. These energy values can be fitted numerically to a multidimensional function. The accuracy of these *ab initio* points depends upon the level of theory used to calculate them. Some methods of obtaining such a fit include cubic splines, Shepard interpolation, and other types of multidimensional fitting functions.

On the fitted potential energy surface important nuclear configurations of interest are determined. The most important is the global minimum for the energy value. This global minimum (defined as point at which an infinitesimal step in any direction leads to an increase in potential energy), which can be found numerically, corresponds to the most stable nuclear configuration. Other interesting features are the reaction coordinate (the path along the potential energy surface that the atoms "travel" during the chemical reaction), saddle points (those places on surface which have zero-gradient, i.e. where  $3N - 6$  independent first derivatives are zero) or local

maxima along this coordinate (which correspond to transition states), and local minima along this coordinate (which correspond to reactive intermediates).

The main difficulty in determining accurate potential energy surface from *ab initio* calculations is that even with elaborate calculations it is difficult to obtain a uniform accuracy over the whole surface. Absolute accuracy, as measured by the total binding energy of the electrons to the nuclei, is not required, but relative accuracy, i.e. a constant error in the total energy at all points on the surface is necessary in order for barrier heights, dissociation energies, etc. to be accurate.

### 2.4.1 Topography

Most diatomic potential energy curves have very simple form; either they have a single minimum corresponding to a bound state of the two atoms or they are repulsive with, generally, only a shallow van der Waals minimum at large internuclear distances. It is comparatively rare (very rare for ground states) to find curves with more than one stationary point and, when observed, this is due to an avoided crossing of two curves.

The potential energy of polyatomic systems are more complex than diatomic potentials, not only because of their greater dimensionality ( $3N$ ) but also because there are features that are specifically associated with greater dimensionality. Most often higher dimensional potential energy surface are referred to as hypersurface. The "(hyper)surface" name comes from the fact that the total energy of an atom arrangement can be represented as a curve or (multidimensional) surface, with atomic positions as variables. The best visualization for a layman would be to think of a landscape, where going North-South and East-West are two independent variables (the equivalent of two geometrical parameters of the molecule), and the height of the land we are on would be the energy associated to a given value of such variables. However, potentials for polyatomics and diatomics are generally smooth. A diatomic potential does not look like a cross-section through the Alps. Polyatomic surfaces are not jagged; a gentle countryside of rolling hills is more representative. This geographical image is important because it implies that the mathematical task of representing the surface by relatively simple functions may be adequate. Just as Morse and Rydberg functions are simple and fairly accurate representation of diatomic curves, so such functions, increased in dimension, may be adequate representation of polyatomic surfaces.

### 2.4.2 Electronic structure calculations

The information about potential energy surfaces are obtained either from experimental techniques such as spectroscopy, gas kinetics and molecular beam experiments or by calculating approximate solutions of the electronic Schrödinger equation. Experimental techniques usually provide information about special local areas of the surface whereas calculations are, in principle, capable of providing information on the whole surface.

The history of quantum mechanical calculations on potential energy surface goes back to the early days of quantum mechanics with studies of the  $H_3$  surface in the 1930s. Until the mid 1960s, calculations on potential energy surfaces were based largely on model Hamiltonians or considerable approximations were made in solving Schrödinger equation for the exact Hamiltonian. However, with increased computer power and suites of quantum mechanical methods, which have been developed, *ab initio* methods have become the industry standard for generating points on the potential energy surface.

## 2.5 Methods

Almost all calculations employ molecular orbital (MO) theory at the self-consistent-field (SCF) level or go beyond that to include configuration interaction (CI). An orbital is the wave function of one electron in an atom or molecule. It is determined by the field of the nuclei and the field arising from the average distribution of all the electrons. In the SCF method there is consistency between the wave function and the field deduced from these wave functions. A configuration is an enumeration of the orbital occupations. As an example, the ground-state configuration of the carbon atom is  $1s^2 2s^2 2p^2$ . An SCF wave function is associated with a single configuration. If the configuration is that of a closed shell (all orbitals are either completely filled by electrons or are empty) then the SCF wave function is an antisymmetrized product of orbital and electron spin functions ( $\alpha$  or  $\beta$ ). This antisymmetrized product of orbitals and in the determinantal form is known as a Slater determinant. In the following section many-body wave function and mathematical formulation of the SCF method is presented.

## 2.6 Many-body Quantum Mechanics

Since inception of quantum mechanics by Heisenberg, Born, and Jordan[54, 55, 56, 57] in 1925, and Schrödinger in 1926[58, 59], there were basically two competing approaches to find the energy of a system of electrons. One approach was rooted in statistical mechanics and the fundamental variable was the total electron density  $\rho(\mathbf{r})$ , i.e., the number of electrons per unit volume at a given point in space (e.g., in cartesian coordinates:  $\mathbf{r} = (x, y, z)$ ). In this approach, electrons were treated as particles forming a special gas, called *electron gas*. The special case, the uniform electron gas, would correspond to the  $\rho(\mathbf{r}) = \text{const.}$

Another approach was to derive the many particle wave function  $\Psi(\mathbf{r}_1, \mathbf{r}_2, \dots, \mathbf{r}_N, t)$  (where the  $\mathbf{r}_1$  denotes the coordinates of the 1st electron,  $\mathbf{r}_2$  the 2nd electron, and so on, and  $t$  is time) and solve the stationary (time-independent) Schrödinger equation for the system:

$$\hat{H}\Psi_k(\mathbf{r}_1, \mathbf{r}_2, \dots, \mathbf{r}_N) = E_k\Psi_k(\mathbf{r}_1, \mathbf{r}_2, \dots, \mathbf{r}_N) \quad (2.13)$$

where  $\hat{H}$  is the hamiltonian, i.e., the operator of the total energy for the system, and calculate the set of possible wave functions (called eigenfunctions)  $\Psi_k$  and corresponding energies (eigenvalues)  $E_k$ .

The eigenfunctions are required to be continuous functions, at least doubly differentiable, should be square integrable and should vanish at infinity (for finite systems),

When the Schrödinger equation is solved **exactly** (e.g., for the hydrogen atom), the resulting eigenfunctions  $E_k$  form a *complete set* of functions, i.e., there is an infinite number of them, they are orthogonal to each other (or can be easily made orthogonal through a linear transformation), and any function which is of “physical quality” can be expressed through the combination of these eigenfunctions. Orthogonal means, that:

$$\int \Psi_k^* \Psi_l d^N \mathbf{r} = 0 \quad \text{if } k \neq l \quad (2.14)$$

The eigenfunction  $\Psi_0$  corresponding to the lowest energy  $E_0$ , describes the ground state of the system, and the higher energy values correspond to excited states. Physicists call  $\Psi$ 's the states (since they contain all possible information about the state), while chemists prefer to call them wave functions or simply functions.

Once the function  $\Psi$  (or its approximation, i.e., in case when the Schrödinger equation is solved only approximately) is known, the corresponding energy of the system can be calculated as an expectation value of the hamiltonian  $\hat{H}$ , as:

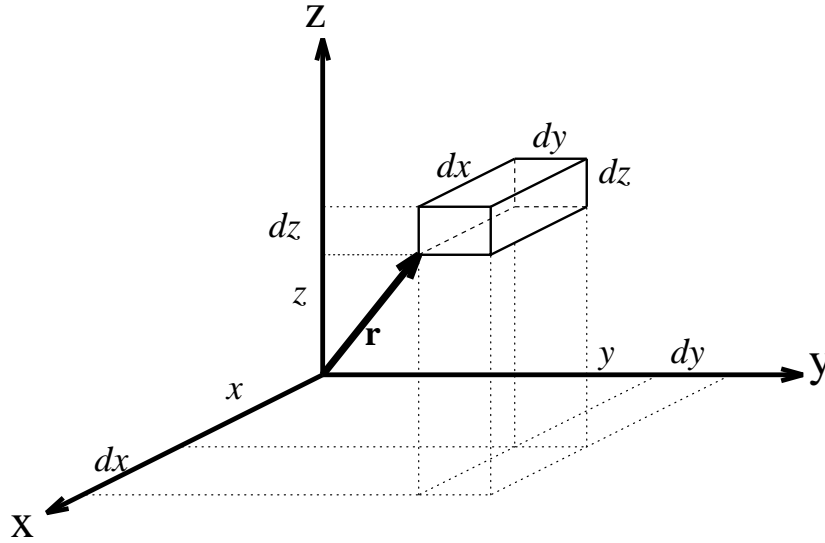


Figure 2.1: Volume element for a particle

$$E = \frac{\int \int \cdots \int \Psi^*(\mathbf{r}_1, \mathbf{r}_2, \cdots \mathbf{r}_N) \hat{H} \Psi(\mathbf{r}_1, \mathbf{r}_2, \cdots \mathbf{r}_N) d\mathbf{r}_1 d\mathbf{r}_2 \cdots d\mathbf{r}_N}{\int \int \cdots \int \Psi^*(\mathbf{r}_1, \mathbf{r}_2, \cdots \mathbf{r}_N) \Psi(\mathbf{r}_1, \mathbf{r}_2, \cdots \mathbf{r}_N) d\mathbf{r}_1 d\mathbf{r}_2 \cdots d\mathbf{r}_N} \quad (2.15)$$

where  $\Psi^*$  denotes the complex conjugate of  $\Psi$  since in general these functions may produce complex numbers. This is needed since the operator in this case represents a physical observable, and the result has to be a real number. This equation is frequently written using Dirac *bra* ( $\langle |$ ) and *ket* ( $| \rangle$ ) notation as:

$$E = \frac{\langle \Psi | H | \Psi \rangle}{\langle \Psi | \Psi \rangle} \quad (2.16)$$

And if  $\langle \Psi | \Psi \rangle = 1$ , i.e., the wave function is normalized, the energy equation above can be written as:

$$E = \langle \Psi | H | \Psi \rangle \quad (2.17)$$

The wave function itself does not correspond to any physical quantity, but the square of the wave function represents the probability density; written as:

$$|\Psi(\mathbf{r}_1, \mathbf{r}_2, \cdots \mathbf{r}_N)|^2 d\mathbf{r}_1 d\mathbf{r}_2 \cdots d\mathbf{r}_N \quad (2.18)$$

represents the probability that electron 1 is in the volume element  $d\mathbf{r}_1$  around point  $\mathbf{r}_1$ , electron 2 is in the volume element of the size  $d\mathbf{r}_2$  around point  $\mathbf{r}_2$ , and so on. If  $\Psi$  describes the system containing only a single electron, the  $|\Psi(\mathbf{r})|^2 d\mathbf{r}$  simply represents the probability of finding an electron in the volume element of a size  $d\mathbf{r}$  centered around point  $\mathbf{r}$  as shown in Figure 2.1.

Since the integral of the function  $\Psi$  over all the space for all the variables (i.e., sum up the probabilities in all the elements  $d\mathbf{r}_i$ ) would be unity. The wavefunction can be multiplied by a normalization constant:

$$\Psi_{\text{normalized}} = \frac{\overbrace{1}^{\text{Normalization constant}}}{\sqrt{\langle \Psi_{\text{unnormalized}} | \Psi_{\text{unnormalized}} \rangle}} \Psi_{\text{unnormalized}} \quad (2.19)$$

## 2.7 The Born-Oppenheimer Approximation

The nonrelativistic Hamiltonian for a molecule, which is the sum of kinetic and potential energy can be written as a sum of five terms:

$$\hat{H} = -\frac{\hbar^2}{2m} \sum_i \nabla_i^2 - \sum_A \frac{\hbar^2}{2M_A} \nabla_A^2 - \sum_{A,i} \frac{Z_A e^2}{r_{Ai}} + \sum_{A>B} \frac{Z_A Z_B e^2}{R_{AB}} + \sum_{i>j} \frac{e^2}{r_{ij}}, \quad (2.20)$$

where  $i, j$  refer to electrons and  $A, B$  refer to nuclei. In atomic units i.e., mass of electron  $m_e = 1$ ;  $\hbar = 1$ ; length is expressed in bohrs (1 bohr = 0.529177249Å; it is the radius of the first Bohr orbit in hydrogen atom); energy is in hartrees (1 hartree is 2 rydbergs, and the ground state energy of hydrogen atom is  $-1$  rydberg, or 0.5 hartree, 1 hartree = 627.51 kcal/mol = 2625.5 kJ/mol). The Hamiltonian can be re-written as:

$$\hat{H} = -\frac{1}{2} \sum_i \nabla_i^2 - \sum_A \frac{1}{2M_A} \nabla_A^2 - \sum_{A,i} \frac{Z_A}{r_{Ai}} + \sum_{A>B} \frac{Z_A Z_B}{R_{AB}} + \sum_{i>j} \frac{1}{r_{ij}}. \quad (2.21)$$

The Schrödinger equation may be written more compactly as

$$\hat{H} = \hat{T}_N(\mathbf{R}) + \hat{T}_e(\mathbf{r}) + \hat{V}_{eN}(\mathbf{r}, \mathbf{R}) + \hat{V}_{NN}(\mathbf{R}) + \hat{V}_{ee}(\mathbf{r}), \quad (2.22)$$

where  $\mathbf{R}$  is the set of nuclear coordinates and  $\mathbf{r}$  is the set of electronic coordinates. If spin-orbit effects are important, they can be added through a spin-orbit operator  $\hat{H}_{so}$

Unfortunately, the  $\hat{V}_{eN}(\mathbf{r}, \mathbf{R})$  term, which depends on both nuclear and electronic coordinates, prevents us from separating  $\hat{H}$  into nuclear and electronic parts, which would allow us to write the molecular wavefunction as a product of nuclear and electronic terms,  $\Psi(\mathbf{r}, \mathbf{R}) = \Psi(\mathbf{r})\chi(\mathbf{R})$ .

The Born-Oppenheimer approximation[60] introduced in 1927 allows us to do so. This approximation is based on the fact that the nuclei are much heavier than electrons (a proton is 1836 times heavier than an electron), they have much larger inertia than electrons, the electrons can adjust their positions instantly whenever the nuclei moves. This approximation allows us to use the electronic hamiltonian  $\hat{H}_{el}$  to study electrons, and add the components of energy coming from nuclei.

The term  $\hat{V}_{eN}(\mathbf{r}, \mathbf{R})$  is large and cannot be neglected; however, nuclear coordinate ( $\mathbf{R}$ ) dependence is made parametric, so that the total wavefunction is given as  $\Psi(\mathbf{r}; \mathbf{R})\chi(\mathbf{R})$ .

Thus the solution of the electronic hamiltonian for a range of  $\mathbf{R}$  would give the potential energy curve along which the nuclei moves.

### 2.7.1 Hartree-Fock theory

The variational principle in quantum mechanics states that the expectation value of energy  $E$ , calculated using some approximate wavefunction  $\Psi$  will be either higher, or equal to the ground state energy  $E_0$  for the system.

$$E = \frac{\langle \Psi | H | \Psi \rangle}{\langle \Psi | \Psi \rangle} \geq E_0 = \frac{\langle \Psi_0 | H | \Psi_0 \rangle}{\langle \Psi_0 | \Psi_0 \rangle} \quad (2.23)$$

The  $E = E_0$  occurs only if  $\Psi$  is equivalent to  $\Psi_0$ , but otherwise,  $E > E_0$ . For the proof of this theorem standard literature is referred, for example: Levine[61], 1983; Slater[62], 1968, or Szabo & Ostlund, 1996[63]).

The first step towards solving a many-body Schrödinger equation is to construct a many-body approximate wave function. The first successful attempt to derive approximate wave functions for atoms was devised by Hartree in 1928[64, 65, 66, 67]. In this approach the many-electron wave function  $\Psi$  is approximated by the product of one-electron functions  $\phi$  for each of the  $N$  electrons:

$$\Psi(\mathbf{r}_1, \mathbf{r}_2, \dots, \mathbf{r}_N) = \phi_1(\mathbf{r}_1)\phi_2(\mathbf{r}_2) \cdots \phi_N(\mathbf{r}_N) \quad (2.24)$$

In this equation,  $\mathbf{r}_i$  are the positional coordinates and a spin coordinate for the  $i$ -th electron. For example, in cartesian coordinate system the position vector is written as;  $\mathbf{r}_i = (x_i, y_i, z_i, m_{s_i})$  where  $m_{s_i}$  can adopt only 2 values:  $+\frac{1}{2}$  (spin up, or  $\alpha$  or  $\uparrow$ ) or  $-\frac{1}{2}$  (spin down,  $\beta$ , or  $\downarrow$ ). The individual one-electron functions  $\phi_i$  are called orbitals, (or spin-orbitals) and describe each electron in the atom (or molecule).

However, it can be seen that this is not a very reasonable approximation, because

1. It assumes that electrons in the atom can be described independently, i.e., their movements do not depend upon each other (uncorrelated) and their interaction is not pairwise, but each electron interacts with some averaged field of other electrons. This is not true reality. Electrons have to avoid each other (correlate their movements), since they repel each other being of the same charge.
2. The function does not have a proper symmetry for interchanging particle indices for fermions. It is known that the many electron wave function has to be antisymmetric to the exchange of neighboring indices, i.e., change sign:

$$\Psi(\mathbf{r}_1, \mathbf{r}_2, \dots, \mathbf{r}_i, \mathbf{r}_{i+1}, \dots, \mathbf{r}_N) = -\Psi(\mathbf{r}_1, \mathbf{r}_2, \dots, \mathbf{r}_{i+1}, \mathbf{r}_i, \dots, \mathbf{r}_N) \quad (2.25)$$

e.g.,

$$\Psi(\mathbf{r}_1, \mathbf{r}_2, \mathbf{r}_3) = -\Psi(\mathbf{r}_1, \mathbf{r}_3, \mathbf{r}_2) = -\Psi(\mathbf{r}_2, \mathbf{r}_1, \mathbf{r}_3) \quad (2.26)$$

If one-electron functions  $\phi_i(\mathbf{r})$ , for each electron is known, the total wave function can be constructed and the total density of the electrons is written as the sum of individual electron densities:

$$\rho_{tot}(\mathbf{r}) = \sum_{i=1}^N \rho_i(\mathbf{r}) = \sum_{i=1}^N |\phi_i(\mathbf{r})|^2 \quad (2.27)$$

However, the  $k$ -th electron does not interact with the whole density  $\rho_{tot}$ , since it is itself a part of it. So the electron cannot interact with itself! This would be called a self-interaction term. So, to evaluate the correct density with which the  $k$ -th electron interacts (denoted by  $\rho^{(k)}(\mathbf{r})$ ), the self interaction term should be subtracted from total density ( $\rho_{tot}$ ):

$$\rho^{(k)}(\mathbf{r}) = \rho_{tot}(\mathbf{r}) - \rho_k(\mathbf{r}) = \left( \sum_{i=1}^N \rho_i(\mathbf{r}) \right) - |\phi_k(\mathbf{r})|^2 = \sum_{\substack{i=1 \\ i \neq k}}^N |\phi_i(\mathbf{r})|^2 \quad (2.28)$$

If some approximate functions for the orbitals is known then the interaction energy of point charge (electron), located at position  $\mathbf{r}$ , with other electrons represented as a smeared electron density can be calculated. The point charge is  $-e$ , which in atomic units is  $-1$ , and the electron density is also negative, resulting in a positive contribution to the energy:

$$\hat{g}_k(\mathbf{r}) = \int \rho^{(k)}(\mathbf{r}') \frac{1}{|\mathbf{r} - \mathbf{r}'|} d\mathbf{r}' \quad (2.29)$$

Under this assumption the electronic hamiltonian,  $\hat{H}_{el}$ , is transformed into the sums of one-electron operators and the many electron Schrödinger equation can be solved as  $N$  independent one electron equations:

$$\left(-\frac{1}{2}\nabla_i^2 + \hat{v}_i + \hat{g}_i\right)\phi_i(\mathbf{r}) = \epsilon_i\phi_i(\mathbf{r}) \quad (2.30)$$

The  $\epsilon_i$  is the energy of the  $i$ -th electron. In practice one can start with some approximate orbitals  $\phi_i$  (e.g., from hydrogen atom), since the  $\hat{g}_i$  depends on them. All  $N$  equations are solved and obtain the  $N$  new  $\phi_i'$ 's. The new  $\phi_i'$ 's are different from the old  $\phi_i$ 's, and these would be better approximations for orbitals. The new  $\phi_i'$ 's are used as a starting point for the next iteration and repeat the process is repeated. At some point,  $\phi_i'$ 's do not change from iteration to iteration, and *self-consistent field* orbitals are obtained. From these orbitals one can form a many electron wave function  $\Psi$ , and then calculate the total energy  $E$  of the ground state. Note, that the total energy is not equal to the sum of orbital energies  $\epsilon_i$ .

Solving equation for  $\phi_1$  and  $\epsilon_1$  includes the Coulomb interactions between electron: (1, 2), (1, 3), (1, 4), etc. The second equation includes interactions: (2, 1), (2, 3), (2, 4), etc. But the interaction (1, 2) is the same as (2, 1), i.e., adding the energies would result in double counting of particle interactions. For this reason, the correct total energy can be represented as:

$$E = \sum_{i=1}^N \epsilon_i + \sum_{i=1}^{N-1} \sum_{j=i+1}^N J_{ij} \quad (2.31)$$

where  $J_{ij}$ 's represent Coulomb interaction of electron  $i$  and  $j$ . They are called Coulomb integrals and are defined as:

$$J_{ij} = \int \int \frac{\rho_i(\mathbf{r}_1)\rho_j(\mathbf{r}_2)}{|\mathbf{r}_1 - \mathbf{r}_2|} d\mathbf{r}_1 d\mathbf{r}_2 = \int \int |\phi_i(\mathbf{r}_1)|^2 \frac{1}{|\mathbf{r}_1 - \mathbf{r}_2|} |\phi_j(\mathbf{r}_2)|^2 d\mathbf{r}_1 d\mathbf{r}_2 \quad (2.32)$$

$$J_{ij} = \int \int \phi_i^*(\mathbf{r}_1)\phi_j^*(\mathbf{r}_2) \frac{1}{|\mathbf{r}_1 - \mathbf{r}_2|} \phi_i(\mathbf{r}_1)\phi_j(\mathbf{r}_2) d\mathbf{r}_1 d\mathbf{r}_2 \quad (2.33)$$

The Hartree approximation works well for atoms. The one-electron functions are quite good, and allow us to produce an approximate many-electron function for the whole atom. However it is known that the interchanging of the electron labels in the wave functions for the system should result in change of sign of the wavefunction. Fock[68] in 1930, and independently Slater[69] in 1930 proposed a fix to the Hartree method. They also used one-electron functions, but the total wave function for the system was not a simple product of orbitals, but an antisymmetrized sum of all the products which can be obtained by interchanging electron labels. It is conveniently represented as a determinant (called Slater determinant):

$$\Psi(\mathbf{r}_1, \mathbf{r}_2, \dots, \mathbf{r}_N) = \frac{1}{\sqrt{N!}} \begin{vmatrix} \phi_1(\mathbf{r}_1) & \phi_2(\mathbf{r}_1) & \cdots & \phi_N(\mathbf{r}_1) \\ \phi_1(\mathbf{r}_2) & \phi_2(\mathbf{r}_2) & \cdots & \phi_N(\mathbf{r}_2) \\ \phi_1(\mathbf{r}_3) & \phi_2(\mathbf{r}_3) & \cdots & \phi_N(\mathbf{r}_3) \\ \vdots & \vdots & \vdots & \vdots \\ \vdots & \vdots & \vdots & \vdots \\ \phi_1(\mathbf{r}_N) & \phi_2(\mathbf{r}_N) & \cdots & \phi_N(\mathbf{r}_N) \end{vmatrix} \quad (2.34)$$

Slater determinant satisfies the Pauli exclusion principle that each electron is described by a different wave function. However, it complicates equations compared to Hartree method and introduces a new term, *electron exchange*. The method of finding the best single determinant

wave function for the system is called Hartree-Fock method.

The expectation value of total energy for the single determinant wave function  $\Psi$  is given by:

$$E = \langle \Psi | H | \Psi \rangle = \sum_{i=1}^N H_i + \frac{1}{2} \sum_{i=1}^N \sum_{j=1}^N (J_{ij} - K_{ij}) \quad (2.35)$$

where:

$$H_i = \int \phi_i^*(\mathbf{r}) \left[ -\frac{1}{2} \nabla_i^2 + \hat{v}_i \right] \phi_i(\mathbf{r}) d(\mathbf{r}) \quad (2.36)$$

is an element of one-electron operator  $\hat{h}_i$  which is defined by equation

$$\hat{h}_i = -\frac{1}{2} \nabla_i^2 + \hat{v}_i \quad (2.37)$$

the  $J_{ij}$  is the Coulomb integral defined by equation (2.32), and  $K_{ij}$  is the new term, called *exchange integral*, which is defined by

$$K_{ij} = \iint \phi_i^*(\mathbf{r}_1) \phi_j(\mathbf{r}_1) \frac{1}{|\mathbf{r}_1 - \mathbf{r}_2|} \phi_i(\mathbf{r}_2) \phi_j^*(\mathbf{r}_2) d\mathbf{r}_1 d\mathbf{r}_2 \quad (2.38)$$

Note, that  $K_{ij}$  is similar in form to the  $J_{ij}$  but the functions  $\phi_i$  and  $\phi_j$  were exchanged. Also, electrons  $i$  and  $j$  have to be of the same spin for  $K_{ij}$  to be nonzero, due to orthogonality of their spin parts. It does not have a simple physical interpretation like  $J_{ij}$  (i.e., purely electrostatic interaction of two charge densities for electron  $i$  and  $j$ ). The exchange integral comes as a result of the determinantal form of  $\Psi$  which sums all possible products of permutations of electrons among orbitals.  $J_{ij}$  and  $K_{ij}$  are equal only when  $i = j$ . This is very important, since there is no contribution to the total energy coming from electron self-interaction. It can be shown that  $J_{ij}$ 's are larger (or equal to)  $K_{ij}$ 's and they are positive numbers.

There are essentially two approaches to HF method: first is purely numerical and the second is the one in which orbitals  $\phi$  are represented as combinations of basis functions. The numerical HF was used at some point to derive orbitals for many-electron atoms. There are also some numerical HF programs for molecules. However, these methods are quite *cpu* intensive. It is much more popular to represent orbitals  $\phi$  as a linear expansion into a set of some basis functions  $\chi$ :

$$\phi_i(\mathbf{r}) = \sum_{k=1}^n C_{ki} \chi_k(\mathbf{r}) \quad (2.39)$$

and optimizing coefficients  $C_{ki}$  rather than basis functions. The derivation of specific equations for Hartree-Fock can be found in many books, (see, e.g.: McWeeny & Sutcliffe[70], 1969; Parr[71], 1963; Pilar[72], 1968; Slater[62], 1968; Szabo & Ostlung[63], 1989) and landmark papers of Roothaan presented in 1951 and 1960[73, 74].

In the SFC LCAO MO (Self Consistent Field – Linear Combination of Atomic Orbitals, Molecular Orbitals) method, the idea is to search for coefficients  $C_{ki}$  which minimize the energy.

They are derived using variational principle, i.e. the goal here is to find a single determinant function  $\Psi$  as represented by equation (2.34) which corresponds to the lowest possible value of energy. It is done by the variational calculus. The condition of minimum of energy is:

$$\delta E_0 \equiv \delta \langle \Psi_0 | H | \Psi_0 \rangle = 0 \quad (2.40)$$

Another condition is that orbitals  $\phi$  have to be orthonormal, i.e.:

$$\langle \phi_i | \phi_j \rangle = \delta_{ij} \quad (2.41)$$

where  $\delta_{ij}$  is called a *Kronecker delta*, and is equal to 1 only if  $i = j$ , but is zero otherwise.

The problem of minimization of a function with some subsidiary conditions is done efficiently with the Lagrange's method of undetermined multipliers. In this method, the constraints are converted into expressions whose value is zero when the constraint is met. Such expressions are then multiplied by an undetermined constant and added (or subtracted, according to taste) to the minimized function. The resulting sum is then minimized:

$$\delta [\langle \Psi_0 | H | \Psi_0 \rangle - E (\langle \Psi_0 | \Psi_0 \rangle - 1)] = 0 \quad (2.42)$$

As a result, one gets Hartree-Fock eigenequations.

$$\hat{f}(\mathbf{r}_1)\phi_i(\mathbf{r}_1) = \epsilon_i\phi_i(\mathbf{r}_1) \quad (2.43)$$

where the Fock operator is defined as:

$$\hat{f}(\mathbf{r}_1) = \hat{h}(\mathbf{r}_1) + \sum_{a=1}^N [\hat{j}_a(\mathbf{r}_1) - \hat{k}_a(\mathbf{r}_1)] \quad (2.44)$$

In these equations, the fact that operators act on certain coordinates is stressed by writing explicitly their dependence on coordinates of electron 1 (it could be any electron number, since it does not matter how they are numbered). The  $\hat{h}(\mathbf{r}_1)$  was defined in equation (2.37). The Coulomb operator,

$$\hat{j}_a(\mathbf{r}_1)\phi_b(\mathbf{r}_1) = \phi_b(\mathbf{r}_1) \int |\phi_a(\mathbf{r}_2)|^2 \frac{1}{|\mathbf{r}_1 - \mathbf{r}_2|} d\mathbf{r}_2 = \phi_b(\mathbf{r}_1) \int \rho_a(\mathbf{r}_2) \frac{1}{|\mathbf{r}_1 - \mathbf{r}_2|} d\mathbf{r}_2 \quad (2.45)$$

and the exchange operator

$$\hat{k}_a(\mathbf{r}_1)\phi_b(\mathbf{r}_1) = \phi_a(\mathbf{r}_1) \int \phi_a^*(\mathbf{r}_2)\phi_b(\mathbf{r}_2) \frac{1}{|\mathbf{r}_1 - \mathbf{r}_2|} d\mathbf{r}_2 \quad (2.46)$$

are defined by the result of their action on a function.

If  $\phi_i$ 's are represented with their expansions into basis functions according to equation (2.39), the eigenproblems become a set of algebraic equations. Substituting equation (2.39) into (2.43) one gets:

$$\hat{f}(\mathbf{r}_1) \sum_{k=1}^n C_{ki} \chi_k(\mathbf{r}_1) = \epsilon_i \sum_{k=1}^n C_{ki} \chi_k(\mathbf{r}_1) \quad (2.47)$$

and multiplying on the left by  $\chi_l(\mathbf{r}_1)$  and integrating over  $\mathbf{r}_1$  one gets:

$$\sum_{k=1}^n C_{ki} \int \chi_l^*(\mathbf{r}_1) \hat{f}(\mathbf{r}_1) \chi_k(\mathbf{r}_1) d\mathbf{r}_1 = \epsilon_i \sum_{k=1}^n C_{ki} \int \chi_l^*(\mathbf{r}_1) \chi_k(\mathbf{r}_1) d\mathbf{r}_1 \quad (2.48)$$

Integrals are further denoted as:

$$(\mathbf{F})_{lk} = F_{lk} = \int \chi_l^*(\mathbf{r}_1) \hat{f}(\mathbf{r}_1) \chi_k(\mathbf{r}_1) d\mathbf{r}_1 \quad (2.49)$$

which is an element of a  $n \times n$  Fock matrix  $\mathbf{F}$ , and

$$(\mathbf{S})_{lk} = S_{lk} = \int \chi_l^*(\mathbf{r}_1) \chi_k(\mathbf{r}_1) d\mathbf{r}_1 \quad (2.50)$$

which is an element of a  $n \times n$  overlap integrals matrix  $\mathbf{S}$ . Where  $n$  is the number of basis functions of such equations, and it is convenient to write them in a matrix form as:

$$\mathbf{F}\mathbf{C} = \mathbf{S}\mathbf{C}\epsilon \quad (2.51)$$

The problem is reduced to find a matrix  $\mathbf{C}$  which diagonalizes  $\mathbf{F}$ , which is a standard procedure in linear algebra. First step is to find a matrix  $\mathbf{X}$  which diagonalizes overlap integrals  $\mathbf{S}$ , which is a step orthogonalizing the basis set (i.e., the basis set is converted to linear combinations of original basis functions, which are mutually orthogonal).

$$\mathbf{X}^\dagger \mathbf{S} \mathbf{X} = \mathbf{1} \quad (2.52)$$

Applying this matrix to equation (2.51) and rearranging:

$$\mathbf{C}'^\dagger \mathbf{F}' \mathbf{C}' = \epsilon \quad (2.53)$$

where  $\mathbf{C} = \mathbf{X}\mathbf{C}'$  and  $\mathbf{F}' = \mathbf{X}^\dagger \mathbf{F} \mathbf{X}$ .

The efficient routines for matrix diagonalization (i.e., obtaining  $\mathbf{C}'$  in this case) are widely available.

While they seem simple, the problem is that elements of  $\mathbf{F}$  depend on orbitals  $\phi$ , i.e., one can solve them only through iterative process as in Hartree's method. Moreover, due to Coulomb and exchange operators, the Fock matrix elements involve a massive number of two-electron integrals of a type:

$$\langle ij|kl \rangle = \int \int \chi_i^*(\mathbf{r}_1) \chi_j^*(\mathbf{r}_2) \frac{1}{|\mathbf{r}_1 - \mathbf{r}_2|} \chi_k(\mathbf{r}_1) \chi_l(\mathbf{r}_2) d\mathbf{r}_1 d\mathbf{r}_2 \quad (2.54)$$

To escape these difficulties and complexities, people tried for many years to describe electron systems using density, rather than wave function. In the HF approach the two-electron integrals  $\langle ij|kl \rangle$  dominate the computational effort. The HF method typically scales as  $N^{3-4}$ ;  $N$  being the number of basis function. Moreover, the HF is an approximation, as it does not account for dynamic correlation due to the rigid form of single determinant wave function. To solve the HF equations, the assumption has to be made that electrons interact with the averaged potential coming from other electrons, while in fact, the interactions between electrons are pairwise. In reality, electrons correlate their movements trying to avoid each other, so there is least amount of electrostatic repulsion. To account for dynamic correlation, one has to go to correlated methods, which use multideterminant wave functions, and these scale as fifth, or even greater powers with the size of the system. While HF method is quite successful for "bounded" geometries, it fails miserably to describe bond breaking or forming (for review on correlated *ab initio* methods, standard literature is referred; Bartlett & Stanton, 1994[75]).

## 2.7.2 Post Hartree-Fock techniques

The best SCF wave function for a specified configuration also known as the Hartree-Fock function, by variation theorem minimizes the energy of the state for this restricted class of function. SCF wave function generally gives reasonably good relative energies between states of the same molecule or states of different molecule which have the same number of electron pairs. However, they poor values for the relative energies of states with different numbers of electron pairs, and this usually means that the dissociation energies for covalent bond breaking are poor. To obtain satisfactory dissociation energies one must, in general, go beyond the SCF level of theory. This can be done by using multi-configuration SCF functions (these are functions that are variationally optimized for a specified set of configurations), or by CI.

The main objective of post SCF methods is to recover the missing electron correlation energy, which can lead to large deviations from experimental results. A collection of methods called post-Hartree-Fock methods, have been devised to include electron correlation to the multi-electron wave function. One of these approaches, Møller-Plesset perturbation theory, treats correlation as a perturbation of the Fock operator. Others expand the true multi-electron wavefunction in terms of a linear combination of Slater determinants - such as Multi-configurational self-consistent field, Configuration interaction, Quadratic configuration interaction, Complete active space SCF (CASSCF). Still others modify the Hartree-Fock wave function by multiplying it by a correlation function (“Jastrow” factor), a term which is explicitly a function of multiple electrons that cannot be decomposed into independent single-particle functions. Correlated calculations scale even less favorably - MP2 as  $N^5$ ; MP4 as  $N^6$  and coupled cluster as  $N^7$ , which makes it impractical for all but simplest systems. In general it is believed that CISD (configuration interaction method including single and double excitations) will scale as  $n^6$  and CISDTQ will scale as  $n^{10}$ ; where  $n$  is the number of orbitals. For very high levels of excitation, including full CI, the number of interacting matrix elements for a given determinant becomes approximately  $N^2 \times n^2$  and the computational cost becomes roughly  $N_{det} \times N^2 \times n^2$ ; where  $N_{det}$  is the dimension of the CI space given by:

$$N_{det} \sim \frac{1}{(m!)^2} N^m n_v^m \quad (2.55)$$

with  $m$  being the level of excitation,  $n_v$  is the number of unoccupied orbitals in the reference (i.e., virtual orbitals).

Two important concepts in electronic structure theory are size-consistency and size-extensivity. There are two primary definitions of size-consistency in use. The first was employed by Pople[76], which states that for the fragments of molecules separated by a large distance (large enough to be considered as non-interacting), the energy calculated for the fragments of the molecules should be exactly twice that calculated non-separated one. This “non-interacting limit” description is the original concept of size-consistency. From this perspective, size-consistency describes what has been referred to as the “additive separability” of the wavefunction. However, a more recently imposed definition[77] requires that the method not only correctly describe the fragmentation limit, but the entire process (in a qualitative sense). For example, both spin-unrestricted Hartree-Fock (UHF) and spin-restricted Hartree-Fock (RHF) wavefunctions are size-consistent. However, for a closed-shell molecule dissociating into open-shell fragments, a RHF wavefunction does not conform to the second definition of size-consistency.

Size-extensivity, on the other hand, is a more mathematically formal characteristic which refers to the correct (linear) scaling of a method with the number of electrons. The term was introduced to electronic structure theory by Bartlett[78], and is based on analogous “extensive” thermodynamic properties. All Hartree-Fock methods qualify as size-extensive, as well as many-body perturbation theory and coupled-cluster theories. Truncated configuration interaction methods, however, are not size-extensive. An important advantage of a size-extensive method is that it allows straightforward comparisons between calculations involving variable numbers of electrons, e.g. ionization processes or calculations using different numbers of active electrons. Lack of size-extensivity implies that errors from the exact energy increase as more electrons enter the calculation.

Coupled cluster solves the size consistency problem of CI by forming a wavefunction where the excitation operators are exponentiated

$$\Psi_{CC} = \exp(\hat{T})\Psi_0 \quad (2.56)$$

where

$$\hat{T} = \hat{T}_1 + \hat{T}_2 + \hat{T}_3 + \dots \quad (2.57)$$

and  $\hat{T}_n$  is a linear combination of all n-type excitations, for example,

$$\begin{aligned} \hat{T}_1\Psi_0 &= \sum_i \sum_a C_i^a \Psi_i^a \\ \hat{T}_2\Psi_0 &= \sum_{i>j} \sum_{a>b} C_{ij}^{ab} \Psi_{ij}^{ab} \end{aligned} \quad (2.58)$$

where  $C_i^a$  and  $C_{ij}^{ab}$  are the coefficients to be determined. Substituting equation set 2.58 into equation 2.56 yields the CCSD(TQ) wavefunction

$$\Psi_{CCSD} = \Psi_0 + \sum_a \sum_i C_i^a \Psi_i^a + \sum_{i>j} \sum_{a>b} C_{ij}^{ab} \Psi_{ij}^{ab} + \sum_{ab} \sum_{ij} C_i^a C_j^b \Psi_{ij}^{ab} + \text{higher order terms} + \dots \quad (2.59)$$

Where S, D, T and Q refer to single, double, triple and quadruple excitations. The advantage of CC theory is that the higher excitations are partially included, but their coefficients are determined by the lower order excitations. The coefficients are determined by projecting Schrödinger's equation on the left with the configurations generated by the  $\hat{T}$  operator. This replaces the eigenvalue problem by a non-linear simultaneous system, requiring iterative solution. However, convergence is fast in most cases. CCSD provides a size-extensive and accurate description of electron correlation effects for non-degenerate ground states of molecules near the equilibrium geometries with computer costs that enable routine calculations for systems with up to 50100 correlated electrons and a few hundred basis functions (hundreds of correlated electrons and over 1000 basis functions when local CCSD(T) is exploited). CCSDT scales as  $N^8$  which is impractical for all but the simplest of systems. A more practical alternative is CCSD(T)[79] where the effect of triples is estimated through perturbation theory with a non-iterative  $N^7$  cost. With large enough basis set CCSD typically recovers 95% of the correlation energy for a molecule at equilibrium geometry, while CCSDT (triple excitation included) gives rise to further five- to ten-fold reduction in error.[80] With such accuracy the coupled cluster method is the method of choice for accurate small-molecule calculations. In the present work electronic structure calculations were performed using CCSD(T) method.

## 2.8 Spectroscopic analysis

The most common method for determining vibrational frequencies is the normal mode analysis, based on the harmonic force constant matrix of energy second derivatives (Hessians). Of course, vibrations are not truly harmonic, and the anharmonicity generally increases as the frequency of the vibration (steepness of the potential) decreases. That is, the more anharmonic a motion is, the less applicable is the traditional approach to determining vibrational frequencies. In such cases, one can use the vibrational self-consistent field (VSCF) method to obtain anharmonic frequencies. The VSCF method is based on a representation of the vibrational wavefunction as a product of single-mode wavefunctions. The VSCF method[81, 82, 83, 84, 85] is also a variational procedure for computation of rovibrational levels of molecules. This method uses energies and gradients along a given normal mode direction to obtain the anharmonic cubic

and quartic terms. In analogy with electronic structure theory, the VSCF method can be augmented by a CI or perturbation theory, in order to obtain improved vibrational frequencies. These methods can accurately solve the problem of coupled vibrations, which physically arise because the vibrationally excited states of polyatomic molecules exhibit displacements so large that anharmonicities become important, causing the harmonic modes to mix. Formally, this can be expressed by starting with the vibrational Hamiltonian corresponding to a single Born-Oppenheimer potential energy surface, expressed in the normal-mode representation.

### 2.8.1 Brief description of theory: VSCF

The complete Watson Hamiltonian[86, 87] for a polyatomic molecule in normal coordinates is given by[88]

$$\hat{H}_{Watson} = -\frac{\hbar^2}{2} \sum_{i=1}^N \frac{\partial^2}{\partial Q_i^2} + \frac{\hbar^2}{2} \sum_{\alpha=1}^3 \sum_{\beta=1}^3 (J_\alpha - \pi_\alpha) \mu_{\alpha\beta} (J_\beta - \pi_\beta) - \frac{\hbar^2}{8} \sum_{\alpha=1}^3 \mu_{\alpha\alpha} + V(Q_1, \dots, Q_N) \quad (2.60)$$

where  $(\alpha, \beta = x, y, z)$  and  $J_\alpha$  and  $\pi_\alpha$  are the components of the total and vibrational angular momentum operator, respectively,  $\mu$  is the effective reciprocal inertia tensor,  $Q_i$  is the mass-weighted normal coordinate for mode  $i$ , and  $N$  is the number of vibrational degrees of freedom (or number of vibrational modes). The potential energy is a function of the normal coordinates and is given as  $V(Q_1, \dots, Q_N)$ . Note that  $V = 0$  at the equilibrium geometry. The first term in the above equation is the kinetic energy operator associated with each normal coordinate, the second term represents the coupling between the components of the angular momentum, and the third term, also known as the Watson term, is usually very small for polyatomic systems and is generally omitted from calculations. However, it is included in the present work.

For a nonrotating system ( $J=0$ ), Watson hamiltonian can be written as( in atomic units):

$$\hat{H} = \frac{1}{2} \sum_{\alpha\beta} \hat{\pi}_\alpha \mu_{\alpha\beta} \hat{\pi}_\beta - \frac{1}{8} \sum_{\alpha} \mu_{\alpha\alpha} - \frac{1}{2} \sum_i \frac{\partial^2}{\partial Q_i^2} + V(Q_i, \dots, Q_N) \quad (2.61)$$

the VSCF method approximates the vibrational wave function as a Hartree product of single-mode wave functions called *modals*.

$$\Psi^n(Q_1, \dots, Q_N) = \prod_i^N \phi_i^{n_i}(Q_i) \quad (2.62)$$

where  $\phi_i(Q_i)$  is the modal associated with normal coordinate  $Q_i$ .  $\mathbf{n}$  denotes a vector  $(n_1, \dots, n_i, \dots, n_N)$  comprising all quantum numbers of the corresponding one-mode wave functions  $\phi_i^{n_i}(Q_i)$ . For a fully decoupled system, i.e., within the harmonic approximation, this ansatz is exact, while it may fail for very strongly coupled systems.

The modals are constrained to be orthonormal (dropping quantum number index for simplicity):

$$\langle \phi_i | \phi_j \rangle = \delta_{ij} \quad (2.63)$$

where  $\delta_{ij}$  is the Kronecker  $\delta$ . The VSCF method is a variational procedure for obtaining the modals, and the optimized wave function of the form in Eq.2.62 is obtained by minimizing the total energy with respect to all the modals subject to the constraint of Eq.2.63, which is enforced by the Lagrange multipliers.

This variational procedure gives a set of differential equations for each modal. Furthermore, the hierarchical expansion of the potential  $V(Q_1, \dots, Q_N)$  in terms of  $n$ -mode contributions, the complete Watson operator can be expressed as

$$\hat{H} = \sum_i \hat{H}_i^{SCF}(Q_i) + \sum_{i < j} \hat{H}_{ij}^{SCF}(Q_i, Q_j) + \sum_{i < j < k} \hat{H}_{ijk}^{SCF}(Q_i, Q_j, Q_k) + \dots \quad (2.64)$$

It has been shown by Carter et al.[89] that the two-mode representation of the operator (or the potential, respectively) is not sufficient for many applications and may result in errors of  $30 \text{ cm}^{-1}$  or even more (vide infra). On the contrary, a four-mode representation usually leads to corrections of not more than one or two wave numbers with respect to a three-mode representation and thus the latter appears to be the optimal choice between accuracy and computational efficiency.

The one-mode operator in Eq. 2.64 is written as:

$$\hat{H}_i^{SCF} \phi_i(Q_i) = \epsilon_i \phi_i(Q_i), \quad (2.65)$$

for  $i = 1, \dots, N$ , where  $\epsilon_i$  is a Lagrange multiplier. Because  $H_i^{SCF}$  depends on the orbitals, this is not a conventional eigenvalue problem; it is called a pseudo-eigenvalue problem, and  $\epsilon_i$  is the modal energy; these equations are solved iteratively. Using Eq.2.60 with total angular momentum  $J$  equal to zero, the SCF Hamiltonian can be written as the following sum of kinetic and potential energy operators

$$H_i^{SCF} \equiv T_i + U_i, \quad (2.66)$$

where  $T_i$  is the kinetic energy operator associated with mode  $i$ , and is given as

$$T_i = \frac{\hbar^2}{2} \frac{\partial^2}{\partial^2 Q_i}, \quad \text{for } i = 1, \dots, N, \quad (2.67)$$

and  $U_i$  is known as the mean field operator and is given as:

$$U_i = \left\langle \prod_{j \neq i}^N \phi_j(Q_j) \middle| V(Q_1, \dots, Q_N) + \frac{\hbar^2}{2} \sum_{\alpha=1}^3 \sum_{\beta=1}^3 \pi_{\alpha} \mu_{\alpha\beta} \pi_{\beta} \middle| \prod_{j \neq i}^N \phi_j(Q_j) \right\rangle \quad (2.68)$$

In order to evaluate  $U_i$ , one must perform an (Full)-dimensional integral over the normal coordinates, which is computationally intensive for most polyatomic systems. To make the calculations tractable, the potential energy term is expanded in a hierarchical fashion. The form of this expansion is:

$$\begin{aligned} V(Q_1, \dots, Q_N) &= \sum_{i=1}^N V_i^{(1)}(Q_i) + \sum_{i=1}^N \sum_{j=1}^i V_{i,j}^{(2)}(Q_i, Q_j) \\ &+ \sum_{i=1}^N \sum_{j=1}^i \sum_{k=1}^j V_{i,j,k}^{(3)}(Q_i, Q_j, Q_k) \\ &+ \sum_{i=1}^N \sum_{j=1}^i \sum_{k=1}^j \sum_{l=1}^k V_{i,j,k,l}^{(4)}(Q_i, Q_j, Q_k, Q_l) + \dots \end{aligned} \quad (2.69)$$

By approximating the N-mode potential as a sum of one-mode, two-mode, three-mode, and four-mode terms, only four-dimensional integral evaluation is required. In principle, one should converge the expansion by including higher-order terms (five-mode, six-mode,...), but earlier calculations have shown that stopping at three-mode coupling is sometimes already well converged. In the present work results obtained with three-mode coupling and four-mode coupling are compared to those obtained with five mode coupling.

The components of the vibrational angular momentum operator ( $\pi_\alpha$  in eqn. 2.60 and eqn. 2.61 ) depend on two normal coordinates via the Coriolis coupling constant and are expressed as

$$\pi_\alpha = -i \sum_{k=1}^N \sum_{l=1}^N \zeta_{k,l}^\alpha Q_k \frac{\partial}{\partial Q_l}, \quad (2.70)$$

where  $\zeta_{k,l}^\alpha$  is the Coriolis coupling constant[90]. The treatment of this term and the Watson term is explained elsewhere[91].

The  $\mu$  tensor occurring in the Coriolis coupling term between the components of the angular momentum and the Watson correction term is the inverse of the corrected moment of inertia tensor  $I'$  (see Ref. 18):

$$\mu_{\alpha\beta} = (\mathbf{I}'^{-1})_{\alpha\beta} \text{ with } \alpha, \beta \in xyz \text{ and } \mathbf{I}'_{\alpha\beta} = \mathbf{I}_{\alpha\beta} \sum_{ijk} \zeta_{ik}^\alpha \zeta_{jk}^\beta Q_i Q_j \quad (2.71)$$

where  $\mathbf{I} = \mathbf{I}(Q_1, \dots, Q_N)$  denotes the moments of inertia tensor at a given point on the potential energy surfaces and  $\zeta_{ij}^\alpha$  are the Coriolis  $\zeta$ -constants with  $\zeta_{ii}^\alpha = 0$ . Using the same expansion of the Watson operator as outlined above, the elements of the first and second order contributions of the Watson correction term are given as

$$\mu_{\alpha\alpha}(Q_i) = \mu_{\alpha\alpha}^0(Q_i) \mu_{\alpha\alpha}^0 \quad (2.72)$$

$$\mu_{\alpha\alpha}(Q_i, Q_j) = \mu_{\alpha\alpha}^0(Q_i, Q_j) - \mu_{\alpha\alpha}(Q_i) - \mu_{\alpha\alpha}(Q_j) - \mu_{\alpha\alpha}^0 \quad (2.73)$$

where  $\mu_{\alpha\alpha}^0(Q_i)$  and  $\mu_{\alpha\alpha}^0(Q_i, Q_j)$  are obtained from

$$\mathbf{I}'_{\alpha\beta}(Q_i) = \mathbf{I}_{\alpha,\beta}(Q_i) - \sum_{l \neq i} \zeta_{il}^\alpha \zeta_{il}^\beta Q_i^2 \quad (2.74)$$

$$\mathbf{I}'_{\alpha\beta}(Q_i, Q_j) = \mathbf{I}_{\alpha,\beta}(Q_i, Q_j) - \sum_{r,s \in \{i,j\}} \sum_{t \neq r,s} \zeta_{rt}^\alpha \zeta_{st}^\beta Q_r Q_s \quad (2.75)$$

Within this notation,  $\mu_{\alpha\alpha}(Q_i, Q_j)$  denotes the difference between the 2D contribution  $\mu_{\alpha\alpha}^0(Q_i, Q_j)$  computed at a 2D grid point and the corresponding 1D difference terms  $\mu_{\alpha\alpha}(Q_i)$ .  $\mu_{\alpha\alpha}^0$  represents the diagonal elements of the  $\mu$  tensor at the equilibrium structure. These pseudo-potential-like contributions can be added to the potential and were found to be converged after the third order term. Likewise, making use of the commutator relation

$$[\hat{\pi}, \mu_{\alpha\beta}] = 0 \quad (2.76)$$

with

$$\hat{\pi}_\alpha = -i \sum_{rs} \zeta_{rs}^\alpha Q_r \frac{\partial}{\partial Q_s} \quad (2.77)$$

the contributions of the Coriolis coupling operator can be evaluated. According to the expansion of the Watson operator [Eq. 2.64] the contributions of the Coriolis coupling operator depend on an increasing number of normal coordinates  $Q_i$ . The first-order contribution vanishes as the summation over  $r$  and  $s$  in Eq. 2.77 is limited to coordinate  $i$  only, which causes the Coriolis coupling constant to be zero. The second order term has nonvanishing elements, but the restriction of the summation over  $r$  and  $s$  to elements  $i$  and  $j$  allows for a number of simplifications.

While VSCF is often of reasonable accuracy, it is obviously desirable to correct for correlation effects between the modes. An effective treatment is the one that uses the fact that

the nonseparability effects are small, and can thus be treated by perturbation theory[92]. This leads to a treatment that is the vibrational analogue[92, 93] of the Møller-Plesset method from electronic structure theory. The VSCF procedure was extended by Carter et al.[88, 94] to study rovibrational states by using the Whitehead Handy[95, 96] implementation of the Watson[86] Hamiltonian. However, the VSCF method is not quantitatively accurate. A more accurate, systematically improvable procedure is vibrational-rotational configuration interaction [88] (VRCI). The convergence of VRCI calculations can be accelerated by optimizing the basis functions using VSCF.[84] A particularly efficient scheme, called virtual configuration interaction (VCI) is to use a ground-state VSCF calculation to generate single-mode functions and to use products of these single-mode functions (called modals) with rotational basis functions as basis functions with linear coefficients optimized by the variational principle.[88, 94] These functions are called configuration state functions (CSFs).

### 2.8.2 VSCF-CI theory

The many-mode wavefunction is expanded in a basis of VSCF states. These states are not orthogonal and this results in a generalized eigenvalue problem. This problem is solved by standard methods. The expansion can be done in several ways. An expansion in increasing energy is recommended to obtain true variational upper bound approximations to the exact eigenvalues and eigenfunctions.

### 2.8.3 VCI theory

The many-mode wavefunction is expanded in terms of the eigenstates (also known as the virtual states) of a given VSCF Hamiltonian. Usually the ground state VSCF Hamiltonian is used. This basis is orthonormal and results in a standard eigenvalue problem. The resulting eigenvalues and eigenfunctions are true variational upper bound approximations to the exact eigenvalues and eigenfunctions.

Since the modes are coupled, one needs to go beyond the VSCF approximation. The eigenfunctions of the ground-state SCF Hamiltonian for  $J = 0$  form an orthonormal basis, and the total vibrational wave function can be expanded in this basis; as mentioned in the introduction, this is called virtual CI (VCI)[88, 94]. For the calculations in this work, the hierarchical expansion of Eq.2.69 is restricted to at most five/four-mode coupling, and the VCI basis is formed by the use of one-mode, two-mode, three-mode, and four-mode excitations from the ground state. The one-mode excitations are limited by specifying the maximum number of quanta each mode can possess. Two-mode, three-mode, and four-mode excitations are limited by two parameters; one of them is the maximum number of quanta each mode can possess (called maxbas), and the other is the sum of quanta in all the modes (called maxsum).

A general basis function for the VCI calculation is called a configurational state function (CSF) and is written as  $|n_1 n_2 \dots n_i \dots n_N \rangle$ , where  $N$  is the number of modes (9 for  $C_2H_3^+$  and 15 for  $C_2H_5^+$ ) and  $n_i$  is the number of quanta in mode  $i$ . All one-mode excitations of the form  $|0_1 0_2 \dots n_i \dots 0_N \rangle$ , are included, provided  $n_i \leq \text{maxbas}(i, 1)$ . All two-mode excited states of the form  $|0_1 0_2 \dots n_i \dots n_j \dots 0_F \rangle$  are included, where the sum  $n_i + n_j$  is less than or equal to  $\text{maxsum}(2)$ , and  $n_i$  and  $n_j$  are less than or equal to  $\text{maxbas}(i, 2)$  and  $\text{maxbas}(j, 2)$ , respectively. Similarly, all three-mode and four-mode excitations of the form  $|0_1 0_2 \dots n_i \dots n_j \dots n_k \dots 0_F \rangle$  and  $|0_1 0_2 \dots n_i \dots n_j \dots n_k \dots n_l \dots 0_F \rangle$  are included, where  $n_i + n_j + n_k$  is less than or equal to  $\text{maxsum}(3)$ , and  $n_i + n_j + n_k + n_l$  is less than or equal to  $\text{maxsum}(4)$ , respectively, and also where  $n_i$  is less than or equal to  $\text{maxbas}(i, 3)$  for three-mode excitations and  $\text{maxbas}(i, 4)$  for four-mode excitations[94, 97].

## 2.9 Quasi-classical trajectory calculations: Description of theory

Classical trajectories are the limits, with high particle masses and high energies, of quantum-mechanical scattering processes. They may also be thought of as the high-information limit of scattering theory. This method comes into play whenever the main interest is in the molecular physics and the chemistry of an actual process, as contrasted with the form and properties of the theory. For almost all chemical reaction, they provide the only feasible connection between laboratory observations and the unknown potential of interaction of the atoms. They are of value in those cases where the potential can be calculated by a *priori* methods. Classical trajectory simulations are widely used to study the dynamics of chemical reactions[98, 99, 100, 101]. In these simulations, the classical equations of motion are numerically integrated to determine the motion of the individual atoms. Normally, cartesian coordinates and momenta are used as the degree of freedom for numerical integration.

Commonly for a reaction which takes by interaction of reactants A and B, could lead to formation of a complex, termed as AB. The complex would then eventually breakup to form products C and D. This reaction is written as:



The technique of classical trajectory calculations for such a reaction involves sampling the reaction events, generating starting conditions, solving the equation of motion and evaluating the results and properties of the product.

### 2.9.1 Initial conditions

A number of decisions must be made for each starting parameter. The first is whether it should be scanned-assigned values which vary systematically from trajectory to trajectory-or whether is should be sampled in a strictly random way (“Monte Carlo”) , or whether some intermediate scheme should be used. The initial conditions relevant for a quasi-classical trajectory calculations, for the reactants A and B in eqn. 2.78, are the rotational-, vibrational-quantum numbers of reactants, relative translational energy and impact parameter.

Initial conditions for a polyatomic reactant can be chosen by orthant sampling, microcanonical normal mode sampling, fixed normal mode energies, local mode sampling, or by sampling a Boltzmann distribution. A diatomic reactant can be either a rotating harmonic or Morse oscillator. In the case of fixed mode normal mode energies, normal mode analysis of reactants A and B is performed on the PES to calculate the normal mode eigenvalues and eigenvectors. The amplitude for each normal mode is computed from

$$A_i = (2E_i)^{1/2}/\omega_i \quad (2.79)$$

where  $\omega_i = 2\pi\nu_i$  and the energy is computed for given vibrational quantum number  $n$ . Random numbers are used to give each normal mode an initial random phase  $2\pi R_i$ . The initial normal mode coordinates and their time derivative is given by:

$$\begin{aligned} Q_i &= A_i \cos(2\pi R_i) \\ \dot{Q}_i &= -\omega_i A_i \sin(2\pi R_i) \end{aligned} \quad (2.80)$$

Transformation to cartesian coordinates  $x$  and momenta  $p_x$  is:

$$\begin{aligned} [x] &= [L_x][Q] + [x_0] \\ [p_x] &= [M][L_x][\dot{Q}] \end{aligned} \quad (2.81)$$

where  $[x_0]$  is the matrix of the equilibrium coordinates.

Rotational energy and angular momentum for the polyatomic molecule is selected by assuming separability of vibrational and rotational motion. The rotational energy can be chosen from thermal distribution by assuming a symmetric top,  $I_x < I_y = I_z$  or  $I_x = I_y < I_z$  or the rotational energy can be fixed for each axis to be equal to  $RT/2$ .

If either of the reactants is a diatom, then the diatomic reactant is treated as a rotating oscillator, for which the Hamiltonian is written as

$$H = \frac{p^2}{2\mu} + V(r) + \frac{J^2}{2\mu r^2} \quad (2.82)$$

The oscillator internal energy  $E_{nj}$  is calculated semiclassically as a function of diatomic number of vibrational and rotational quanta  $n$  and  $J$ . The linear momentum  $p$  for the rotating oscillator is chosen from

$$p = \pm(2\mu)^{1/2}[E_{nj} - J(J+1)/2\mu r^2 - V(r)]^{1/2} \quad (2.83)$$

The following steps are followed for calculating the initial conditions for the diatomic reactant.

- Given the equilibrium coordinates and number of vibrational ( $n$ ) and rotational ( $J$ ) quanta, normal mode analysis is performed for the diatomic reactant on the global potential energy surface.
- The oscillator internal energy is firstly initialized to

$$E_{nj} = (n + \frac{1}{2})\nu \quad (2.84)$$

where  $\nu$  is the normal mode frequency for the diatom. Further, parameters for an oscillator with given  $n$  and  $J$  is initialized by semiclassical EBK quantization. To select the initial relative coordinate and momenta for the diatom, the classical turning points are calculated by semiclassical quantization procedure. A value of  $r = r^- + (r^+ - R^-)xR_1$ , where  $R_1$  is a random number. Using this  $r$  linear momentum  $p$  is computed. The  $r$  and  $p$  are accepted if  $P(r)/P^0(r)$  is greater than a second random number  $R_2$ .

The relative translational energy  $E_{rel}$  can either be fixed or chosen from the Boltzmann distribution<sup>1</sup> at temperature  $T_{rel}$

$$P(E_{rel}) = \frac{E_{rel}}{(k_B T_{rel})^2} \exp\left[-\frac{E_{rel}}{k_B T_{rel}}\right] \quad (2.85)$$

If using this distribution, the rate constant versus temperature  $T_{rel}$  should be calculated via

$$\begin{aligned} k(T_{rel}) &= \left(\frac{8k_B T_{rel}}{\pi\mu}\right)^{1/2} \int_0^\infty \sigma(E_{rel})P(E_{rel})dE_{rel} \\ &= \left(\frac{8k_B T_{rel}}{\pi\mu}\right)^{1/2} \pi b_{max}^2 \frac{N_r}{N_t} \end{aligned} \quad (2.86)$$

where  $\sigma(E_{rel})$  is the reactive cross section at  $E_{rel}$ ,  $\mu$  is the reduced mass of the two reactants,  $b_{max}$  is the maximum impact parameter,  $N_t$  is the total trajectory number, and  $N_r$  is the reactive trajectory number.

## 2.9.2 Product properties

Properties of the products C and D for the chemical reaction that are of interest are the C+D relative translational energy, the C and D vibrational and rotational energies, and the scattering angle between the initial A+B and final C+D relative velocity vectors. The property of the products can be calculated from the space fixed cartesian coordinates and momenta at the termination of a classical trajectory.

The product relative velocity is the difference between the velocities of the center of mass of C and D is give by

$$\begin{aligned} X_D &= \frac{1}{M_D} \sum_{i=1}^{n_D} m_i x_i \\ \dot{X}_D &= \frac{1}{M_D} \sum_{i=1}^{n_D} m_i \dot{x}_i \end{aligned} \quad (2.87)$$

where the sum  $n_D$ , is the sum over number of atoms in D. The  $m_i$  are masses of the atoms and the  $x_i$  are the x coordinates of the atoms in the system center-of-mass frame of reference.  $M_D$  is the mass of D. (Upper case X, Y and Z are used to identify center-of-mass positions and velocities of the products) The relative velocity of the products is then the time derivative of the vector  $\mathbf{R}$  defining the separation between the center-of-mass of C and D.

$$\begin{aligned} \mathbf{R} &= (X_D - X_C)\hat{i} + (Y_D - Y_C)\hat{j} + (Z_D - Z_C)\hat{k} \\ &= R_x\hat{i} + R_y\hat{j} + R_z\hat{k} \end{aligned} \quad (2.88)$$

and

$$\dot{\mathbf{R}} = \dot{R}_x\hat{i} + \dot{R}_y\hat{j} + \dot{R}_z\hat{k} \quad (2.89)$$

The relative energy between the products is given by

$$E_{rel} = \frac{\mu_{CD}\dot{\mathbf{R}} \cdot \dot{\mathbf{R}}}{2} \quad (2.90)$$

where  $\mu_{CD}$  is the CD reduced mass. The relative energy may also be written as the sum of, the relative translational energy from the components of the relative velocity along the line-of-centers of the products C and D (i.e. the radial motion) and the energy from the orbital (i.e. angular) motion of C and D:

$$E_{rel} = \frac{\mu_{CD}\dot{\mathbf{R}}^2}{2} + \frac{l^2}{2\mu_{CD}R^2} \quad (2.91)$$

with

$$R = (\mathbf{R} \cdot \mathbf{R})^{1/2} \quad (2.92)$$

and

$$\dot{\mathbf{R}} = \frac{\dot{R}_x R_x + \dot{R}_y R_y + \dot{R}_z R_z}{R} \quad (2.93)$$

The term  $l$  in Eq. 2.91 is the orbital angular momentum, which is given by

$$\begin{aligned} l &= \mu_{CD} \dot{\mathbf{R}} \times \mathbf{R} \\ &= l_x\hat{i} + l_y\hat{j} + l_z\hat{k} \end{aligned} \quad (2.94)$$

The velocity scattering angle  $\theta$  is defined as the angle between the relative velocity vector for the reactants  $\dot{\mathbf{R}}'$  and the product's relative velocity vector  $\dot{\mathbf{R}}$  given above

$$\theta_s = \cos^{-1} \left( \frac{\dot{\mathbf{R}} \cdot \dot{\mathbf{R}}'}{\dot{\mathbf{R}} \dot{\mathbf{R}}'} \right) \quad (2.95)$$

To calculate the internal rotational and vibrational energy of a product molecule requires the coordinates and velocities of each atom in the molecule in the center-of-mass frame of reference fixed with the molecule. Evaluation of the components of the center-of-mass position and velocity of product D is given by Eq. 2.87. The coordinates and velocities of the atoms D in the molecule fixed center-of-mass frame (denoted by a prime) are:

$$\begin{aligned} x'_i &= x_i - X_D \\ \dot{x}'_i &= \dot{x}_i - \dot{X}_D \end{aligned} \quad (2.96)$$

index  $i$  runs over all atoms in product molecule D ( $n_D$ ). The internal energy of D is

$$E_D = T_D + V_D \quad (2.97)$$

where  $T_D$  and  $V_D$  are the kinetic and potential energy of D respectively.  $V_D$  is easily determined from the potential energy surface and the kinetic energy is given by

$$T_D = \sum_{i=1}^{n_D} \frac{m_i(\dot{x}'_i{}^2 + \dot{y}'_i{}^2 + \dot{z}'_i{}^2)}{2} \quad (2.98)$$

The rotational angular momentum  $j$  of the product molecule D is the sum of the angular momenta  $j_i$  of the individual atoms of D rotating about the D center of mass

$$j_D = \sum_{i=1}^{n_D} j_i = j_x \hat{i} + j_y \hat{j} + j_z \hat{k} \quad (2.99)$$

where  $j_x$ ,  $j_y$ , and  $j_z$  are the magnitudes of the components of  $\mathbf{j}$ . The atomic angular momenta are given by

$$j_i = m_i \mathbf{r}'_i \times \dot{\mathbf{r}}'_i = j_{xi} \hat{i} + j_{yi} \hat{j} + j_{zi} \hat{k} \quad (2.100)$$

where  $\mathbf{r}'_i$  defines the position of atom  $i$  with respect to the D center-of-mass

$$\mathbf{r}'_i = x'_i \hat{i} + y'_i \hat{j} + z'_i \hat{k} \quad (2.101)$$

and  $\dot{\mathbf{r}}'_i$  is the time derivative of  $\mathbf{r}'_i$ . The  $x$ ,  $y$ , or  $z$  component of  $\mathbf{j}$  is a sum of the  $x$ ,  $y$ , or  $z$  component of  $\mathbf{j}_i$  for the individual atoms:

$$j_x = \sum_{i=1}^{n_D} j_{xi} \quad (2.102)$$

The total angular momentum  $\mathbf{L}$  of the C+D products is the vector sum

$$\mathbf{L} = \mathbf{l} + \mathbf{j}_C + \mathbf{j}_D \quad (2.103)$$

It may also be evaluated by summing the angular momenta of all the  $n_C + n_D$  atoms calculate in the center-of-mass space fixed frame for the complete molecular system, i.e.

$$\mathbf{L} = \sum_{i=1}^{n_C+n_D} m_i \mathbf{r}_i \times \dot{\mathbf{r}}_i \quad (2.104)$$

where  $\mathbf{r}_i$  given by

$$\mathbf{r}_i = x_i \hat{i} + y_i \hat{j} + z_i \hat{k} \quad (2.105)$$

defines the position of atom  $i$  with respect to the system's center of mass and  $\dot{\mathbf{r}}_i$  is the time derivative.

The rotational and vibrational properties of the products C and D can be also calculated from the quasi-classical trajectory calculations. The rotational quantum number  $J$  for D is found from the quantum mechanical expression for the rotational angular momentum:

$$j = \sqrt{J(J+1)}\hbar \quad (2.106)$$

where  $j$  is computed from eqn. 2.99. Since the calculation is classical, noninteger values are obtained for  $J$ . Integer values are often obtained by rounding  $J$  to the nearest integer values.

The vibrational quantum number  $n$  for the diatomic is found from the Einstein-Brillouin-Keller (EBK) semiclassical quantization condition[102], which states that the phase space area  $\int \int \mu_{12} dr d\dot{r}$  is  $(n + \frac{1}{2})h$ . Another notation for this integral is

$$\oint p_r dr = (n + \frac{1}{2})h \quad (2.107)$$

where momentum  $p_r = \mu\dot{r}$  and the cyclic integral denotes integration over one vibrational period (i.e. orbit).

If the product of the reaction is polyatomic, then it is not simple to calculate quantum numbers for its vibrational and rotational degrees of freedom. If the motion of the product is regular then the semiclassical quantization described above can be applied. However, because of vibrational-rotational coupling, the multidimensionality of the problem and possible resonances between the vibrational modes, performing the semiclassical quantization is often difficult. Another less rigorous approach involves calculating average energies of the normal modes of the molecule.

## 2.10 Density Functional Theory

Electron density has always been more attractive, since it depends only on  $x, y, z$ , and eventually, there may be two densities for spin polarized systems, one for spin up electrons  $\rho_\uparrow(\mathbf{r})$  and one for spin down electrons  $\rho_\downarrow(\mathbf{r})$ , as opposed to many particle wave function which depends on all coordinates of all particles, i.e., for  $\mathbf{N}$  electrons, it depends on  $3\mathbf{N}$  variables (or  $4\mathbf{N}$  if spin is also included). The fact that the ground state properties are functionals of the electron density  $\rho(\mathbf{r})$  was proved by Hohenberg and Kohn in 1964[103] and it provides the basic framework for modern Density Functional methods.

According to the theorem proved by Hohenberg and Kohn(HK), the total ground state energy of an electron system can be written as a functional of the electronic density, and this energy is at minimum if the density is an exact density for the ground state. The theorem of HK is an existence proof of such a functional, but there is no prescription how to construct it. Unfortunately the exact form of energy functional is not known and it becomes necessary to use approximations regarding parts of the functional dealing with kinetic energy and exchange and correlation energies of the system of electrons.

The simplest approximation is the local density approximation (LDA) which leads to a Thomas-Fermi[104, 105] term for kinetic energy and to Dirac[106] term for the exchange energy. The corresponding functional is called Thomas-Fermi-Dirac energy. These functionals can be further improved but the results are not that encouraging for molecular systems. But, on

the other hand, the Thomas-Fermi-Dirac+improvements method is a true density functional method, since all components of energy can be expressed via density alone, without using many particle wave functions. However, it seems that there is no way to avoid wave functions in molecular calculations and for accurate calculations they have to be used as a mapping step between the energy and density. For example, the Thomas-Fermi theory does not predict chemical bonds. While "pure" density functional theories are very useful in studying solid phase (e.g., conductivity), they fail to provide meaningful results for molecular systems.

### 2.10.1 The Hohenberg and Kohn theorems

The field of rigorous density functional theory was born in 1964 with the publication of the Hohenberg and Kohn[103]. They proved the following:

- I. Every observable of a stationary quantum mechanical system (including energy), can be calculated, in principle exactly, from the ground-state density alone, i.e., every observable can be written as a functional of the ground-state density.

Since  $\rho(\mathbf{r})$  determines number of electrons,  $N$ :

$$N = \int \rho(\mathbf{r}) d\mathbf{r} \quad (2.108)$$

and  $\rho$  determines the  $\hat{V}_{ext}$ , the knowledge of total density is as good, as knowledge of  $\Psi$ , i.e., the wave function describing the state of the system; which was proved through contradiction. Since,  $\rho(\mathbf{r})$  determines  $N$  and  $\hat{V}_{ext}$ , it also determines all properties of the ground state, including the kinetic energy of electrons  $T_e$  and energy of interaction among electrons  $U_{ee}$ , i.e., the total ground state energy is a functional of density with the following components

$$E[\rho] = T_e[\rho] + V_{ext}[\rho] + U_{ee}[\rho] \quad (2.109)$$

Additionally, HK grouped together all functionals which are secondary (i.e., which are responses) to the  $V_{ext}[\rho]$ :

$$E[\rho] = V_{ext}[\rho] + F_{HK}[\rho] = \int \rho(\mathbf{r}) \hat{V}_{ext}(\mathbf{r}) d\mathbf{r} + F_{HK}[\rho] \quad (2.110)$$

The  $F_{HK}$  functional operates only on density and is universal, i.e., its form does not depend on the particular system under consideration (note that N-representable densities integrate to N, and the information about the number of electrons can be easily obtained from the density itself).

- II. The ground state density can be calculated, in principle exactly, using the variational method involving only density.

If for some trial density  $\tilde{\rho}(\mathbf{r})$ ; such that  $\tilde{\rho}(\mathbf{r}) \geq \mathbf{0}$  and for which some density represents the correct number of electrons,  $\int \tilde{\rho}(\mathbf{r}) d\mathbf{r} = N$ ,

$$E_0 \leq E[\tilde{\rho}] \quad (2.111)$$

the total energy calculated from this density cannot be lower than the true energy of the ground state.

As to the necessary conditions for this theorem, there is still some controversy concerning the, so called, representability of density. The  $N$ -representability, i.e., the fact that the trial  $\tilde{\rho}$  has to sum up to  $N$  electrons is easy to achieve by simple rescaling. It is automatically insured if  $\rho(\mathbf{r})$  can be mapped to some wave function (for further discussion see: Parr & Yang, 1989; Gilbert, 1975; Lieb, 1982; and Harriman, 1980). Assuring that the trial density has also  $V_{ext}$ -representability (usually denoted in the literature as  $v$ -representability) is not that easy. Levy (1982) and Lieb (1983) have shown, that there are some “reasonable” trial densities, which are not the ground state densities for any possible  $V_{ext}$  potential, i.e., they do not map to any external potential. Such densities do not correspond therefore to any ground state, and their optimization will not lead to a ground state. Moreover, during energy minimization, if the system gets stuck into some non  $v$ -representable density then the calculations will never be able to converge to a physically relevant ground state density. Assuming that, only to trial densities which are both  $N$  and  $v$  representable are used and the variational principle for density is easily proven since each trial density  $\tilde{\rho}$  defines a hamiltonian  $\hat{H}_{el}$ . From the hamiltonian the corresponding wave function  $\tilde{\Psi}$  for the ground state represented by this hamiltonian can be derived. And according to the traditional variational principle, this wave function  $\tilde{\Psi}$  will not be a ground state for the hamiltonian of the real system  $\hat{H}_{el}$ :

$$\tilde{\rho} \rightarrow \hat{H}_{el} \rightarrow \tilde{\Psi}; \quad \langle \tilde{\Psi} | H | \tilde{\Psi} \rangle = E[\tilde{\rho}] \geq E[\rho_0] \equiv E_0 \quad (2.112)$$

where  $\rho_0(\mathbf{r})$  is the true ground state density of the real system.

The condition of minimum for the energy functional:  $\delta E[\rho(\mathbf{r})] = 0$  needs to be constrained by the  $N$ -representability of density which is optimized. It also needs to be constrained by  $v$ -representability. There exist *constrained search* formulation by Levy (Levy, 1982) and *local-scaling transformation* by Petkov *et al*, 1986 which assure  $v$ -representability during density optimization. The Lagrange’s method of undetermined multipliers is a very convenient approach for the constrained minimization problems. In this method the constraints is represented in such a way that their value is exactly zero when they are satisfied.

### 2.10.2 Kohn and Sham Method

The idea of constrained minimization provides a prescription of minimizing energy by changing corresponding density. Unfortunately, the expression relating kinetic energy to density is not known with satisfactory accuracy. The current expressions, even those improved upon from the original Thomas-Fermi theory, are quite crude and quite unsatisfactory for atoms and molecules in particular. On the other hand, the kinetic energy is easily calculated from the wave function, provided that it is known. For that reason, Kohn & Sham[107] proposed an ingenious method of combining wave function and density approach.

They repartitioned the total energy functional into following parts:

$$E[\rho] = T_0[\rho] + \int [\hat{V}_{ext}(\mathbf{r}) + \hat{U}_{cl}(\mathbf{r})] \rho(\mathbf{r}) d\mathbf{r} + E_{xc}[\rho] \quad (2.113)$$

where  $T_0[\rho]$  is the kinetic energy of electrons in a system which has the same density  $\rho$  as the real system, but in which there is no electron-electron interactions. This is frequently called a system on noninteracting electrons, but the electrons still interact with nuclei.

$$\hat{U}_{cl}(\mathbf{r}) = \int \frac{\rho(\mathbf{r}')}{|\mathbf{r}' - \mathbf{r}|} d\mathbf{r}' \quad (2.114)$$

is a pure Coulomb (“classical”) interaction between electrons. It includes electron self-interaction explicitly, since the corresponding energy is

$$E_{cl}[\rho] = \int \int \frac{\rho(\mathbf{r}')\rho(\mathbf{r})}{|\mathbf{r}' - \mathbf{r}|} d\mathbf{r}d\mathbf{r}' \quad (2.115)$$

and it represents interaction of  $\rho$  with itself.

$\hat{V}_{ext}(\mathbf{r})$  is the external potential, i.e., potential coming from nuclei:

$$\hat{V}_{ext} = \sum_{\alpha} \frac{-Z_{\alpha}}{|\mathbf{R}_{\alpha} - \mathbf{r}|} \quad (2.116)$$

The last functional,  $E_{xc}[\rho]$ , called exchange-correlation energy, is defined by this equation.  $E_{xc}[\rho]$  includes all the energy contributions which were not accounted for by previous terms, i.e.:

- electron exchange
- electron correlation, since non-interacting electrons do need to correlate their movements. However, this correlation component is not the same as defined by Löwdin for *ab initio* methods.
- a portion of the kinetic energy which is needed to correct  $T_0[\rho]$  to obtain true kinetic energy of a real system  $T_e[\rho]$ .
- correction for self-interaction introduced by the classical coulomb potential.

All the difficult things are made part of this functional. However, better and better approximations for this functional are being published. Assuming that the energy functional is known reasonably well and applying variational principle, chemical potential can be written as:

$$\mu = \frac{\delta E[\rho(\mathbf{r})]}{\delta \rho(\mathbf{r})} = \frac{\delta T_0[\rho(\mathbf{r})]}{\delta \rho(\mathbf{r})} + \hat{V}_{ext}(\mathbf{r}) + \hat{U}_{cl}(\mathbf{r}) + \frac{\delta E_{xc}[\rho(\mathbf{r})]}{\delta \rho(\mathbf{r})} \quad (2.117)$$

collecting all terms, except the noninteracting electron kinetic energy term, into an effective potential depending upon  $\mathbf{r}$ :

$$\mu = \frac{\delta E[\rho(\mathbf{r})]}{\delta \rho(\mathbf{r})} = \frac{\delta T_0[\rho(\mathbf{r})]}{\delta \rho(\mathbf{r})} + \hat{V}_{eff}(\mathbf{r}) \quad (2.118)$$

where the effective potential term is written as:

$$\hat{V}_{eff}(\mathbf{r}) = \hat{V}_{ext}(\mathbf{r}) + \hat{U}_{cl}(\mathbf{r}) + \hat{V}_{xc}(\mathbf{r}) \quad (2.119)$$

the exchange correlation potential in the above equation is defined as a functional derivative of exchange correlation energy:

$$\hat{V}_{xc}(\mathbf{r}) = \frac{\delta E_{xc}[\rho(\mathbf{r})]}{\delta \rho(\mathbf{r})} \quad (2.120)$$

The form of equation (2.118) is precisely the same as the equation which would be obtained for a non-interacting system of particles moving in an external potential  $\hat{V}_{eff}$ . To find the ground-state density  $n_0(\mathbf{r})$  for this non-interacting system, Schrödinger equation can be solved for noninteracting particles:

$$\left[ -\frac{1}{2}\nabla_i^2 + \hat{V}_{eff}(\mathbf{r}) \right] \phi_i^{KS}(\mathbf{r}) = \epsilon_i \phi_i(\mathbf{r})^{KS} \quad (2.121)$$

It is very similar to the eigenequation of the Hartree-Fock method, with the difference that it is much simpler. The Fock operator in equation (2.44) contains the potential which is **nonlocal**, i.e., different for each electron. The Kohn-Sham operator depends only on  $\mathbf{r}$ , and not upon the index of the electron. It is the same for all electrons. The Kohn-Sham orbitals,  $\phi_i(\mathbf{r})^{KS}$ , which are quite easily derived from equation 2.121 can be used immediately to compute the total density: If expansion into basis sets is used, the matrix equation (2.53) for expansion coefficients is identical as in Hartree-Fock method. The total density is using Kohn-Sham orbitals is:

$$\rho(\mathbf{r}) = \sum_{i=1}^N |\phi_i^{KS}(\mathbf{r})|^2 \quad (2.122)$$

which can be used to calculate an improved potential  $\hat{V}_{eff}(\mathbf{r})$ , i.e., lead to a new cycle of *self-consistent field*<sup>1</sup>.

Density can also be used to calculate the total energy from equation (2.113), in which the kinetic energy  $T_0[\rho]$  is calculated from the corresponding orbitals, rather than density itself:

$$T_0[\rho] = \frac{1}{2} \sum_{i=1}^N \langle \phi_i^{KS} | \nabla_i^2 | \phi_i^{KS} \rangle \quad (2.123)$$

and the rest of the total energy as:

$$V_{eff}[\rho] = \int \hat{V}_{eff}(\mathbf{r}) \rho(\mathbf{r}) d\mathbf{r} \quad (2.124)$$

In practice, total energy is calculated more economically using orbital energies  $\epsilon_i$  as:

$$E[\rho] = \sum_{i=1}^N \epsilon_i - \frac{1}{2} \int \int \frac{\rho(\mathbf{r})\rho(\mathbf{r}')}{|\mathbf{r} - \mathbf{r}'|} d\mathbf{r}d\mathbf{r}' - \int \hat{V}_{xc}(\mathbf{r})\rho(\mathbf{r})d\mathbf{r} + E_{xc}[\rho] \quad (2.125)$$

The electrons described by these equations move in an effective potential  $\hat{V}_{eff}(\mathbf{r})$  which includes electron interaction, somewhat in an artificial way.

### 2.10.3 The local density approximation

The results for the Kohn-Sham equations are exact, provided the functional form of  $E_{xc}[n]$  is known. The problem of determining the functional form of the universal Hohenberg-Kohn density functional has now been transferred to this one term, and therefore this term is not known exactly. Remarkably, it is possible to make simple approximations for the exchange-correlation energy which work extremely well, and the simplest of these, is the local density approximation (LDA).

In the LDA, the contribution to the exchange-correlation energy from each infinitesimal volume in space,  $d\mathbf{r}$ , is taken to be the value it would have if the whole of space were filled with a homogeneous electron gas with the same density as is found in  $d\mathbf{r}$  i.e.

$$E_{xc}[n] = \int d\mathbf{r} \epsilon_{xc}(n(\mathbf{r})) n(\mathbf{r}) \quad (2.126)$$

where  $\epsilon_{xc}(n(\mathbf{r}))$  is the exchange-correlation energy per electron in a homogeneous electron gas of density  $n(\mathbf{r})$ . The exchange-correlation potential  $V_{xc}(\mathbf{r})$  then takes the form

<sup>1</sup>It has to be stressed that  $\phi_i(\mathbf{r})^{KS}$ 's are not the real orbitals, and they do not correspond to a real physical system. Their only role in the theory is to provide a mapping between kinetic energy and density. For one, the total KS wave function is a single determinant and is unable to model situations where more determinants are needed to describe the system (e.g., for cases when molecules dissociate to atoms)

$$V_{xc}(\mathbf{r}) = \frac{\delta E_{xc}[n]}{\delta n(\mathbf{r})} = \epsilon_{xc}(n(\mathbf{r})) + n(\mathbf{r}) \frac{d\epsilon_{xc}(n)}{dn} \Big|_{n=n(\mathbf{r})} \quad (2.127)$$

The LDA is exact in the limit of slowly-varying densities, however, the density in systems of interest is generally rapidly varying, and the LDA would appear to be a crude approximation for those cases. Its use is justified a posteriori by its surprising success at predicting physical properties in real systems. This success may be due in part to the fact that the sum rule for the exchange-correlation hole, which must be obeyed by the real functional, is reproduced by the LDA[108].

#### 2.10.4 Implementations of Kohn and Sham method

First implementations of the Kohn-Sham method were using the local approximations to the exchange correlation energy. The appropriate functionals were taken from data on homogeneous electron gas. There were two variants of the method: spin unpolarized (LDF/LDA – Local Density Functional/Approximation) and spin polarized (LSD – Local Spin Density) where arguments require both  $\alpha$  and  $\beta$  electron densities, rather than a total density.

For historical reasons, the exchange correlation energy was partitioned into 2 parts:

$$E_{xc}[\rho] = E_x[\rho] + E_c[\rho] \quad (2.128)$$

the exchange energy, and correlation energy. This partition is quite arbitrary, since exchange and correlation have slightly different meaning than in *ab initio* approaches. The correlation energy was expressed as:

$$E_c[\rho] = \int \rho(\mathbf{r}) \epsilon_c[\rho_\uparrow(\mathbf{r})\rho_\downarrow(\mathbf{r})] d\mathbf{r} \quad (2.129)$$

where  $\epsilon_c[\rho_\uparrow(\mathbf{r})\rho_\downarrow(\mathbf{r})]$  is the correlation energy per one electron in a gas with spin densities  $\rho_\uparrow(\mathbf{r})$  and  $\rho_\downarrow(\mathbf{r})$ . This function is not known analytically, but is constantly improved on the basis of quantum Monte Carlo simulations, and fitted to analytical expansion. The local functionals derived from electron gas data worked surprisingly well, taking into account that they substantially underestimate the exchange energy (by as much as 15%) and grossly overestimate the correlation energy, sometimes by a 100%. The error in exchange is however larger than the correlation error in absolute values. LSD/LDF is known to overbind normal atomic bonds, on the other hand, it produces too weak hydrogen bonds.

Early attempts to improve functionals by GEA (Gradient Expansion Approximation), in which  $E_{xc}[\rho]$  was expanded in Taylor series versus  $\rho$  and truncated at a linear term, did not improve results too much. Only GGA (Generalized Gradient Approximation) provided notable improvements by expanding  $E_{xc}[\rho]$ . The expansion here is not a simple Taylor expansion, but tries to find the right asymptotic behaviour and right scaling for the usually nonlinear expansion. These enhanced functionals are frequently called nonlocal or gradient corrections, since they depend not only upon the density, but also the magnitude of the gradient (i.e., first derivative) of density at a given point. While the term corrections has a historical meaning, where the corrections were added on the top of local density functionals, it is probably no longer correct, since modern nonlocal functionals are quite complicated functions in which the value of density and its gradient are integral parts of the formula. For review of the existing functionals see e.g.: Clementi (1994), Johnson *et al* (1993), Seminario & Politzer (1995), Ziegler (1991). The most widely used local potentials are: Slater for exchange (Slater, 1974), and VWN for correlation (Vosko *et al*, 1980). Probably the most frequently in use today are:

- For exchange: B88 (Becke, 1988), PW86 (Perdew & Wang, 1986)

- For correlation: P86 (Perdew, 1986), LYP (Lee *et al.*, 1988),

Most molecular DFT programs use basis functions, with a notable exception of a totally basis free NUMOL (Becke & Dickinson, 1990) program. Quite impressive variety of basis sets is used. Since most energy components have to be calculated via numerical integration, the use of contracted gaussians as a basis is not that essential. But most program use them, as it allows a substantial code reuse from the well developed traditional *ab initio* techniques.

Typical SCF-KS calculation for performing single geometry SCF cycle or geometry optimization starts with a density (for the 1st iteration, superposition of atomic densities is typically used). Further steps involve establishing grid for charge density and exchange correlation potential. KS matrix is computed, which is equivalent to the  $\mathbf{F}$  matrix in Hartree-Fock method in equation (2.53) elements and overlap integrals matrix. The KS equations are solved for expansion coefficients to obtain KS orbitals and new density  $\rho = \sum_{i=occ} |\phi_i(\mathbf{r})|^2$  is computed.

It is quite popular to limit expense of numerical integration during the SCF cycle. It is frequently done by fitting auxiliary functions to charge density and exchange correlation potential. This allows for much faster integral evaluation. These auxiliary fitting functions are usually uncontracted gaussians (though quite different from the atomic basis sets) for which the integrals required for KS matrix can be calculated analytically. Different auxilliary sets are used for fitting charge density and exchange-correlation potential (see e.g., Dunlap & Rösch, 1990). The need for fitting is recently questioned (see e.g., Johnson, 1995) since it scales as  $N^3$  even for very large systems, however, it is still very popular in DFT programs. The fitting procedures are in general non sparse, while for large molecules many contributions coming from distant portions may be neglected leading to less steep scaling with molecular size.

### 2.10.5 Periodic systems

Exploiting the results of the previous section the motion of non-interacting particles in a static potential can be described by the time-independent Schrödinger equation. In the study of bulk crystals, the system is infinite but periodic, and so it is necessary to be able to reduce this problem to the study of a finite system. This approach turns out to have several advantages so that it is often easiest to study even aperiodic systems by imposing some false periodicity. The system is contained within a supercell which is then replicated periodically throughout space. The supercell must be large enough so that the systems contained within each one, which in reality are isolated, do not interact significantly.

The system of non-interacting particles moving in a static potential  $V(\mathbf{r})$  may be considered to be moving in the Kohn-Sham effective potential  $V_{KS}(\mathbf{r})$ . In a perfect crystal, the nuclei are arranged in a regular periodic array described by a set of Bravais lattice vectors  $\{\mathbf{R}\}$ . The system, being infinite, is invariant under translation by any of these lattice vectors, and in particular the potential is also periodic i.e.

$$V(\mathbf{r} + \mathbf{R}) = V(\mathbf{r}) \quad (2.130)$$

for all Bravais lattice vectors  $\mathbf{R}$ .

The Schrödinger equation which describes the motion of a single particle in this potential is

$$\hat{H}|\psi\rangle = \left[ -\frac{1}{2}\nabla^2 + V(\mathbf{r}) \right] |\psi\rangle = \varepsilon|\psi\rangle \quad (2.131)$$

and translation operators  $\hat{T}_{\mathbf{R}}$  for each lattice vector  $\mathbf{R}$  which act in the following manner on any function of position  $f(\mathbf{r})$  are defined as:

$$\hat{T}_{\mathbf{R}}f(\mathbf{r}) = f(\mathbf{r} + \mathbf{R}) \quad (2.132)$$

Since the potential and hence the Hamiltonian are periodic i.e.  $\hat{H}(\mathbf{r} + \mathbf{R}) = \hat{H}(\mathbf{r})$ , these operators commute with the translation operators:

$$\hat{T}_{\mathbf{R}}\hat{H}(\mathbf{r})\psi(\mathbf{r}) = \hat{H}(\mathbf{r} + \mathbf{R})\psi(\mathbf{r} + \mathbf{R}) = \hat{H}(\mathbf{r})\psi(\mathbf{r} + \mathbf{R}) = \hat{H}(\mathbf{r})\hat{T}_{\mathbf{R}}\psi(\mathbf{r}) \quad (2.133)$$

i.e.  $[\hat{H}, \hat{T}_{\mathbf{R}}] = 0$ , and the translation operators commute with each other i.e.  $\hat{T}_{\mathbf{R}}\hat{T}_{\mathbf{R}'} = \hat{T}_{\mathbf{R}'}\hat{T}_{\mathbf{R}} = \hat{T}_{\mathbf{R}+\mathbf{R}'}$ .

There must, therefore, exist a good quantum number corresponding to each lattice vector  $\mathbf{R}$ , and it must also be possible to choose the eigenstates of the Hamiltonian to be simultaneous eigenstates of all the translation operators;

$$\hat{H}|\psi\rangle = \varepsilon|\psi\rangle \quad (2.134)$$

$$\hat{T}_{\mathbf{R}}|\psi\rangle = c(\mathbf{R})|\psi\rangle \quad (2.135)$$

From the commutation relations of the translation vectors it follows that the eigenvalues must satisfy

$$c(\mathbf{R} + \mathbf{R}') = c(\mathbf{R})c(\mathbf{R}') \quad (2.136)$$

The eigenvalues for the three primitive lattice vectors  $\{\mathbf{a}_i\}$  are defined in terms of three complex numbers  $\{x_i\}$  by

$$c(\mathbf{a}_i) = \exp(2\pi i x_i) \quad (2.137)$$

Since all lattice vectors can be expressed in the form  $\mathbf{R} = n_1\mathbf{a}_1 + n_2\mathbf{a}_2 + n_3\mathbf{a}_3$ , where the  $n_i$  are integers, it follows from equation 2.136 that

$$c(\mathbf{R}) = c(\mathbf{a}_1)^{n_1} c(\mathbf{a}_2)^{n_2} c(\mathbf{a}_3)^{n_3} \quad (2.138)$$

which is equivalent to

$$c(\mathbf{R}) = \exp(i\mathbf{k} \cdot \mathbf{R}), \quad (2.139)$$

$$\mathbf{k} = x_1\mathbf{g}_1 + x_2\mathbf{g}_2 + x_3\mathbf{g}_3 \quad (2.140)$$

where the  $\{\mathbf{g}_i\}$  are the reciprocal lattice vectors satisfying  $\mathbf{g}_i \cdot \mathbf{a}_j = 2\pi\delta_{ij}$ , and the  $\{x_i\}$  are complex numbers in general.

Thus, it has been shown that

$$\hat{T}_{\mathbf{R}}\psi(\mathbf{r}) = \psi(\mathbf{r} + \mathbf{R}) = c(\mathbf{R})\psi(\mathbf{r}) = \exp(i\mathbf{k} \cdot \mathbf{R})\psi(\mathbf{r}) \quad (2.141)$$

which is one statement of Bloch's theorem. Consider the function  $u(\mathbf{r}) = \exp(-i\mathbf{k} \cdot \mathbf{r})\psi(\mathbf{r})$ .

$$u(\mathbf{r} + \mathbf{R}) = \exp(-i\mathbf{k} \cdot [\mathbf{r} + \mathbf{R}])\psi(\mathbf{r} + \mathbf{R}) = \exp(-i\mathbf{k} \cdot \mathbf{r})\psi(\mathbf{r}) = u(\mathbf{r}) \quad (2.142)$$

i.e. the function  $u(\mathbf{r})$  also has the periodicity of the lattice, and so the wave-function  $\psi(\mathbf{r})$  can also be expressed as

$$\psi(\mathbf{r}) = \exp(i\mathbf{k} \cdot \mathbf{r})u(\mathbf{r}), \quad (2.143)$$

where  $u(\mathbf{r})$  is a strictly cell-periodic function i.e.  $u(\mathbf{r} + \mathbf{R}) = u(\mathbf{r})$ .

Assigning labels to the eigenstates of the Hamiltonian and the translation operators  $|\psi_{n\mathbf{k}}\rangle$  where  $n$  is the good quantum number labelling different eigenstates of the Hamiltonian with the same good quantum vector  $\mathbf{k}$ , related to the translational symmetry.

Note that a periodic function can always be expressed as a Fourier series i.e.

$$u(\mathbf{r}) = \sum_{\mathbf{G}} \tilde{u}_{\mathbf{G}} \exp(i\mathbf{G} \cdot \mathbf{r}) \quad (2.144)$$

where  $\mathbf{G}$  is reciprocal lattice vector  $\mathbf{G} = m_1\mathbf{g}_1 + m_2\mathbf{g}_2 + m_3\mathbf{g}_3$  and the  $m_i$  are integers. Thus the state  $|\psi_{n\mathbf{k}}\rangle$  can be expressed as a linear combination of plane-waves:

$$\psi_{n\mathbf{k}}(\mathbf{r}) = \exp(i\mathbf{k} \cdot \mathbf{r})u_{n\mathbf{k}}(\mathbf{r}) = \sum_{\mathbf{G}} c_{n\mathbf{k}}(\mathbf{G}) \exp[i(\mathbf{k} + \mathbf{G}) \cdot \mathbf{r}] \quad (2.145)$$

Instead of having to solve for a wave-function over all of (infinite) space, the problem now becomes one of solving for wave-functions only within a single (super)cell, albeit with an infinite number of possible values for  $\mathbf{k}$ . In order to simplify the problem to manageable proportions, it is necessary to impose some boundary conditions on the wave-function, which restrict the allowed values of  $\mathbf{k}$ .

### 2.10.6 Brillouin zone sampling

The infinite periodic system is modelled by a large number of primitive cells  $N_{\text{cells}} = N_1N_2N_3$  stacked together, with  $N_i$  cells along the  $\mathbf{a}_i$  direction, and periodic or generalised Born-von Karman boundary conditions is applied to the wave-functions, which can be interpreted by saying that a particle which leaves one surface of the crystal simultaneously enters the crystal at the opposite surface. In fact it can be shown that the choice of boundary conditions does not affect the bulk properties of the system. This condition is expressed mathematically as

$$\psi(\mathbf{r} + N_i\mathbf{a}_i) = \psi(\mathbf{r}), \quad i = 1, 2, 3. \quad (2.146)$$

Applying Bloch's theorem 2.141 gives

$$\psi(\mathbf{r} + N_i\mathbf{a}_i) = \exp(iN_i\mathbf{k} \cdot \mathbf{a}_i)\psi(\mathbf{r}) \quad (2.147)$$

so that the values of  $\mathbf{k}$  are restricted such that

$$\exp(iN_i\mathbf{k} \cdot \mathbf{a}_i) = \exp(2\pi iN_ix_i) = 1, \quad i = 1, 2, 3 \quad (2.148)$$

using equation 2.140. Therefore the values of the  $\{x_i\}$  are required to be real and equal to

$$x_i = \frac{l_i}{N_i}, \quad i = 1, 2, 3, \quad (2.149)$$

where the  $\{l_i\}$  are integers, so that the general allowed form for the Bloch wave-vectors  $\mathbf{k}$  is

$$\mathbf{k} = \sum_{i=1}^3 \frac{l_i}{N_i} \mathbf{g}_i. \quad (2.150)$$

Taking the limit to the true infinite perfect crystal ( $N_i \rightarrow \infty$ ) it is seen that there is still an infinite number of allowed  $\mathbf{k}$ -vectors, but that they are now members of a countably infinite set. Furthermore, the  $\mathbf{k}$ -vectors which differ only by a reciprocal lattice vector are in fact equivalent. Consider two such wave-vectors related by  $\mathbf{k}' = \mathbf{k} + \mathbf{G}$ , then the corresponding Bloch states are also related by

$$\begin{aligned} \psi_{n\mathbf{k}'}(\mathbf{r}) &= \exp(i\mathbf{k}' \cdot \mathbf{r})u_{n\mathbf{k}'}(\mathbf{r}) = \exp(i\mathbf{k} \cdot \mathbf{r}) [u_{n\mathbf{k}'}(\mathbf{r}) \exp(i\mathbf{G} \cdot \mathbf{r})] \\ &= \exp(i\mathbf{k} \cdot \mathbf{r})\tilde{u}(\mathbf{r}) = \psi_{n'\mathbf{k}}(\mathbf{r}) \end{aligned} \quad (2.151)$$

Since the expression in square brackets on the first line is a cell-periodic function the whole expression is a valid Bloch wave-function with wave-vector  $\mathbf{k}$ . Thus, only those  $\mathbf{k}$ -vectors which lie within the first Brillouin zone are of interest. Where the first Brillouin zone is defined as the volume of reciprocal-space. This volume encloses the origin, bounded by the planes which perpendicularly bisect lines from the origin to surrounding lattice points.

Thus for each allowed  $\mathbf{k}$ -vector within the first Brillouin zone, the occupied Hamiltonian eigenstates must be calculated in order to construct the density. However, the wave-functions and other properties such as Hamiltonian eigenvalues vary smoothly over the Brillouin zone so that in practice only a finite set of points need to be chosen, and methods for making efficient choices have been developed. From the calculation of the wave-functions at a certain set of  $\mathbf{k}$ -points,  $\mathbf{k} \cdot \mathbf{p}$  perturbation theory can be used to approximate the wave-functions at other nearby  $\mathbf{k}$ -points.

The volume of the Brillouin zone  $\Omega_{\text{BZ}}$  is related to the volume of the supercell  $\Omega_{\text{cell}}$  by

$$\Omega_{\text{BZ}} = \frac{(2\pi)^3}{\Omega_{\text{cell}}} \quad (2.152)$$

so that for large systems, the Brillouin zone volume is very small and only a few  $\mathbf{k}$ -points need to be considered to describe the variation across the Brillouin zone accurately. In the present work only wave-functions at the centre of the Brillouin zone,  $\mathbf{k} = 0$ , known as the  $\Gamma$ -point are computed. This has the added advantage that at this  $\mathbf{k}$ -point the wave-functions can be chosen to be real (recall that there is always an arbitrary global phase factor) without loss of generality.

### 2.10.7 The pseudopotential approximation

It has been observed that the core electrons are relatively unaffected by the chemical environment of an atom and that their (large) contribution to the total binding energy does not change when isolated atoms are brought together to form a molecule or crystal. The actual energy differences of interest are the changes in valence electron energies, and so if the binding energy of the core electrons can be subtracted out, the valence electron energy change will be a much larger fraction of the total binding energy, and hence much easier to calculate accurately. Also the strong nuclear Coulomb potential and highly localised core electron wave-functions are difficult to represent computationally.

Since the atomic wave-functions are eigenstates of the atomic Hamiltonian, they must all be mutually orthogonal. Since the core states are localised in the vicinity of the nucleus, the valence states must oscillate rapidly in this core region in order to maintain this orthogonality with the core electrons. This rapid oscillation results in a large kinetic energy for the valence electrons in the core region, which roughly cancels the large potential energy due to the strong Coulomb potential. Thus the valence electrons are much more weakly bound than the core electrons.

It is therefore convenient to attempt to replace the strong Coulomb potential and core electrons by an effective pseudopotential which is much weaker, and replace the valence electron wave-functions, which oscillate rapidly in the core region, by pseudo-wave-functions, which vary smoothly in the core region [109, 110]. For reviews; Heine[111] and also Ref.[112, 113].

The conditions of a good pseudopotential are that it reproduces the logarithmic derivative of the wave-function (and thus the phase-shifts) correctly for the isolated atom, and also that the variation of this quantity with respect to energy is the same to first order for pseudopotential

and full potential. Having replaced the full potential by a pseudopotential Schrödinger equation can be solved again in the core region to obtain the pseudo-wave-function, with radial part  $R_{ps,\ell}(r, E)$ .

Pseudopotential generation has itself been the subject of a great deal of study. The pseudopotentials generated by the method of Troullier and Martins[114] fall into the category of norm-conserving pseudopotentials. With one notable exception[115], all of the recent methods have used norm-conservation to guarantee that the phase-shifts are correct to first order in the energy (correction to higher orders is also possible[116]).

### 2.10.8 Performance of DFT

DFT methods have been applied to wide ranging systems over the past few decades. DFT methods have been shown to work very well for various systems and the shortcomings have been improved. The G1 database of Pople and coworkers is a benchmark for accuracy of the traditional *ab initio* methods. The database contains 55 molecules for which experimental values of atomization energies are known within 1 kcal/mol. Curtiss *et al* (1991) achieved the 1.2 kcal/mol mean absolute error for these 55 atomization energies using the G2 procedure, which is a quite involved prescription incorporating higher order correlated methods. Becke (1992) was able to reproduce values in this database with a mean absolute error of 3.7 kcal/mol using his NUMOL program with gradient corrected functionals. This result was additionally improved by Becke (1993) to 2.4 kcal/mol when portion of the electron exchange entering the exchange-correlation energy,  $E_{xc}$  was calculated exactly from Kohn-Sham orbitals. While the error in DFT is considered still too big, these results were obtained with a method which is substantially less computationally demanding than original correlated *ab initio* procedures. Obviously, the errors refer to absolute atomization energies, which in general are very difficult to calculate with good accuracy (for review see, e.g., Hehre *et al*, 1986). The relative differences are usually reproduced much better with DFT methods.

Earlier studies have shown that even without gradient corrections DFT results for bond dissociation energies are usually much better than the Hartree-Fock (which routinely underbinds) results, though they have an overbinding tendency. The LDA results are approximately of MP2 quality. The inclusion of gradient corrections to DFT provides bond dissociation energies which pair in accuracy with MP4 and CC results. Molecular geometries even with LSD are much better than corresponding HF results and are of the MP2 quality. However, LSD fails to correctly treat hydrogen bonding. This deficiency is removed when one uses gradient corrected DFT approaches. Quite astonishingly, DFT provides excellent results for molecules which are notoriously difficult for traditional *ab initio* approaches like FOF, FON, and metalorganic or inorganic moieties. Transition states of organic molecules are frequently not reproduced well with "pure" DFT. However, it seems that admixture of exact exchange (see Becke, 1993) via ACM dramatically improves the problem cases. DFT is however a method of choice for transition states in metalorganic reactions. These systems are notoriously difficult to treat with even high quality *ab initio* and have problems with convergence. Vibrational frequencies are well reproduced even by LSD, though gradient corrections improve agreement with experiment even further. Ionization potentials, electron affinities, and proton affinities are reproduced fairly well within gradient corrected DFT.

Density-functional theory together with the pseudopotential approximation is now a well established method of choice for performing large-scale *ab initio* quantum-mechanical calculations. In particular, the fact that the kinetic energy operator is diagonal in momentum-space, that the Hartree and local pseudopotential contributions are straightforward to calculate in

momentum-space, the development of fast Fourier transforms (FFTs) to efficiently switch between momentum-space and real-space and their natural relation to periodic boundary conditions has led the plane-wave basis set and momentum-space formalism to become the most widely accepted method for performing such calculations. Efficient methods to solve the Kohn-Sham equations have been developed which iteratively diagonalise the Hamiltonian. All of these plane-wave methods require a computational effort which scales as the cube of the system-size, and an amount of memory which scales as the square. Although these methods have made first-principles quantum-mechanical calculations available as a tool to a wide range of scientists in a variety of disciplines, this scaling ultimately limits the maximum system-size.

## 2.11 Subsumption

In this chapter the basic theory of the various methods used in the present work was introduced. The theories presented in this chapter are the elements of the atomistic multiscale approach followed in the present work. At the microscopic level, high-accuracy HF and post-HF calculations (section 2.5) is performed for hydrocarbons up to seven atoms. These *ab initio* calculations spanning over the nuclear configuration hypersurface are used in generating semi- and global- potential energy surface (section 2.4). Results of these studies are presented in chapter 3 through 5.

Moving to systems with larger length scales, DFT theory is applied (introduced in section 2.10) to perform molecular dynamics of systems relevant to fusion applications. Results of these calculations are presented in chapter 6.

Finally the theory of classical molecular dynamics is applied (introduced in section 2.2.2) to simulate system consisting of 1000's of atoms which are of important relevance to plasma-material interaction in fusion studies. The results of these studies will be presented in chapter 7.

# Chapter 3

## Potential Energy Surface

### 3.1 Introduction

The Born-Oppenheimer approximation allows us to separate electronic and nuclear motion in a parametric way. The solution of the electronic Schrödinger equation for a fixed nuclear configuration gives the energy of the molecule as a function of the positions of the nuclei. Calculations over thousands of such points, where each point represents a unique nuclear configuration on the hypersurface, spanned by the nuclear degrees of freedom would represent the potential energy surface (PES) for the molecule under study. Thus, PES describes the energy of a molecule in terms of its structure. Molecular structures can be determined from the potential energy surface, where the minimum would correspond to an equilibrium structure and the first order saddle point would correspond to a transition state for a reaction. Reaction path on the PES can be defined as the steepest descent path connecting a transition state to minima. Dynamics of the molecules involve movement of the molecule or its fragments on the potential energy surface. Also, small amplitude motions of one reference configuration results in normal modes of vibrations for the reference minima or saddle point, whereas, large amplitude motions would result in dissociation of the molecule.

The knowledge of the PES is essential in understanding the energetics of nuclear configurations, vibrational modes and dynamics of the molecules. In chapter 2; section 2.4, the basic idea behind the molecular potential energy surface, also in a visual way, was introduced. In this chapter the method followed in the present work for the development of PES for small hydrocarbons is presented. The PES was generated for  $C_2H_3^+$  and  $C_2H_5^+$ . Since this method is not restricted to any specific molecule, this method can followed to generate a PES, in principle for any small molecule. The results and properties of the PES are presented latter in this chapter.

### 3.2 Coordinate

There is not one set of coordinates for defining the geometry of a polyatomic system which is convenient for all types of dynamical calculation. Spectroscopists generally favour valance coordinates, a mixture of bond lengths and bond angles or normal coordinates, whereas for non-reactive scattering it would be most convenient to use the distance between the center of mass and the internal coordinates of the colliding molecules.

For both spectroscopic and scattering studies it is often sufficient to have a potential which is limited to certain regions of the full configuration space. For such studies it is convenient to derive potential functions, where the coordinate system has one atom placed in a different context to the other two. In such coordinate systems, either one atom in the molecule is the center of the coordinate system and bond lengths and bond angles are independent variables, or, an atom placed separately in relation to the other fragment (e.g diatom). However, if one wants a potential covering the whole configuration space, which can, in principle, be used for any dynamical study, then it is more sensible to use a coordinate system, in which the potential energy is a function of inter-nuclear distances only.

If a molecule contains two or more identical atoms then its potential energy surface must be invariant to permutations of these atoms. An equivalent statement is that the potential can contain only totally symmetric combinations of inter nuclear distances coordinates;  $R_1, R_2, R_3 \dots R_N$ . The technique for generation of such symmetric combinations is derived from point group symmetry and use of permutation groups. Taking an example of  $O_3$ , Murrell and coworkers[117] showed that the permutation group of three ( $S_3$ ) is isomorphic with the point group  $C_{3v}$ . The combinations of basis functions which transforms as the irreducible representation of the point group can be obtained by projection operator technique. This technique is used to find those combinations of the variable  $R_1, R_2, R_3$  for  $O_3$  example, which transform as irreducible representations of the  $S_3$  group.

If the potential energy function is to be totally symmetric to permutation of the inter nuclear distances variables, then it must be represented in terms of a irreducible basis or totally symmetric combinations of irreducible basis elements. Advantage of such a method over other has been presented by Murrell and coworkers[117].

### 3.3 Many-body expansion

In the present work the idea of many-body expansion and use of invariant polynomials proposed and developed by Braams and co-workers is adopted for generation of potential energy surface. Following the many-body expansion, potential energy for a  $N$  atom molecule can be written as:

$$V_{ABC\dots N} = \sum V_A^{(1)} + \sum V_{AB}^{(2)}(R_{AB}) + \sum V_{ABC}^{(3)}(R_{AB}, R_{BC}, R_{CA}) + \dots + V_{ABC\dots N}^{(N)}(R_i) \quad (3.1)$$

such a representation for a single-valued potential energy surface is known as many-body expansion, where,  $V_A^{(1)}$  is the energy of atom A in the state which is produced by adiabatically removing this atom from the cluster.  $\sum V_A^{(1)}$  is the sum of all one-body terms.  $\sum V_{AB}^{(2)}(R_{AB})$  is a two body term which is a function of the separation of the two atoms and which tends asymptotically to zero as  $R_{AB}$  approaches infinity, the sum indicates sum of all such terms.  $\sum V_{ABC}^{(3)}$  is a three-body energy which depends on the dimensions of the ABC triangle. A three-body term must become zero if any of the three atoms is removed to infinity, and this condition is likely to be most easily imposed by using internuclear distances as variables. The last term in the expansion is the n-body term for an n-atom cluster. This term will become zero if any one of the atoms is removed to infinity.  $V^{(n)}$  is, therefore, like the complete potential, a function of  $3N - 6$  internal coordinates of the system.

The many-body expansion leads to a simplification of the problem if either the series converges rapidly, and some of the high order terms can be neglected, or there exist simple functional forms for the higher terms in the expansion. Many-body representation also guarantees to satisfy all dissociation limits. Another advantage is that the many-body expansion suggests a strategy for building up a polyatomic potential by studying the potentials for all the fragments. Thus, the two body terms can be deduced from diatomic potentials and the three-body terms are given by the difference between triatomic potential and the sum of the one- and two-body components.

### 3.4 Invariant Polynomials

For the 7-nucleus system, say  $H_5C_2^+$  ( $N = 7$ ), taking into account translational and rotational invariance, at least 15 ( $3N - 6 = 15$ ) coordinates are required to specify the configuration for

evaluating the potential. The PES is represented as a function of all 21 internuclear distances, so using redundant coordinates, this immediately guarantees that the PES is invariant under translation, rotation, and reflection. The functional form of the PES is chosen so that it is also invariant under any permutation of like nuclei.

In the following,  $i$  and  $j$  will generally be used as nuclear indices, ranging from 0 to 6: indices 0...4 for the five hydrogens and indices 5 and 6 for the two carbons. Let  $\mathbf{r}(i)$  be the position of the  $i$ -th nucleus and let  $r_{i,j} = \|\mathbf{r}(i) - \mathbf{r}(j)\|$  be the distance between nuclei  $i$  and  $j$ . The independent variables of the PES fit are the 21 internuclear distances  $r_{i,j}$  (and it is understood that  $i \neq j$  and that  $r_{i,j}$  and  $r_{j,i}$  denote the same variable).

Auxiliary variables  $x_{i,j} = \exp(-r_{i,j}/a)$  and  $y_{i,j} = \exp(-r_{i,j})/r_{i,j}$  are introduced, and in terms of these the expression for  $V$  is written as:

$$V = p(x) + \sum_{i < j} q_{i,j}(x) y_{i,j} \quad (3.2)$$

Here,  $x \in \mathbf{R}^{21}$  denotes a vector with components  $x_{i,j}$ , and  $p$  and the  $q_{i,j}$  are polynomials in  $x$ . For  $p$ , 7th degree polynomial is used and the  $q_{i,j}$  have been 3rd degree polynomials, restricted in such a way that the PES is invariant under permutations of like nuclei. Numerical experimentation guided us to chose  $a = 3$  in the definition of the  $x_{i,j}$ .

The technical complexity of this representation is due entirely to the permutation symmetry requirement, and the construction of a polynomial basis that has the required symmetry is described below. Assuming that the basis is available and that there are  $m$  basis functions and  $n$  configurations in the database (with  $m \leq n$ ) then the polynomial coefficients are determined by a weighted least squares system of dimension  $n \times m$ . The solution of the system involves a singular value decomposition of the associated matrix, for which DGESVD routine from LAPACK[118] is used. The computational cost scales as  $m^2n$ . If the  $k$ -th entry in the database has *ab initio* energy  $f(k)$  then the corresponding entry in the least squares system is given weight  $\delta/(\delta + f(k) - f_{\min})$  where  $f_{\min}$  denotes the global minimum potential energy over all entries in the database and where the parameter  $\delta$  was set to 0.1 hartree.

The problem of specifying a basis of the space of polynomials invariant under some permutation symmetry belongs to computational invariant theory, and specifically the theory of invariants of finite groups. For their implementation Braams and co-workers relied on the exposition of computational invariant theory by Derksen and Kemper[119] and on the procedures for invariant computation[120, 121] in the Magma computer algebra system[122].

For the purpose of representing polynomial  $p$  of eqn. 3.2 one requires a basis, truncated at some degree, for polynomials of  $x$  that are invariant under the group  $\text{Sym}(5) \times \text{Sym}(2)$  acting on the 21-dimensional space of  $x$  by a permutation of the variables to be described. ( $\text{Sym}(k)$  denotes the symmetric group on  $k$  letters.) Let  $\sigma \in \text{Sym}(5) \times \text{Sym}(2)$ ; then  $\sigma$  has a natural action on the nuclear indices, permuting the hydrogens among themselves and the carbons among themselves. Letting  $\sigma : x \rightarrow x'$  where  $x'_{\sigma(i),\sigma(j)} = x_{i,j}$  and that gives the representation of  $\text{Sym}(5) \times \text{Sym}(2)$  on the 21-dimensional space of  $x$ .

A Magma computation gives very quickly, by way of the Hilbert Series, the dimension of the relevant space of invariant polynomials at each degree. For the present problem the Hilbert Series is  $1 + 3t + 12t^2 + 43t^3 + 159t^4 + 554t^5 + 1879t^6 + 6066t^7 + 18755t^8 + \dots$ , where the coefficient of  $t^k$  is the dimension of the space of homogeneous invariant polynomials of degree  $k$ . The total

dimension of the approximation space for polynomial  $p$  at some degree is obtained by taking the partial sum, and this leads to a dimension 2651 at degree 6 and 8717 at degree 7. The heart of the evaluation of the fitted PES, for any given nuclear configuration, is therefore the evaluation of the 8717 invariant polynomials that make up the basis at total degree up to 7. Because of the symmetry requirement, any of these polynomials might be a sum of 240 ( $5!2!$ ) terms.

For efficient evaluation of this basis Braams and co-workers used Computational Invariant Theory[Ch.3][119], which states that the algebra of invariant polynomials is generated by a small number of *primary* invariants and a larger number of *secondary* invariants. In the present case there are 21 primary invariants (number equal to the number of independent variables,  $N(N - 1)/2$  where  $N$  is the number of nuclei) and after selection of the primary invariants a Magma computation turns up 1436 secondary invariants of degree at most 7 (including the trivial secondary invariant that is the constant 1). Any invariant polynomial in the resulting basis has a unique representation as a product of a secondary invariant and a polynomial in the primary invariants. The 1436 secondary invariants split into 766 *irreducible* secondary invariants and 670 secondary invariants that are products of irreducible ones. The costly part of the evaluation of the basis is the evaluation of the 766 irreducible secondaries, and this results in the gain (in this case) of a factor of about 10 over a procedure in which each of the 8717 polynomials in the basis would be computed independently.

As expressed in eqn. 3.2 the representation for the potential also employs polynomials  $q_{i,j}$ . If these are restricted to degree 0 (so each is a constant) then there are three independent associated coefficients: one for the HH pair, one for the HC pair, and one for the CC pair. More generally three independent polynomials are used - one for each pair of kinds of nuclei - and given a pair of kinds of nuclei then the various  $q_{i,j}$  for  $(i, j)$  making up that pair differ only by a permutation of the argument vector. These three polynomials are denote as  $q_{HH}$ ,  $q_{HC}$ , and  $q_{CC}$ . The PES, eqn. 3.2, must be invariant under  $\text{Sym}(5) \times \text{Sym}(2)$  and one can work out the derived symmetry requirement for  $q_{HH}$ ,  $q_{HC}$ , and  $q_{CC}$ . They all must be invariant under some subgroup of  $\text{Sym}(5) \times \text{Sym}(2)$ . In the case of  $q_{HH}$  two of the five hydrogens are special and the subgroup is  $\text{Sym}(3) \times \text{Sym}(2) \times \text{Sym}(2)$ , in the case of  $q_{HC}$  the relevant subgroup is just  $\text{Sym}(4)$ , and in the case of  $q_{CC}$  the subgroup is the entire  $\text{Sym}(5) \times \text{Sym}(2)$ . In the implementation developed by Braams and co-workers imposed on all three of them the symmetry group  $\text{Sym}(5) \times \text{Sym}(2)$ . They are only expanded to relatively low degree, and their most important role is to cover the short range repulsion for which the constant terms at degree zero already suffices.

### 3.5 Dipole moment surface

The dipole moment is a vector quantity and so it cannot be expressed simply in terms of the internuclear distances. Instead, representation of the following kind was suggested:

$$\mathbf{d} = \sum_i f_i(x) \mathbf{r}(i) \quad (3.3)$$

Here,  $\mathbf{d}$  is the fitted dipole moment vector,  $i$  runs over the nuclear indices,  $x$  is as described following eqn. 3.2, and  $\mathbf{r}(i)$  is the vector position of the  $i$ -th nucleus. The functions  $f_i$  are polynomials that are constrained so that  $\mathbf{d}$  satisfies the required permutational invariance and behaves correctly under translation, and the coefficients of the  $f_i$  are determined by least squares fitting.

Of the 7 ( $N = 7$ ) polynomials  $f_i$  only two are fundamentally distinct: one for the case that  $i$  refers to an H nucleus and one for the case that  $i$  refers to an C nucleus; all the  $f_i$  for

$i$  referring to a nucleus of one kind are obtained from each other by a simple permutation of the variables. Let us denote the two fundamentally distinct polynomials by  $f_H$  and  $f_C$ . The permutational symmetry of  $f_H$  should correspond to that of a fictitious  $H_4YC_2$  molecule (one of the five hydrogens is special), and likewise the permutational symmetry of  $f_C$  should be that of a fictitious  $H_5CY$  molecule. Braams and co-workers calculated the basis for polynomials of the required symmetry in a similar way that was done for the complete  $H_5C_2$  symmetry group and then truncated the space of polynomials at total degree 4. At that total degree the polynomial  $f_H$  has 650 free coefficients and the polynomial  $f_C$  has 355 free coefficients.

Finally, the required behavior of  $\mathbf{d}$  under translation: if the entire configuration is displaced by a vector  $\mathbf{z}$  then  $\mathbf{d}$  should change by  $Z_{\text{tot}}\mathbf{z}$  where  $Z_{\text{tot}}$  is the total charge of the molecule, so  $Z_{\text{tot}} = 1$  in the present case. This simply means that  $\sum_i f_i(x) = Z_{\text{tot}}$  for each configuration  $x$ , and impose an additional set of equations in the least squares procedure.

### 3.6 Potential Energy Surface of $C_2H_3^+$

The method proposed by Braams and co-workers in the previous sections were used for generation of PES in the present work. The generation of the PES and results obtained in the present work is reported in this section.

$C_2H_3^+$ , known as protonated acetylene and the vinyl cation, has been of special interest in the fields of plasma chemistry,[123, 124, 125, 126] astrophysics,[127] quantum chemistry,[128, 129, 130, 131] spectroscopy[132, 133] and experimental determination of molecular structure.[131, 134, 135] The  $C_2H_3^+$  molecule is known to have two interesting structures lying energetically close to one another; shown in Fig. 3.1(a) and Fig. 3.1(b). In the lower-lying structure, referred to as the “bridged” structure (or carbonium or nonclassical structure), one proton forms a triangle with the two carbon nuclei, as shown in Fig. 3.1(a). The other two hydrogen nuclei in this structure are nearly collinear to the C-C bond axis. Another slightly higher energy structure, referred to as “Y-shaped” (or vinyl-cationic or classical structure), is shown in Fig. 3.1(b). Many theoretical and experimental studies have been made to determine the energy separation between the classical and nonclassical isomers.[130, 132, 136, 137]

The earliest theoretical work focusing on  $C_2H_3^+$  was done at the Hartree-Fock level by Zurewsky *et al.*[131] in 1973 and it indicated the existence of these two structures. Their calculations indicated an energy difference of about 7 kcal/mol between the bridged and the Y-shape structure, the bridged structure being lower in energy. Lee and Schaefer[138] calculated the equilibrium geometries and harmonic vibrational frequencies of the classical and non-classical structures of  $C_2H_3^+$  with the configuration interaction (CI) method in 1986. Their calculations at their highest level of theory (CI including all single, double and triple excitations) predicted the bridged structure to be lower by only 0.7 kcal/mol. The energy difference reported in later works were 4.0 kcal/mol by Liang *et al.*[130] in 1990, 4.5 kcal/mol by Klopper *et al.*[136] also in 1990 and  $3.7 \pm 1.3$  kcal/mol by Lindh *et al.*[137] in 1991. All the quantum chemical electronic structure calculations[129, 136, 137, 138, 139, 140, 141] based on high-level of theory have unambiguously led to the conclusion that the global minimum on the potential energy surface of  $C_2H_3^+$  corresponded to the non-classical bridged structure (Fig. 3.1(a)).

#### 3.6.1 Potential Energy Surface

The  $C_2H_3^+$  potential energy surface (PES) has the form of a many-body (cluster) expansion using basis functions that are invariant under interchange of like nuclei, with coefficients fitted

to *ab initio* calculations. It is noted that the general cluster approach is not new and was used for 3- and 4-atom systems by Murrell and coworkers starting in the 1970s[117]. This approach was developed anew by Braams and co-workers in recent years, which makes use of permutationally invariant expansions to obtain potential energy surfaces for molecules of up to 7 atoms [142, 143, 144, 145, 146, 147, 148].

The present surface is based on *ab initio* calculations employing the restricted coupled cluster method with singles and doubles and perturbative treatment of triples [RCCSD(T)][149, 150] and the augmented correlation-consistent polarized valence triple zeta (aug-cc-pVTZ)[151, 152] basis set as implemented in the MOLPRO 2006 [153] code system. Since RCCSD(T)/aug-cc-pVTZ calculations are expensive an initial potential energy surface employing second order Møller-Plesset theory (MP2) and the valence double zeta (VDZ) basis is constructed first. For this initial low-level surface configurations were generated quite haphazardly. This initial surface was further used to sample configurations using classical molecular dynamics and diffusion Monte Carlo calculations. This methods is used to iteratively improve the surface still at the MP2/VDZ level, and then sample from it to obtain configurations for the high-level RCCSD(T)/aug-cc-pVTZ calculations. A total number of 12527 converged high-level *ab initio* calculations in the  $C_2H_3^+$  complex region was employed for the final surface.

The many-body expansion for the  $C_2H_3^+$  potential has the form

$$V = V_H + V_C + V_{H_2} + V_{HC} + V_{C_2} + V_{H_3} + V_{H_2C} + V_{HC_2} + V_{H_3C} + V_{H_2C_2} + V_{H_3C_2}. \quad (3.4)$$

The terms on the right hand side represent all possible one-, two-, three-, four- and five-body subsystems. Each such term is itself a sum over all choices of nuclei that give the correct composition, for example

$$V_{H_2C} = \sum_{i < j; i, j \in \text{“H”}} \sum_{k \in \text{“C”}} f_{H_2C}(r_{ij}, r_{ik}, r_{jk}) \quad (3.5)$$

The notation  $i \in \text{“H”}$  is used to denote an index for an H nucleus. The  $f_{H_2C}$  is a function of the internuclear distances among the three nuclei that make up the  $H_2C$  subsystem. This function is expanded as a polynomial times a damping function: let  $\mathbf{x}$  denote the vector of internuclear distances and drop the  $H_2C$  subscript (so describing a generic term in the cluster expansion) then

$$f(\mathbf{x}) = p(\mathbf{x}) q(\text{rms}(\mathbf{x})) \quad (3.6)$$

Here  $p(\mathbf{x})$  is a polynomial with coefficients to be determined,  $\text{rms}(\mathbf{x})$  is the root mean square of the elements of  $\mathbf{x}$  (so the root mean square internuclear distance), and for the damping function  $q$ , for the case of the 3-body and higher terms the following form is used:

$$q(t) = (\max(0, 1 - t/a))^5 \quad (3.7)$$

and for the 2-body terms

$$q(t) = \frac{1}{t} (\max(0, 1 - t/a))^5 \quad (3.8)$$

The parameter  $a$  has the dimension of length, and although it could be chosen independently for each term in the fit, it was kept fixed it (based on experience) at 8 Bohr for all terms. The one-body terms are just constants,

$$\begin{aligned} V_{\text{H}} &= 3f_{\text{H}} \\ V_{\text{C}} &= 2f_{\text{C}} \end{aligned} \quad (3.9)$$

where the value assigned to  $f_{\text{H}}$  is an energy of  $2/3$  times the free neutral hydrogen atom energy (factor  $2/3$  to reflect the charge on  $\text{C}_2\text{H}_3^+$ ) and  $f_{\text{C}}$  the free neutral carbon energy. The coefficients in the polynomials in the 2-body through 5-body terms were fitted, and polynomials of total degree up to 8, 8, 7 and 6, respectively for the 2-body, 3-body, 4-body and 5-body terms were used.

Finally, the polynomials are expanded in a basis that explicitly obeys the required invariance under permutations of like nuclei. To construct such a basis, as has been done for all possible molecular compositions of up to 7 atoms, the methods of computational invariant theory [119] and on the Magma computational algebra system were applied.[122]

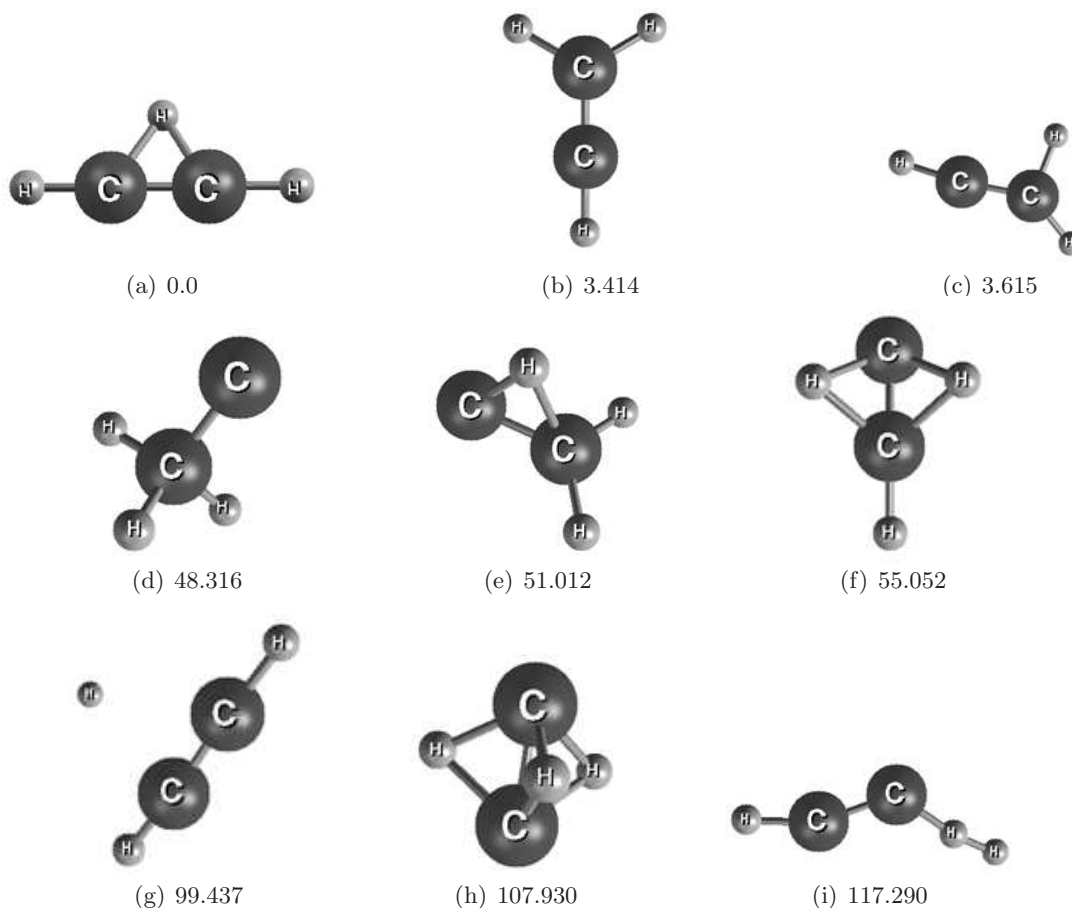


Figure 3.1: 3.1(a) Absolute ground state energy for bridged structure (kcal/mol)(-77.444169 Hartree). 3.1(b) - 3.1(i) Energy for Y-shape structure and stationary points on the PES (kcal/mol) relative to the global min

### 3.6.2 Properties of the PES

The PES for  $\text{C}_2\text{H}_3^+$  reported here has a root mean square(rms) fitting error of  $4.67 \times 10^{-4}$  Hartree ( $\approx 0.3$  kcal/mol) for the 4928 configurations in the range from 0.0 to 0.1 Hartree (0 to

62.7 kcal/mol) above the global minimum. For 0.1 to 0.2 and 0.2 to 0.5 Hartree range above the global minimum, the rms errors are  $1.66 \times 10^{-3}$  and  $4.92 \times 10^{-3}$ , respectively. The global minimum on the calculated PES is found to be the bridged structure of  $C_2H_3^+$  at an energy of -77.444169 Hartree. The energy difference between the global minimum (bridged structure; Figure.3.1(a)) and the Y-shape structure (Figure.3.1(b)) is calculated to be 3.414 kcal/mol. This value is in agreement with the value of 3.43 kcal/mol, based on CCSD(T)/ANO1 calculations, reported by Lindh *et al.*[137].

Stationary points calculated on the PES include a low-lying, first-order saddle point separating the bridged and Y-structure minima shown in Figure. 3.1(c) and three, much high-lying ones shown in Figures. 3.1(d) - 3.1(f). These four stationary points were not explicitly included in the *ab initio* data set used to obtain the PES. To verify that they are not artifacts of the fit, new *ab initio* calculations were performed to locate and characterize these stationary points. In all cases these stationary points were obtained. For the low-lying one, which is the most relevant one to further vibrational calculations, presented in the next chapter, direct RCCSD(T)/aug-cc-pVTZ calculations were performed and are found to be in excellent agreement with the PES prediction, i.e., the largest bond-length difference is 0.0017 bohr and the harmonic normal-mode frequencies differ by at most  $14 \text{ cm}^{-1}$ . For the three much higher-lying stationary points in Figure. 3.1(d) - 3.1(f)) much less *cpu*-intensive MP2/aug-cc-pVTZ calculations were done. These verified the existence of these predicted stationary points and the respective rms differences are:  $1.3 \times 10^{-2}$ ,  $2.9 \times 10^{-2}$ ,  $3.2 \times 10^{-2}$  bohr for the three bond lengths, 0.4, 3.3, and 4.8 kcal/mol for the energies, and 44.1, 57.3, and  $83.5 \text{ cm}^{-1}$  for the normal mode frequencies. Thus, the PES does accurately represent (indeed predicted) these four stationary points. These high energy stationary points play no role in the vibrational calculations, hence detailed comparison of the PES and MP4 results is avoided here. However, it is important to note that these are important to identify because reaction dynamics calculations might cross over these saddle points.

### 3.7 Potential Energy Surface of $C_2H_5^+$

In this section we report the generation of *ab initio*-based semi-global potential energy surface for  $C_2H_5^+$ . The *ab initio* electronic energies for this molecule are calculated using the fourth order MÖLLER-PLESSET[154, 155] (MP4) perturbation theory with contributions due to single, double, triple and quadruple excitations to the electron correlation energy.[156, 157] (MP4(SDTQ)) The MP4(SDTQ) method is used with the correlation-consistent polarized valence triple-zeta basis augmented with diffuse functions[151, 152] (aug-cc-pVTZ). The *ab initio* potential energy surface is represented by a many-body (cluster) expansion, each term of which uses functions that are fully invariant under permutations of like nuclei, as introduced earlier. The fitted potential energy surface is validated by comparing normal mode frequencies at the global minimum and low lying stationary points with the previous and new direct *ab initio* frequencies.

Chemically interesting singlet carbocation  $C_2H_5^+$ , known as the ethyl cation, has been of special interest in the fields of plasma chemistry,[123, 124, 125, 126] astrophysics, specially in the ionosphere of titan[158, 159, 160, 161] quantum chemistry,[131, 162, 163, 164, 165, 166] spectroscopy and theoretical study of molecular structure.[131, 165, 166] The calculations performed at the lowest level of theory[167] have found the classical form to be a real minimum and the bridged structure to be less stable than the classical form.[167, 168] However, as soon as correlation effects are taken into account the classical form turns out to be a first order saddle point, shown in Fig. 3.2(b) and less stable than the nonclassical form.[167] The most refined calculations have shown that for  $C_2H_5^+$  molecule there is only one minimum on the corresponding potential energy surface namely the nonclassical singly bridged ( $C_{2v}$ ) form shown in Fig. 3.2(a).

In the lower-lying structure, referred to as the “bridged” structure (or nonclassical structure), one hydrogen forms a bridge with the two carbon nuclei, as shown in Fig. 3.2(a). The other four hydrogen atoms (two hydrogen on each carbon nuclei) are nearly co-planar with the two C atoms. The other slightly higher energy structure, referred to as “Y-shaped” (or classical structure), is shown in Fig. 3.2(b).

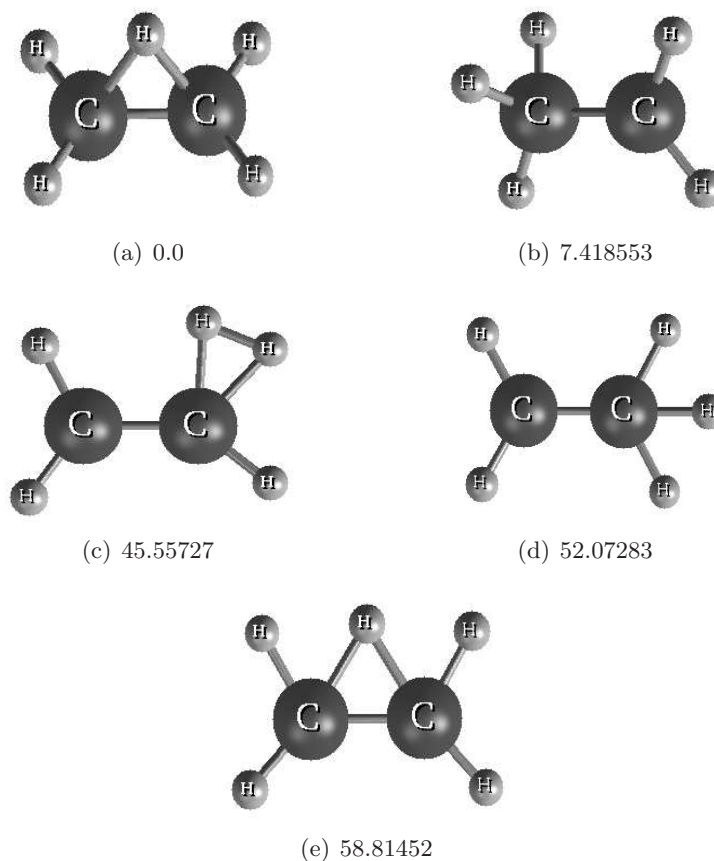


Figure 3.2: 3.2(a) Absolute ground state energy for bridged structure (kcal/mol)( -78.71112003 Hartree). 3.2(b) - 3.2(e) Energy for Y-shape structure and stationary points on the PES (kcal/mol) relative to the global min.

Since the early 70’s theoretical studies have been reported for this carbocation. In one of the earliest work, Zurawski *et al.*[131] found the bridged structure to be lower in energy by about 9 kcal/mol. At the Hartree-Fock level of theory they found the energies of nonclassical and classical structure of  $C_2H_5^+$  to be practically the same. In some of the later works, the absolute energies and relative stability was calculated using various methods and basis sets. Lischka and Köhler[169] found the nonclassical form to be more stable by 9.26 kcal/mol using IEPA method and 8.0 kcal/mol using MINDO/3. Raghavachari *et al.*[166] found the nonclassical form to be more stable by 6.5 kcal/mol at the MP4(SDQ) level of theory with 6-31G\*\* basis. Trinquier[165] calculated the relative stability to be 0.4 kcal/mol at SCF and 7.6 kcal/mol at MP4 level of theory using DZP basis, in favour of the bridged structure. The latest calculation on this molecule was reported in 2002 by Quapp and Heidrich.[164] In their work Quapp and Heidrich.[164] reported the nonclassical structure to be more stable by 7.6 kcal/mol (6.60 kcal/com at 0 K) at the MP2 level of theory using 6-31G\*\* basis.

### 3.7.1 Potential Energy Surface

The  $\text{C}_2\text{H}_5^+$  potential energy surface (PES) has the form of a many-body (cluster) expansion using basis functions that are invariant under interchange of like nuclei, with coefficients fitted to *ab initio* calculations. Since MP4(SDTQ)/aug-cc-pVTZ calculations are *cpu* intensive we constructed an initial potential energy surface employing second order Møller-Plesset theory (MP2) and the valence double zeta (VDZ) basis. For this initial low-level surface we could afford to use configurations generated quite haphazardly, we then sampled from the surface using classical molecular dynamics and diffusion Monte Carlo calculations, iteratively improved the surface still at the MP2/VDZ level, and then sampled from it to obtain configurations for the high-level MP4(SDTQ)/aug-cc-pVTZ calculations. A total number of 19617 converged high-level *ab initio* calculations in the  $\text{C}_2\text{H}_5^+$  complex region was employed for the final surface.

The many-body expansion for the  $\text{C}_2\text{H}_5^+$  potential has the form

$$V = V_{\text{H}} + V_{\text{C}} + V_{\text{H}_2} + V_{\text{HC}} + V_{\text{C}_2} + V_{\text{H}_5} + V_{\text{H}_2\text{C}} + V_{\text{HC}_2} + V_{\text{H}_5\text{C}} + V_{\text{H}_2\text{C}_2} + V_{\text{H}_5\text{C}_2}. \quad (3.10)$$

The terms on the right hand side represent all possible one-, two-, three-, four- and five-body subsystems. Each such term is itself a sum over all choices of nuclei that give the correct composition. The functional form for each of the terms in the above equation are similar to equations presented for  $\text{C}_2\text{H}_3^+$ , from eqn. 3.5 to eqn. 3.8

### 3.7.2 Properties of the PES

The PES for  $\text{C}_2\text{H}_5^+$  reported here has a root mean square(rms) fitting error of  $2.2 \times 10^{-3}$  Hartree over all configurations ( $\approx 1.4$  kcal/mol). The nuclear configurations(15870) in the range from 0.0 to 0.1 Hartree (0 to 62.7 kcal/mol) above the global minimum had a rms fitting error of  $6.05 \times 10^{-4}$  Hartrees ( $\approx 0.38$  kcal/mol). For 0.1 to 0.2 and 0.2 to 0.5 Hartree range above the global minimum, the rms errors are  $2.35 \times 10^{-3}$  and  $1.05 \times 10^{-2}$  Hartrees, respectively. Large error for the configurations in the range of 0.2 to 0.5 can be ignored since we are interested in the configurations around the global minimum. Also the highest energy stationary point shown in Fig. 3.2 is at an energy of  $9.4 \times 10^{-2}$  Hartree above the global minimum, which falls in the first bracket for which rms error is relatively low.

The global minimum located on the PES is found to be the bridged structure of  $\text{C}_2\text{H}_5^+$  at an energy of -78.71112003 Hartree. The energy difference between the global minimum (bridged structure; Figure.3.2(a)) and the Y-shape structure (Figure.3.2(b)) is calculated to be 7.418553 kcal/mol. This value is in agreement with the value of 7.6 kcal/mol, based on the MP2 level of theory calculations using 6-31G\*\* basis reported by Quapp and Heidrich[164]. Stationary points calculated on the PES include a low-lying first order saddle point, the Y-shape structure (Figure.3.2(b)) and three high-lying second order saddle points shown in Figures.3.2(c) - 3.2(e). These four stationary points (Y-shapes structure and other stationary points) were not explicitly included in the *ab initio* data set used to obtain the PES. To verify that they are not artifacts of the fit, new *ab initio* calculations were performed to locate and characterize these stationary points. In all cases these stationary points were obtained. For the low-lying stationary points direct MP4(SDTQ)/aug-cc-pVTZ calculations were performed and were found to be in excellent agreement with the predictions from the PES, i.e., the largest bond-length difference is 0.0009 bohr and the harmonic normal-mode frequencies differ by at most  $30 \text{ cm}^{-1}$  for the Y-shaped stationary point. Also, for the three much higher-lying stationary points shown in Figure. 3.2(c) - 3.2(e) MP4/aug-cc-pVTZ calculations were done. These verified the existence of these predicted stationary points and the differences in the energies were found to be 1.5, 8.3, and 15.2 kcal/mol respectively. Thus, the PES does accurately represent (indeed predicted) these four

stationary points. The normal mode frequencies for the non-classical and classical structures of  $C_2H_5^+$  were calculated using the present PES and also directly using MP4(SDTQ)/aug-cc-pVTZ. and also for the stationary points shown in Figure. 3.2(c) - 3.2(e). Results of these calculations are presented in chapter 4.

### 3.8 Subsumption

In this chapter the basic scheme for the generation of potential energy surface, based on high-accuracy *ab initio* electronic structure calculations was presented. The method presented in this chapter was applied to two important hydrocarbon molecules,  $C_2H_3^+$  and  $C_2H_5^+$ . The rms error between the fitted value and the direct *ab initio* value was around 1 mH over the entire, sampled configuration space. However, the rms error for low lying structures (for configurations lying between the global minimum and 0.1 Hartree above that) was found to be less than 1 mH. The global and local minima and other important stationary points on the fitted surface were accurately identified, although these points were not explicitly included in the fitting procedure. The stationary points are in excellent agreement with direct *ab initio* calculations and also with the published values.

An high-accuracy fitted potential energy surface is an important pre-requisite for performing anharmonic vibrational SCF followed by VCI calculations. Starting with harmonic calculations (*ab initio* vibrational calculations) full dimensional vibrational calculations is performed which is presented in chapter 4.

The semi-global potential energy surface is further expanded by including fragment data into the fit, thus creating a global potential energy surface capable of representing dissociation of the complex configuration. More details are presented in chapter 5.

# Chapter 4

## Spectroscopic calculation

### 4.1 Introduction

A molecular vibration occurs when atoms in a molecule are in periodic motion while the molecule as a whole has constant translational and rotational motion. The frequency of the periodic motion is known as a vibration frequency. A nonlinear molecule with  $n$  atoms has  $3n-6$  normal modes of vibration, whereas a linear molecule has  $3n-5$  normal modes of vibration as rotation about its molecular axis cannot be observed. A diatomic molecule thus has one normal mode of vibration. The normal modes of vibration of polyatomic molecules are independent of each other, each involving simultaneous vibrations of different parts of the molecule.

To a first approximation, the motion in a normal vibration can be described as a kind of simple harmonic motion. In this approximation, the vibrational energy is a quadratic function with respect to the atomic displacements and the first overtone would have twice the frequency of the fundamental. In reality, vibrations are anharmonic and the first overtone has a frequency that is slightly lower than twice that of the fundamental. Excitation of the higher overtones involves progressively less and less additional energy and eventually leads to dissociation of the molecule, as the potential energy of the molecule is more like a Morse potential.

The vibrational states of a molecule can be probed in a variety of ways. The most direct way is through infrared spectroscopy, as vibrational transitions typically require an amount of energy that corresponds to the infrared region of the spectrum. Raman spectroscopy, which typically uses visible light, can also be used to measure vibration frequencies directly.

Accurate potential energy surface description around the nuclear configuration for which normal mode analysis is performed is an important prerequisite for the vibrational analysis of a molecular system. In the present work a potential energy surface based on accurate *ab initio* electronic structure calculations has been generated. The fitted surface has an accuracy of 1 milli-hartree around the global minimum and important saddle point. We reported the properties of the potential energy surface for  $C_2H_3^+$  and  $C_2H_5^+$  in the previous chapter. We perform high accuracy normal mode analysis to further validate that our surface indeed can produce the harmonic frequencies. Further, we perform high accuracy quantum mechanical vibration analysis for the selected hydrocarbons. In this chapter the results of vibrational analysis for these hydrocarbons are reported.

### 4.2 Vibrational Analysis of $C_2H_3^+$

Infrared spectroscopy measurements for  $C_2H_3^+$  were first reported by Oka and co-workers in 1989[132] and by Gabrys in 1995[133]. The spectroscopic results have been interpreted to favor the bridged non-classical structure as being the most stable configuration. In 1986 Kanter *et al.*[170] measured the structure of the low-energy stereostructure of  $C_2H_3^+$  using Coulomb explosion imaging. Their study suggested a nonplanar configuration of  $C_2H_3^+$  with a proton located at the approximate bridging position but delocalized around the C—C bond. In 1989 Crofton *et*

*al.* reported a limited infrared spectroscopic analysis of  $C_2H_3^+$ . [132] Based on a one-dimensional internal-rotation model, the energy difference between the classical and nonclassical structure was predicted to be  $\geq 6.0$  kcal/mol. Later, in 1993, Vager *et al.* presented experimental evidence for anomalous nuclear delocalization in the structure of  $C_2H_3^+$  by an advanced Coulomb explosion imaging method.[135] Laasonen and co-workers[171] and Marx and Parrinello[128] investigated this problem with *ab initio* molecular dynamics and quantum simulation methods, respectively. They both described the quantum ground state structure of  $C_2H_3^+$  as a quasi-planar, bridged structure broadened significantly by anisotropic delocalization of the protons due to zero point motion.

The normal mode frequencies for the non-classical and classical structures of  $C_2H_3^+$  were calculated using the present PES and also directly at the RCCSD(T)/aug-cc-pVTZ level of theory. In Table 4.1 and Table 4.2 (atom indexing for mode description adopted from Ref. [137]) we compare the normal mode frequencies calculated in the present work with those published by Lee and Schaefer[138] and by Lindh *et al.*[137] for the bridged and Y-shape structure respectively. It is important to note that the normal mode frequencies published by Lee and Schaefer[139] were calculated using a DZ+P basis set at the SCF/CISD level of theory and the frequencies published by Lindh *et al.*[137] were calculated using a TZ2Pf basis set at the MP2 level of theory. Since the *ab initio* method and the basis sets used in the present calculations are different from the previous publications, the normal mode frequencies listed in Table 4.1 and Table 4.2 are not expected to be the same.

Table 4.1: Harmonic frequencies ( $cm^{-1}$ ) and zero point vibrational energy (kcal/mol) for nonclassical bridged structure of  $C_2H_3^+$

Mode Number	Mode Description	Symmetry	PES <sup>1</sup>	RCCSD(T) <sup>2</sup>	Lee <sup>3</sup> and Schaefer	Lindh <i>et al.</i> <sup>4</sup>
1	HCCH asymm opb <sup>5</sup>	$a_2$	534	572	587	617
2	HCCH asymm ipb <sup>6</sup>	$b_2$	594	580	513	696
3	HCCH symm opb	$b_1$	775	751	757	770
4	HCCH symm ipb	$a_1$	928	908	923	917
5	CHC ipb	$b_2$	1258	1255	1279	1315
6	CC stretch	$a_1$	1929	1932	2000	1939
7	CHC stretch	$a_1$	2358	2352	2471	2385
8	HCCH asymm stretch	$b_2$	3245	3265	3339	3304
9	HCCH symm stretch	$a_1$	3355	3370	3443	3403

<sup>1</sup> Normal mode frequencies calculated from fitted PES.

<sup>2</sup> Frequencies calculated at the RCCSD(T) level of theory with aug-cc-pVTZ basis.

<sup>3</sup> Frequencies calculated using a DZ+P basis set at the SCF/CISD level of theory.[138]

<sup>4</sup> Frequencies calculated using a TZ2Pf basis set at the MP2 level of theory.[137]

<sup>5</sup> opb = out-of-plane bend.

<sup>6</sup> ipb = in-plane bend.

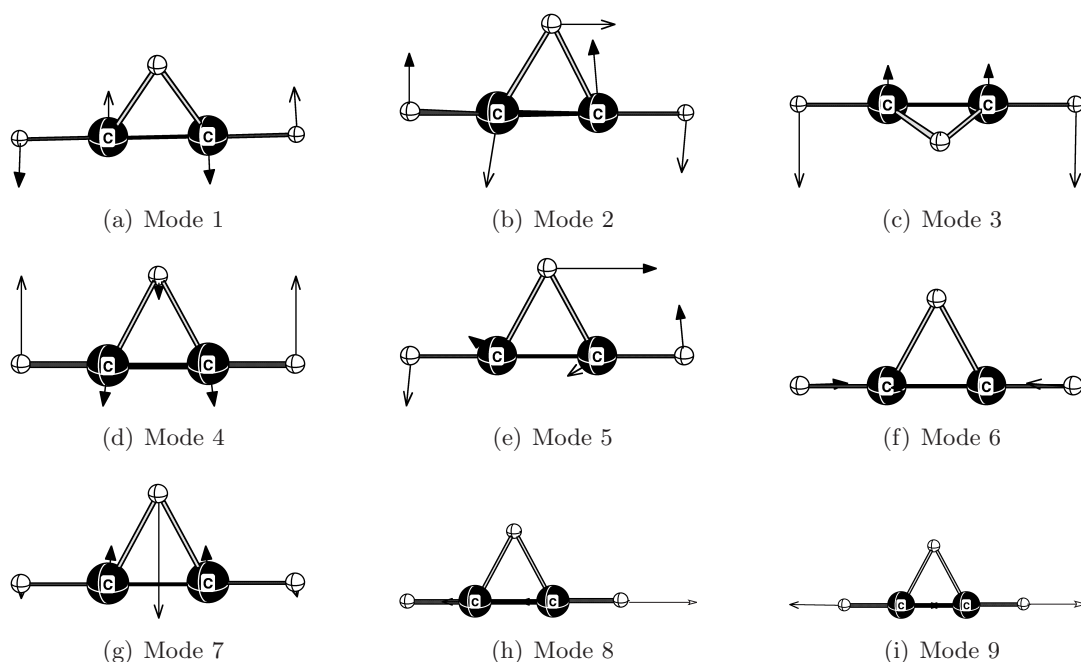


Figure 4.1: Normal Modes for the non-classical bridged structure

Table 4.2: Harmonic frequencies ( $\text{cm}^{-1}$ ) and zero point vibrational energy (kcal/mol) for classical Y-Shaped structure of  $\text{C}_2\text{H}_3^+$ 

Mode Number	Mode Description <sup>1</sup>	Symmetry	PES <sup>2</sup>	RCCSD(T) <sup>3</sup>	Lee <sup>4</sup> and Schaefer	Lindh <i>et al.</i> <sup>5</sup>
1	Coupled frequency mode <sup>6</sup>	$b_2$	199	193	345	193i
2	$\text{CCH}_5$ opb <sup>7</sup>	$b_1$	591	614	601	686
3	$\text{CCH}_{3,4}$ symm opb	$b_1$	801	815	873	815
4	$\text{CCH}_5$ ipb <sup>8</sup>	$b_2$	1077	1078	1106	1097
5	$\text{CCH}_{3,4}$ symm ipb	$a_1$	1159	1176	1254	1161
6	CC stretch	$a_1$	1730	1724	1753	1783
7	$\text{CH}_{3,4}$ symm stretch	$a_1$	3017	3009	3126	3028
8	$\text{CH}_{3,4}$ asymm stretch	$b_2$	3084	3073	3217	3103
9	$\text{CH}_5$ stretch	$a_1$	3288	3280	3364	3327

<sup>1</sup> Atom label and index from Fig. 3.1(b)<sup>2</sup> Normal mode frequencies calculated from fitted PES.<sup>3</sup> Frequencies calculated at the RCCSD(T) level of theory with aug-cc-pVTZ basis.<sup>4</sup> Frequencies calculated using a DZ+P basis set at the SCF/CISD level of theory.[138]<sup>5</sup> Frequencies calculated using a TZ2Pf basis set at the MP2 level of theory.[137]<sup>6</sup>  $\text{H}_4\text{C}_2\text{H}_3$  asymm ipb +  $\text{C}_2\text{C}_1\text{H}_5$  ipb<sup>7</sup> opb = out-of-plane bend.<sup>8</sup> ipb = in-plane bend.

#### 4.2.1 Single Reference Calculations

The code MULTIMODE(MM)[172] performs quantum mechanical rovibrational energy calculations of polyatomic molecules based on the full Watson Hamiltonian,[86, 87, 95, 173] which is an exact Hamiltonian for rovibrational motion expressed in mass-scaled normal modes  $Q_i$ . The

theoretical approach used in MM-SR builds on a vibrational self-consistent field (VSCF)[81] wavefunction for a given reference state labeled by a set of quantum numbers. The potential  $V(\mathbf{Q})$  is represented as an  $n$ -mode representation in terms of  $N$  normal modes (denoted collectively as  $\mathbf{Q}$ ), which permits calculations for many-mode systems (thus for fairly large molecules). The exact hierarchical  $n$ -mode representation of the potential is written as shown in Eq. 2.69.

In this expression the one-mode representation (1MR) of the potential contains only  $V_i^{(1)}(Q_i)$  terms, which can be interpreted as a cut through the hyperspace of normal coordinates with just one coordinate varying at a time. The two-mode representation of the potential contains 1MR terms plus the  $V_{ij}^{(2)}(Q_i, Q_j)$  terms, where any pairs of normal modes vary, etc. With this representation of the potential, truncated at 5MR, the dimensionality of integrals involving  $V$  has a maximum value of 5, for any number of normal coordinates. Matrix elements of the potential are calculated using the numerical quadratures at optimized quadrature points (determined by the one mode terms), and at most five-dimensional quadrature is required. An important feature of MM-SR is the option to vary the  $n$ -mode representation of the potential to test the convergence of the vibrational energies with respect to  $n$ .

Eigenvalues and eigenfunctions of the Watson Hamiltonian [86, 87] are obtained using the approach denoted as ‘‘VCI’’. The size of the VCI Hamiltonian matrix grows nonlinearly with the size of the molecule, and the numerical evaluation of the matrix elements can be computationally expensive. The vibrational calculations begin with a vibrational self-consistent field (VSCF) approach[81, 83, 174] introduced in chapter 2; section 2.8.1.

In MM-SR, a reference stationary geometry is specified at which normal-mode analysis is to be performed. The reference geometry in the present work is the global minimum on the PES of  $C_2H_3^+$ , which is the standard choice for MM-SR. In the present work we report MM-SR calculations using three-mode (3MR), four-mode (4MR) and five-mode (5MR) representation of the potential. Results of these calculations are given in section 4.3.1.

## 4.2.2 Reaction Path Hamiltonian Analysis

The MULTIMODE single-reference approach (MM-SR) is expected to provide fairly accurate values, i.e., within  $10\text{ cm}^{-1}$  or so, for the fundamentals of  $C_2H_3^+$  using the the minimum bridged configuration as the reference since the barrier to isomerization to the secondary (Y-shaped) minimum is fairly large, i.e.,  $1264\text{ cm}^{-1}$  (cf. the barrier to internal rotation of  $374\text{ cm}^{-1}$  in methanol, for example). However, this approach cannot obtain the tunnelling splittings that are to be expected between equivalent structures along the isomerization path (six in total). Also, to pass from one structure to the next involves several low-frequency ‘floppy’ vibrations, and the nature of these will necessarily change as isomerization takes place. A more realistic picture of the dynamics of the vibrational motion should therefore be sought, and this is to be found in the MULTIMODE Reaction Path Hamiltonian approach (MM-RPH)[175].

The bridged and Y-shaped minima of  $C_2H_3^+$  are both planar, and a pseudo-internal rotation angle  $\tau$  which interconverts these structures has been proposed by Escribano and Bunker.[176] This definition of the ‘‘reaction path’’ has been adopted in this work and is shown in Fig. 4.2.

An inspection of Fig. 4.2 shows that for  $\tau = 0$ , the molecule takes on the bridged structure, and for  $\tau = 30$  it takes on the Y-shaped structure. There are therefore a total of six such pairs of structures as  $\tau$  goes from 0 to  $2\pi$ . The principle behind the Reaction Path Hamiltonian [177] which is incorporated in MM-RPH is to treat the coordinate  $\tau$  as a special curvilinear coordinate and to increment  $\tau$  by some small constant amount (0.5 degrees in the present work)

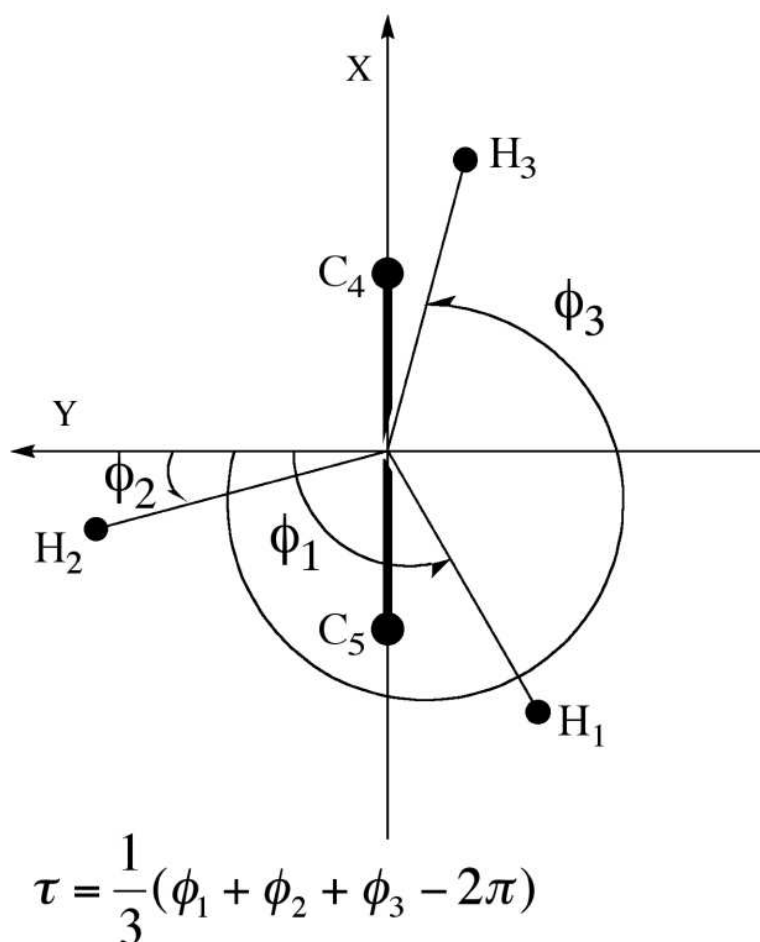


Figure 4.2: Definition of reaction path. Coordinate  $\tau$  is in terms of internal angle  $\phi_i (i = 1, 3)$

over the entire Reaction Path from  $\tau = 0$  to  $2\pi$ . In practice it is only necessary to use the unique structures between  $\tau = 0$  and  $\tau = 30$  deg; all subsequent structures can be obtained by reflection. For each value of  $\tau$ , we minimized the energy with respect to the seven independent coordinates of the in-plane structure (the  $z$ -coordinates of all atoms are constrained to zero). These coordinates are  $R(\text{OH}_1)$ ,  $R(\text{OH}_2)$ ,  $R(\text{OH}_3)$ ,  $R(\text{C}_4\text{C}_5)$ ,  $\phi_1$ ,  $\phi_2$ ,  $\phi_3$ , and are converted to cartesian coordinates for a direct link to our potential energy surface. In the above definition  $O$  is the mid-point of the  $\text{C}-\text{C}$  bond and also the origin of the chosen coordinate system (Fig. 4.2).

The resulting minimum-energy path is shown in Fig. 4.3 between  $\tau = 0$  to  $\tau = 60$  degrees. As an additional test for our potential energy surface we compare the PES energies with the *ab initio* energies calculated on this path. As seen in Fig. 4.3, there is extremely good agreement between the PES energies and *ab initio* ones.

The details of the MM-RPH calculations follows exactly those described in earlier work.[175] At each path point a normal coordinate analysis is done in which the path coordinate  $\tau$  is projected out to leave  $3N - 7 = 8$  normal coordinates orthogonal to the path. An optimized harmonic-oscillator basis in these normal coordinates is obtained for the equilibrium bridged structure for use at all angles  $\tau$ ; a basis in  $\cos(m\tau)$  and  $\sin(m\tau)$  is used for the path coordinate.

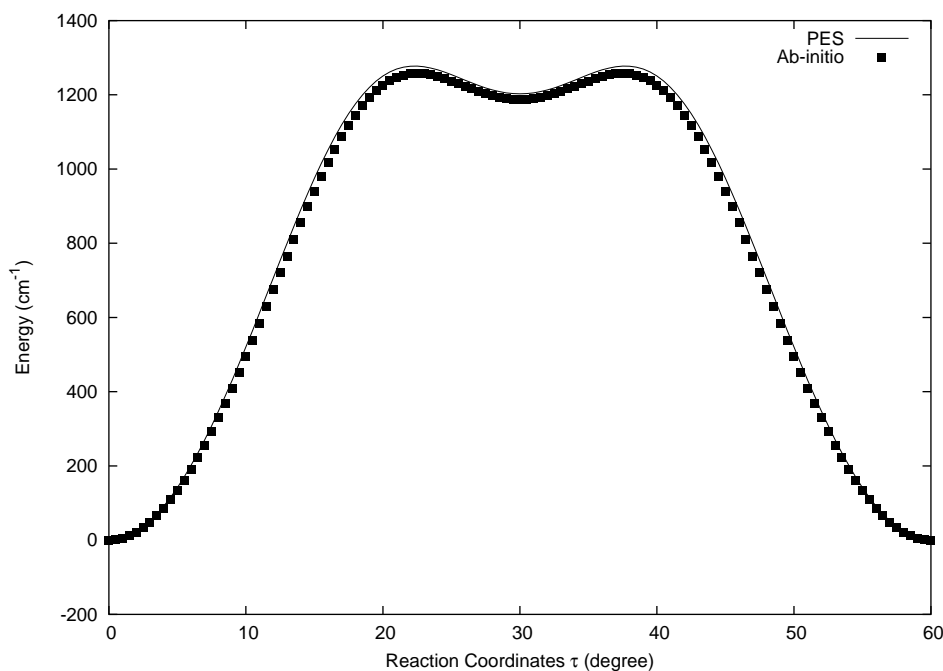


Figure 4.3: PES energy compared with *ab initio* energy for the first period of the reaction path.

Numerical integration of matrix elements is done by Gaussian quadrature, including integration over  $\tau$ . This follows from the modified  $n$ -mode expression for the potential  $V$ , where we replace  $V(Q_1, Q_2, \dots, Q_N)$  by  $V(\tau; Q_1, Q_2, \dots, Q_{N-1})$ . Apart from this, the model is identical to that of the MM-SR algorithm; a vibrational SCF is first carried out using individually optimized one-dimensional functions of  $\mathbf{Q}$  and  $\tau$ , and this is followed by a virtual CI in the one-dimensional SCF basis functions.

## 4.3 Results and Discussion

### 4.3.1 Single Reference Calculation

In this section single reference vibrational analysis using the lowest energy structure (non-classical, bridged structure) on our PES as the reference geometry is presented. In these calculations, the basis sizes used in CI symmetry blocks for the bridged  $\text{C}_2\text{H}_3^+$  structure are 16128 in  $A_1$ , 9191 in  $B_2$ , 14589 in  $B_1$  and 9191 in  $A_2$  for a total basis size of 49099. Eighteen primitive harmonic-oscillator functions, 15 contracted functions and 16 HEG points are used for each mode in the vibrational calculation. Techniques used to determine optimized quadratures points have been described elsewhere[88]. The vibrational energies up to  $4000 \text{ cm}^{-1}$  above the zero-point energy using the 5MR, 4MR and 3MR of the potential for zero total angular momentum and converged with respect to size of the CI basis are listed in Table 4.3.

Table 4.3: Theoretical vibrational energies (in  $\text{cm}^{-1}$ ) of  $\text{C}_2\text{H}_3^+$  using 5, 4 and 3 mode coupling in MultiMode calculations.

State	5MR	5MR-4MR	5MR-3MR
(000000000) Zero-Point Energy	7367.0	-35.5	-4.8
(010000000) $b_2$	535.0	2.4	-11.1
(100000000) $a_2$	562.1	3.3	-11.3
(001000000) $b_1$	767.8	3.4	-10.3
(000100000) $a_1$	859.3	4.3	-20.3
(020000000) $a_1$	1067.1	2.3	-27.1
(000010000) $b_2$	1134.2	2.3	-4.9
(110000000) $b_1$	1139.9	7.5	-10.2
(200000000) $a_1$	1143.5	6.3	-27.5
(011000000) $a_2$	1311.1	3.7	-5.1
(101000000) $b_2$	1347.2	-5.5	-10.7
(100100000) $a_2$	1463.9	14.1	-15.0
(002000000) $a_1$	1528.3	7.8	-27.3
(010100000) $b_2$	1617.8	0.6	-31.3
(001100000) $b_2$	1673.5	10.6	-6.9
(100010000) $b_1$	1729.7	2.9	-0.1
(010010000) $a_1$	1747.6	8.6	-47.7
(000200000) $a_1$	1874.7	4.7	-55.9
(000001000) $a_1$	1897.5	1.7	3.2
(001010000) $a_2$	1924.7	5.5	1.5
(000110000) $b_2$	2158.3	4.6	-7.2
(000020000) $a_1$	2226.9	6.0	-13.6
(000000100) $a_1$	2308.4	1.9	-12.8
(010001000) $b_2$	2424.5	2.6	-8.6
(100001000) $a_2$	2454.4	-4.8	-3.0
(001001000) $b_1$	2678.3	6.4	-7.2
(000101000) $a_1$	2776.2	6.6	-13.4
(100000100) $a_2$	2901.4	-1.1	-9.0
(010000100) $b_2$	2923.6	1.1	-9.0
(000011000) $b_2$	3042.4	1.4	9.0
(001000100) $b_1$	3104.6	3.4	-11.1
(000000010) $b_2$	3119.6 (3142.2) <sup>1</sup>	0.3	22.8
(000100100) $a_1$	3201.8	6.5	1.7
(000000001) $a_1$	3219.2	-4.2	6.7
(000010100) $b_2$	3442.9	4.2	-3.1
(010000010) $a_1$	3656.6	1.6	30.9
(100000010) $b_1$	3681.6	1.3	50.9
(010000001) $b_2$	3751.1	1.0	38.2
(100000001) $a_2$	3774.3	8.2	43.3
(000002000) $a_1$	3783.9	2.6	4.0
(001000010) $a_2$	3880.5	0.9	-38.7
(001000001) $b_1$	3977.5	-3.2	-23.0
(000100010) $b_2$	3985.4	3.2	-4.2

<sup>1</sup> The experimental data taken from Oka and co-workers

The zero-point energy is also given here and the states are all assigned according to symmetry and mode excitation. The purpose in showing these three nMR results is to examine convergence with respect to this very important parameter of MM calculations. Thus, we show the differences in energies for the 3MR and 4MR calculations relative to the 5MR energies. As seen the 3MR results differ from the 5MR ones by a few to tens of wave-numbers. By contrast the 4MR energies differ by generally less than  $10\text{ cm}^{-1}$ . This strongly suggests that the 5MR energies are converged to less than  $10\text{ cm}^{-1}$  for a single-reference calculation. Interestingly the zero-point energy shows the largest difference between the 4MR and 5MR calculations, suggesting that the 5MR zero-point energy is less well converged than the excitation energies. We will return to this point below when we present the MM-RPH results.

We also include in this table the one experimental energy (for the (000000010)  $b_2$  state) [132, 133] shown in parentheses. The present 5MR energy of  $3119.6\text{ cm}^{-1}$  is only  $22\text{ cm}^{-1}$  lower than the experimental value. Next we present the energies from the MM-RPH calculation.

### 4.3.2 Reaction Path Hamiltonian

One important difference between VSCF and VCI calculations performed for MM-SR and for MM-RPH lies in the large number of basis functions in  $\tau$  that are required in the RPH calculations to ensure convergence along the RP coordinate itself. We require around 24 such functions to converge the energies of interest in this work (cf, 12 required for the roughly equivalent mode 2 in the present MM-SR calculations). This means that the VCI basis involving multiple excitations in  $\tau$  and the remaining 8 normal modes can become very large, especially as the number of modes increases. This explosion of VCI basis occurs despite the fact that we impose maximum quanta and maximum sum-over-quanta on our VCI basis construction[88]. However, this can be substantially reduced by making full use of symmetry. In  $C_{2v}$  (see later) we reduce the problem to four matrices of orders 104526 ( $A_1$ ), 104441 ( $B_2$ ), 76359 ( $B_1$ ) and 76371 ( $A_2$ ). These matrix sizes are much larger than those in the MM-SR calculations and as a result of the extra computational effort in the MM-RPH calculations we restricted to potential coupling to 3MR in the 8 normal modes orthogonal to the path plus one for the path for a total of 4MR. We have done some examination of convergence of the results with respect to nMR and based on these we believe the results we present below are converged to within  $10\text{ cm}^{-1}$ .

The permutational inversion symmetry of  $C_2H_3^+$  (the relevant symmetry for the MM-RPH calculations) is  $G_{12}$ , [133] which is isomorphic to  $D_{3h}$ . This means that in-plane vibrations split into  $A'_1$ ,  $A'_2$  and two  $E'$  components (six in total). For fundamentals of  $A'_1$  symmetry, there will be  $2 \times A'_1$  and  $2 \times E'$  tunnelling components. The six different vibrational energy levels arise due to the tunnelling through the  $1264\text{ cm}^{-1}$  potential barrier to isomerization between bridged- and Y-structures; these splittings cannot be described in the MM-SR calculations.

At present MM-RPH (and MM-SR) can only deal with the reduced symmetry  $C_{2v}$  point group. This is the full symmetry at the bridged reference and so the symmetry is not reduced in the MM-SR calculations; however, it is for the MM-RPH ones. The result is that the  $E'$  components will appear in  $A_1$  and  $B_2$  blocks, and their degeneracies will not be guaranteed, except by numerical convergence of each block. We do not anticipate such high-accuracy here, but we will see that very good agreement between most  $E'$  components is achieved. The six different vibrational energy levels arise due to the tunnelling through the  $1264\text{ cm}^{-1}$  potential barrier to isomerization between bridged- and Y-structures, which can not be achieved for MM-SR calculations. However, the tunnelling is anticipated to be small for a barrier of such height, and as a consequence we would expect the MM-SR and MM-RPH energies to be similar and

this is born out in Table 4.4 where we compare the zero point energies (ZPEs) and fundamental energies. Tunnelling splittings obtained in the present MM-RPH calculations are also reported.

Table 4.4: Single Reference Multimode calculation (MM-SR) and Reaction Path Multimode calculation (MM-RPH) data at the ZPE and fundamental levels, specified in  $D_{3h}$  symmetry. RPH results include tunneling splitting.

State	MM-SR	MM-RPH (Sym. label)	State	MM-SR	MM-RPH (Sym. label)
(000000000) ZPE <sup>1</sup>	7367	7383	(000010000) $A'_2$	1134	1169
		0.0129 $E'$			6.3644 $E'$
		0.0137 $E'$			10.9457 $E'$
		0.3204 $E'$			11.4049 $E'$
		0.3206 $E'$			11.4257 $E'$
		0.3494 $A'_1$			12.9434 $A'_2$
(010000000) $A'_2$	535	541	(000001000) $A'_1$	1897	1888
		4.6287 $E'$			0.3859 $E'$
		4.8025 $E'$			0.3869 $E'$
		4.7512 $A'_2$			1.4813 $E'$
		5.2049 $E'$			1.4975 $E'$
		5.2487 $E'$			1.6663 $A'_1$
(100000000) $A''_1$	562	562	(000000100) $A'_1$	2308	2269
		0.0599 $E''$			3.1332 $E'$
		0.0632 $E''$			3.4976 $E'$
		0.3778 $E''$			5.7821 $A'_1$
		0.3909 $E''$			6.5170 $E'$
		0.5128 $A''_1$			7.0746 $E'$
(001000000) $A''_2$	768	763	(000000010) $A'_2$	3120 (3142) <sup>2</sup>	3103
		0.0512 $E''$			0.5145 $E'$
		0.0538 $E''$			1.6696 $E'$
		0.3969 $E''$			1.4611 $A'_2$
		0.4056 $E''$			1.5783 $E'$
		0.5024 $A''_2$			2.1024 $E'$
(000100000) $A'_1$	859	843	(000000001) $A'_1$	3219	3204
		0.5408 $E'$			-0.7133 $E'$
		0.6404 $E'$			0.2332 $E'$
		5.5603 $A'_1$			0.4825 $E'$
		5.6066 $E'$			0.5717 $E'$
		5.8661 $E'$			1.4676 $A'_1$

<sup>1</sup> Zero-point energy was also calculated using Diffusion Monte Carlo (DMC) method. The DMC ZPE is 7389.3  $\text{cm}^{-1}$  with a statistical error of 2.1  $\text{cm}^{-1}$ .

<sup>2</sup> The experimental data taken from Oka and co-workers

Focusing first on the ZPEs we see that the MM-SR result is 17  $\text{cm}^{-1}$  below the presumably more accurate MM-RPH one. We have done an independent Diffusion Monte Carlo calculations of the ZPE and obtain a value of 7389  $\text{cm}^{-1}$  with a statistical uncertainty of 2.1  $\text{cm}^{-1}$ , in very

good agreement with the MM-RPH ZPE. Note the MM-RPH ZPE is roughly  $6\text{ cm}^{-1}$  below the full mode-coupled DMC one, which we present as the benchmark value. (The fact that the MM energy is slightly below the DMC does not mean that the MM calculations are not variational. They are variational for the given  $n$ -mode representation of the potential. Approximations made by that representation of the potential can lead to errors in the energy eigenvalues that can be positive or negative.) Overall there is good agreement between the MM-SR and the MM-RPH excitation energies. Another measure of the convergence of the MM-RPH energies is the degree of numerical degeneracy of the various  $E'$  components. These range from  $10^{-3}\text{ cm}^{-1}$  to a wavenumber or so. Finally, as anticipated, the  $1264\text{ cm}^{-1}$  potential barrier does indeed result in very little tunnelling for most of the fundamentals shown in this table.

Experimental tunneling splittings for the anti-symmetric CH-stretch fundamental have been reported [132, 133] and are in the range of a few hundredths to a few tenths of a wavenumber, depending on the rotational transition. These results are smaller by roughly an order of magnitude than our calculations; however, if we use the splittings of the zero-point level as a common reference for both experiment and the present calculations we obtain agreement with experiment of about one order of magnitude greater splitting for this excited vibrational state. (The experimental splittings of the ZPE was unobservable and so presumably much smaller than  $0.01\text{ cm}^{-1}$ .)

It must be noted that the *ab initio* calculation of tunneling splittings of the order of  $0.01\text{ cm}^{-1}$  is exceedingly demanding. However, adjusting the barrier height by a relatively small amount can be done to improve the level of agreement with experiment. Indeed a model calculation given by Oka and co-workers [132, 133] arrived at the energy difference between the bridged and Y-structure minimum of  $1400\text{ cm}^{-1}$ . This is roughly  $140\text{ cm}^{-1}$  larger than the present *ab initio* value of  $1264\text{ cm}^{-1}$  and interestingly the increasing the barrier would result in smaller tunneling splittings which would bring theory and experiment into closer agreement and suggests that the present energy barrier is slightly low.

#### 4.4 Spectroscopic calculations for $\text{C}_2\text{H}_5^+$

The normal mode frequencies for the non-classical and classical structures of  $\text{C}_2\text{H}_5^+$  were calculated using the present PES and also directly using MP4(SDTQ)/aug-cc-pVTZ. In Table 4.5 and Table 4.6 we compare the normal mode frequencies calculated in the present work with those published by Quapp and Heidrich[164] and by Trinquier[165] for the bridged and Y-shape structure respectively. It is important to note that the normal mode frequencies published by Quapp and Heidrich[164] were calculated using a 6-31G\*\* basis set at the MP2 level of theory and the frequencies published by Trinquier[165] were calculated using a DZP basis set at the SCF level of theory. Since the *ab initio* method and the basis sets used in the present calculations are different from the previous publications, the normal mode frequencies listed in Table 4.5 and Table 4.6 are not expected to be the same. We observe that, except for the high energy modes, all the fundamentals show good agreement with the theoretical values reported by Quapp and Heidrich[164] (less than  $\text{cm}^{-1}$ ) and also agree reasonably well with those reported by Trinquier[165] (except for the first mode) for the global minimum structure.

Table 4.5: Harmonic frequencies ( $\text{cm}^{-1}$ ) for the nonclassical bridged structure of  $\text{C}_2\text{H}_5^+$ 

Mode Number	Symmetry	PES <sup>1</sup>	MP4(SDTQ) <sup>2</sup>	Quapp and Heidrich <sup>3</sup>	Trinquier <sup>4</sup>
1	$B_2$	753.4	733.72	763	425
2	$B_1$	817.5	827.60	865	902
3	$A_2$	1094.9	1081.36	1113	1136
4	$B_1$	1108.7	1104.49	1156	1223
5	$A_1$	1132.7	1138.32	1177	1233
6	$A_2$	1260.2	1251.80	1291	1336
7	$B_2$	1276.3	1283.77	1347	1384
8	$A_1$	1347.9	1351.07	1398	1428
9	$B_2$	1450.5	1476.49	1527	1568
10	$A_1$	1574.0	1569.44	1626	1696
11	$A_1$	2163.8	2175.33	2273	2316
12	$B_2$	3126.7	3136.51	3234	3283
13	$A_1$	3136.2	3139.82	3237	3290
14	$A_2$	3250.7	3243.94	3351	3397
15	$B_1$	3257.7	3261.09	3366	3413

<sup>1</sup> Normal mode frequencies calculated from fitted PES.

<sup>2</sup> Frequencies calculated at the MP4(SDTQ) level of theory with aug-cc-pVTZ basis.

<sup>3</sup> Frequencies calculated using a 6-31G\*\* basis set at the MP2 level of theory.[164]

<sup>4</sup> Frequencies calculated using a DZP basis set at the SCF level of theory.[165]

Comparing the normal mode frequencies for the bridged structure, calculated using the present PES with those computed directly at the MP4(SDTQ) level of theory, we note that for most of the modes the agreement is within  $10 \text{ cm}^{-1}$ , except for Mode 9 (Figure.4.4(i)) for which the difference between PES and direct *ab initio* calculation is  $26 \text{ cm}^{-1}$ . Mode 1(Figure.4.4(a)) agrees within  $20 \text{ cm}^{-1}$  and modes 3 (Figure.4.4(c)) and 11 (Figure.4.4(k)) agree within  $15 \text{ cm}^{-1}$ . The difference of  $26 \text{ cm}^{-1}$  between the PES and MP4(SDTQ) for Mode 9 is the largest difference observed in the present work. For Mode 11(Figure.4.4(c)) to Mode 15(Figure.4.4(i)), comparing the PES normal mode frequencies (column 3 of Table 4.5) with Quapp and Heidrich[164] and Trinquier[165], we observe a largest difference of 5% (lower). The difference for all the modes between the present work and two previous theoretical calculations are in the ranges of 1-5% and 3-10%, respectively, except for mode 1 in case of Trinquier. This large difference for mode 1 can be attributed to the fact that the calculations performed by Trinquier were at the SCF level of theory.

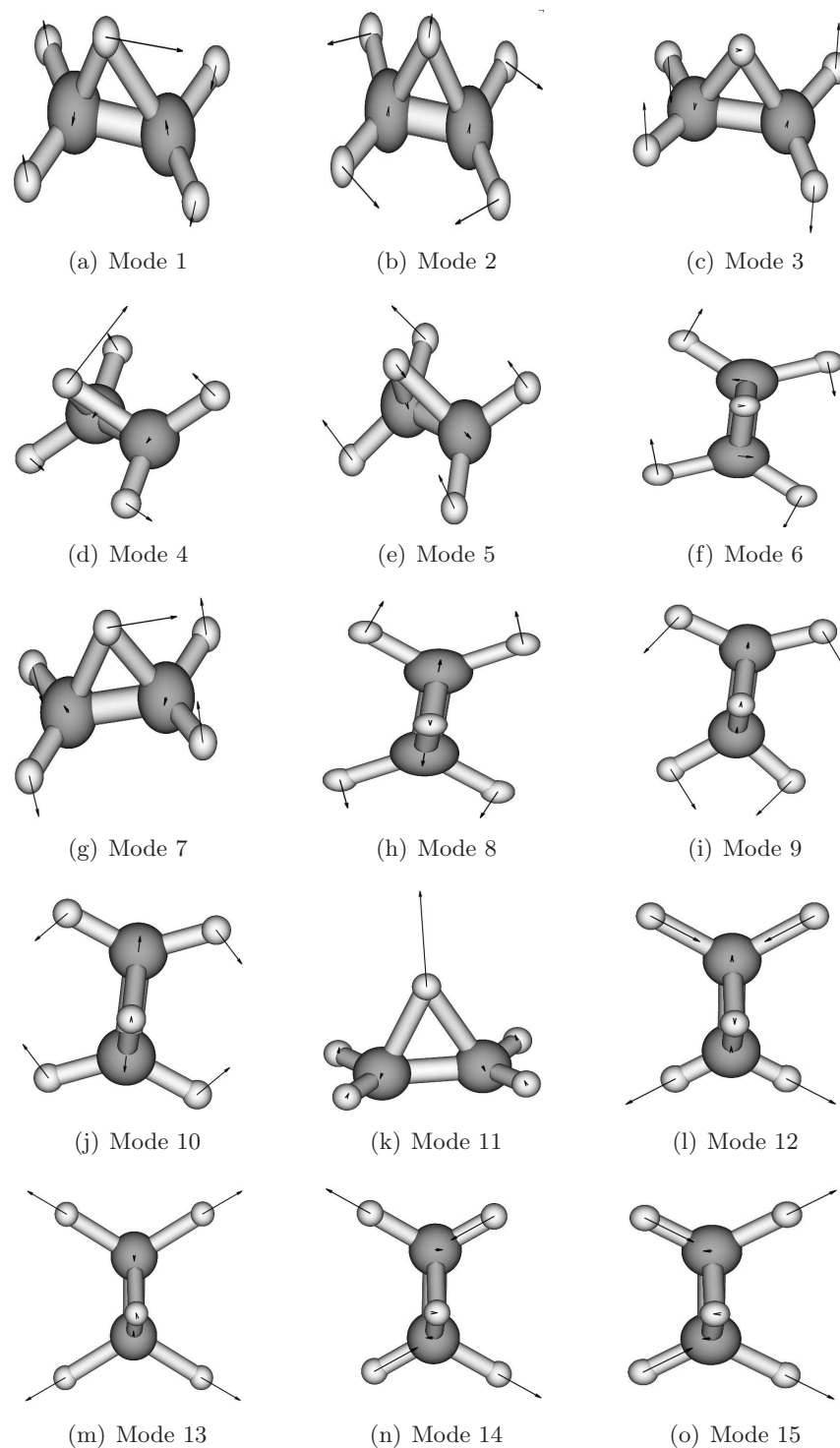


Figure 4.4: 4.4(a) - 4.4(i) Normal Modes for the non-classical bridged structure

Table 4.6: Harmonic frequencies ( $\text{cm}^{-1}$ ) for the classical Y-Shaped structure of  $\text{C}_2\text{H}_5^+$ 

Mode Number	Symmetry	PES <sup>1</sup>	MP4(SDTQ) <sup>2</sup>	Quapp and Heidrich <sup>3</sup>	Trinquier <sup>4</sup>
1	$A''$	-368.2	-381.99	367i	293
2	$A''$	754.2	759.16	766	551
3	$A'$	800.6	795.17	828	893
4	$A'$	1042.5	1071.64	1118	1219
5	$A'$	1154.8	1185.71	1227	1305
6	$A'$	1253.2	1267.75	1304	1334
7	$A''$	1256.9	1268.66	1315	1413
8	$A''$	1395.8	1399.54	1444	1439
9	$A'$	1461.0	1458.98	1503	1565
10	$A'$	1551.5	1558.39	1614	1657
11	$A''$	2883.2	2892.53	2994	2849
12	$A'$	2896.0	2894.27	3015	3252
13	$A'$	3114.0	3117.48	3221	3278
14	$A'$	3221.9	3213.72	3319	3351
15	$A'$	3230.7	3230.82	3344	3397

<sup>1</sup> Normal mode frequencies calculated from fitted PES.

<sup>2</sup> Frequencies calculated at the MP4(SDTQ) level of theory with aug-cc-pVTZ basis.

<sup>3</sup> Frequencies calculated using a 6-31G\*\* basis set at the MP2 level of theory.[164]

<sup>4</sup> Frequencies calculated using a DZP basis set at the SCF level of theory.[165]

For the Y-shape structure (Table 4.2), we observe excellent agreement between the PES and MP4(SDTQ) frequencies, with both finding the Y-structure to be a first order saddle point. The normal mode frequencies for the Y-shape structure show better agreement with the theoretical values reported by Quapp and Heidrich[164] than those reported by Trinquier[165]. For Mode 6, the PES frequency has a value of  $1253 \text{ cm}^{-1}$  which is 4% lower than the corresponding value from Ref. [164] and 6% lower than that from Ref. [165]. The most interesting normal mode is mode 1, which involves asymmetric in-plane-bend of the bridging hydrogen. For this mode the SCF method of Trinquier reports this to be a real frequency whereas our calculations, in agreement with the calculations of Quapp and Heidrich finds this to be the first order saddle point.

In the present work we also perform direct MP4(SDTQ) calculations for three high-lying, first- and second-order saddle points. The geometry of these saddle points are shown in Fig. 3.2(c) through 3.2(e). The normal mode frequencies are listed in Table 4.7 through 4.9. Comparing the normal mode frequencies calculated directly from the PES with those computed at the *ab initio* level, we note that the agreement for some modes is within  $10 \text{ cm}^{-1}$ . For most the modes the agreement is in the range of  $100 \text{ cm}^{-1}$ . However, for a couple of modes, for all the three stationary points, the difference is as large as  $300 \text{ cm}^{-1}$ . This is consistent with the fact the rms error between the *ab initio* energy and the PES is around 1 mHartree (approx  $300 \text{ cm}^{-1}$ ). Also the configurations on the hypersurface have been sampled in a random fashion and lack of data along a certain normal mode can be expected. However, it is important to note that the PES is able to identify the first- and second-order saddle points correctly.

Table 4.7: Harmonic frequencies ( $\text{cm}^{-1}$ ) of low lying stationary point shown in Fig. 3.2(c) (first order saddle point) of  $\text{C}_2\text{H}_5^+$ 

Mode Number	Symmetry	PES <sup>1</sup>	MP4(SDTQ) <sup>2</sup>
1	-	-1176.5	-1089.51
2	A''	419.9	661.93
3	A'	735.7	680.87
4	A''	889.0	919.25
5	A''	1044.2	1014.70
6	A'	1070.2	1064.90
7	A'	1376.7	1234.90
8	A'	1421.4	1412.63
9	A'	1570.6	1572.59
10	A'	1651.5	1619.35
11	A'	2041.3	2118.73
12	A'	2983.1	3152.55
13	A'	3185.4	3175.05
14	A'	3296.2	3261.71
15	A'	3415.3	3266.22

<sup>1</sup> Normal mode frequencies calculated from fitted PES.

<sup>2</sup> Frequencies calculated at the MP4(SDTQ) level of theory with aug-cc-pVTZ basis.

Table 4.8: Harmonic frequencies ( $\text{cm}^{-1}$ ) of low lying stationary point shown in Fig. 3.2(d) (second order saddle point) of  $\text{C}_2\text{H}_5^+$ 

Mode Number	Symmetry	PES <sup>1</sup>	MP4(SDTQ) <sup>2</sup>
1	-	-991.8	-1092.98
2	-	-941.5	-1092.50
3	$B_1$	579.4	571.65
4	$B_2$	585.1	888.63
5	$A_2$	1109.2	960.50
6	$B_1$	1219.8	1037.31
7	$B_2$	1349.5	1275.09
8	$A_1$	1361.3	1281.06
9	$A_1$	1463.0	1436.30
10	$A_1$	1718.9	1569.67
11	$A_1$	2393.7	2701.90
12	$A_1$	2584.5	2833.19
13	$B_2$	2862.7	2910.30
14	$A_1$	3161.0	3173.74
15	$B_2$	3179.3	3288.55

<sup>1</sup> Normal mode frequencies calculated from fitted PES.

<sup>2</sup> Frequencies calculated at the MP4(SDTQ) level of theory with aug-cc-pVTZ basis.

Table 4.9: Harmonic frequencies ( $\text{cm}^{-1}$ ) of low lying stationary point shown in Fig. 3.2(e) (second order saddle point) structure on  $\text{C}_2\text{H}_5^+$  PES

Mode Number	Symmetry	PES <sup>1</sup>	MP4(SDTQ) <sup>2</sup>
1	–	-1323.8	-1573.64
2	–	-1114.3	-800.81
3	$A_1$	468.2	573.78
4	$A_2$	886.4	798.40
5	$B_1$	937.6	903.34
6	$A_2$	1043.8	966.58
7	$B_2$	1081.5	1190.43
8	$A_1$	1199.5	1277.21
9	$A_1$	1389.8	1441.41
10	$B_2$	1603.1	1485.90
11	$A_1$	2012.1	2282.57
12	$B_2$	2915.3	2968.09
13	$A_1$	2966.0	2971.71
14	$B_2$	3125.1	3186.36
15	$A_1$	3227.5	3196.48

<sup>1</sup> Normal mode frequencies calculated from fitted PES.

<sup>2</sup> Frequencies calculated at the MP4(SDTQ) level of theory with aug-cc-pVTZ basis.

#### 4.4.1 Single Reference Calculations

We perform quantum mechanical rovibrational energy calculations for  $\text{C}_2\text{H}_5^+$  molecule based on the full Watson Hamiltonian,[86, 87, 95, 173] which is an exact Hamiltonian for rovibrational motion expressed in mass-scaled normal modes  $Q_i$ . The theoretical approach used in MM-SR builds on a vibrational self-consistent field (VSCF)[81] wavefunction for a given reference state labeled by a set of quantum numbers. The potential  $V(\mathbf{Q})$  is represented as an  $n$ -mode representation in terms of  $N$  normal modes (denoted collectively as  $\mathbf{Q}$ ), which permits calculations for many-mode systems (thus for fairly large molecules). Matrix elements of the potential are calculated using the numerical quadratures at optimized quadrature points (determined by the one mode terms), and at most five-dimensional quadrature is required. An important feature of MM-SR is the option to vary the  $n$ -mode representation of the potential to test the convergence of the vibrational energies with respect to  $n$ .

Eigenvalues and eigenfunctions of the Watson Hamiltonian [86, 87] are obtained using the approach denoted as "VCI" (explained earlier). In MM-SR, a reference stationary geometry is specified at which normal-mode analysis is to be performed. The reference geometry in the present work is the global minimum on the PES of  $\text{C}_2\text{H}_5^+$ , which is the standard choice for MM-SR. In the present dissertation we report MM-SR calculations using three-mode (3MR) and four-mode (4MR) representation of the potential.

In this section we present the single reference vibrational analysis using the lowest energy structure (non-classical, bridged structure) on our PES as the reference geometry. In these calculations, the basis sizes used in CI symmetry blocks for the bridged  $\text{C}_2\text{H}_5^+$  structure are 23056 in

$A_1$ , 18435 in  $B_2$ , 16837 in  $B_1$  and 16821 in  $A_2$  for a total basis size of 75149, for 3MR converged calculations. Thirty seven primitive harmonic-oscillator functions, 14 contracted functions and 40 HEG points are used for each mode in the vibrational calculation. Techniques used to determine optimized quadratures points have been described elsewhere.[88]

Table 4.10: Theoretical vibrational energies (in  $\text{cm}^{-1}$ ) of  $\text{C}_2\text{H}_5^+$  using 4 and 3 mode coupling in Multimode calculations.

State	4MR	4MR-3MR
ZPE <sup>1</sup> 0000000000000000	13324.4761	-1.64
$b_2$ 1000000000000000	652.6	-4.8
$b_1$ 0100000000000000	922.4	-4.9
$a_2$ 0010000000000000	1022.7	-5.2
$a_1$ 0000100000000000	1094.3	-5.9
$b_1$ 0001000000000000	1114.1	-5.3
$b_2$ 0000001000000000	1261.0	-4.8
$a_1$ 0000000100000000	1361.4	-5.1
$a_1$ 0200000000000000	1889.2	-4.9
$a_1$ 1000001000000000	1910.9	-4.1
$b_2$ 1000100000000000	1936.1	-3.4
$b_2$ 0110000000000000	1986.3	-4.2
$b_2$ 1000000100000000	2054.7	-3.9
$a_1$ 0101000000000000	2093.6	-4.6
$a_1$ 1000000010000000	2162.7	-4.8
$b_2$ 0011000000000000	2165.8	-5.1
$a_1$ 0000000001000000	2218.0	-5.2
$b_2$ 0100010000000000	2226.1	-3.7
$a_2$ 0100001000000000	2230.9	-4.1
$b_2$ 1000000001000000	2256.1	-4.7
$b_1$ 0010001000000000	2316.9	-3.7
$a_1$ 0010010000000000	2341.6	-4.0
$a_2$ 0100000010000000	2415.9	-3.5
$b_2$ 0001010000000000	2437.8	-4.2
$b_1$ 0100000001000000	2510.1	-3.3
$b_1$ 0001000100000000	2517.1	-4.3
$a_1$ 0000002000000000	2521.5	-4.6
$b_1$ 0010000010000000	2529.8	-4.2
$b_2$ 0000101000000000	2536.9	-3.6
$b_2$ 2000001000000000	2575.7	-4.3
$b_2$ 0000001100000000	2670.3	-3.1
$b_2$ 1000000000100000	2966.5	-3.0
$a_2$ 0111000000000000	3141.2	-4.9
$a_1$ 0100010010000000	3695.3	-4.3

<sup>1</sup> Zero Point Energy

The vibrational energies up to  $4000 \text{ cm}^{-1}$  above the zero-point energy using the 4MR and 3MR of the potential for zero total angular momentum and converged with respect to size of

the CI basis are listed in Table 4.10. The zero-point energy is also given there and the states are all assigned according to symmetry and mode excitation. The purpose in showing these three nMR results is to examine convergence with respect to this very important parameter of MM calculations. Thus, we show the differences in energies for the 3MR calculations relative to the 4MR energies. As seen the 3MR results differ from the 4MR ones by a few to tens of wave-numbers. This strongly suggests that the 4MR energies are converged to less than  $10\text{ cm}^{-1}$  for a single-reference calculation. The zero-point energy shows the best agreement between 3MR and 4MR calculations.

## 4.5 Subsumption

A full-dimensional calculations of vibrational energies of  $\text{C}_2\text{H}_3^+$  and  $\text{C}_2\text{H}_5^+$  using the VSCF method followed by VCI, using the high dimensional PES developed was performed in the present work. Normal mode analysis was done at the so-called bridged and Y-minima and shows good agreement with previous theoretical studies and our own direct *ab initio* calculations. Two types of calculations were done for  $\text{C}_2\text{H}_3^+$ , one based on a single-reference configuration to define the normal modes and another based on a reaction path. The level of mode-coupling in the former calculation was explicitly examined and concluded that the 5-mode coupling excitation energies are well converged. For the computationally expensive MM-RPH calculations 4-mode coupling, including the torsional mode, was used. Excitation energies were compared with the MM-SR ones and agreement in the range of  $5\text{-}40\text{ cm}^{-1}$  was found. The MM-RPH ZPE is  $16\text{ cm}^{-1}$  above the MM-SR one. A diffusion Monte Carlo calculation of the ZPE gives a value only  $6\text{ cm}^{-1}$  above the MM-RPH one. Thus the convergence of vibrational energies is in the range of  $10\text{ cm}^{-1}$  or so. Comparison with the one band, the CH-stretch, measured experimentally by Oka and co-workers[132] shows agreement to within roughly  $40\text{ cm}^{-1}$  for the MM-RPH calculations and  $20\text{ cm}^{-1}$  for the MM-SR ones.

Tunneling splittings for the fundamental excitations and ZPE were also reported from the MM-RPH calculations. In general they are in the range of several to  $.01\text{ cm}^{-1}$ . For the measured CH-stretch they are roughly ten times larger than for the ZPE, which agrees qualitatively with the experimental estimate. However, the calculated splittings are roughly an order of magnitude larger than the experimental findings. It is argued that the calculated splittings are too large because the barrier separating the global minimum bridged structure and the Y-shaped one may be low by roughly  $150\text{ cm}^{-1}$ .

Similar single reference calculations and normal mode analysis for  $\text{C}_2\text{H}_5^+$  show good agreement with the earlier published values and direct *ab initio* calculations.

It is concluded that the potential energy surface is able to accurately represent the vibrational modes and energies. Expanding the semi-global potential energy surface to include fragment data allows to generate a global potential energy surface which can represent dissociation of the molecules. A global potential energy surface for  $\text{C}_2\text{H}_3^+$  was developed. Details of the dynamical studies using this potential energy surface are presented in the next chapter.

## Chapter 5

# Global potential energy surface and dynamics

### 5.1 Introduction

In principle a potential energy surface is capable of representing all the vibration modes, small- and large-scale oscillations around the minimas and saddle points, dissociation dynamics, abstraction and scattering reactions. *Ab initio* calculations begin with a Hartree-Fock calculation and subsequently correct for electron-electron repulsion, referred to also as electronic correlation. Møller-Plesset perturbation theory (MPn) and coupled cluster theory (CC) are examples of these post-Hartree-Fock methods. In some cases, particularly for bond breaking processes, the Hartree-Fock method is inadequate and this single-determinant reference function is not a good basis for post-Hartree-Fock methods. It is then necessary to start with a wave function that includes more than one determinant such as Multi-configurational self-consistent field (MCSCF) and make use of methods that use these multi-determinant references for improvements. Such multi-reference methods are capable of providing information about various excited states for the molecule. Each of these excited states would then constitute a potential energy surface. Thus, for a molecule there exists various potential energy surfaces each corresponding to a particular electronic state.

The Born-Oppenheimer electronic states might change their energy order as molecular geometry is changed continuously along a path. In the process their energies may become equal at some points, the surfaces are said to cross, or only come relatively close, then the crossing of the surfaces is said to be avoided. If the electronic states are of the same symmetry, the surface crossing is always avoided in diatomics and usually avoided in polyatomic. In a molecule, vibrational and electronic interactions are interrelated and influence each other, which are neglected within the BO approximation. However, these coupling terms become large (and cannot be neglected) in the case two adiabatic potential energy surfaces come close to each other, i.e. when the energy gap between them is of the order of magnitude of one oscillation quantum. This usually happens in the neighbourhood of an avoided crossing of potential energy surfaces corresponding to distinct electronic states of the same spatial and spin symmetry. A simpler way to include these effects is to switch from the adiabatic to the diabatic representation of the potential energy surfaces. The diabatic states can be obtained from the adiabatic ones by means of unitary transformation and the representation is called diabatic representation. In the diabatic representation the nuclear kinetic energy operator is diagonal, the potential energy surfaces are smoother and the coupling is due to the electronic energy and is a scalar quantity which is much more easy to estimate numerically.

### 5.2 Global potential energy surface

The potential energy surface described in chapter 3 spanned the region of configuration space in which the molecules are in the complex region or partially fragmented. The justification of such

a PES is that we were mostly interested in correctly identifying the stationary points and performing accurate ro-vibrational calculations for the global minimum and interesting stationary points on the PES. In order to study dissociation process and perform reaction dynamics the PES must be extended to span the region of space where the molecule is completely fragmented. The PES should be able to represent the energy of each of these fragments accurately.

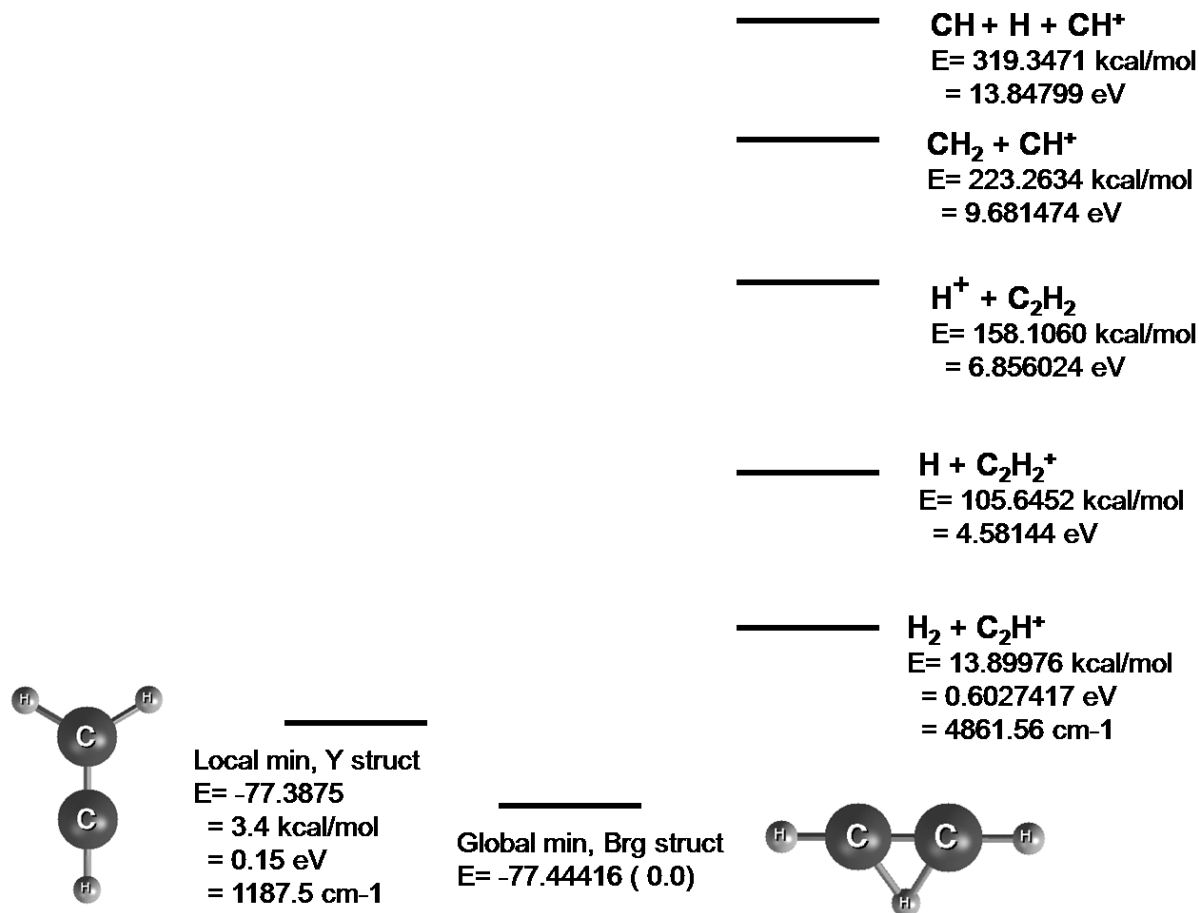
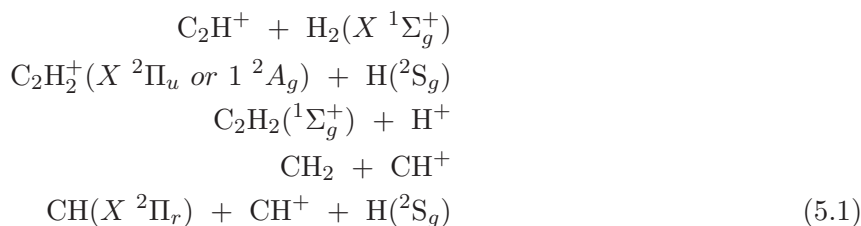


Figure 5.1: Schematic energy diagram for the various fragments included in the generation of global potential energy surface.

In an attempt to generate a global potential energy surface for C<sub>2</sub>H<sub>3</sub><sup>+</sup>, *ab initio* energy was calculated for the following fragments:



The energy calculations were performed at the same level of theory as used for the complex region configurations (RCCSD(T)/aug-cc-pvtz). The distance between the fragments was set large enough to avoid any spurious results (15 Å). Figure 5.1 sketches the asymptotic energies

of various fragments relative to the global minimum on the PES.

It is seen that the asymptotic energy for  $\text{C}_2\text{H}^+(\text{singlet}) + \text{H}_2(\text{singlet})$  is about 14 kcal/mol above the global minimum. The energy difference on between the asymptotic energies of  $\text{C}_2\text{H}_2 + \text{H}^+$  and  $\text{C}_2\text{H}_2^+ + \text{H}$  is 52.5 kcal/mol (2.28 eV). This shows that the charge exchange reaction for the the proton impinging on acetylene is exothermic and energetically favourable by 2.28 eV, which is in agreement with earlier published works (Reference [178], Pg. 90). The reaction  $\text{H} + \text{C}_2\text{H}_2^+ \rightarrow \text{H}_2 + \text{C}_2\text{H}^+$ , the hydrogen abstraction reaction, in which the incident H atom picks another H atom from  $\text{C}_2\text{H}_2^+$  to form an  $\text{H}_2$  molecule as an product. This is an important reaction and is of great interest in the field of plasma physics and astrophysics. Within the BO approximation the electronic structure of H atom and its isotopes (D and T) is approximately the same, except for some small relativistic correction. Within this approximation any of H atom in the above reaction can be replaced by a Deuterium or Tritium isotope and isotope exchange reactions can be studied. The hydrogen abstraction reaction is energetically favourable and exothermic by approximately 4.0 eV. Since, charge exchange and hydrogen abstraction reactions are of interest to us, we do not discuss the high energy fragments, the ones in which C-C bond is broken.

To study the reactions stated earlier we develop a global potential energy surface by creating a fit over all the fragment data (Fig. 5.1) and complex region data. In the dataset we included 13672 *ab initio* points for  $\text{C}_2\text{H}_3^+$  complex region, 7327 for  $\text{C}_2\text{H}^+ + \text{H} + 2$ , 6008 for  $\text{C}_2\text{H}_2^+ + \text{H}$ , 7357 for  $\text{C}_2\text{H}_2 + \text{H}^+$ , 7610 for  $\text{CH}_2 + \text{CH}^+$ , and 500 *ab initio* points for  $\text{CH} + \text{H} + \text{CH}^+$ .

### 5.3 Results and Discussion

Before performing dynamical calculations we run some trivial checks on the PES to see that the PES is able to represent the dissociation correctly. We calculate 1-D potential energy curves by moving on H atom from the bridged global minimum and Y-shaped minimum on the PES. In Fig.5.2 we show comparison of potential energy from PES and direct *ab initio* calculations. The abscissa is the distance of the bridging hydrogen from the center of the C-C bond. The PES is able to accurately represent the complex region and also the asymptotic region. However, we observe that in the intermediate fragmented region, between 3 to 4.5 Å the coupled cluster method fails to converge. This results in lack of *ab initio* data in the partially fragmented region. The reason for the failure of RCCSD(T) method is due to fact that it is a single reference method and the problem is essentially multi-reference in character.

We perform multi-reference calculation for the above reaction path. The result for MRCI calculations are shown in Fig. 5.3

Analysing the electronic occupation of configuration state functions and CI coefficients we observe that the potential energy surfaces of  $\text{C}_2\text{H}_2^+$  with H crosses with the potential energy surface of  $\text{C}_2\text{H}_2$  with  $\text{H}^+$ . This is generally expected for most of the charge exchange reactions. To such a reaction multiple electronic surface and transition probabilities between these surfaces are required.

The low lying reaction fragments  $\text{C}_2\text{H}^+$  with  $\text{H}_2$  are both in the singlet spin states and so is the complex  $\text{C}_2\text{H}_3^+$ . Thus the reaction  $\text{C}_2\text{H}^+ + \text{H}_2 \rightarrow \text{C}_2\text{H}_2^+ + \text{H}$  would take place on one surface.

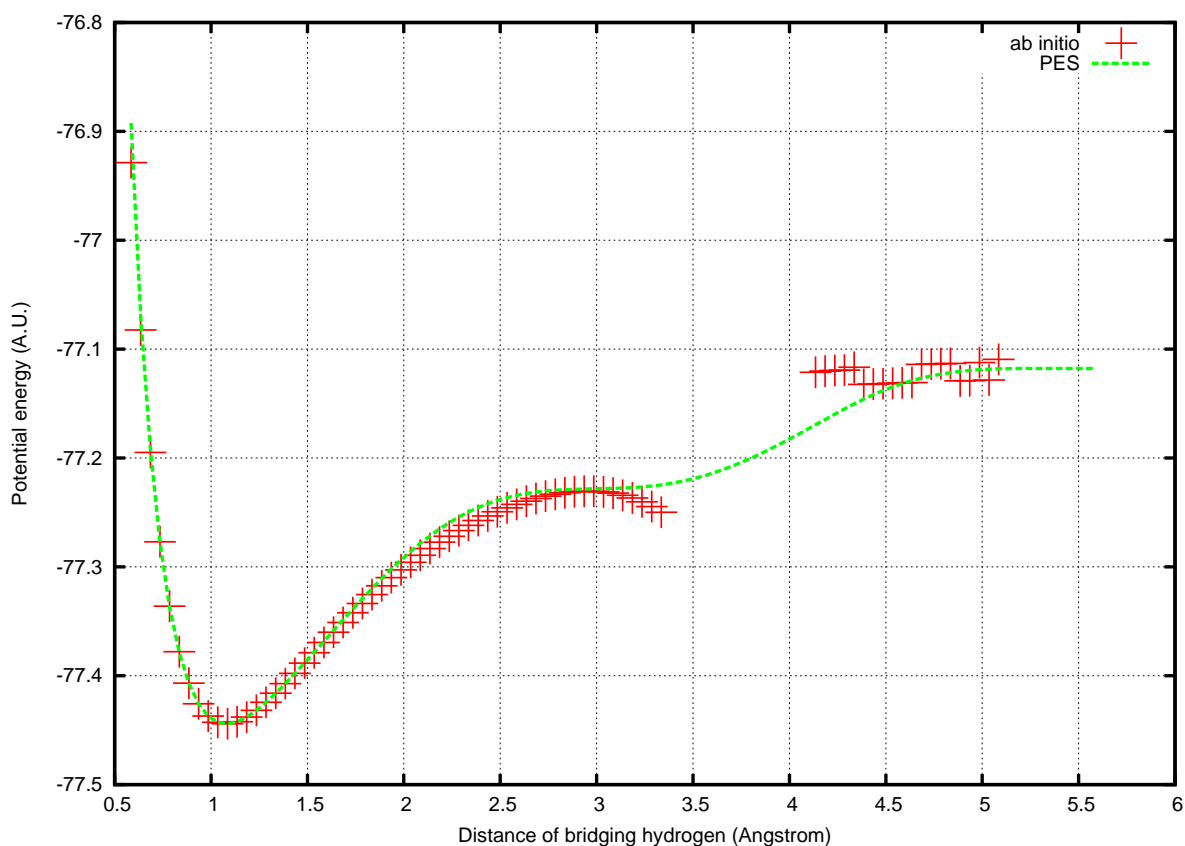
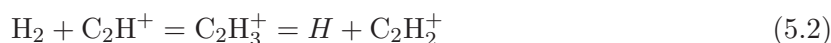


Figure 5.2: Potential energy vs distance of bridging hydrogen from the center of C-C bond for the bridged global minimum.

In the present work we focus our work on the following reaction



The global  $\text{C}_2\text{H}_3^+$  potential energy surface (PES) is based on *ab initio* calculations employing the restricted coupled cluster method with singles and doubles and perturbative treatment of triples [RCCSD(T)] [149, 150] and the augmented correlation-consistent polarized valence triple zeta (aug-cc-pVTZ) [151, 152] basis set as implemented in the MOLPRO 2006 [153] code system.

The VENUS96 general chemical dynamics program [179] was modified to perform reaction dynamics calculations on the fitted potential energy surface. Theory outlined in chapter 2; section 2.9 was used to sample the reactants initial quasiclassical states, to integrate the classical equations of motion, and to analyze product state distributions. The initial internal coordinates and momenta associated with the "quasiclassical state" corresponding to the quantum ground rovibrational state (the only internal state significantly populated at the temperatures of interest here) were obtained by treating the diatomic as a rotating oscillator and determining the quantized energy of the "quasiclassical state" by Einstein-Brillouin-Keller (EBK) [102] semi-classical quantization of action. Values of the internuclear separation were randomly sampled according to the usual classical distribution. The initial momentum was determined from energy conservation and its sign randomly assigned. Separation of rotation and vibration was assumed in sampling quasiclassical initial conditions for the polyatomic ion.

The equations of motion were integrated with a sixth-order Adams-Moulton method using

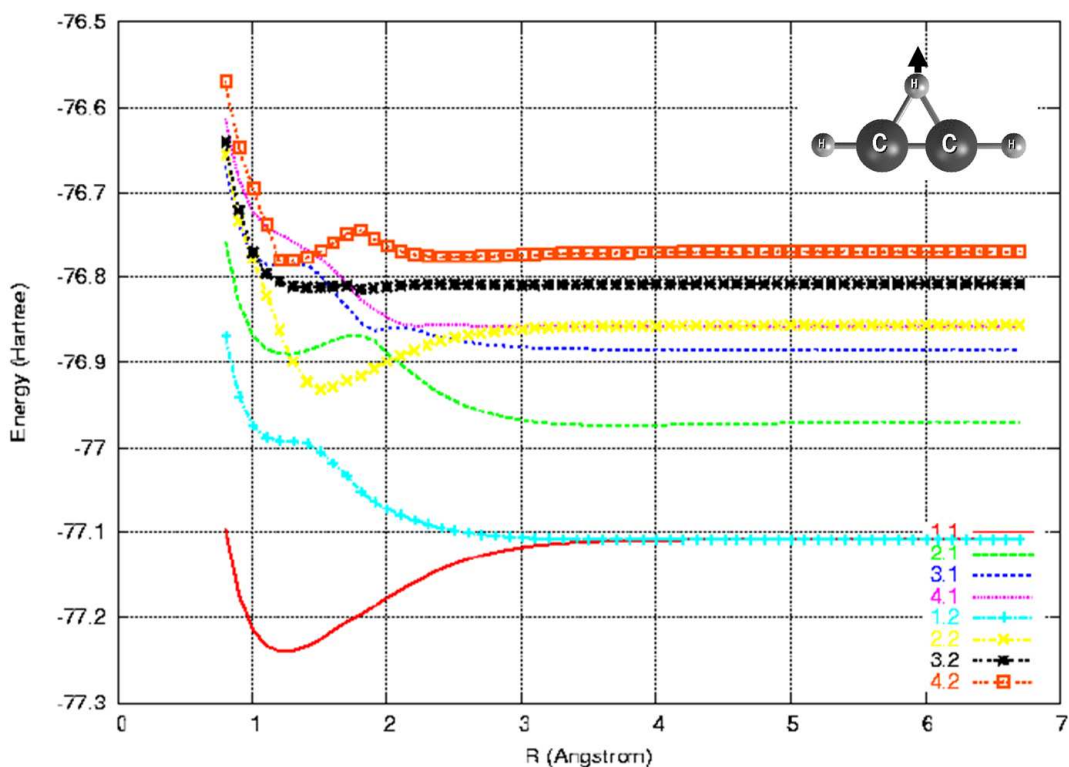


Figure 5.3: Potential energy curves (MRCI) of singlet  $C_2H_3^+$  ( $C_s$  symmetry) along the reaction path shown in the inset. x.1, x=1,4 are the first four states with  $A'$  and x.2,x=1,4 are the first four states with symmetry  $A''$ )The abscissa is the distance between the center of C-C bond and the H atom.

a time step of 0.05 fs. This step size was sufficient to ensure conservation of energy to six significant figures for the vast majority of trajectories (in excess of 98%) despite the occurrence of appreciable numbers of long-lived trajectories at all the energies considered here. For the reactants we perform normal mode analysis on the fitted PES in order to assign fixed mode energies to each normal mode. For  $H_2$  we obtain a normal mode frequency of  $4429\text{ cm}^{-1}$  which is in good agreement with  $4410\text{ cm}^{-1}$  calculated at RCCSD(T)/aug-cc-pvtz level of theory. The normal mode frequencies for  $C_2H^+$  were calculated to be  $793$ ,  $1687$  and  $3100\text{ cm}^{-1}$  which are also in close agreement with direct *ab initio* values of  $691$ ,  $1583$  and  $3107\text{ cm}^{-1}$ . The number of quanta in each mode of vibration was chosen to be equal to one and calculations were performed for zero total angular momentum for both the reactants. Relative translation energy was chosen to be equal to  $23.061\text{ kcal/mol}$  ( $1\text{ eV}$ ). The trajectories were integrated up to 5.0 ps. In the present calculation we find that most of trajectories ended up in the complex region and the products did not separate by an appreciable distance to stop the trajectory. In figure 5.4 we present the potential energy profile as a function of integration steps (output every 100th step) for a sample run. It is seen that the potential energy decreases as the reactants approach each other and stays in the complex region. We observe small- and large-amplitude oscillation and scrambling of three hydrogens around the C-C bond.

This presents a computational challenge, not the least of which is the very long integration

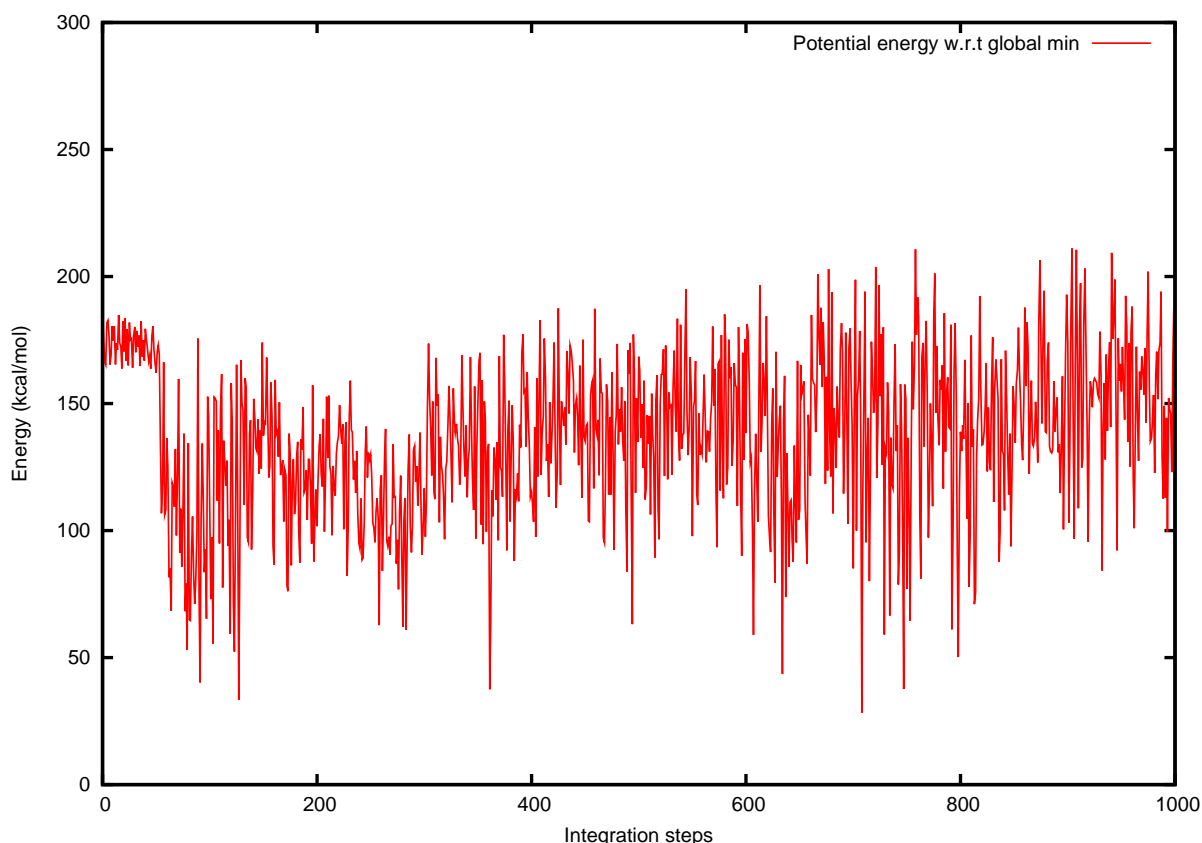


Figure 5.4: Potential energy profile for a sample QCT trajectory.

time needed to obtain complete trajectories. The present calculations indicate that the standard QCT approach is computationally prohibitive for such low translational energies. The major source of obstacle in the present calculations is the number of trajectories that remain incomplete after a large number of integration steps. This is a consequence of the increasing lifetime of the collision complexes for low translational energies, which means that calculations have to be performed for a greater number of impact parameters.

## 5.4 Subsumption

In this chapter the extension of the global potential energy surface to be used for dynamic calculations of  $\text{C}_2\text{H}_3^+$  was reported. *Ab initio* calculations were performed for the  $\text{C}_2\text{H}_3^+$  fragments and a global fit was generated to explore charge exchange and abstraction reaction. It was identified that the charge exchange reaction leads to surface crossing and multi-reference calculations were performed to identify the ground state dynamics. The general chemical dynamics program (VENUS96) was modified to perform reaction dynamics on our global surface. It is observed that the QCT method resulted in long lived trajectories which requires much more computational effort beyond the scope of this thesis.

The Hartree-Fock (HF) method typically scales as  $N^{3-4}$ ;  $N$  being the number of basis function. Moreover, the HF is an approximation, as it does not account for dynamic correlation due to the rigid form of single determinant wave function. To account for dynamic correlation, one has to go to correlated methods, which use multideterminant wave functions, and these scale as fifth (up to eight), or even greater powers with the size of the system. Thus, beyond small

molecules the HF and post-HF methods become intractable. For system with few hundreds of atoms such as atomic clusters, bio-molecules and crystalline systems, Density functional theory (DFT) provides the most reasonable potential description using reasonable computer resources. To study the diffusion of H atom between graphite planes, plane-wave base DFT using normconserving pseudopotentials is applied to perform *ab initio* molecular dynamics. Details are presented in the next chapter.

# Chapter 6

## DFT studies

### 6.1 Introduction

The construction of accurate analytical fitted potential energy and dipole moment surfaces (PES and DMS) that are full-dimensional and describe all relevant spectroscopic information and reaction channels was reported in earlier chapters. The results reported are extremely encouraging for small hydrocarbon molecules. The extension of a semi-global PES to generate a global-PES showed that reactivation dynamics could be performed at the quantum-mechanical level of theory. However, these methods could not be extended beyond small molecules due to the fact that the HF and post-HF method scale badly with system size. Hence the method of choice for treating system with hundreds of atoms or small atomic clusters is the plane-wave based Density functional theory (DFT) in which interaction of core electrons is replaced by normconserving pseudopotentials.

Plasma-material interactions (PMIs) have been recognized as a key issue in the realization of practical fusion power since the beginning of magnetic fusion research. As early as 1951, the threat to plasma purity by impurities arising from PMIs was recognized and the use of divertor was proposed to help alleviate the problem. The early days discharges were severely contaminated primarily with carbon and oxygen desorbed from the wall, arising due to plasma-wall interaction, resulting in large central radiation losses. By the mid-1980s, many tokamaks were operating with graphite limiters and/or divertor plates. In addition, extensive laboratory tests/simulations on graphite had begun, primarily aimed at understanding the chemical reactions between graphite and hydrogenic plasmas, i.e. chemical erosion. Early laboratory results suggested that carbon would be eroded by hydrogenic ions with a chemical erosion yield of  $\approx 0.1$  C/D+, a yield several times higher than the maximum physical sputtering yield. At higher temperatures radiation enhanced sublimation (RES) might lead to further increase in the erosion rates of carbon. The ability of carbon to trap hydrogenic species in co-deposited layers became recognized.

Carbon has been the dominant choice as the plasma-wall facing material in the major tokamaks worldwide, with the exception of Alcator C-Mod at MIT, USA[180], which uses molybdenum, and FT-U at Frascati, Italy[181], which has used a variety of moderate to high Z materials. Many machines expanded the coverage of graphite to include virtually all of the vacuum vessel wall, in addition to the limiter/divertor plates (e.g. DIII-D[182]). In some cases, the inner wall was used as a large area limiter, and such structures, if carefully constructed, are able to handle enormous power loads, greatly exceeding the power limits of divertor plates (e.g. TFTR[183, 184, 185]).

Carbon has been favoured as a plasma facing material as it has excellent thermal properties. Further, carbon impurities in the plasma lead to only small increases in radiated power. Carbon and tungsten are the present candidates for use in the ITER divertor. The plasma compatibility of carbon and tungsten impurities in a burning plasma experiment has to be assessed from two different points of view. Firstly, the tolerable amount of carbon (concentration

$< 1.5\%$ ) in the plasma is limited by the dilution of the fuel (dilution limited) while that for tungsten (concentration  $< 2 \times 10^{-5}$ ) is limited by radiation losses in the plasma core. Secondly, carbon has a relatively high chemical sputtering yield (1 to 2%) at hydrogen (H, D, T) fluxes lower than  $10^{22} \text{ m}^{-2} \text{ s}^{-1}$ . This large source term of carbon could pollute the plasma beyond the above mentioned limit even when considering the relatively good impurity retention in a divertor.

Implantation of energetic particles into solids is fairly well understood[186]. Plasma facing materials are bombarded by energetic ions and neutrals from the plasma with energies of up to a few keV. As these energetic particles penetrate into a solid they lose their kinetic energy, mainly to electrons, and are deflected by collisions with atoms, thereby transferring kinetic energy to atoms in the solid. Some of the incident particles scatter back out of the material with a significant fraction of their initial energy, leaving the surface mainly as neutrals. The fraction of particles which backscatter is higher for lower incident energies and higher Z target materials and can exceed 50%[186, 187] Particles that do not backscatter eventually reach thermal energies within the material and settle into an atomic configuration, which has a local energy minimum. The depth distribution of these implanted particles depends on the energy and atomic number of the incident particles and on the target material.

Carbon differs from metals in the behavior of implanted hydrogen, mainly because of the C-H chemical reactivity. Implantation of hydrogen into carbon creates broken carbon bonds where hydrogen can be strongly bound through the formation of C-H chemical bonds. At low doses, hydrogen implanted into carbon is nearly all retained near the end of its implantation range. As the dose increases, the local hydrogen concentration increases until it reaches a saturation value that is about 0.4-0.5 H/C for carbon at room temperature and for incident H energy more than a few tens of eV. The saturation level decreases with increasing temperature[188, 189, 190, 191]. Additional hydrogen, implanted into a region already saturated, will either be released or transported further into the bulk.

The issues of bulk trapping of hydrogen and permeation of hydrogen into graphite beyond the range of implantation have been an interesting area of study for some time. The permeation depends strongly on the microstructure of the[192, 193, 194, 195]. In high density monocrystal graphite, there is essentially no permeation of hydrogen beyond the implantation zone, and the fluence dependence of H retention is essentially flat once the implantation zone is saturated [192, 195]. In high density pyrolytic graphite, some increase in H retention with increasing incident fluence beyond the saturation fluence is observed, which indicates hydrogen transport further into the bulk[192, 193, 195].

Some studies conclude that short range atomic diffusion of hydrogen through the graphite lattice occurs at high temperatures ( $> 1270 \text{ K}$ ) mainly along the basal planes [193, 196]. Recent measurements of CFC tiles from the JET divertor showed surprisingly large fractions of tritium in the bulk[197].

Beyond fusion, hydrogen adsorption and absorption on carbon materials play an important role in many areas such as semiconductor technology, astrophysics, carbon-based nanomaterials, carbon nanotubes and graphite nanofibers.

## 6.2 Motivation

As stated in the previous section, hydrogen carbon interaction can take place in various physical states of carbon, from purely crystalline, to partially damaged, to purely amorphous structural phases. This complex structural scenario of graphite is the main cause of uncertainty in the extrapolation of chemical sputtering yield to higher relevant fluxes. For example, starting from the macroscopic picture, graphite can be pictured as collection of granules of size around a few microns separated by voids which are typically of the order of  $0.1 \mu$ . The granules themselves are made up of crystallites (regions of crystal graphite) which are a few nanometers wide. The crystallites are separated by micro-voids which are a few Å wide.

To understand the dynamics of hydrogen interaction at various length scales one needs to adopt a multi-scale model, in which, transport properties (ex. diffusion coefficient) are computed at the atomistic level and used as parameters for further higher length scales. Typically, transport properties are computed using molecular dynamics[198] at varying temperatures and initial conditions. In order to understand the physical microscopic processes contributing to the macroscopic transport, it is essential to use the insights gained from the microscopic models (consisting of a few hundreds of atoms over a time scale of a few picoseconds), and from experiments, into modelling the hydrogen isotope reactions and transport at the meso-scale and further into the macro-scale (typically a centimeter over a time scale of several seconds). Therefore a multi-scale (both in length and time) approach to modelling plasma surface interaction is necessary.

In the past, classical molecular dynamics has been used, along with the empirical fitted hydrocarbon potential[199](Brenner), with the long range interaction correction term[200] to simulate hydrogen diffusion in crystalline graphite. It was observed that the interstitial does not show any cross graphene layer diffusion at any of the simulated graphite temperatures (150K - 900K). Diffusion with a short step-size was seen at all target temperatures, with a long step-size diffusion making its appearance at higher temperatures ( $\geq 450K$ ).

Since, the molecular dynamics results are only as good as the inter-atomic potential description and the empirical Brenner potentials was fitted to a limited set of hydrocarbons, it is believed that the Brenner potential will only work for a selective system and for some range of parameters[200, 201]. To analyze this further, we revisit this problem of hydrogen diffusion in crystalline graphite at the quantum mechanical level of theory using density functional formulation.

## 6.3 Ab initio MD

In the last ten years, *ab initio* molecular dynamics, which uses interatomic forces computed directly from the electronic structure rather than requiring an empirical interaction potential as input, has opened entirely new avenues in the investigation of chemically complex environments. In the Car-Parrinello (CP) MD method[35, 36, 202, 203] the electronic structure is modeled using the Kohn-Sham formulation[107] of density functional theory (DFT)[103], and the Kohn-Sham orbitals are represented using a plane wave basis. The key to the CPMD approach is that the plane wave expansion coefficients are treated as fictitious dynamical variables that are propagated adiabatically with respect to the nuclei. The net effect is that they describe the instantaneous ground state Born-Oppenheimer surface at each time step, so the need to solve the Kohn-Sham equations explicitly is avoided. DFT method had been successfully applied to study the bulk and surface properties for graphite in the past. Various methods

such as LDA and GGA have been tested for graphite. Also, studies have been performed in recent past to see how well the properties of graphite match with different pseudopotentials[204].

In the present work we perform first-principles atomistic scale calculation to study diffusion of hydrogen within the graphite planes (graphene). We also compare our results with earlier calculations performed by Warrier *et. al.* [198].

## 6.4 Hydrogen diffusion in bulk Graphite

In the present calculation, the simulation supercell consists of  $4 \times 4 \times 1$  primitive graphite cells. The supercell consists of two graphite planes with an interplanar separation of  $3.35 \text{ \AA}$  and shifted relative to each other as shown in Fig. 6.1. The labels A-E indicate the configuration of hydrogen atom between the graphite planes. Site-A refers to the H atom position in which H atoms is positioned between two carbon atoms of the consecutive planes. Site-B refers to the configuration in which H atoms bounded by C atoms from the bottom plane and sees the hollow hexagonal cage from the top plane. Sites C-E should be self-explanatory from Fig. 6.1.

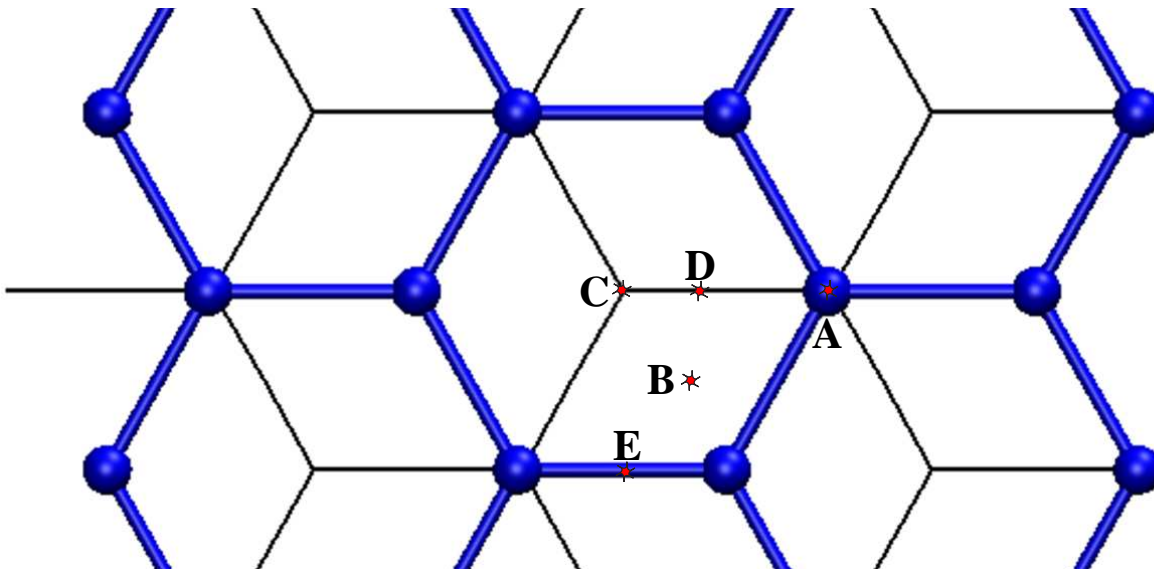


Figure 6.1: Hydrogen atom positions relative to C atoms and graphite planes.

Each graphite layer consists of 32 C atoms with the first nearest neighbor distance of  $1.412 \text{ \AA}$ , second neighbor distance of  $2.44 \text{ \AA}$  and third neighbor distance of  $2.83 \text{ \AA}$ , as can be seen in the radial distribution function shown in Fig. 6.2

The graphite supercell was chosen large enough to avoid H-H interaction between the simulation cell and the mirror images. In the present calculations the electron-ion interaction is described by the Troullier and Martins normconserving pseudopotentials, and the Kohn-Sham equations are solved using plane wave basis with kinetic energy up to 80 Ryd. The exchange-correlation energy is represented by the gradient corrected BLYP functional and Kleinman-Bylander integration scheme is adopted for the calculation of the nonlocal parts of the pseudopotential. As a first step towards the preparation of the initial sample, wavefunction optimization is performed using the ODIIS method. Further on, the optimized wavefunction was used to perform geometry optimization. This optimized geometry was used as the starting geometry for further calculations.

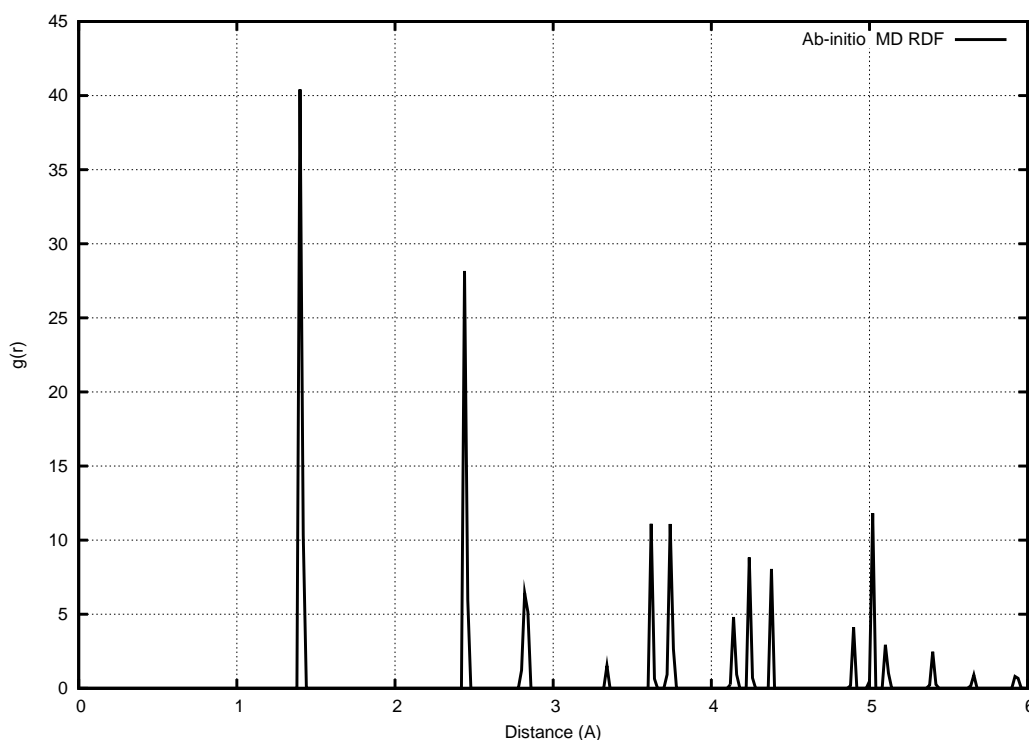


Figure 6.2: Radial distribution function of graphite sample used in *ab initio MD calculations*. Peaks around 1.412 Å, 2.44 Å and 2.83 Å refer to first, second and third nearest neighbours respectively

Freezing the C atom position from the optimized geometry, 1-D cuts through the potential energy hypersurface for various H atom positions between the two graphite planes is calculated. Figure 6.3 shows the potential energy curves for the H atom placed at various positions between two graphite layers, as a function of the normal distance of the H atom from the center of the two graphite layers. The labels A to E refer to various H atom positions shown in Fig. 6.1. The energies are given with respect to the case when the H atom is infinitely far from the graphite layers (i.e.  $V=0.0$  in Fig. 6.3).

It is seen from Fig. 6.3, that the potential energy at the center ( $Z=0.0$  Å) is relatively higher compared to the other H atom positions along the normal to the plane. This makes the position of H atom in the center to be less favorable. This can be attributed to the fact that there is small overlap between the  $s$  orbital of H atom and the  $p_z$  orbital of C atoms. The potential energy curve for site-A shows a well defined minimum at 0.5 Å from the center of the graphite layer and towards the C atom. The minimum refers to C-H bond, which has a dissociation energy of about 0.5 eV. For site-C, there is a well defined minimum towards the C atom and in the direction towards the hollow hexagonal cage the potential energy increases with increasing  $Z$ . The barrier to cross the graphite layer is extremely high and unlikely to happen. This is in agreement with the earlier studies which have shown that the probability for the H atom to cross the graphite plane is extremely low. The potential energy curves for other sites are higher compared to sites A and C. Site-D has a minimum towards the bottom plane because the H atom bonds with two carbon atoms from the bottom plane. However, as the H atoms moves from the bottom plane and towards the top plane the bonding changes and H atom bonds only with one C atom shown as A in Fig. 6.1. Potential energy curve for site-B is most symmetric and flat due to the fact

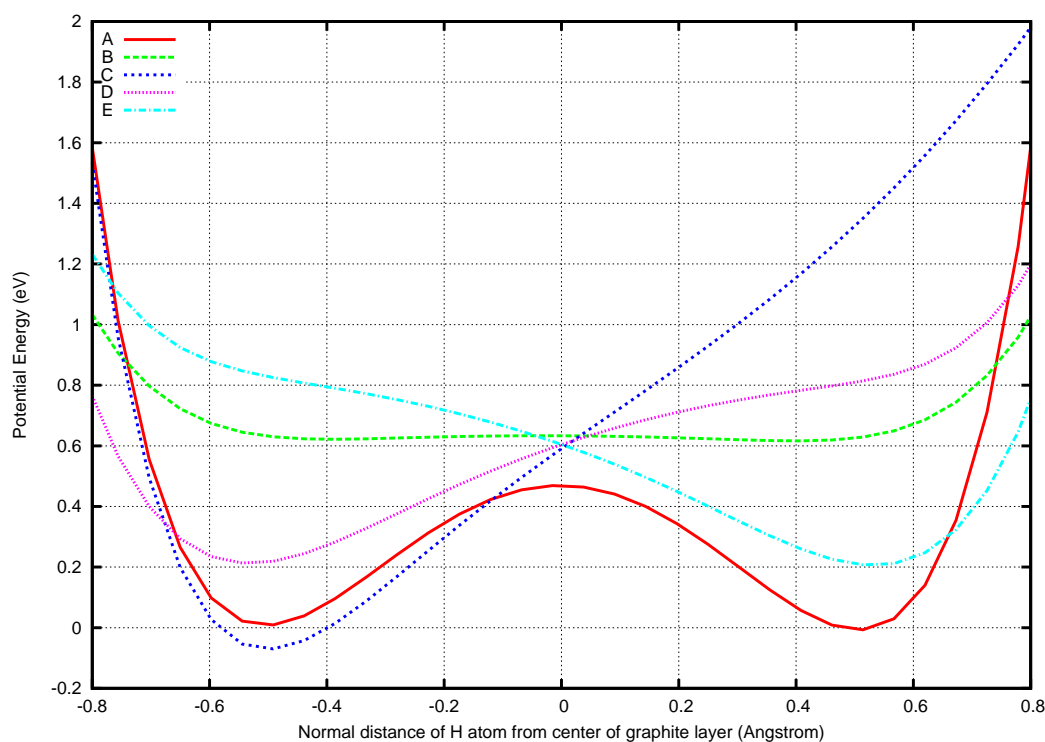


Figure 6.3: Calculated potential energy curves for the interaction of a H atom with graphite layers as a function of the normal distance from the center of the graphite layers. Labels A-E are explained in text and Fig. 6.1

that first neighbor C-H bond distances remain same at both ends. Site-E energy profile is the inverse of site-D due to inverse bonding character at two ends compared to site-D. Thus it is seen, that it is energetically favorable for the H atom to be found in one of the minima and not at the center of the graphite layer. Naively speaking, in case of a dynamical calculations the hydrogen atom to diffuse a small distance and then fall into one of the lower energy minima. However, if the temperature of the sample is high enough to break the C-H bond, then the H atoms would diffuse between the graphite planes, assisted by phonon vibrations.

This observation is contradictory to the earlier molecular dynamics calculations using empirical Brenner potential. The earlier calculations have shown that H atom diffuses almost freely at all temperatures. Diffusion of H atom takes place with short step-size at all target temperatures, with the long step-size diffusion making its appearance at higher temperatures ( $\geq 450K$ )[198]. To explain the differences between DFT calculations and classical MD calculations using empirical Brenner potential we calculate similar 1-D cuts using empirical Brenner potential which has been corrected to include long range interaction correction and graphite interlayer potential. The initial sample was equilibrated at 10K and frozen equilibrated geometry was used for calculating the potential energy curves shown in Fig. 6.4. The supercell in case of classical MD simulations consists of  $10 \times 12 \times 2$  unit cells, a total of 960 atoms. The simulation cell has a dimension of 25.56, 25.5235, and 13.396 Å in x, y, and z direction respectively. In order to be sure that the difference is not due to the structural differences between the graphite samples used in the two cases, we compare the radial distribution function of graphite sample used in case of classical MD simulations with that of *ab initio* geometry, shown in Fig. 6.4. Comparing Fig. 6.4 with Fig. 6.3 it is observed that the first, second, and third nearest neighbours distances are 1.42, 2.5 and 2.8 Å respectively. These can also be seen as the first three peaks in radial

distribution profile shown in Fig. 6.4. Thus the difference in energy profile cannot be attributed to the structural differences.

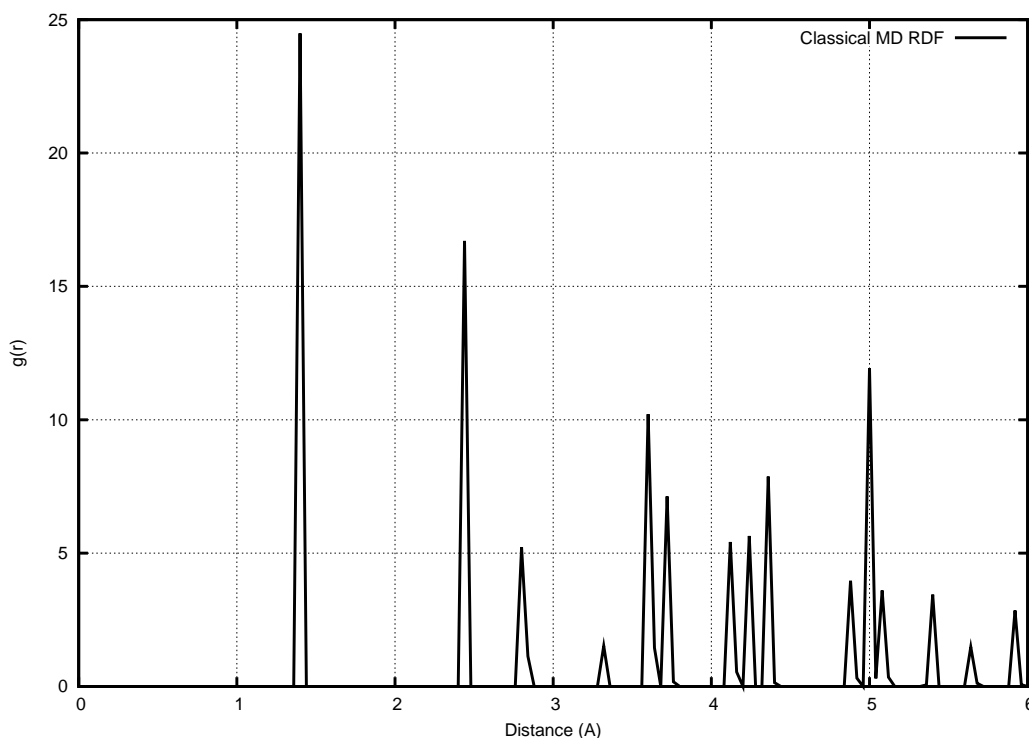


Figure 6.4: Radial distribution function for equilibrated graphite structure used in classical MD simulation. The supercell consists of 10x12x2 unit cells (960 atoms).

The potential energy curves for various sites are shown in Fig. 6.5. The labels A to E in Fig. 6.5 correspond to atomic site for H atom shown in Fig. 6.1.

The potential energy curves for empirical Brenner potential show a clear minima in the central region between the two graphite planes. This would explain the fact that the H atom between the two graphite plane can diffuse freely. However, in the direction towards the graphite planes, the H atom should cross the repulsive barrier shown in Fig. 6.5. This, make  $Z=0$ , central region between the graphite planes a favourable configuration for the H atom. We note that the potential energy curves shown in Fig. 6.5 and Fig. 6.3 can only be compared qualitatively, since the total energy term in DFT calculations also contains contribution from local pseudopotential energy, nonlocal pseudopotential energy and exchange-correlation energy. To compare the values of potential energy we must plot the electrostatic potential energy from *ab initio* DFT calculations. In Fig. 6.6 the DFT electrostatic potential energy is compared to the potential energy curve calculated using empirical Brenner potential. In the same figure the absolute value of DFT nonlocal pseudopotential energy contribution to the total energy is also shown. Note that the zero in potential energy, shown in the bottom figure, is the potential energy for each curve at  $Z=0$  (center between the two graphite planes). Comparing DFT electrostatic potential energy with empirical Brenner potential energy it is observed that the difference in potential increases as we move towards the graphite layer. However, the difference near the center is not too large.

It is interesting to note that the DFT electrostatic potential energy curve is flat in the central

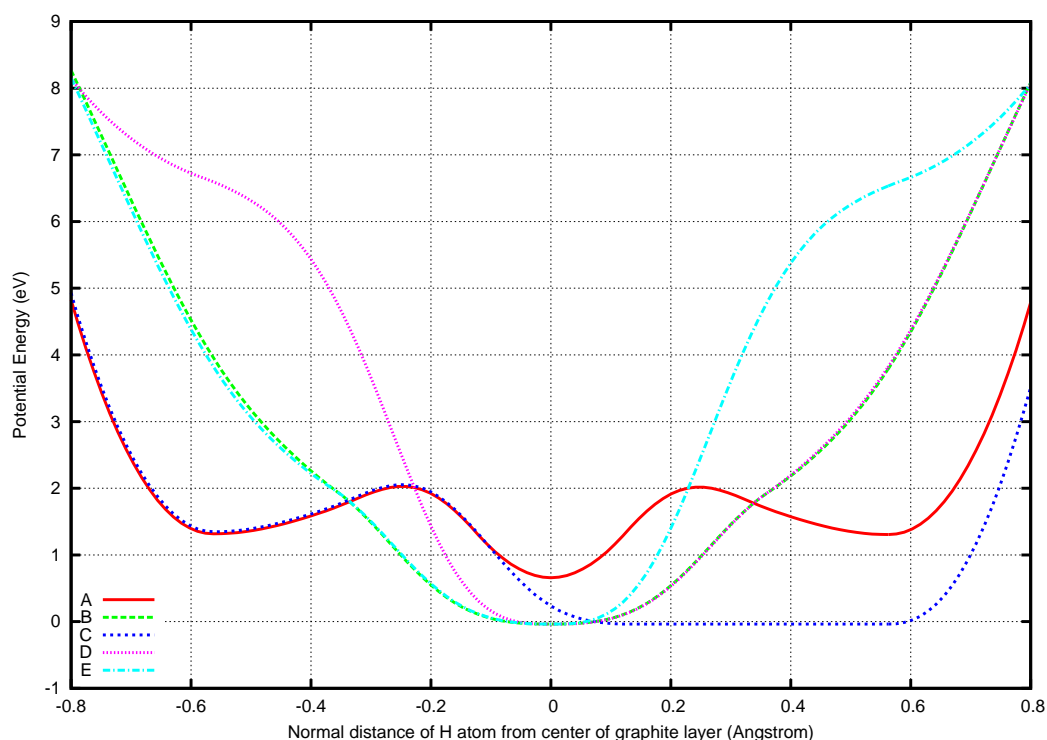


Figure 6.5: Potential energy curves for the interaction of a H atom with graphite layers calculated with Brenner potential as a function of the normal distance from the center of the graphite layers. Labels A-E are explained in text

region. However, if we add the DFT nonlocal pseudopotential energy (shown in the top part of Fig. 6.6) the potential energy in the central region becomes higher thus making it less favourable position for H atom. Thus, we conclude that contribution due to nonlocal energy component is critical in determining the lowest energy configuration for H atom between the two graphite planes.

### 6.4.1 Ab initio molecular dynamics

In order to study the diffusion of H atom in inter-layer graphite region we perform *ab initio* molecular dynamics at temperatures of 10 and 300 Kelvin. In the present calculations we perform molecular dynamics based on the Car-Parrinello formalism which postulates that the electronic and ionic relaxation can take place simultaneously. Car-Parrinello based on plane waves is used for the present simulation. These simulations require parameters (cutoff energies, characteristic frequencies for thermostats) and adequate pseudopotentials. In the present calculations we make use of normconserving pseudopotentials, which ensures that outside of a cutoff-radius, the pseudo-wavefunctions are identical to the real all-electron wavefunctions. The electron-ion interaction is described by Troullier and Martins (MT) pseudopotentials with gradient corrections (BLYP) and Kleinman-Bylander integration scheme is adopted for the calculation of the nonlocal parts of the pseudopotential. This is required because the normconserving MT pseudopotentials is different for different angular momentum i.e. nonlocal.

The system adopted for plane-wave CPMD simulations consists of orthogonal unit cell containing 64 carbon atoms of dimension 9.8, 8.5, and 6.7 Å in x, y, and z direction respectively. Temperature was controlled using the Nosé-Hoover scheme and kept constant at 10 K. A ther-

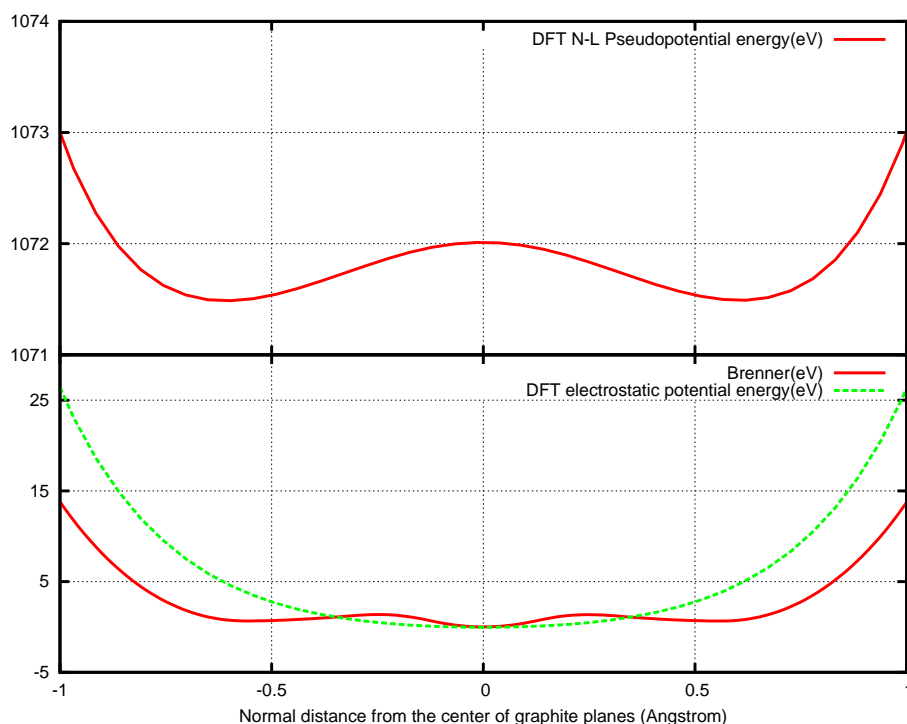


Figure 6.6: Bottom figure shows comparison on empirical potential energy with DFT electrostatic potential energy. The potential energy is set equal to zero independently at  $Z=0$ . Top figure shows the absolute value of DFT nonlocal pseudopotential energy contribution to the total energy.

mal Boltzmann distribution (10 K) was used in order to generate the initial velocity of H atom. The size of the box is large enough to insure the zero derivative of the potential energy and to avoid spurious interaction between neighboring cells. A set of plane waves (PW) with an energy cutoff between 60 Ry was used as the basis set for the KohnSham calculations (using the BLYP functional[205, 206]), with the TroullierMartins norm-conserving pseudopotential[114, 207] using the KleinmanBylander separation scheme[208] for the representation of the core electrons of the C atoms and for the hydrogen atom. Most importantly, the fictitious kinetic energy of the electrons is found to perform bound oscillations around a constant of 0.0013 a.u., i.e. the electrons do not heat up systematically during the simulation, this is an important measure for deviations from the exact Born-Oppenheimer surface.

The result of the dynamical calculation is shown in Fig. 6.7.

We observe that the fictitious kinetic energy of the electrons oscillates around a constant of 0.0013 a.u. and the temperature of the system stays around 10 K. We observe that the total energy for the system drops from the starting initial value and then remains constant. This is due to the fact that at the start of the simulation the hydrogen atom is placed at the center, between the graphite layers, and as the simulation evolves the H atom moves to a lower energy configuration, shown in Fig. 6.8.

This is consistent with the potential energy curves shown in Fig. 6.3, which show higher potential energy states between the two graphite layers ( $Z=0$  Å). We observed similar results for simulations performed at 300K.

Kushita *et. al.* performed experimental observation of diffusion of tritium in pseudo-

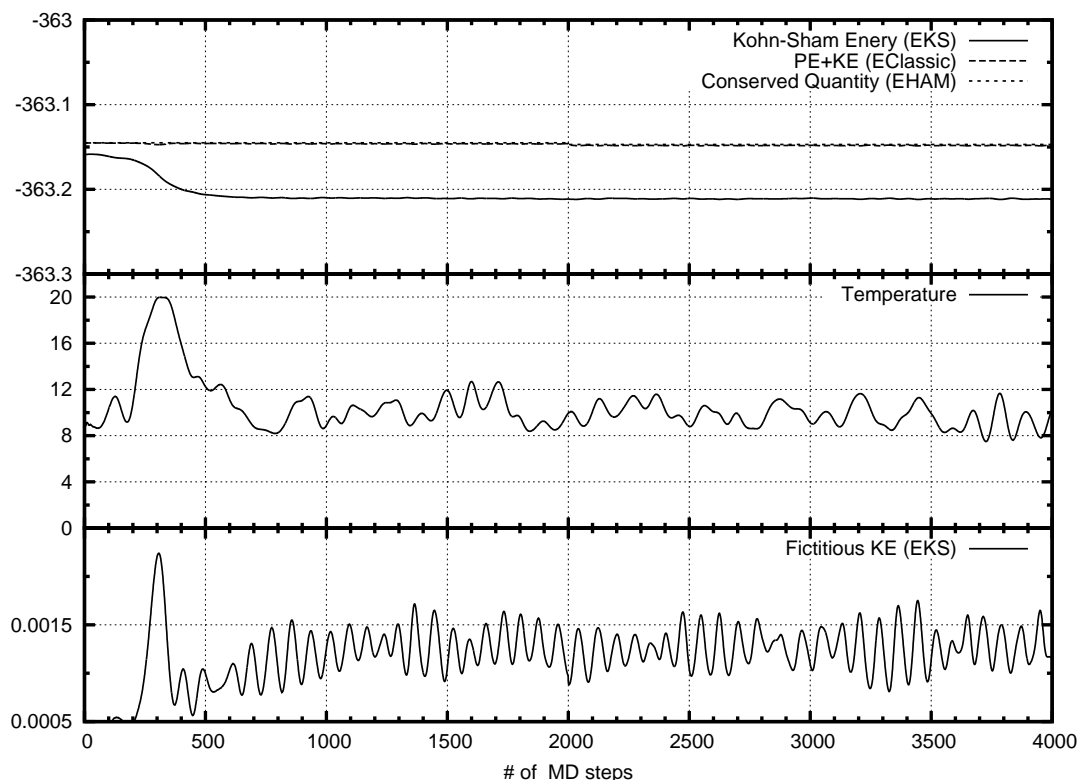


Figure 6.7: Evolution of fictitious kinetic energy, temperature and energy during the dynamical evolution of a H atom in graphite at 10K.

monocrystal graphite[196]. In their work, the graphite samples were implanted with tritium and annealed for long intervals at temperature ranging from 375 to 1975 Kelvin. However, results were reported only for temperatures higher than 800K. Their observations cannot be directly compared with the present theoretical work, since the graphite sample used in the experimental work is not perfectly crystalline and had cracks along the basal plane. It is possible that the tritium could have been lost by processes other than basal plane diffusion into the cracks.

The calculations performed in the present work indicated that the H atom would not diffuse between the graphene planes, at least up to 300K. The deepest potential well in Fig. 6.3 has a value of around 0.6 eV. However, this would be lowered at higher temperature and phonon assisted diffusion would be possible.

## 6.5 Hydrocarbon interaction with amorphous a-C:H surface

Co-deposition of hydrogen isotopes with carbon in fusion experiments is a topic of great importance and interest for a next-step device. Physical sputtering, chemical erosion, and chemical sputtering of carbon by hydrogen isotopes lead to release of hydrocarbon species which are transported to plasma shaded regions which results in deposition of co-deposited layers. It is believed that during the plasma operation, hydrocarbons would be adsorbed and again desorbed from the plasma facing materials. Initially the hydrocarbons would interact with the bare material, however, after a sufficient period of time a layer of hydrocarbons would be deposited and the further incoming hydrocarbon radicals would only see a amorphous hydrocarbon (a-C:H)

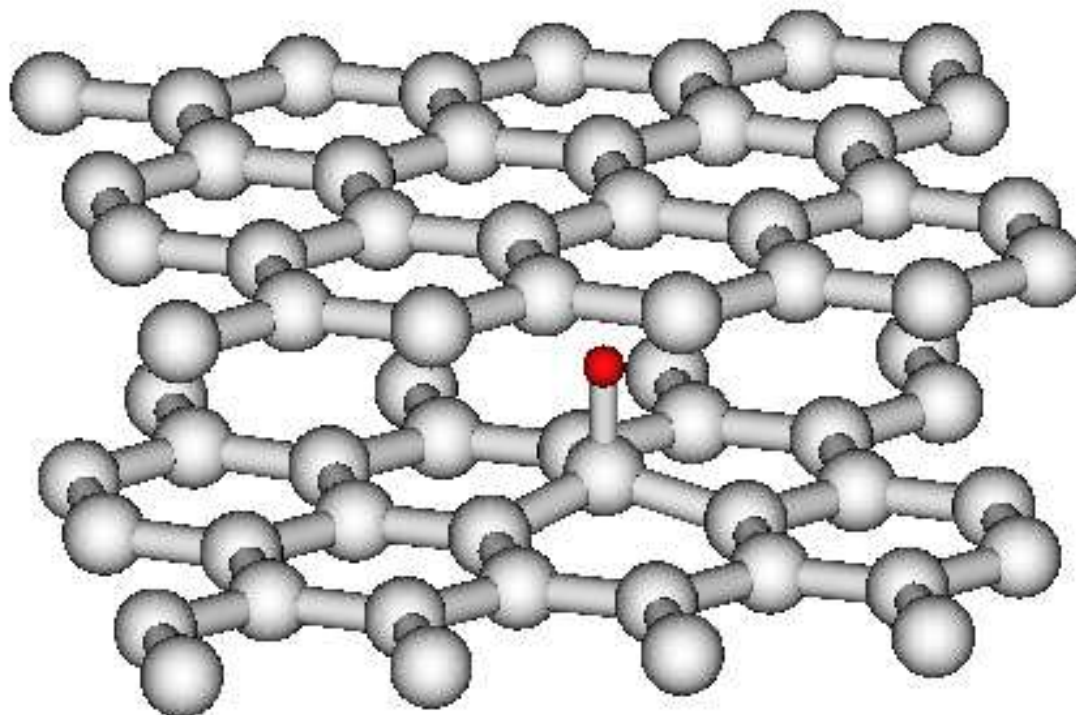


Figure 6.8: Frame slice showing sticking of H atom to one of the C atoms of graphite.

surface. The thickness of the co-deposited layer depends on large number of dynamical factors, such erosion yield, ion fluxes, sticking coefficients, etc.

To study interaction of hydrocarbon molecule and radicals with such co-deposited layer, we created a amorphous hydrocarbon structure of 200 atoms (76 H and 124 C atoms). Applying the DFT methods described in the earlier section we first optimized the wavefunctions for this system. The system under study has 572 electrons and a cubic supercell with dimension 15Å. However, it turns out that for such random structure DFT convergence is extremely difficult to achieve. We observed that even with the optimized wavefunctions the system quickly deviates from the Born-Oppenheimer surface.

Such complex systems can, however, be treated by the use of classical molecular dynamics with the use of empirical Brenner potential. Brenner potential is an empirical many-body potential developed for hydrocarbons that could model intramolecular chemical bonding in a variety of small hydrocarbon molecules. The potential function is based on Tersoffs covalent-bonding formalism with additional terms that correct for an inherent overbinding of radicals. Since the amorphous co-deposited structure pretty-much contains a random network of hydrocarbons, the dynamics of such a system would be governed by the local chemical bonding and has a diminishing long range order. Thus, we believe that the empirical potential would be able to treat the amorphous structure in a accurate way. More details and calculations are presented in chapter 7.

## 6.6 Subsumption

In the present chapter we successfully applied DFT method based on plane waves and normconserving pseudopotentials to study the diffusion of H atom in inter-layer graphite region. The *ab initio* molecular dynamics calculations at the temperatures of 10 and 300 Kelvin shows that the H atom quickly finds a low energy configuration by forming a chemical bond with the C atom of graphene. At these low temperatures the H atom is not able to overcome the barrier and thus is not able to diffuse. These results are drastically different from those obtained by the use of the empirical Brenner potential. The potential energy curves calculated using the Brenner potential for various atomic sites between the graphene planes show a flat region of potential resulting in a barrier free diffusion region. In case of DFT, the contribution due to non-local terms is responsible for the higher potential in the central region .

We also approach the problem of hydrocarbon molecule and radical interaction with co-deposited layers. The amorphous hydrocarbon structure of co-deposits can be characterized as “continuous random network” of small hydrocarbons. It turns out that it becomes extremely difficult to control adiabaticity of such systems in DFT calculations. However, since the dynamics is mostly governed by the local hydrocarbon bonding, the empirical Brenner potential developed for hydrocarbons is a suitable choice for studying such system. Thus, we perform classical molecular dynamics using empirical Brenner potential. With this approach we are able to treat system with much larger length scales. More details on this is presented in the next chapter (Ch.7).

# Chapter 7

## MD simulation of hydrocarbon interaction with a-C:H

### 7.1 Introduction

In the previous chapter we showed certain shortcomings of the Brenner potential for the study of H atom diffusion in crystalline graphite. These shortcomings are expected due to the fact that empirical Brenner potential was developed as many-body potential for hydrocarbons that could model intramolecular chemical bonding in a variety of small hydrocarbon molecules. The earlier application of Brenner potential to study crystalline graphite showed that the Brenner potential itself could not bind the carbons together to form graphite planes[200] and also inter-layer interaction was missing. However, since the Brenner potential is able to represent the chemical bonding for small hydrocarbons and the hydrocarbon co-deposits are continuous random network of small hydrocarbons, in which the inter-hydrocarbon-molecule play an important role, we believe that the Brenner potential would be suitable choice for simulating hydrocarbon co-deposits.

Hydrocarbon formation, transformation and deposition is a crucial problem for fusion devices[209]. The co-deposited layers, referred to the carbon and hydrocarbon layers deposited beyond the divertor and not in direct contact with the plasma, remain a serious issue due to hydrogen isotope retention in these layers[210]. Co-deposited layers with varying thickness have been observed in major machine operations, such as JET[211], TEXTOR[212] and ASDEX Upgrade[213, 214, 215, 216]. Small-scale experiments have been performed to study the transport and deposition of hydrocarbons in a steady-state plasma. One such experimental device is PSI-2 in which in-situ measurements on film growth for different plasma parameters[217, 218] were performed. The transport of injected gas molecules and the growth rates of the CH-film in PSI-2 were simulated with the 3D Monte Carlo code ERO[219] using three different reaction rate coefficients[220, 221, 222, 223]. However, the observed deposition rates in the experiments [218] are much higher than the values obtained by the ERO code[224]. A possible explanation for this discrepancy is the inaccuracy of the sticking coefficient data used in the ERO modelling. Presumably the energy dependence of the sticking coefficients plays an important role in predicting the right deposition rates.

### 7.2 Modelling

The HCParcas molecular dynamics code with the empirical Brenner potential[199] for hydrogen carbon interaction was used in the present study. Potential cutoff of 2.0 Å, for carbon-carbon interaction was used in the present calculation. High accuracy tight binding molecular dynamics simulations to calculate the sticking of molecules are computationally expensive and only suited for smaller systems [225].

An amorphous structure was prepared by starting with a random arrangement of hydrogen and carbon atoms (986 atoms in total) with a H:C-ratio of 0.66 with periodic boundary conditions in three dimensions. Four cycles of heating up to 3000K and subsequent cooling

down to 200K were applied to avoid local minima in the initial configuration. Switching to periodic boundary conditions only in the x and y directions and slowly heating to 300K was followed by very long runs (300 nsec) for relaxation in the z direction. This allows for sample preparation with a relaxed surface in the z-direction, to avoid artificial sputtering of atoms and molecules from the surface due to the relaxation of the surface rather than due to impinging molecules/radicals.

The incident hydrocarbon molecules and radicals studied in the present work are separately equilibrated for energies of the incident particles up to a maximum energy at which the molecule/radical are structurally stable. The equilibrated energy is the average kinetic energy of the incident molecules. This procedure allows the molecules to have rotational and vibrational degrees of freedom as they approach the sample surface. This approach represents the true physical picture as there are no means in the PSI-2 experiments to suppress the rotational-vibrational excitations. It is also known that the total energy gained by the molecules in the plasma would have translational, rotational and vibrational contributions[226, 227, 228, 229, 230, 231, 232]. Spectroscopic measurements of the vibrational states have been made in TEXTOR[226]. Also the distribution of the  $H_2$  molecules within the many vibrational levels of the electronic ground state has been studied theoretically[227, 228] and experimentally[229, 230, 231, 232]. Equilibration of the molecule/radical at the desired incident energy poses the limit to which the molecules can be accelerated. It is observed that at higher energies the molecules/radicals become structurally unstable and dissociate before approaching the surface. For a non-rotating linear molecule, such as CH, with translational freedom along the z-axis, vibrational modes are excited along the translational direction of motion. At higher energies, the vibrational amplitude is high enough to knock-off the lower mass hydrogen atom by the heavier carbon atom, thus dissociating the molecule. Structural instability is more pronounced in molecules such as  $C_2H_3$  and  $C_2H_5$  where hydrogen atoms are known to be “floppy”[233, 234, 235].

The starting position coordinates for the molecules and radicals are sampled uniformly over the surface and rotational freedom allows to sample all possible interaction configurations. This is specially important for linear molecules such as CH,  $C_2H$  and  $C_2H_2$  which otherwise would approach the surface at fixed orientations.

Ruzic and Alaman have already performed a similar molecular dynamics studies to calculate the reflection and dissociation coefficients of hydrocarbons [236]. However, the surface used in their work Ref.[236] was prepared by bombarding a graphite lattice with hydrogen atoms, which leaves lattice planes at every depth in the sample. Such surfaces can be compared with plasma-exposed surfaces[236], which are typical for carbon divertor target plates. The hard and soft surfaces in Ref.[236] have an average H to C ratio of 0.42 and 0.4 respectively, which differs significantly from the H to C ratio of 0.66, used in the present work. The H to C ratio of the present sample represents a co-deposited layer in fusion devices and is much softer than the surface used in Ref.[236]. In Fig. 7.1 the hydrogen to carbon ratio of the prepared sample as a function of the distance from the surface into the sample is presented.

Depth profile shown in Fig. 7.1 is plotted as function of distance into the surface.  $Z=0$  refers to the surface atoms with a bin width of 1.532 Å. The radial distribution function, shown in Fig. 7.2 indicates that the structure is amorphous as no clear peaks are visible beyond 2.0 Å. The first peak in the radial distribution function is the average H-H distance of around 0.8 Å and second peak around 1.2 Å is the average C-H and C-C distance.

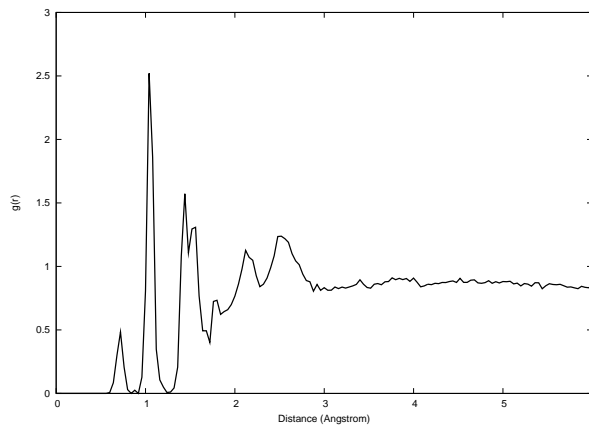
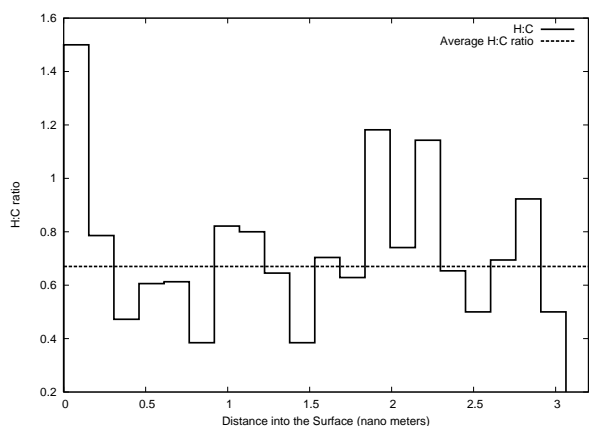


Figure 7.1: Depth profile showing H:C ratio; more details in text

Figure 7.2: Radial distribution function of amorphous hydrocarbon (a-C:H) sample.

## 7.3 Results and discussion

### 7.3.1 Reflection coefficients

The reflection coefficients for atomic carbon, molecules/radicals such as  $C_2$ , CH,  $CH_2$ ,  $CH_3$ ,  $CH_4$ ,  $C_2H$ ,  $C_2H_2$ ,  $C_2H_3$ ,  $C_2H_4$ ,  $C_2H_5$  and  $C_2H_6$  incident on the above described sample are reported in this section. In the present work, the reflection coefficient for a given species is defined as the ratio of the number of reflected atoms or molecules of this species to the number of incident molecules/radicals. In case of  $C_2H_x$  incidence, the total carbon reflection coefficient is calculated by summing-up the partial reflection coefficients of  $C_2H_{x'}$  reflected species and one-half of the  $CH_x$  reflection coefficients. For the sake of clarity, statistical uncertainty in the calculated reflection coefficient is shown only for selected species.

Here, the influence of the rotational freedom of the incident molecule on the reflection coefficient from the amorphous hydrocarbon surface has to be considered. Non-rotating hetero-nuclear linear molecule (ex. CH) impinging on the surface can have many possible orientations with respect to the normal of the surface. Two extreme orientations for CH are with C down (i.e. the bond axis for the molecule is parallel to the normal to the surface and the molecule approaches the surface with the carbon atom towards and the hydrogen atom away from the surface) and H down (i.e. the hydrogen atom is towards the surface and the carbon atom is positioned away from the surface). It can be seen from Fig. 7.3 that

the reflection coefficient for the case with C down is lower (higher sticking) than the case with H down. Higher carbon sticking is favoured due to open carbon bonded chains at the surface which act as trap sites for carbon bonding. Also higher concentration of hydrogen on the surface contributes to higher reflection in the case of the H down orientation. The region between the upper and lower curve gives an estimate of the spread in the reflection coefficient due to various possible orientations at the time of molecule impact. The average reflection coefficient of a rotating CH molecule incident on the surface is expected to lie within the band with a possible deviation due to statistical errors.

Fig. 7.4 shows the energy dependence of reflection coefficients for atomic carbon and  $C_2$  incident on an amorphous hydrocarbon surface for normal incidence. Normal incidence was chosen as there is no known angular dependence of the reflection coefficient as a function of incident energy[236]. The calculated reflection coefficients of 0.43 at thermal energies and 0.042

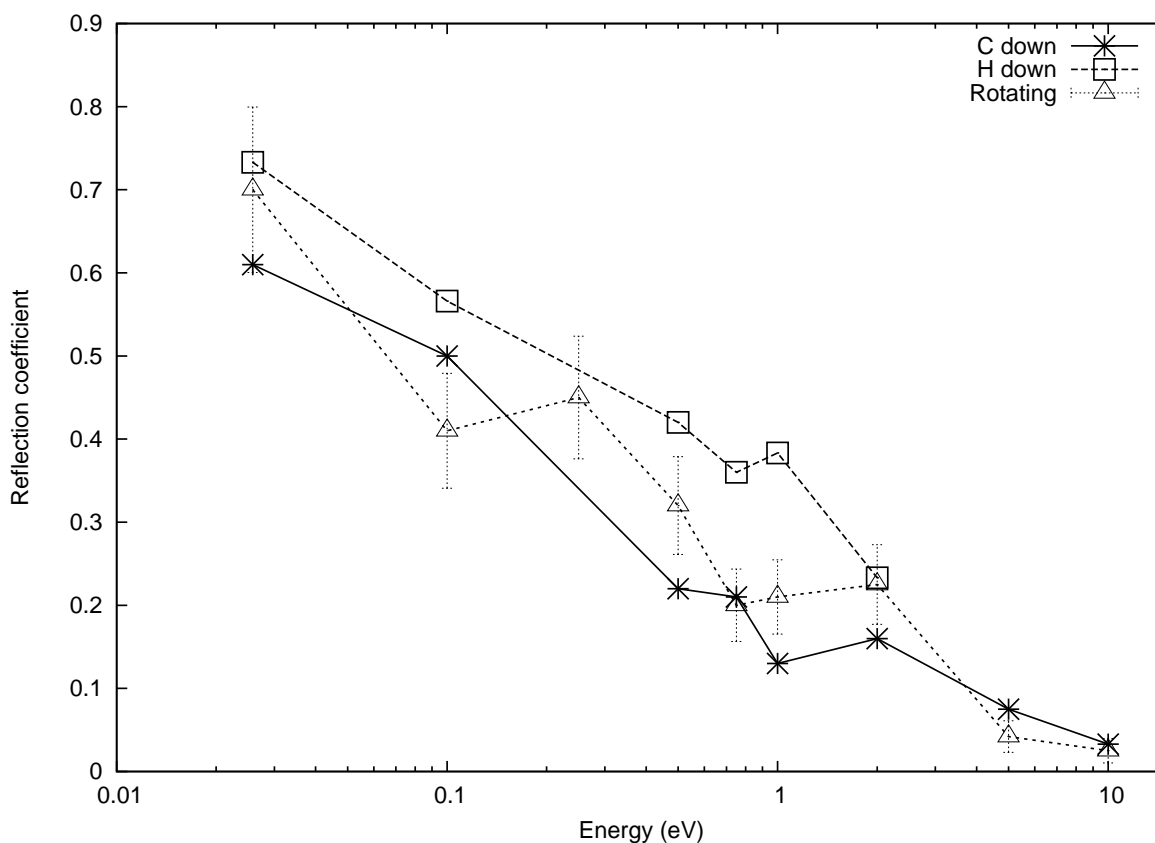


Figure 7.3: Spread in reflection coefficient due to different orientation of CH incidence.

at 10 eV for atomic carbon reflection, compared with Ref.[236] are lower by 10 to 17% respectively, but show the same general trends. This difference in the reflection coefficients is attributed to the higher H to C ratio in the surface layer used in the present calculations, which makes the surface softer compared with the surface used in Ref.[236]. A softer surface allows for deeper penetration into the surface, thus increasing the sticking probability. The probability of hydrogen release during C<sub>2</sub> bombardment from the surface increases from less than 1% at 5 eV to 15% at 10 eV. The probability of complex hydrocarbon release at 10 eV is less than 1%.

Similar to the above observation, the C<sub>2</sub> reflection coefficient of 0.4 (Fig. 7.4) at thermal energy is lower than the value of 0.5, and follows the same decreasing trend as reported in Ref.([236]) However, C<sub>2</sub> shows a high probability for hydrogen capture from the surface, thus strongly lowering its reflection probability as explained in more detail in section 7.3.4.

### 7.3.2 Reflection coefficients for CH<sub>x</sub> (x=1-4)

In Fig. 7.5 reflection coefficients of CH, CH<sub>2</sub>, CH<sub>3</sub> and CH<sub>4</sub> as a function of energy is shown. The general trend shows that the reflection coefficient decreases with increasing energy. CH<sub>4</sub> shows a 100% probability of reflection up to 0.75 eV. In the energy range between 2 and 5 eV all molecules show a decrease in reflection coefficients. This can be explained by studying the break-up pattern of these molecules, discussed in section 7.3.4.

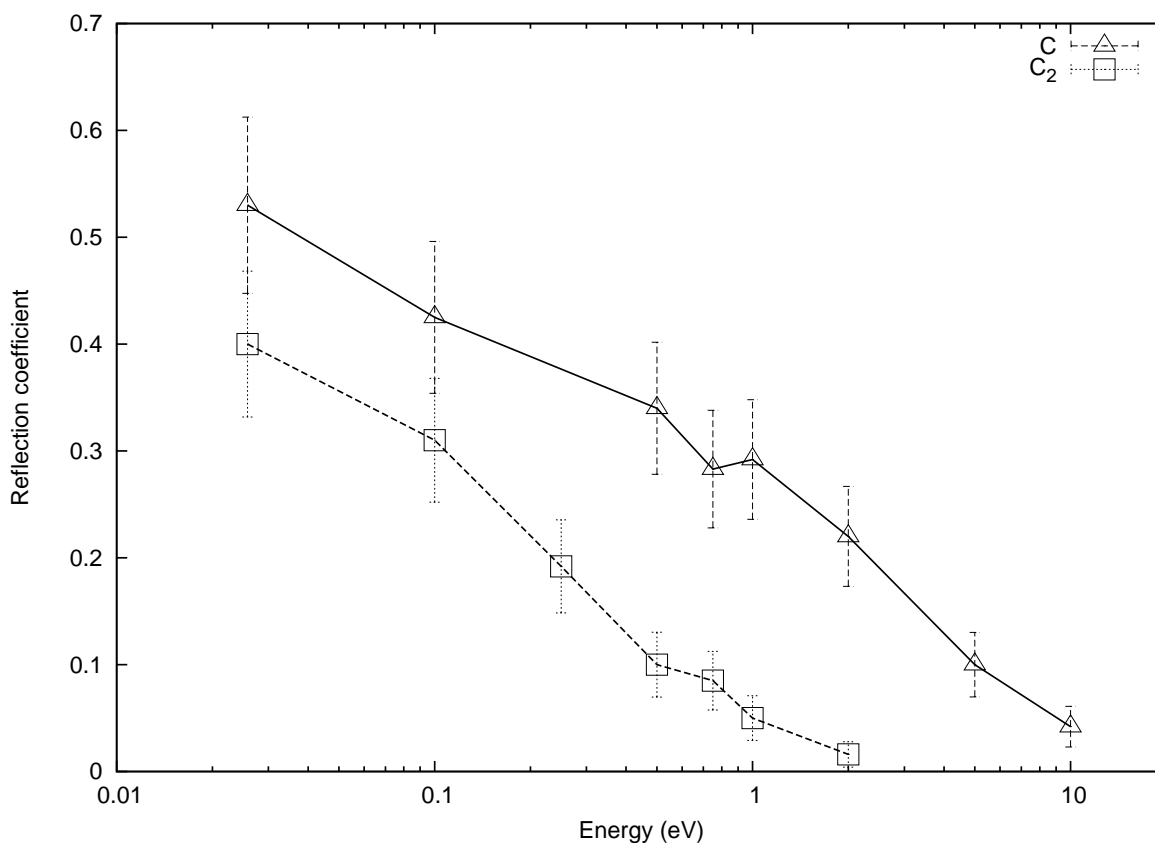


Figure 7.4: Reflection coefficient for atomic carbon and carbon dimer. For C<sub>2</sub>, the bond axis of the molecule is parallel to the normal to the surface.

### 7.3.3 Reflection coefficients for C<sub>2</sub>H<sub>x</sub> (x=1-6)

Reflection coefficients for C<sub>2</sub>H<sub>x</sub> (x=1-6) presented in Fig.(7.6) show that they are higher for molecules with an even number of hydrogen atoms compared to those with an odd number. This is expected, as hydrocarbons with an odd number of hydrogen atoms are radicals and have higher reactivity with surface atoms.

C<sub>2</sub>H<sub>2</sub>, C<sub>2</sub>H<sub>4</sub> and C<sub>2</sub>H<sub>6</sub> show 100% chance of reflection in the energy range from thermal to 0.5 eV. The reflection of C<sub>2</sub>H<sub>2</sub> decreases marginally to 92% at 1 eV. Beyond 1 eV the reflection of C<sub>2</sub>H<sub>6</sub> and C<sub>2</sub>H<sub>4</sub> rapidly decreases with increasing energy. The decrease in the reflection coefficient can be partly attributed to higher sticking. The other factor responsible for the decrease is the reflection of the incident molecule in modified hydrocarbon forms due to hydrogen/carbon capture/dissociation. Radicals, such as, C<sub>2</sub>H, C<sub>2</sub>H<sub>3</sub> and C<sub>2</sub>H<sub>5</sub> show a steep drop of the reflection coefficient due to their higher reactivity with the surface atoms. C<sub>2</sub>H<sub>3</sub> is known to have a “floppy” structure with the hydrogen atoms tunneling between two carbon atoms[233, 234]. This molecule has a low threshold for hydrogen dissociation and hence can not be stabilized at higher energies than 1.0 eV. The reflection probability for C<sub>2</sub>H<sub>3</sub> decreases from 90% at thermal energy to 37% at 0.75 eV.

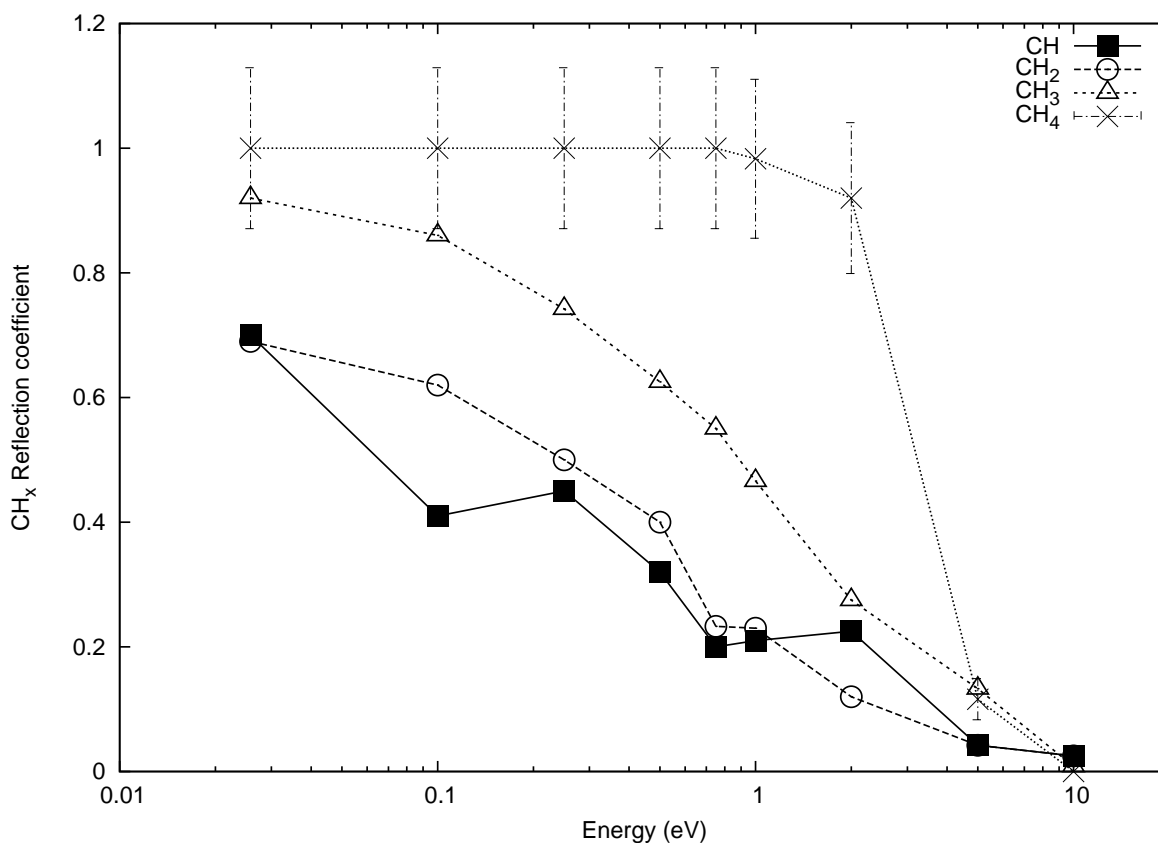


Figure 7.5: Reflection coefficient for  $\text{CH}_x$  ( $x=1-4$ ) bombardment on amorphous hydrocarbon surface.

### 7.3.4 Break-up pattern

The decrease in the reflection coefficient of the incident molecules/radicals as seen in Fig. 7.5 and Fig. 7.6 can be explained by studying the break-up pattern in the hydrocarbon reflection process. As an example, shown in Fig. 7.7, the reflection coefficient and break-up pattern for  $\text{C}_2\text{H}_6$  is discussed. The  $\text{C}_2\text{H}_6$  molecule shows 100% reflection up to energy of 1 eV with no secondary hydrocarbon sputtering.  $\text{H}_2$  release observed over the entire energy range is due to the release of weakly bonded hydrogen atoms in the sample. Surface relaxation triggers the release of such atoms and is not a consequence of direct chemical interaction. Secondary sputtering of  $\text{H}_2$  molecules will be different for other calculations, as the surface prepared with different methods and a different H to C ratio will relax differently. Above 1 eV energy, other than the incident  $\text{C}_2\text{H}_6$  reflection, the most probable mechanism is the reflection of  $\text{C}_2\text{H}_5$  where one H bond (CH bond energy = 4.3 eV) is likely to be broken with a probability of 2.5%. At 5 eV, two hydrogen atoms are likely to be stripped off the incident molecule, resulting in a 4.2% chance of  $\text{C}_2\text{H}_2$  reflection. The carbon-carbon bond dissociation (C-C bond energy in ethane = 3.94 eV) has a probability of 9.2% which results in the increased release of  $\text{CH}_3$  at 5 eV.

Atomic carbon, incident on the surface is either purely reflected as atomic carbon or absorbed at the surface. Above 5 eV incident energy, the energy dumped by the incident atom/molecule supported by higher H to C ratio in surface layer (Fig. 7.5) favours sputtering of hydrogen atoms from the surface.

Carbon dimer and  $\text{CH}_x$  ( $x=1-4$ ) are purely reflected below 0.75 eV. Around 1 eV, there

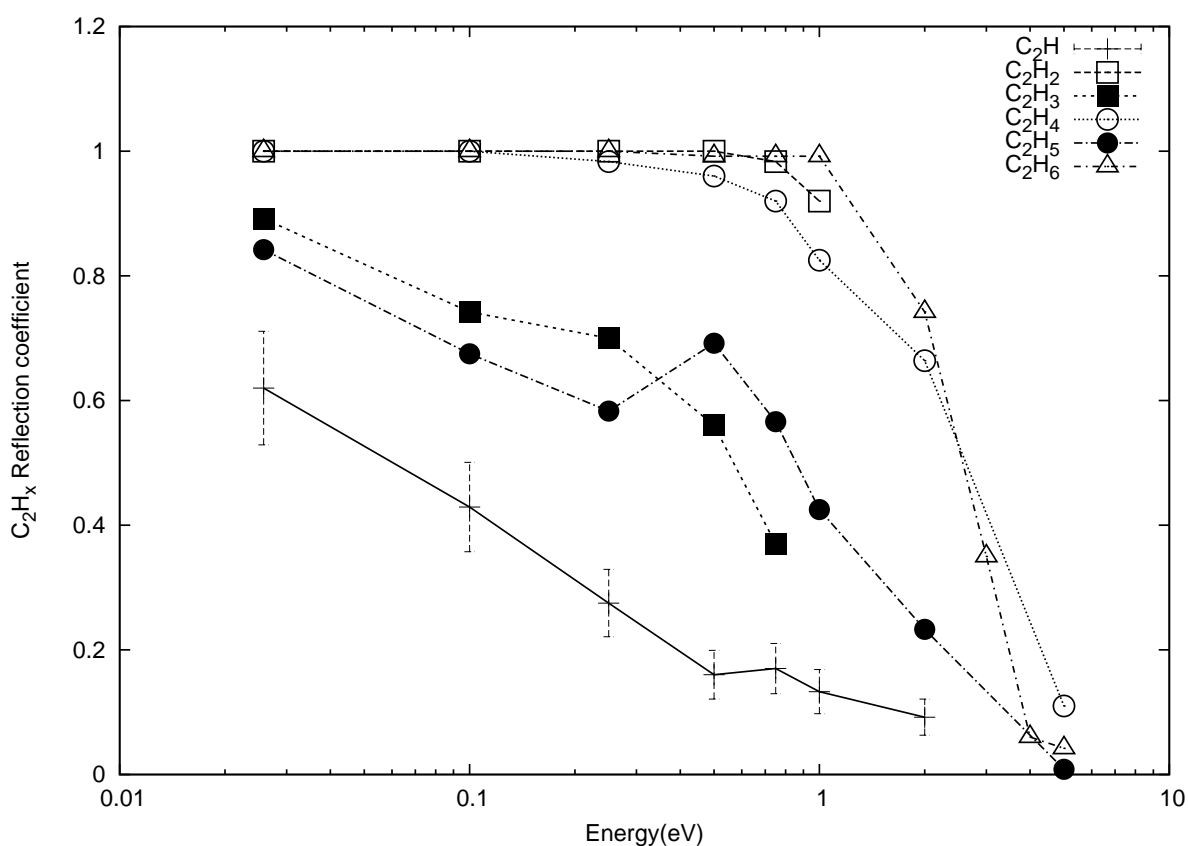


Figure 7.6: Reflection coefficient for  $C_2H_x$  ( $x=1-6$ ) bombardment on amorphous hydrocarbon surface.

is an increased probability for  $C_2$ ,  $CH$ ,  $CH_2$  and  $CH_3$  to capture a hydrogen atom from the surface due to the large number of available hydrogen atoms on the surface layer. However, in case of  $CH_4$  incidence, the probability to strip one hydrogen atom from the incident molecule and reflect as  $CH_3$ , increases from 2.5% at 2 eV incident energy to 12.5% at 5 eV. Above 1 eV more complex hydrocarbons with two or three carbon atoms are released from the surface.  $C_2H_x$  ( $x=1-6$ ) show similar distribution in reflected molecules. General trends observed in the break-up pattern for  $C$ ,  $C_2$ ,  $CH_x$  ( $x=1-4$ ) and  $C_2H_x$  ( $x=1-6$ ) are presented in more detail in Ref.[237]

## 7.4 Subsumption

The reflection coefficients of atomic carbon,  $C_2$ ,  $CH$ ,  $CH_2$ ,  $CH_3$ ,  $CH_4$ ,  $C_2H$ ,  $C_2H_2$ ,  $C_2H_3$  and  $C_2H_4$  show a decreasing trend with increasing incident energy. This trend in the reflection coefficient also holds for surfaces with H to C different than 0.66[236]. However, numerical values of the reflection coefficient and reflection break-up pattern are sensitive to the hydrogen and carbon stacking in the sample surface.

Reflection coefficient for  $CH_x$  ( $x=1-4$ ) increases with increasing number of hydrogen atoms. At energies above 1 eV these molecules have a higher probability to either capture a hydrogen atom from the surface or to break a hydrogen bond from the molecule. Above 2 eV carbon reflection is in the form of complex hydrocarbon emission with two or three carbon atoms. Also

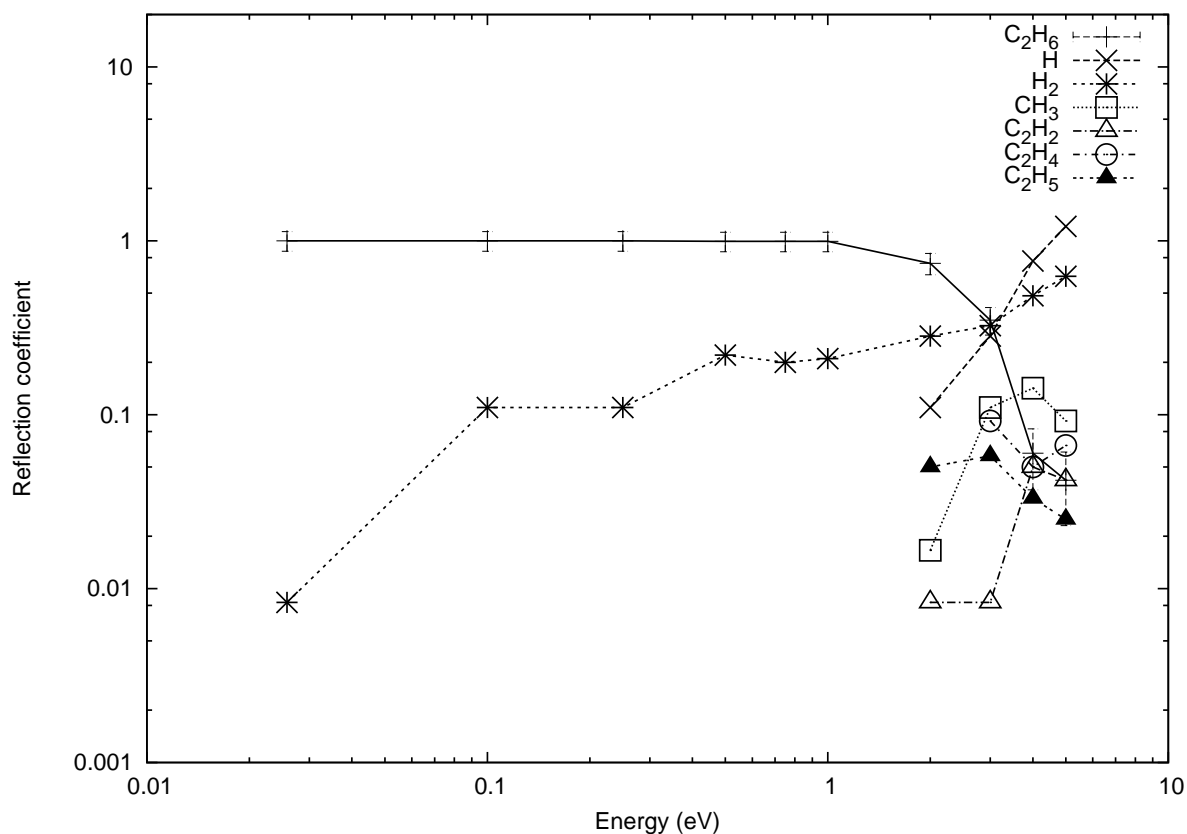


Figure 7.7: Break-Up pattern for  $C_2H_6$  bombardment on amorphous hydrocarbon surface.

the reflection coefficient increases as the hybridization changes from  $sp$  to  $sp^3$ .  $C_2H_x$  ( $x=1-6$ ) have higher reflection coefficient for an even number of hydrogen atoms and a lower reflection coefficient for odd number of hydrogen atoms. Above 1 eV, hydrogen capture or break-up is dominant in the reflection pattern. With increasing energy more than one hydrogen atom or carbon-carbon bond break-up is observed. The energy dependence of the reflection coefficient was used in the ERO modelling of PSI-2 by Bohmeyer *et al.*[218].

## Chapter 8

# Conclusions and Summary

The work presented in this dissertation is motivated by the atomistic multiscale approach to model hydrocarbons under varying conditions such as those in the low-temperature plasmas, interstellar medium and in the plasma-wall interaction region. Such varying conditions impose a need to simulate hydrocarbons at different length scales. At the smallest length scale, small hydrocarbon molecules, molecule-, radical-molecule interaction are of interest. For such small molecules, most accurate quantum-mechanical calculations such as the Hartree-Fock method followed by post-HF methods are known to recover close to 100% of the true energy.

In the present work, methods developed by Braams and co-workers was used to develop potential energy surfaces (PES) for two carbocations, namely  $\text{C}_2\text{H}_3^+$  and  $\text{C}_2\text{H}_5^+$ . The PES has the form of a many-body (cluster) expansion and used basis functions that were made to satisfy the criterion of invariance under interchange of like nuclei, with coefficients fitted to *ab initio* calculations. In order to scan the nuclear configuration space and generate configurations for the fit, dynamical sampling was performed using molecular dynamics (MD) and diffusion Monte Carlo (DMC) calculations, thus localised sampling was avoided. Potential energy for each of these nuclear configurations was computed at the most accurate quantum-mechanical level of theory. Restricted coupled cluster method with singles and doubles and perturbative treatment of triples [RCCSD(T)] and the augmented correlation-consistent polarized valence triple zeta (aug-cc-pVTZ) was used for  $\text{C}_2\text{H}_3^+$  and MØLLER-PLESSET (MP4) perturbation theory with aug-cc-pVTZ was used for  $\text{C}_2\text{H}_5^+$ . The choice of method was based on the time estimate needed for each individual runs and on the total number of configurations that would be needed to achieve a reasonable fit. The PES for  $\text{C}_2\text{H}_3^+$  had a root mean square (rms) fitting error of  $4.67 \times 10^{-4}$  Hartree ( $\approx 0.3$  kcal/mol) for the 4928 configurations in the range from 0.0 to 0.1 Hartree (0 to 62.7 kcal/mol) above the global minimum. For configurations which were in the range of 0.1 to 0.2 and 0.2 to 0.5 Hartree above the global minimum, the rms errors was  $1.66 \times 10^{-3}$  and  $4.92 \times 10^{-3}$ , respectively. A total number of 19617 converged high-level *ab initio* calculations were used for generating the PES for  $\text{C}_2\text{H}_5^+$  with a root mean square (rms) fitting error of  $2.2 \times 10^{-3}$  Hartree over all configurations ( $\approx 1.4$  kcal/mol). The global and local minima and other important stationary points on the fitted surface were accurately identified, although these points were not explicitly included in the fitting procedure. The stationary points were found to be in excellent agreement with direct *ab initio* calculations and also with the published values.

The fitted PES were used to perform normal mode analysis (NMA) and vibrational self-consistent field (VSCF) followed by virtual configuration interaction (VCI) to obtain anharmonic frequencies. NMA and full-dimensional calculations of vibrational energies for  $\text{C}_2\text{H}_3^+$  and  $\text{C}_2\text{H}_5^+$  using the “single-reference” vibrational methods show excellent agreement with the direct *ab initio* calculations and with published values, in one case also with experimental value. Tunneling splittings for the fundamental excitations and zero point energy (ZPE) was calculated using the “reaction path” Hamiltonian. The barrier separating the global minimum bridged structure and the Y-shaped one for  $\text{C}_2\text{H}_3^+$  was calculated to be equal to  $150 \text{ cm}^{-1}$ . Extending the semi-local potential energy surface a global potential energy surface was generated for  $\text{C}_2\text{H}_3^+$ .

In the global fit, 13672 *ab initio* points for  $C_2H_3^+$  complex region, 7327 for  $C_2H^+ + H + 2$ , 6008 for  $C_2H_2^+ + H$ , 7357 for  $C_2H_2 + H^+$ , 7610 for  $CH_2 + CH^+$ , and 500 *ab initio* points for  $CH + H + CH^+$  were used. It was observed that the PES was able to correctly dissociate to the asymptotic potential energy value of the fragments. It was identified that the charge exchange reaction leads to surface crossing and multi-reference calculations were performed to identify the ground state dynamics. The general chemical dynamics program VENUS96 was modified to perform reaction dynamics ( $C_2H^+ + H_2 \rightarrow C_2H_2^+ + H$ ) on the fitted global surface. Long lived trajectories are observed, which require much more computational effort beyond the scope of this work.

The high accuracy electronic structure methods scale badly with system size and are intractable for a system with few hundreds of atoms. The method of choice for such systems is the Density functional theory. Due to the reaction of thermalised ions (mostly hydrogen) implanted within the surface of plasma facing material, hydrogenation of carbon atoms takes place, leading to formation of hydrocarbon complexes and trapping of hydrogen atom within crystalline carbon. Modelling the diffusion process of such trapped species requires the simulation of a system with few hundreds of atoms. Density functional theory based on plane waves and normconserving pseudopotentials was used in the present work. *Ab initio* dynamics was performed to study the diffusion of atomic hydrogen implanted and trapped within crystalline graphite. An important difference has been observed between *ab initio* dynamical calculations and the classical molecular dynamics simulations using the famous empirical Brenner potential. The *ab initio* molecular dynamics calculations at 10 and 300 K showed that the H atom quickly finds a low energy configuration by forming a chemical bond with the C atom of graphene. At these low temperatures the H atom was not able to overcome the barrier and thus was not able to diffuse. These results were found to be drastically different from those obtained by the use of the empirical Brenner potential, which showed free diffusion. Potential energy curves were calculated using DFT and Brenner potential for various atomic sites between the graphene planes. Brenner potential showed a flat region of potential resulting in a barrier free diffusion region, however, DFT has higher potential energy region in the center. In case of DFT, the contribution due to non-local terms was found to be responsible for the higher potential in the central region.

Finally, to simulate the hydrocarbon co-deposits and interaction of hydrocarbon radicals and molecules with the amorphous surface, large length scale classical molecular dynamics simulations were performed. The reflection/sticking coefficients for atomic carbon,  $C_2$ , CH,  $CH_2$ ,  $CH_3$ ,  $CH_4$ ,  $C_2H$ ,  $C_2H_2$ ,  $C_2H_3$  and  $C_2H_4$  was calculated on an amorphous hydrocarbon sample. The reflection coefficients show a decreasing trend with increasing incident energy. However, numerical values of the reflection coefficient and reflection break-up pattern were found to be sensitive to the hydrogen and carbon stacking in the sample surface. Reflection coefficient for  $CH_x$  ( $x=1-4$ ) increased with increasing number of hydrogen atoms. At energies greater than 1 eV, the molecules had a higher probability to either capture a hydrogen atom from the surface or to break a hydrogen bond from the molecule. Above 2 eV, carbon reflection was in the form of complex hydrocarbon emission with two or three carbon atoms. Also the reflection coefficient increased as the hybridization changed from *sp* to *sp*<sup>3</sup>. For  $C_2H_x$  ( $x=1-6$ ), reflection coefficient for molecules with an even number of hydrogen atoms was higher compared to the ones with odd number of hydrogen atoms. Above 1 eV, hydrogen capture or break-up was found to be dominant in the reflection pattern. With increasing incident energy more than one hydrogen atom or carbon-carbon bond break-up was observed.

Hydrocarbons are still a complex problem and this thesis tries to contribute to a better

fundamental understanding utilizing a multi-scale approach: small systems were studied with *ab initio* quantum methods (Hartree-Fock and post Hartree-Fock, DFT) and larger systems with classical MD.

# Bibliography

- [1] R. Behrisch (ed). *Sputtering by Particle Bombardment I, Topics in Applied Physics, Vol. 47*. Springer, Berlin, 1981.
- [2] R. Behrisch (ed). *Sputtering by Particle Bombardment II, Topics in Applied Physics, Vol. 52*. Springer, Berlin, 1983.
- [3] W.O. Hofer and J. Roth (eds). *Physical Processes of the Interaction of Fusion Plasmas with Solids*. Academic Press, London, 1996.
- [4] J. Roth and C. García-Rosales. Analytic description of the chemical erosion of graphite by hydrogen ions. *Nuclear Fusion*, 36(12):1647–1659, 1996.
- [5] J. Küppers. The hydrogen surface chemistry of carbon as a plasma facing material. *Surface Science Reports*, 22(7–8):249–322, 1995.
- [6] A. Horn, A. Schenk, J. Biener, B. Winter, C. Lutterloh, M. Wittmann, and J. Kupperts. H-atom impact-induced chemical erosion reaction at c-h film surfaces. *Chemical Physics Letters*, 231(2-3):193 – 198, 1994.
- [7] M. Wittmann and J. Kupperts. A model of hydrogen impact induced chemical erosion of carbon based on elementary reaction steps. *Journal of Nuclear Materials*, 227(3):186 – 194, 1996.
- [8] C. García-Rosales. Erosion processes in plasma wall interactions. *Journal of Nuclear Materials*, 211:202–214, (1994).
- [9] B. Lipschultz, X. Bonnin, G. Counsell, A. Kallenbach, et al. Plasma&ndash;surface interaction, scrape-off layer and divertor physics: implications for ITER. *Nuclear Fusion*, 47(9):1189–1205, 2007.
- [10] E. Herbst and W. Klemperer. The Formation and Depletion of Molecules in Dense Interstellar Clouds. *Astrophysical Journal*, 185:505–534, October 1973.
- [11] S. Atreya. Planetary science: Titan’s organic factory. *Science*, 316(5826):843–845, 2007.
- [12] J. H. Jr. Waite, H. Niemann, R. V. Yelle, W. T. Kasprzak, T. E. Cravens, J. G. Luhmann, et al. Ion Neutral Mass Spectrometer Results from the First Flyby of Titan. *Science*, 308(5724):982–986, 2005.
- [13] D. T. Young, J.J. Berthelier, M. Blanc, J.L. Burch, et al. Cassini plasma spectrometer investigation. *Space Science Reviews*, 114(1-4):1 – 112, 2004.
- [14] J. H. Jr. Waite, D. T. Young, T. E. Cravens, A. J. Coates, F. J. Crary, B. Magee, and J. Westlake. The process of tholin formation in titan’s upper atmosphere. *Science*, 316(5826):870–875, 2007.

- 
- [15] P. H. Hauschildt and E. Baron. A 3d radiative transfer framework i. non-local operator splitting and continuum scattering problems. *Astronomy & Astrophysics*, 451(1):273 – 284, 2006.
- [16] P. H. Hauschildt. Radiative equilibrium in rapidly expanding shells. *Astrophysical Journal*, 398(1):224 – 233, 1992.
- [17] P. H. Hauschildt. Multilevel non-lte radiative-transfer in expanding shells. *Journal of Quantitative Spectroscopy & Radiative Transfer*, 50(3):301 – 318, 1993.
- [18] C. K. Westbrook and F. L. Dryer. Chemical kinetic modeling of hydrocarbon combustion. *Progress in Energy and Combustion Science*, 10(1):1 – 57, 1984.
- [19] H. A. Arbib, Y. Goldman, J. B. Greenberg, and Y. M. Timnat. A numerical-model of high-intensity confined hydrocarbon combustion. *Combustion And Flame*, 38(3):259 – 270, 1980.
- [20] R. C. Brown, C. E. Kolb, S. Y. Cho, R. A. Yetter, F. L. Dryer, and H. Rabitz. Kinetic-model for hydrocarbon-assisted particulate boron combustion. *International Journal Of Chemical Kinetics*, 26(3):319 – 332, 1994.
- [21] E. Fernandez-Tarrazo, A. L. Sanchez, A. Linan, and F. A. Williams. A simple one-step chemistry model for partially premixed hydrocarbon combustion. *Combustion And Flame*, 147(1-2):32 – 38, 2006.
- [22] X. C. Guo and R. J. Madix. Hydrocarbon combustion at high oxygen coverage on palladium: A model study on pd(100). *Catalysis Letters*, 39(1-2):1 – 4, 1996.
- [23] P. H. Hauschildt and L. M. Ensmann. Analysis of the early spectra and light-curve of sn-1987a. *Astrophysical Journal*, 424(2):905 – 923, 1994.
- [24] P. H. Hauschildt, S. Starrfield, S. N. Shore, R. Gonzalezriestra, G. Sonneborn, and F. Allard. The early spectral evolution of nova cassiopeiae 1993. *Astronomical Journal*, 108(3):1008 – 1015, 1994.
- [25] P. H. Hauschildt and E. Baron. Non-lte treatment of fe-ii in astrophysical plasmas. *Journal of Quantitative Spectroscopy & Radiative Transfer*, 54(6):987 – 999, 1995.
- [26] E. Baron, P. H. Hauschildt, D. Branch, S. Austin, P. Garnavich, H. B. Ann, R. M. Wagner, A. V. Filippenko, T. Matheson, and J. Liebert. Non-lte spectral-analysis and model constraints on sn-1993j. *Astrophysical Journal*, 441(1):170 – 181, 1995.
- [27] F. Allard and P. H. Hauschildt. Model atmospheres for m (sub)dwarf stars .1. the base model grid. *Astrophysical Journal*, 445(1):433 – 450, 1995.
- [28] B. J. Alder and T. E. Wainwright. Phase transition for a hard sphere system. *The Journal of Chemical Physics*, 27(5):1208–1209, 1957.
- [29] B. J. Alder and T. E. Wainwright. Studies in molecular dynamics. i. general method. *The Journal of Chemical Physics*, 31(2):459–466, 1959.
- [30] A. Rahman. Correlations in the motion of atoms in liquid argon. *Phys. Rev.*, 136(2A):A405–A411, Oct 1964.
- [31] L. Verlet. Computer ”experiments” on classical fluids. i. thermodynamical properties of lennard-jones molecules. *Physical Review*, 159(1):98, Jul 1967.

- 
- [32] Y. Duan, L. Wang, and P. A. Kollman. The early stage of folding of villin headpiece subdomain observed in a 200-nanosecond fully solvated molecular dynamics simulation. *Proceedings of the National Academy of Sciences of the USA*, 95(17):9897 – 9902, 1998.
- [33] Q. Zhong, P. B. Moore, D. M. Newns, and M. L. Klein. Molecular dynamics study of the ls3 voltage-gated ion channel. *FEBS Letters*, 427(2):267 – 270, 1998.
- [34] Q. Zhong, Q. Jiang, P. B. Moore, D. M. Newns, and M. L. Klein. Molecular dynamics simulation of a synthetic ion channel. *Biophysics Journal*, 74(1):3–10, 1998.
- [35] R. Car and M. Parrinello. Unified approach for molecular-dynamics and density-functional theory. *Physical Review Letters*, 55(22):2471 – 2474, 1985.
- [36] V Pontikis and M Meyer, editors. volume 3. Proc. of ASI, Aussois (France), 1991, Kluwer Academic Publishers, Dordrecht, The Netherlands, 1991.
- [37] F. H. Stillinger and A. Rahman. Improved simulation of liquid water by molecular dynamics. *The Journal of Chemical Physics*, 60(4):1545–1557, 1974.
- [38] J. A. Mccammon, B. R. Gelin, and M. Karplus. Dynamics of folded proteins. *Nature*, 267(5612):585 – 590, 1977.
- [39] William C. Swope, Hans C. Andersen, Peter H. Berens, and Kent R. Wilson. A computer simulation method for the calculation of equilibrium constants for the formation of physical clusters of molecules: Application to small water clusters. *The Journal of Chemical Physics*, 76(1):637–649, 1982.
- [40] M. E. Tuckerman, C. J. Mundy, and G. J. Martyna. On the classical statistical mechanics of non-hamiltonian systems. *Europhysics Letters*, 45(2):149 – 155, 1999.
- [41] H. J. C. Berendsen, J. P. M. Postma, W. F. van Gunsteren, A. DiNola, and J. R. Haak. Molecular dynamics with coupling to an external bath. *The Journal of Chemical Physics*, 81(8):3684–3690, 1984.
- [42] Hans C. Andersen. Molecular dynamics simulations at constant pressure and/or temperature. *The Journal of Chemical Physics*, 72(4):2384–2393, 1980.
- [43] William G. Hoover. Canonical dynamics: Equilibrium phase-space distributions. *Phys. Rev. A*, 31(3):1695–1697, Mar 1985.
- [44] M. P. Allen and D. J. Tildesley. *Computer simulation of liquids*. Clarendon Press, Oxford, 1987.
- [45] G. Ciccotti, D. Frenkel, and I. R. McDonald. *Simulation of Liquids and Solids*. North Holland, Amsterdam, 1987.
- [46] R. Haberlandt, S. Fritzsche, G. Peinel, and K. Heinzinger. *Molekulardynamik - Grundlagen und Anwendungen, mit einem Kapitel ber Monte-Carlo-Simulationen von Monte-Carlo-Verfahren*. H.-L.V'ortler, Lehrbuch, Vieweg, Wiesbaden, 1995.
- [47] D. Frenkel and B. Smit. *Understanding Molecular Simulation - From Algorithms to Applications*. Academic Press, San Diego, 1996.
- [48] K. Binder and G. (ed.) Ciccotti. *Monte Carlo and Molecular Dynamics of Condensed Matter Systems*. Editrice Compositori, Bologna, Italy, 1996.

- 
- [49] B. J. Berne, G. Ciccotti, and Coker D. F. (Eds). *Classical and Quantum Dynamics in Condensed Phase Simulations*. Singapore: World Scientific, 1998.
- [50] R. Esser, P. Grassberger, J. Grotendorst, and M. (Eds.) M. Lewerenz. *Molecular Dynamics on Parallel Computers*. World Scientific, Singapore, 2000.
- [51] J. C. Tully. *Modern Theoretical Chemistry: Dynamics of Molecular Collisions, Part B, p. 217*, ed. W. H. Miller. Plenum Press, New York, 1976.
- [52] R. Schinke. *Photodissociation Dynamics*. Cambridge University Press, Cambridge,, 1995.
- [53] F. London. Quantenmechanische deutung der vorgaenge der aktivierung. *Zeitschrift für Elektrochemie*, 35:552–555, 1929.
- [54] M. Born, P. Jordan, and L. Nordheim. Zur Theorie der Stoßanregung von Atomen und Molekülen. *Naturwissenschaften*, 13:969–970, 1925.
- [55] M. Born and P. Jordan. Zur Quantentheorie aperiodischer Vorgänge. *Zeitschrift für Physik*, 33:479–505, 1925.
- [56] M. Born and P. Jordan. Zur Quantenmechanik. *Zeitschrift für Physik*, 34:858–888, 1925.
- [57] M. Born, W. Heisenberg, and P. Jordan. Zur Quantenmechanik. II. *Zeitschrift für Physik*, 35:557–615, 1926.
- [58] E. Schrödinger. über das verhältnis der heisenberg-born-jordanschen quantenmechanik zu der meinen. *Annalen der Physik*, 384:734–756, 1926.
- [59] E. Schrödinger. Der stetige übergang von der mikro- zur makromechanik. *Naturwissenschaften*, 14:664–666, 1926.
- [60] M. Born and J. R. Oppenheimer. Zur quantentheorie der molekeln. *Annalen d. Physik*, 84:457–484, 1927.
- [61] I. N. Levine. *Quantum Chemistry*. Allyn and Bacon, Boston, Boston, 1983.
- [62] J. C. Slater. *Quantum Theory of Matter*. McGraw-Hill, New York, McGraw-Hill, New York, 1968.
- [63] A. Szabo and N. S. Ostlund. *Modern Quantum Chemistry, Introduction to Advanced Electronic Structure Theory*. Dover Publications, New York, 1996.
- [64] D. R. Hartree. The wave mechanics of an atom with a non-coulomb central field. part i-theory and methods. *Proceedings of Cambridge Philosophical Society*, 24:89–110, 1928.
- [65] D. R. Hartree. The wave mechanics of an atom with a non-coulomb central field. part ii—some results and discussion. *Proceedings of Cambridge Philosophical Society*, 24:111–132, 1928.
- [66] D. R. Hartree. Wave mechanics of an atom with a non-coulomb central field. iii. term values and intensities in series in optical spectra. *Proceedings of Cambridge Philosophical Society*, 24:426–437, 1928.
- [67] D. R. Hartree. Further results relating to terms of the optical spectrum. *Proceedings of Cambridge Philosophical Society*, 25:310–314, 1929.

- [68] V. A. Fock. Näherungsmethode zur lösung des quantenmechanischen mehrkörperproblems. *Zeitschrift für Physik*, 61:126–148, 1930.
- [69] J. C. Slater. Note on hartree’s method. *Physical Review*, 35(2):210–211, Jan 1930.
- [70] R. McWeeny and B. T. Sutcliffe. *Methods of Molecular Quantum Mechanics*. Academic Press, London, London, 1969.
- [71] R. G. Parr. *Quantum Theory of Molecular Electronic Structure*. Benjamin, New York, New York, 1963.
- [72] F. L. Pilar. *Elementary Quantum Mechanics*. McGraw-Hill, New York, New York, 1968.
- [73] C. C. J. Roothaan. New developments in molecular orbital theory. *Reviews of Modern Physics*, 23(2):69–89, Apr 1951.
- [74] C. C. J. Roothaan. Self-consistent field theory for open shells of electronic systems. *Reviews of Modern Physics*, 32(2):179–185, Apr 1960.
- [75] R. J. Bartlett and J. F. Stanton. *Reviews in Computational Chemistry, Volume V, Lipkowitz K.B. and Boyd D.B.(Editors)*. VCH Publishers, New York, New York, 1994.
- [76] J. A. Pople, R. Krishnan, H. B. Schlegel, and J. S. Binkley. Electron correlation theories and their application to study of simple reaction potential surfaces. *International Journal of Quantum Chemistry*, 14(5):545 – 560, 1978.
- [77] P. R. Taylor. *Lecture Notes in Quantum Chemistry: European Summer School*. Springer-Verlag, Berlin, Berlin, 1994.
- [78] R. J. Bartlett. Many-body perturbation-theory and coupled cluster theory for electron correlation in molecules. *Annual Review Of Physical Chemistry*, 32:359 – 401, 1981.
- [79] K. Raghavachari, G. W. Trucks, J. A. Pople, and M. Headgordon. A 5th-order perturbation comparison of electron correlation theories. *Chemical Physics Letters*, 157(6):479 – 483, 1989.
- [80] M. Head-Gordon. Quantum chemistry and molecular processes. *Journal of Physical Chemistry*, 100(31):13213–13225, 1996.
- [81] J. M. Bowman. Self-consistent field energies and wavefunctions for coupled oscillators. *Journal of Chemical Physics*, 68(2):608 – 610, 1978.
- [82] T. C. Thompson and D. G. Truhlar. SCFCI calculations for vibrational eigenvalues and wavefunctions of systems exhibiting fermi resonance. *Chemical Physics Letters*, 75(1):87 – 90, 1980.
- [83] J. M. Bowman. The self-consistent-field approach to polyatomic vibrations. *Accounts of Chemical Research*, 19(7):202 – 208, 1986.
- [84] R. B. Gerber and M. A. Ratner. Self-consistent-field methods for vibrational excitations in polyatomic systems. *Advances in Chemical Physics*, 70:97 – 132, 1988.
- [85] D. A. Jelski, R. H. Haley, and J. M. Bowman. New vibrational self-consistent field program for large molecules. *Journal of Computational Chemistry*, 17(14):1645 – 1652, 1996.
- [86] J. K. G. Watson. Simplification of molecular vibration-rotation hamiltonian. *Mol. Phys.*, 15(5):479 – 490, 1968.

- 
- [87] J. K. G. Watson. Vibration-rotation hamiltonian of linear molecules. *Mol. Phys.*, 19(4):465 – 487, 1970.
- [88] S. Carter, J. M. Bowman, and N. C. Handy. Extensions and tests of "multimodes": a code to obtain accurate vibration/rotation energies of many-mode molecules. *Theoretical Chemistry Accounts*, 100(1-4):191 – 198, 1998.
- [89] S. Carter, J. M. Bowman, and L. B. Harding. Ab initio calculations of force fields for H<sub>2</sub>CN and ClHCN and vibrational energies of H<sub>2</sub>CN. *Spectrochimica Acta. A.*, 53(8):1179 – 1188, 1997.
- [90] D. Papoušek and M. R. Aliev. *Molecular Vibrational-Rotational Spectra*. (Elsevier, New York, 1982.
- [91] S. Carter, Susan J. Culik, and Joel M. Bowman. Vibrational self-consistent field method for many-mode systems: A new approach and application to the vibrations of co adsorbed on cu(100). *Journal of Chemical Physics*, 107(24):10458–10469, 1997.
- [92] Joon O. Jung and R. Benny Gerber. Vibrational wave functions and spectroscopy of (H<sub>2</sub>O)<sub>n</sub>, n = 2, 3, 4, 5: Vibrational self-consistent field with correlation corrections. *The Journal of Chemical Physics*, 105(23):10332–10348, 1996.
- [93] Joon O. Jung and R. Benny Gerber. Vibrational wave functions and energy levels of large anharmonic clusters: A vibrational SCF study of (Ar)<sub>13</sub>. *The Journal of Chemical Physics*, 105(24):10682–10690, 1996.
- [94] S. Carter and J. M. Bowman. The adiabatic rotation approximation for rovibrational energies of many-mode systems: Description and tests of the method. *Journal of Chemical Physics*, 108(11):4397–4404, 1998.
- [95] R. J. Whitehead and N. C. Handy. Variational calculation of vibration-rotation energy-levels for triatomic-molecules. *Journal of Molecular Spectroscopy*, 55(1-3):356 – 373, 1975.
- [96] R. J. Whitehead and N. C. Handy. Variational calculation of low-lying and excited vibrational levels of water molecule. *Journal Of Molecular Spectroscopy*, 59(3):459 – 469, 1976.
- [97] S. Carter, H. M. Shnider, and J. M. Bowman. Variational calculations of rovibrational energies of ch<sub>4</sub> and isotopomers in full dimensionality using an ab initio potential. *The Journal of Chemical Physics*, 110(17):8417–8423, 1999.
- [98] D.L. Bunker. Classical trajectory methods. *Methods Computational Physics*, 10:287–325, 1971.
- [99] R. N. Porter and L. M. Raff. *Dynamics of Molecular Collisions*, edited by W. H. Miller, *Modern Theoretical Chemistry*. Plenum, New York, 1976.
- [100] D. G. Truhlar and J. T. Muckerman. *Reactive Scattering Cross Sections: Quasiclassical and Semiclassical Methods in Atom-Molecule Collision Theory: A Guide for the Experimentalist*, edited by R. B. Bernstein. Plenum Press, New York, 1979.
- [101] L. M. Raff and D. L. Thompson. *Theory of Chemical Reaction Dynamics, Vol. III, M. Baer (Ed.)*. CRC Press, Boca Raton, FL., 1985.
- [102] M. C. Gutzwiller. *Chaos in Classical and Quantum Mechanics*. Springer-Verlag, New York, 1990.

- 
- [103] P. Hohenberg and W. Kohn. Inhomogeneous electron gas. *Physical Review*, 136(3B):B864–B871, Nov 1964.
- [104] E. Fermi. Eine statistische Methode zur Bestimmung einiger Eigenschaften des Atoms und ihre Anwendung auf die Theorie des periodischen Systems der Elemente. *Z. f. Physik*, 48:73–79, 1928.
- [105] L. H. Thomas. The calculation of atomic fields. *Proceedings Cambridge*, 23:542–548, 1927.
- [106] P. A. M. Dirac. Note on exchange phenomena in the Thomas atom. *Proceedings Cambridge*, 26:376–385, 1930.
- [107] W. Kohn and L. J. Sham. Self-consistent equations including exchange and correlation effects. *Physical Review*, 140(4A):A1133–A1138, Nov 1965.
- [108] R. O. Jones and O. Gunnarsson. The density functional formalism, its applications and prospects. *Reviews Of Modern Physics*, 61(3):689 – 746, 1989.
- [109] J. C. Phillips. Energy-band interpolation scheme based on a pseudopotential. *Physical Review*, 112(3):685 – 695, 1958.
- [110] J. C. Phillips and L. Kleinman. New method for calculating wave functions in crystals and molecules. *Physical Review*, 116(2):287 – 294, 1959.
- [111] Volker Heine. *The Pseudopotential Concept, vol. 24 of Solid State Physics, p. 1*. Academic Press, New York, 1970.
- [112] J. Ihm. Total energy calculations in solid-state physics. *Reports On Progress In Physics*, 51(1):105 – 142, 1988.
- [113] W. E. Pickett. Pseudopotential methods in condensed matter applications. *Computer Physics Reports*, 9(3):115 – 197, 1989.
- [114] N. Troullier and J. L. Martins. Efficient pseudopotentials for plane-wave calculations. *Physical Review B*, 43(3):1993 – 2006, 1991.
- [115] D. Vanderbilt. Soft self-consistent pseudopotentials in a generalized eigenvalue formalism. *Physical Review B*, 41(11):7892 – 7895, 1990.
- [116] E. L. Shirley, D. C. Allan, R. M. Martin, and J. D. Joannopoulos. Extended norm-conserving pseudopotentials. *Physical Review B*, 40(6):3652 – 3660, 1989.
- [117] J. N. Murrell, S. Cater, S. C. Farantos, P. Huxley, and A. J. C. Varandas. *Molecular Potential Energy Functions*. Wiley-Interscience, 1984.
- [118] E. Anderson, Z. Bai, C. Bischof, S. Blackford, J. Demmel, J. Dongarra, J. Du Croz, A. Greenbaum, S. Hammarling, A. McKenney, and D. Sorensen. Lapack users’ guide, 3rd ed., 22 Aug 1999.
- [119] H. Derksen and G. Kemper. *Computational Invariant Theory*. Springer Verlag, Berlin, Heidelberg, New York, 2002.
- [120] G. Kemper and A. Steel. Some algorithms in invariant theory of finite groups, proceedings of the euroconference on computational methods for representations of groups and algebras, p. draexler, g.o. michler, and c.m. ringel, eds., 1998.

- 
- [121] G. Kemper and A. Steel. Computational methods for representations of groups and algebras, progress in mathematics, 1999.
- [122] C. Playoust W. Bosma, J. Cannon. The magma algebra system I: The user language. *J. Symbolic Comput.*, 24:235–265, 1997.
- [123] R. K. Janev and D. Reiter. Collision processes of  $\text{CH}_y$  and  $\text{CH}_y^+$  hydrocarbons with plasma electrons and protons. *Physics of Plasmas*, 9(9):4071 – 4081, 2002.
- [124] R. K. Janev and D Reiter. Collision processes of hydride species in hydrogen plasmas: Iii. the silane family. *Contributions to Plasma Physics*, 43(7):401 – 417, 2003.
- [125] R. K. Janev and D Reiter. Unified analytic representation of hydrocarbon impurity collision cross-sections. *Journal of Nuclear Materials*, 313-316:1202 – 1205, 2003.
- [126] R. K. Janev and D Reiter. Collision processes of  $\text{c}_2\text{h}_y$  and  $\text{c}_2\text{h}_y^+$  hydrocarbons with electrons and protons. *Physics of Plasmas*, 11(2):780 – 829, 2004.
- [127] A. E. Glassgold, A. Omont, and M. Guelin. Protonated acetylene - an important circumstellar and interstellar ion. *Astrophysical Journal*, 396(1):115 – 119, 1992.
- [128] D. Marx and M. Parrinello. The effect of quantum and thermal fluctuations on the structure of the floppy molecule  $\text{C}_2\text{H}_3^+$ . *Science*, 271(5246):179 – 181, 1996.
- [129] R. Lindh, B. O. Roos, and W. P. Kraemer. A CASSCF study of the hydrogen migration potential in protonated acetylene,  $\text{C}_2\text{H}_3^+$ . *Chemical Physics Letters*, 139(5):407 – 416, 1987.
- [130] C. Liang, T. P. Hamilton, and H. F. Schaefer III. Classical and nonclassical forms of the vinyl cation: A coupled cluster study. *Journal of Chemical Physics*, 92(6):3653–3658, 1990.
- [131] B. Zurawski, R. Ahlrichs, and W. Kutzelnigg. Have ions  $\text{c}_2\text{h}_3^+$  and  $\text{c}_2\text{h}_5^+$  classical or non-classical structure. *Chemical Physics Letters*, 21(2):309 – 313, 1973.
- [132] M. W. Crofton, Mary-Frances Jagod, Brent D. Rehfuss, and Takeshi Oka. Infrared spectroscopy of carbo-ions. v. classical vs nonclassical structure of protonated acetylene  $\text{C}_2\text{H}_3^+$ . *Journal of Chemical Physics*, 91(9):5139–5153, 1989.
- [133] C. M. Gabrys, D. Uy, M. F. Jagod, T. Oka, and T. Amano. Infrared-spectroscopy of carboions .8. hollow-cathode spectroscopy of protonated acetylene,  $\text{C}_2\text{H}_3^+$ . *Journal of Physical Chemistry*, 99(42):15611 – 15623, 1995.
- [134] L. Knoll, Z. Vager, and D. Marx. Experimental versus simulated coulomb-explosion images of flexible molecules: Structure of protonated acetylene  $\text{C}_2\text{H}_3^+$ . *Physical Review A*, 67(2):022506, 2003.
- [135] Z. Vager, D. Zajfman, T. Graber, and E. P. Kanter. Experimental-evidence for anomalous nuclear delocalization in  $\text{C}_2\text{H}_3^+$ . *Physical Review Letters*, 71(26):4319 – 4322, 1993.
- [136] W. Klopper and W. Kutzelnigg. MP2 – R12 calculations on the relative stability of carbocations. *Journal of Physical Chemistry*, 94(14):5625 – 5630, 1990.
- [137] R. Lindh, J. E. Rice, and T. J. Lee. The energy separation between the classical and nonclassical isomers of protonated acetylene - an extensive study in one-particle and n-particle space saturation. *Journal of Chemical Physics*, 94(12):8008 – 8014, 1991.

- [138] T. J. Lee and H. F. Schaefer III. The classical and nonclassical forms of protonated acetylene,  $C_2H_3^+$  structures, vibrational frequencies, and infrared intensities from explicitly correlated wave functions. *Journal of Chemical Physics*, 85(6):3437–3443, 1986.
- [139] G. P. Raine and H. F. Schaefer III. Vibrational frequencies for the classical and nonclassical forms of protonated acetylene- $C_2H_3^+$ . *Journal of Chemical Physics*, 81(9):4034–4037, 1984.
- [140] J. A. Pople. The structure of the vinyl cation. *Chemical Physics Letters*, 137(1):10 – 12, 1987.
- [141] Larry A. Curtiss and J. A. Pople. Theoretical study of structures and energies of acetylene, ethylene, and vinyl radical and cation. *Journal of Chemical Physics*, 88(12):7405–7409, 1988.
- [142] A. Brown, B. J. Braams, A. Christoffel, Z. Jin, and J. M. Bowman. Classical and quasi-classical spectral analysis of  $CH_5^+$  using an ab initio potential energy surface. *Journal of Chemical Physics*, 119:8790–8793, 2003.
- [143] A. Brown, A. B. McCoy, B. J. Braams, Z. Jin, and J. M. Bowman. Quantum and classical studies of vibrational motion of  $cH_5^+$  on a global potential energy surface obtained from a novel ab initio direct dynamics approach. *Journal of Chemical Physics*, 121:4105–4116, 2004.
- [144] X. Huang, B. J. Braams, and J. M. Bowman. Ab initio potential energy and dipole moment surfaces of  $(H_2O)_2$ . *Journal of Physical Chemistry A*, 110(2):445 – 451, 2006.
- [145] X. Huang, B. J. Braams, and J. M. Bowman. Ab initio potential energy and dipole moment surfaces for  $H_5O_2^+$ . *Journal of Chemical Physics*, 122(044308):044308–12, 2005.
- [146] X. Huang, B. J. Braams, S. Carter, and J. M. Bowman. Quantum calculations of vibrational energies of  $H_3O_2^-$  on an ab initio potential. *Journal of American Chemical Society*, 126(16):5042–5043, 2004.
- [147] A. B. McCoy, B. J. Braams, A. Brown, X. Huang, X. Jin, and J. M. Bowman. Ab initio diffusion monte carlo calculations of the quantum behavior of  $CH_5^+$  in full dimensionality. *Journal of Physical Chemistry A*, 108(23):4991–4994, 2004.
- [148] S. C. Park, B. J. Braams, and J. M. Bowman. Construction of a global potential energy surface from novel ab initio molecular dynamics for the  $O(3P) + C_3H_3$  reaction. *Journal of Theoretical & Computational Chemistry*, 4(1):163–173, 2005.
- [149] P. J. Knowles, C. Hampel, and H.-J. Werner. Coupled-cluster theory for high-spin, open-shell reference wave-functions. *Journal of Chemical Physics*, 99(7):5219 – 5227, 1993.
- [150] P. J. Knowles, C. Hampel, and H.-J. Werner. Coupled cluster theory for high spin, open shell reference wave functions (vol 99, pg 5219, 1993). *Journal of Chemical Physics*, 112(6):3106 – 3107, 2000.
- [151] T. H. Dunning. Gaussian-basis sets for use in correlated molecular calculations .1. the atoms boron through neon and hydrogen. *Journal of Chemical Physics*, 90(2):1007 – 1023, 1989.
- [152] R. A. Kendall, T. H. Dunning Jr., and R. J. Harrison. Electron affinities of the first-row atoms revisited. systematic basis sets and wave functions. *Journal of Chemical Physics*, 96(9):6796–6806, 1992.

- 
- [153] H. J. Werner, P. J. Knowles, R. Lindh, F. R. Manby, M. Schütz, et al. Molpro, version 2006.1, a package of ab initio programs, 2006. see <http://www.molpro.net>.
- [154] C. Møller and M. S. Plesset. Note on an approximation treatment for many-electron systems. *Physical Review*, 46(7):618 – 622, 1934.
- [155] JA Pople, JS Binkley, and R Seeger. Theoretical models incorporating electron correlation. *International Journal of Quantum Chemistry*, pages 1 – 19, 1976.
- [156] R. Krishnan, M. J. Frisch, and J. A. Pople. Contribution of triple substitutions to the electron correlation-energy in 4th order perturbation-theory. *Journal of Chemical Physics*, 72(7):4244 – 4245, 1980.
- [157] M. J. Frisch, R. Krishnan, and J. A. Pople. A systematic study of the effect of triple substitutions on the electron correlation-energy of small molecules. *Chemical Physics Letters*, 75(1):66 – 68, 1980.
- [158] T. E. Cravens, I. P. Robertson, J. H. Waite, R. V. Yelle, W. T. Kasprzak, C. N. Keller, S. A. Ledvina, H. B. Niemann, J. G. Luhmann, R. L. McNutt, WH Ip, V De la haye, I Mueller-Wodarg, JE Wahlund, VG Anicich, and V Vuitton. Composition of titan’s ionosphere. *Geophysical Research Letters*, 33(7):L07105, 2006.
- [159] T. E. Cravens, J Vann, J Clark, J Yu, C. N. Keller, and C Brull. The ionosphere of titan: an updated theoretical model. *Planetary Atmospheres, Ionospheres And Plasma Interactions*, 33(2):212 – 215, 2004.
- [160] C. N. Keller, V. G. Anicich, and T. E. Cravens. Model of titan’s ionosphere with detailed hydrocarbon ion chemistry. *Planetary And Space Science*, 46(9-10):1157 – 1174, 1998.
- [161] J. L. Fox and R. V. Yelle. Hydrocarbon ions in the ionosphere of titan. *Geophysical Research Letters*, 24(17):2179 – 2182, 1997.
- [162] M. Wolfsberg L. J. Massa, S. Ehrenson. Gaussian molecular orbital calculations of the barrier to internal rotation in the ethyl cation. *International Journal of Quantum Chemistry*, 4(6):625–630, 1970.
- [163] L. J. Massa, S. Ehrenson, M. Wolfsber, and C. A. Frishber. Gaussian molecular orbital calculations of hyperconjugation in ethyl cation. *Chemical Physics Letters*, 11(2):196 – 197, 1971.
- [164] W. Quapp and D. Heidrich. Exploring the potential energy surface of the ethyl cation by new procedures. *Journal of Molecular Structure-Theochem*, 585:105 – 117, 2002.
- [165] G. Trinquier. Polymorphism in the heavier analogs of the ethyl cation. *Journal of the American Chemical Society*, 114(17):6807 – 6820, 1992.
- [166] K. Raghavachari, R. A. Whiteside, J. A. Pople, and P. V. Schleyer. Molecular-orbital theory of the electronic-structure of organic-molecules .40. structures and energies of c-1-c-3 carbocations, including effects of electron correlation. *Journal of the American Chemical Society*, 103(19):5649 – 5657, 1981.
- [167] P. C. Hariharan, W. A. Lathan, and J. A. Pople. Molecular-orbital theory of simple carbonium-ions. *Chemical Physics Letters*, 14(4):385 – 388, 1972.

- [168] R. Sustmann, J. E. Williams, M. J. S. Dewar, L. C. Allen, and P. V. Schleyer. Molecular orbital calculations on carbonium ions .2. methyl, ethyl, and vinyl cations . series  $C_3H_7^+$ . *Journal of the American Chemical Society*, 91(19):5350 – 5357, 1969.
- [169] H. Lischka and H. J. Kohler. Structure and stability of carbocations  $C_2H_3^+$  and  $C_2H_4X^+$ ,  $X = H, F, Cl$ , and  $CH_3$  - ab-initio investigation including electron correlation and a comparison with MINDO – 3 results. *Journal Of The American Chemical Society*, 100(17):5297 – 5305, 1978.
- [170] E. P. Kanter, Z. Vager, G. Both, and D. Zajfman. A measurement of the low-energy stereostructure of protonated acetylene,  $C_2H_3^+$ . *Journal of Chemical Physics*, 85(12):7487 – 7488, 1986.
- [171] J. S. Tse, D. D. Klug, and K. Laasonen. Structural dynamics of protonated methane and acetylene. *Physical Review Letters*, 74(6):876 – 879, 1995.
- [172] J. M. Bowman, S. Carter, and X. Huang. Multimode: a code to calculate rovibrational energies of polyatomic molecules. *International Reviews in Physical Chemistry*, 22:533–549, 2003.
- [173] H. Meyer. The molecular hamiltonian. *Annual Review of Physical Chemistry*, 53:141 – 172, 2002.
- [174] M. A. Ratner and R. B. Gerber. Excited vibrational states of polyatomic molecules: the semiclassical self-consistent field approach. *Journal Of Physical Chemistry*, 90(1):20 – 30, 1986.
- [175] S. Carter and N. C. Handy. The vibrations of  $H_2O_2$ , studied by “multimode,” with a large amplitude motion. *Journal of Chemical Physics*, 113(3):987–993, 2000.
- [176] R. Escribano and P. R. Bunker. Rotation and internal-rotation in the vinyl cation  $c_2h_3^+$ . *JMS*, 122(2):325 – 340, 1987.
- [177] W. H. Miller, N. C. Handy, and John E. Adams. Reaction path hamiltonian for polyatomic molecules. *Journal of Chemical Physics*, 72(1):99–112, 1980.
- [178] R. K. Janev and D. D. Reiter. Collision processes of hydrocarbon species in hydrogen plasmas. ii. ethane & propane families. Technical Report Juel-Report 4005, Forschungszentrum Jülich, Jülich, July 2004.
- [179] W. L. Hase, R. J. Duchovic, X. Hu, A. Komornicki, et al. Venus96: A general chemical dynamics computer program. *Quantum Chemistry Program Exchange* 16, 671, 1996.
- [180] I. H. Hutchinson, R. Boivin, F. Bombarda, P. Bonoli, S. Fairfax, C. Fiore, J. Goetz, S. Golovato, et al. 1st results from ALCATOR – C – MOD. *Physics of Plasmas*, 1(5):1511 – 1518, 1994.
- [181] M. L. Apicella, G. Apruzzese, M. Borra, G. Bracco, M. Ciotti, I. Condrea, F. Crisanti, et al. Experiments in ftu with different limiter materials. *Nuclear Fusion*, 37(3):381 – 396, 1997.
- [182] G. L. Jackson, D. R. Baker, K. L. Holtrop, S. Konoshima, R. Maingi, G. M. Staebler, and W. P. West. Effects of particle fueling and plasma wall interactions on DIII – D discharges. *Journal of Nuclear Materials*, 222:173 – 177, 1995.

- 
- [183] M. D. Mcsmith, G. D. Loesser, and D. K. Owens. Modification and final alignment of the TFTR bumper limiter. *Fusion Technology*, 26(3):498 – 502, 1994.
- [184] M. Ulrickson. A review of carbon blooms on JET and TFTR. *Journal of Nuclear Materials*, 176:44 – 50, 1990.
- [185] J. D. Strachan, M. Bell, A. Janos, S. Kaye, S. Kilpatrick, D. Manos, D. Mansfield, D. Mueller, K. Owens, C. S. Pitcher, J. Snipes, and J. Timberlake. Experiments on TFTR supersonic plasmas. *Journal of Nuclear Materials*, 196:28 – 34, 1992.
- [186] J.F. Ziegler. *Handbook of Ion Implantation Technology*. North Holland, Amsterdam, 1992.
- [187] W. Eckstein. Reflection, atomic and plasma-material interaction data for fusion, vol. 1, nucl. fusion supplement, 1991.
- [188] B. L. Doyle, D. K. Brice, and W. R. Wampler. Hydrogen in fusion 1st wall surfaces. *IEEE Transactions On Nuclear Science*, 28(2):1300 – 1303, 1981.
- [189] B. L. Doyle, W. R. Wampler, D. K. Brice, and S. T. Picraux. Saturation and isotopic replacement of deuterium in low-z materials. *Journal of Nuclear Materials*, 93-4(October):551 – 557, 1980.
- [190] J. W. Davis and A. A. Haasz. Reemission of hydrogen and deuterium from graphite for temperatures between 1000-k and 1600-k. *Journal of Nuclear Materials*, 183(3):229 – 232, 1991.
- [191] J. W. Davis, A. A. Haasz, and D. S. Walsh. Flux and fluence dependence of H<sup>+</sup> trapping in graphite. *Journal of Nuclear Materials*, 176:992 – 999, 1990.
- [192] S. Chiu and A. A. Haasz. Chemical-release of implanted deuterium in graphite. *Journal of Vacuum Science & Technology A-Vacuum Surfaces And Films*, 9(3):747 – 752, 1991.
- [193] R. A. Causey. The interaction of tritium with graphite and its impact on tokamak operations. *Journal of Nuclear Materials*, 162:151 – 161, 1989.
- [194] V. N. Chernikov, W. R. Wampler, A. P. Zakharov, and A. E. Gorodetsky. Deuterium trapping in deep traps of differently oriented pyrolytic graphite exposed to D<sub>2</sub> gas at 1473 k. *Journal of Nuclear Materials*, 264(1-2):180 – 197, 1999.
- [195] A. A. Haasz and J. W. Davis. Fluence dependence of deuterium trapping in graphite. *Journal of Nuclear Materials*, 209(2):155 – 160, 1994.
- [196] K. N. Kushita, I. Youle, A. A. Haasz, and J. A. Sawicki. Tritium diffusion in pseudo-monocrystal graphite, observed with a tritium imaging camera. *Journal of Nuclear Materials*, 179:235 – 238, 1991.
- [197] R. D. Penzhorn, N. Bekris, U. Berndt, J. P. Coad, H. Ziegler, and W. Nagele. Tritium depth profiles in graphite and carbon fibre composite material exposed to tokamak plasmas. *Journal of Nuclear Materials*, 288(2-3):170 – 178, 2001.
- [198] M. Warrior. *Multi-scale modeling of hydrogen isotope transport in porous graphite*. PhD thesis, Ernst Moritz Arndt University of Greifswald, 2004.
- [199] D. W. Brenner. Empirical potential for hydrocarbons for use in simulating the chemical vapor-deposition of diamond films. *Physical Review B*, 42(15):9458 – 9471, 1990.

- 
- [200] K. Nordlund, J. Keinonen, and T. Mattila. Formation of ion irradiation induced small-scale defects on graphite surfaces. *Physical Review Letters*, 77(4):699–702, Jul 1996.
- [201] N. A. Marks, N. C. Cooper, D. R. McKenzie, D. G. McCulloch, P. Bath, and S. P. Russo. Comparison of density-functional, tight-binding, and empirical methods for the simulation of amorphous carbon. *Phys. Rev. B*, 65(7):075411, Jan 2002.
- [202] R. Car and M. Parrinello. The unified approach to density functional and molecular-dynamics in real space. *Solid State Communications*, 62(6):403 – 405, 1987.
- [203] R. Car and M. Parrinello. Structural, dynamical, and electronic-properties of amorphous-silicon - an abinitio molecular-dynamics study. *Physical Review Letters*, 60(3):204 – 207, 1988.
- [204] N. Ooi, A. Rairkar, and J. B. Adams. Density functional study of graphite bulk and surface properties. *Carbon*, 44(2):231 – 242, 2006.
- [205] Axel D. Becke. Density-functional thermochemistry. III. the role of exact exchange. *Journal of Chemical Physics*, 98(7):5648–5652, 1993.
- [206] C. Lee, W. Yang, and R. G. Parr. Development of the colle-salvetti correlation-energy formula into a functional of the electron density. *Physics Review B*, 37(2):785–789, Jan 1988.
- [207] N. Troullier and J. L. Martins. Efficient pseudopotentials for plane-wave calculations .2. operators for fast iterative diagonalization. *Physical Review B*, 43(11):8861 – 8869, 1991.
- [208] L. Kleinman and D. M. Bylander. Efficacious form for model pseudopotentials. *Physics Review Letters*, 48(20):1425–1428, May 1982.
- [209] W. Jacob. Redeposition of hydrocarbon layers in fusion devices. *Journal of Nuclear Materials*, 337-339:839–846, 2005.
- [210] G. Federici, C. H. Skinner, J. N. Brooks, J. P. Coad, C. Grisolia, A. A. Haasz, A. Hassanein, V. Philipps, C. S. Pitcher, J. Roth, W. R. Wampler, and D. G. Whyte. Plasma-material interactions in current tokamaks and their implications for next step fusion reactors. *Nuclear Fusion*, 41(12):1967–2137, 2001.
- [211] J. P. Coad, N. Bekris, J. D. Elder, S. K. Erents, D. E. Hole, K. D. Lawson, G. F. Matthews, R. D. Penzhorn, and P. C. Stangeby. Erosion/deposition issues at jet. *Journal of Nuclear Materials*, 290-293:224–230, 2001.
- [212] M. Mayer, V. Philipps, P. Wienhold, H. G. Esser, J. von Seggern, and M. Rubel. Hydrogen inventories in nuclear fusion devices. *Journal of Nuclear Materials*, 290-293:381–388, 2001.
- [213] V. Rohde, M. Mayer, and the ASDEX Upgrade Team. On the formation of a – C : D layers and parasitic plasmas underneath the roof baffle of the ASDEX upgrade divertor. *Journal of Nuclear Materials*, 313-316:337–341, 2003.
- [214] V. Rohde, M. Mayer, and the ASDEX Upgrade Team. Characterisation and formation of a – C : D layers below the divertor of ASDEX upgrade. *Physica Scripta*, T103:25–28, 2003.
- [215] M. Mayer, V. Rohde, A. von Keudell, and the ASDEX Upgrade Team. Characterisation of deposited hydrocarbon layers below the divertor and in the pumping ducts of ASDEX upgrade. *Journal of Nuclear Materials*, 313-316:429–433, 2003.

- 
- [216] M. Mayer, V. Rohde, J. Likonen, E. Vainonen-Ahlgren, K. Krieger, X. Gong, J. Chen, and ASDEX Upgrade Team. Carbon erosion and deposition on the ASDEX upgrade divertor tiles. *Journal of Nuclear Materials*, 337-339:119–123, 2005.
- [217] W. Bohmeyer, D. Naujoks, A. Markin, I. Arkhipov, B. Koch, D. Schrder, and G. Fussmann. Transport and deposition of injected hydrocarbons in plasma generator PSI – 2. *Journal of Nuclear Materials*, 337-339:89–93, 2005.
- [218] W. Bohmeyer, A. Markin, D. Naujoks, B. Koch, G. Krenz, M. Baudach, and G. Fussmann. Decomposition and sticking of hydrocarbons in the plasma generator PSI – II. *Journal of Nuclear Materials*, 363-365:122–130, 2006.
- [219] A. B. Erhardt and W. D. Langer. Collisional processes of hydrocarbons in hydrogen plasmas. Technical Report PPPL-2477, Princeton Plasma Physics Laboratory, September 1987.
- [220] D. A. Alman and D. N. Ruzic. A model of hydrocarbon reactions in low temperature hydrogen plasmas. *Physics of Plasmas*, 7:1421–1432, 2000.
- [221] J. N. Brooks, Z. Wang, D. N. Ruzic, and D. A. Alman. Hydrocarbon rate coefficients for proton and electron impact ionization, dissociation, and recombination in a hydrogen plasma: revised copy. Technical Report ANL/FPP/TM-297 REV, Argonne National Lab, May 1999.
- [222] R. K. Janev and D. D. Reiter. Collision processes of hydrocarbon species in hydrogen plasmas. I. the methane family. Technical Report Jul3966, Forschungszentrum Jülich, Jülich, July 2002.
- [223] D. Naujoks, D. Coster, H. Kastelewicz, and R. Schneider. Transport of hydrocarbon molecules in the edge plasma of fusion experiments. *Journal of Nuclear Materials*, 266-269:360–364, 1999.
- [224] D. Naujoks. Transport and deposition of hydrocarbons in the plasma generator PSI – 2. *Physica Scripta*, 111:80–85, 2004.
- [225] P. Träskelin, E. Salonen, K. Nordlund, J. Keinonen, and C. H. Wu. Molecular dynamics simulations of CH<sub>3</sub> sticking on carbon surfaces, angular and energy dependence. *Journal of Nuclear Materials*, 334:65–70, 2004.
- [226] A Pospieszczyk, G Sergienko, and D Rusbuldt. Molecular spectroscopy in TEXTOR. *Contributions To Plasma Physics*, 40(1-2):162 – 166, 2000.
- [227] J. R. Hiskes. The vibrational population-distribution for hydrogen molecules in a hydrogen discharge. *Bulletin Of The American Physical Society*, 25(8):981 – 981, 1980.
- [228] J. R. Hiskes. Identification of H<sub>2</sub>( $v''$ ) vibrational-excitation processes in a hydrogen discharge. *Applied Physics Letters*, 57(3):231 – 233, 1990.
- [229] G. C. Stutzin, A. T. Young, A. S. Schlachter, K. N. Leung, and W. B. Kunkel. Insitu measurement of rovibrational populations of H<sub>2</sub> ground electronic state in a plasma by vuv laser-absorption. *Chemical Physics Letters*, 155(4-5):475 – 480, 1989.
- [230] G. C. Stutzin, A. T. Young, H. F. Dobelev, A. S. Schlachter, K. N. Leung, and W. B. Kunkel. Insitu density and temperature-measurements of vibrationally excited hydrogen molecules in ion-source plasmas. *Review of Scientific Instruments*, 61(1):619 – 621, 1990.

- [231] P. J. Eenshuistra, J. H. M. Bonnie, J. Los, and H. J. Hopman. Observation of exceptionally high vibrational-excitation of hydrogen molecules formed by wall recombination. *Physical Review Letters*, 60(4):341 – 344, 1988.
- [232] P. J. Eenshuistra, R. M. A. Heeren, A. W. Kleyn, and H. J. Hopman. Dissociation and vibrational-excitation of H<sub>2</sub>-molecules and wall influence on the densities in a multicusp ion-source. *Physical Review A*, 40(7):3613 – 3625, 1989.
- [233] D. Marx and M. Parrinello. The effect of quantum and thermal fluctuations on the structure of the floppy molecule C<sub>2</sub>H<sub>3</sub><sup>+</sup>. *Science*, 271(5246):179–181, 1996.
- [234] Z. Vager, D. Zajfman, T. Graber, and E. P. Kanter. Experimental-evidence for anomalous nuclear delocalization in C<sub>2</sub>H<sub>3</sub><sup>+</sup>. *Physical Review Letters*, 71(26):4319–4322, 1993.
- [235] B. J. Braams, C. Chen, X. Huang, Z. Jin, Z. Xie, X. Zhang, J. M. Bowman, A. R. Sharma, and R. Schneider. Development of global potential energy surfaces for hydrocarbons up to C<sub>2</sub>H<sub>5</sub><sup>+</sup>. *231st ACS National Meeting, Atlanta, GA, March 26-30*, PHYS 433, 2006.
- [236] D. A. Alman and D. N. Ruzic. Molecular dynamics simulation of hydrocarbon reflection and dissociation coefficients from fusion-relevant carbon surfaces. *Physica Scripta*, T111:145–151, 2004.
- [237] A. R. Sharma, R. Schneider, U. Toussaint, and K. Nordlund. Hydrocarbon radicals interaction with amorphous carbon surface. *Journal of Nuclear Materials*, 363-365:1283 – 1288, 2007.

# Declaration

*I hereby declare that this work has so far neither been submitted to the Faculty of Mathematics and Natural Sciences at the Ernst-Moritz-Arndt-University of Greifswald nor to another scientific institution for the purpose of the degree of doctorate. Furthermore I declare that I have written this work by myself and that I have not used any other resources, other than mentioned earlier in this work.*

*Hiermit erkläre ich, dass diese Arbeit bisher von mir weder an der Mathematisch-Naturwissenschaftlichen Fakultät der Ernst-Moritz-Arndt-Universität Greifswald noch einer anderen wissenschaftlichen Einrichtung zum Zwecke der Promotion eingereicht wurde. Ferner erkläre ich, dass ich diese Arbeit selbstständig verfasst und keine anderen als die darin angegebenen Hilfsmittel benutzt habe.*

**Amit Raj Sharma**

# Curriculum Vitae

**Name:** Amit Raj Sharma

**Date of Birth:** 02 June 1973

**Place of Birth:** Kanker, India

**Gender:** Male

**Marital Status:** Married

**Citizenship:** Indian

**Address:** A-10, Bahnhofstraße 23, 17489 Greifswald

**Telephone:** 0049(0)3834-862644

**Email:** Amit.Raj.Sharma@ipp.mpg.de

## Employment History:

- **June 2005-till date:** Max-Planck-Institut für Plasmaphysik, Greifswald (Ph.D student)
- **Sep 1998-May 2005:** Institute For Plasma Research, Gandhinagar, India (Researcher)
- **Sep 1997 Aug 1998:** Government Engineering College, Raipur, India (Lecturer)

## Education:

- **Aug 1995 - Jul 1997:** Masters in Physics, School of Studies in Physics, Pt. Ravishankar Shukla University, Raipur, India
- **June 1992 - May 1995:** Bachelors in Science, St. Thomas College, Bilai, India
- **May 1989 - June 1991:** Higher Secondary School, Senior Secondary School, Sector-10, Bilai, India

# List of Publications

- “Hydrocarbon radicals interaction with amorphous carbon surface”, A. R. Sharma, R. Schneider, U. Toussaint, K. Nordlund, *Journal of Nuclear Materials*, 363-365, 1283 – 1288, 2007.
- “Introduction to molecular dynamics”, R. Schneider, A. R. Sharma, A. Rai, Lecture notes in physics 739, *Computational Many-Particle Physics*, (Ed.) H. Fehske, R. Schneider and A. Weisse, Springer Verlag, Berlin Heidelberg, 3-40, 2008, Wilhelm & Else Heraeus Summer school, in press.
- “Potential energy surface and multimode vibrational analysis of  $C_2H_3^+$ ”, A. R. Sharma, J. Wu, B. Braams, S. Carter, R. Schneider, B. Shepler and J. M. Bowman, *Journal of Chemical Physics*, 125, 224306, 2006.
- “Multimode vibrational analysis of  $C_2H_5^+$  using full dimensional *ab initio* potential energy surface and dipole moment surface”, A. R. Sharma, B. Braams, S. Carter, R. Schneider, B. Shepler and J. M. Bowman, to be submitted, 2007.
- “*Ab initio* molecular dynamics of hydrogen diffusion between Graphite Layers”, A. R. Sharma and R. Schneider, to be submitted, 2007.